

Engineering of supramolecular self-assembly in solution-processed organic semiconductors

THÈSE N° 7994 (2017)

PRÉSENTÉE LE 1 SEPTEMBRE 2017

À LA FACULTÉ DES SCIENCES DE BASE

LABORATOIRE D'INGÉNIERIE MOLÉCULAIRE DES NANOMATÉRIAUX OPTOÉLECTRONIQUES

PROGRAMME DOCTORAL EN CHIMIE ET GÉNIE CHIMIQUE

ÉCOLE POLYTECHNIQUE FÉDÉRALE DE LAUSANNE

POUR L'OBTENTION DU GRADE DE DOCTEUR ÈS SCIENCES

PAR

Xavier Adrian JEANBOURQUIN

acceptée sur proposition du jury:

Prof. J.-E. Moser, président du jury

Prof. K. Sivula, directeur de thèse

Prof. N. Banerji, rapporteuse

Dr O. Enger, rapporteur

Prof. F. Nüesch, rapporteur



ÉCOLE POLYTECHNIQUE
FÉDÉRALE DE LAUSANNE

Suisse
2017

*À Natacha,
Marianne et Pascal*

« I am enough of an artist to draw freely upon my imagination. Imagination is more important than knowledge. Knowledge is limited. Imagination encircles the world. »

A. Einstein

Acknowledgements

Looking back on my thesis, it has been a great journey with always enough motivation and positive attitude to overcome the raising challenges. Of course, it would have been impossible on my own, without the great support of all the people around me.

First of all, thank you Kevin for giving me the opportunity to be part of the LIMNO genesis. Your advices and support on my projects as well as your constant enthusiasm in developing new setups meant a lot to me.

I am also deeply grateful to all my colleagues who made this time in EPFL a joyful experience. Andrea, thank you for your energy, dedication and constant motivation which helped me along my projects. Aiman, this thesis would not have been possible without your great synthetic skills and collaboration as well as the inspiring jam sessions. Thank you Nestor for your constant support and discussion. I will miss your amazing stories. Mathieu, always there for adventure; thanks for your good mood and motivation whether in lab, in the Alps or in Bayonne. Pauline, my compatriot in LIMNO, thank you for your kindness and generosity. Florian, always ready to help and have fun, many thanks. And also thank you Xiaoyun, Melissa, Liang, Jun-Ho and Arvin for all your help and fruitful collaborations.

I would like to take this opportunity to also thank the Jury members for your interest in this thesis and taking time to go through it. And also, Kevin, Aiman, Mathieu, Florian, Nestor, Liang and Natacha for helping me with the revision of the thesis.

Many thanks also to my friends for helping me taking my mind off the thesis, especially Christina, Soraya, Tiffany, Lisa, Alain (*aka* Fox), Frédéric, Nicolas and Renato.

Finally, I would like to thank my loving wife, my brother and my parents without whom this thesis would not have been possible. Merci Loic de tous les moments partagés. Merci Marianne et Pascal d’avoir toujours cru en moi et pour votre soutien inconditionnel. Natacha merci de me supporter au quotidien et de toujours m’amener à donner le meilleur de moi-même.

Summary

Organic semiconductors have recently emerged as a promising alternative to standard inorganic semiconductors for many commercial applications. Their ability to be processed from solution combined with their unique mechanical resistance paves the way for low cost roll-to-roll production of flexible devices. While, for screen and lighting applications, organic light emitting diodes are already well-established on the market, further understanding and development remains to be achieved for organic-based field effect transistor and photovoltaic devices to be commercially viable. Especially, the impact of supramolecular self-assembly on the opto-electronic properties of organic semiconductors persist in being a key challenge.

The original work presented in this thesis explores the poorly understood relationship between supramolecular assembly of solution-processed organic semiconductors and the corresponding performances in transistor and photovoltaic applications. Additionally, novel strategies and tailored molecular tools are developed as to permit rational engineering of the self-assembly and offer unprecedented control over the device performances.

In brief, this thesis first addresses the controversial band-like temperature dependence of the charge carrier mobility in organic semiconductors. An alternative physical origin for this behaviour is proposed by considering a temperature dependent biphasic equilibrium in solid-state using a small molecule, coded DPP(TBFu)₂, which offers a unique case study for this new model. This work then explores the underlying mechanism behind aliphatically-linked organic semiconductors to control the crystal structure, focusing on two distinct dimers based on DPP(TBFu)₂. The linker position in these dimers is found to greatly affect the self-assembly and the driving force governing crystallization events, overall leading to either enhanced hole mobility in transistor or enhanced thermal stability in photovoltaic devices. Following work demonstrate a simple charge cascade self-assembly in solar cells based on crystallinity differences between a host blend and an amorphous ternary compound, exceeding 30 % enhancement in the power conversion efficiency. Finally, the effect of the polymer molecular weight on blend self-assembly and photovoltaic performances is investigated for an amorphous polymer coded PDPP4T-TT and a semicrystalline one, coded PBTTT.

Keywords: *Organic semiconductors, organic field effect transistors, organic photovoltaics, hopping transport, self-assembly, supramolecular assembly, aliphatic linker, ternary photovoltaic, bulkheterojunction.*

Résumé

Dans le but d'une application commerciale potentielle, les semiconducteurs organiques se sont récemment révélés être une alternative prometteuse aux semiconducteurs inorganiques. En effet, la possibilité de les imprimer à partir d'une solution permet une fabrication plus économique. Qui plus est, leur résistance mécanique unique rend possible le développement de technologies sur des substrats flexibles. Bien que les nouvelles technologies en matière d'écrans ou simplement d'éclairage soient de plus en plus basées sur des semiconducteurs organiques, il reste énormément d'efforts à fournir afin d'étendre leur utilisation aux transistors pour l'électronique ou aux technologies photovoltaïques. Cependant, le rôle crucial de l'assemblage supramoléculaire sur les propriétés optoélectroniques de ces matériaux demeure une barrière pour leur utilisation à grande échelle.

Les travaux originaux présentés dans cette thèse explorent la relation entre la structure supramoléculaire de ces semiconducteurs organiques et leurs performances en tant que transistors et cellules solaires. En vue d'améliorer le contrôle de cet assemblage intermoléculaire, de nouvelles stratégies ainsi que des outils de type moléculaire sont développés. Ils permettent ainsi une ingénierie rationnelle de la structure supramoléculaire sans précédent.

En bref, cette thèse traite tout d'abord de la controverse concernant le transport de bande dans les matériaux organiques. Celui-ci est suggéré par la dépendance de la mobilité des porteurs de charge sur la température. Cependant, ce phénomène peut aussi être considéré comme le résultat d'un équilibre biphasique dépendant de la température et dans lequel les porteurs de charge sont en fait localisés. Cette nouvelle théorie permet d'expliquer le comportement unique de transistors, basés sur une molécule codée DPP(TBFu)₂, avec la température. Ce travail explore ensuite les mécanismes sous-jacents qui permettent à des dimères, c'est-à-dire deux molécules de DPP(TBFu)₂ attachées par des chaînes aliphatiques, de contrôler la structure cristalline. La position d'attache du dimère influence énormément sur les résultats obtenus. Dans un cas, le dimère aide la mobilité des porteurs de charge dans les transistors alors que dans l'autre, il permet d'améliorer la stabilité thermique des cellules photovoltaïques.

En vue de permettre un auto-assemblage facile de cellules solaires avec une structure ternaire offrant une cascade de charges, une stratégie est ensuite développée. Cette dernière permet d'améliorer le

rendement de conversion de plus de 30 %. En conclusion, l'effet du poids moléculaire sur l'assemblage supramoléculaire et les performances dans les cellules solaires est étudié pour deux polymères, un amorphe codé PDPP4T-TT et un semicristallin codé PBTTT.

Table of contents

<i>Acknowledgements</i>	v
<i>Summary</i>	vii
<i>Résumé</i>	ix
Chapter 1 Introduction	1
1.1 Organic semiconductors	1
1.1.1 <i>Transport in organic semiconductors</i>	2
1.1.2 <i>Self-assembly and molecular engineering</i>	5
1.2 Organic field effect transistor	7
1.2.1 <i>Working principle</i>	8
1.2.2 <i>Recent advances and challenges in OFET</i>	10
1.3 Organic photovoltaic	13
1.3.1 <i>Working principle</i>	14
1.3.2 <i>Recent advances and challenges in OPV</i>	18
1.4 Stability of organic semiconductor based technology	20
1.5 References	21
Chapter 2 Experimental methods	27
2.1 Purification technique	27
2.1.1 <i>Size exclusion chromatography</i>	27
2.2 Opto-electronic properties characterization	28
2.2.1 <i>Cyclic voltammetry</i>	28
2.2.2 <i>Ultraviolet-visible spectroscopy</i>	29
2.3 Supramolecular assembly characterization	30
2.3.1 <i>Differential scanning calorimetry</i>	30
2.3.2 <i>Atomic force microscopy</i>	31
2.3.3 <i>X-ray spectroscopy</i>	37
2.4 Electrical characterization	38
2.4.1 <i>Organic field effect transistor</i>	38
2.4.2 <i>Organic photovoltaic</i>	39
2.4.3 <i>Space charge limited current</i>	39
2.4.4 <i>Quantum efficiency</i>	40
2.4.5 <i>Impedance spectroscopy</i>	41
2.5 References	43
Chapter 3 Observation of bell-shaped temperature dependence of hole mobility in hopping regime	45
3.1 Introduction	46
3.2 Results	48
3.2.1 <i>Temperature dependent FET measurements</i>	48
3.2.2 <i>Effect of annealing on the supramolecular assembly</i>	51
3.2.3 <i>Insight into the degree of aggregation by temperature dependent UV-vis</i>	54

3.3	Discussion	55
3.3.1	<i>Beyond band theory</i>	55
3.3.2	<i>Exploring field dependence of the mobility</i>	56
3.3.3	<i>Exploring transfer integral variation with temperature</i>	57
3.3.4	<i>Theory and modelling behind variation in electronic coupling</i>	58
3.3.5	<i>Application of the isodesmic model</i>	62
3.4	Conclusions	65
3.5	References	66
Chapter 4	<i>Engineering the self-assembly of diketopyrrolopyrrole-based molecular semiconductors via an aliphatic linker strategy</i>	69
4.1	Introduction	70
4.2	Results and Discussion	72
4.2.1	<i>Impact of the flexible linker on the supramolecular assembly</i>	73
4.2.2	<i>Effect on the charge carrier mobility</i>	79
4.2.3	<i>Structural stability enhancement of the bulk heterojunction</i>	82
4.3	Conclusion	87
4.4	References	88
Chapter 5	<i>Amorphous ternary energy cascade molecules for bulk heterojunction photovoltaics</i>	93
5.1	Introduction	94
5.2	Results and discussion	95
5.2.1	<i>Optoelectronic and packing properties of the ternary molecules</i>	95
5.2.2	<i>Exclusion of ternary molecules from crystalline phases</i>	96
5.2.3	<i>Effect of the ternary molecules in OPV</i>	99
5.2.4	<i>Confirming the ideal self-assembly</i>	102
5.3	Conclusions	106
5.4	References	107
Chapter 6	<i>Effect of molecular weight in diketopyrrolopyrrole-based and thienothiophene-based polymers for photovoltaic applications</i>	109
6.1	Introduction	110
6.2	Results and discussion	112
6.2.1	<i>Fractionation of the polymers</i>	112
6.2.2	<i>The effect of PDPP4T-TT's M_n on the photovoltaic performance</i>	113
6.2.3	<i>The effect of PBTtT's M_n on the photovoltaic performance</i>	116
6.3	Conclusion	118
6.4	References	118
Chapter 7	<i>Concluding remarks and perspectives</i>	121
Appendix A		A-1
Appendix B		B-1

Appendix C _____ *C-1*

Curriculum vitae _____ *CV-1*

Table of figures & tables

Figure 1-1. Neutral (left) and polaronic (right) structures of poly-3-hexylthiophene as reported in Ref 14.	3
Figure 1-2. Self-assembly mechanism of OS either (a) isodesmic (elongation with a single equilibrium constant) and (b) cooperative (activation step followed by elongation). (c) schematic representation of the degree of aggregation as function of temperature for the respective mechanisms.	6
Figure 1-3. Schematic of a bottom-gate, bottom-contacts OFET. Architecture can also vary with for example top-contact and/or top gate electrodes.	8
Figure 1-4. Schematic of the gate / gate dielectric / active material junctions when (a) no gate bias is applied and under (b) negative gate bias and (c) positive gate bias.	9
Figure 1-5. Schematic of the lamellar 2D paracrystalline packing structure of P3HT.	11
Figure 1-6. Schematic of the transport mechanism in polymer. On the left, highly crystalline blend with transport limited at the grain boundaries. On the right, poorly crystalline polymer with numerous small aggregation sites yielding a good balance between inter- and intramolecular transport.	14
Figure 1-7. Schematic of a typical bulkheterojunction solar cell architecture.	15
Figure 1-8. (a) schematic depicting the main physical processes involved in solar to current energy conversion (i-iv) and the main competing detrimental mechanisms (D and R). HOMO and LUMO levels are drawn as well defined energy levels for simplicity, though an equivalent Gaussian distribution is shown as reminder that they actually consist of a distribution of energy levels. (i) absorption of light leading to the formation of a Frenkel exciton. (ii) Diffusion of the exciton to the donor-acceptor interface. (iii) Electron transfer to the acceptor allowing formation free charge carriers. (iv) Free charge carrier transport to the interface. (D) Excitonic decay. (R) Charge carrier recombination. (b) schematic representing an ideal donor (red) and acceptor (purple) intermixed morphology. Processes contributing to current generation are shown in green while potential detrimental process (R) is shown in red dashed line. (c) schematic of an non ideal morphology presenting isolated domains without percolation pathway to electrodes as well as large domains in which exciton decay before reaching the interface.	16
Figure 1-9. Typical J-V characteristic of a photovoltaic device under dark and light conditions and the main figures of merit.	18
Figure 2-1. Schematic of a GPC setup with porous beads in green. The polymer is represented in red with long chains migrating faster than short chains due to difference in interaction with the porous beads. Absorption is measured in function of time at a selected wavelength resulting in a typical Gaussian distribution.	28

Figure 2-2. Schematic of a 1st order phase transition with position of onset temperature and the associated enthalpy. _____ 31

Figure 2-3. Schematic of atomic force microscopy operating in tapping mode to scan the surface profile. The surface presents DNA-wrapped carbon nanotubes. _____ 32

Figure 2-4. Schematic of force curve measurements with the 3 main regions: (i) non-contact, (ii) attractive force bend the tip downwards and (iii) repulsive forces bend the tip upwards. _____ 34

Figure 2-5. (Top) schematic depicting the 2 pass working principle of KPFM in tapping and electrical mode. (bottom) energy level schematic of the surface and tip (i) before electrical contact, (ii) after electrical contact but without any DC bias so that the presence of a dielectric layer between the tip and surface leads to a force bending the tip and (iii) in electrical contact after the force exerted on tip has been cancelled by a DC bias. _____ 36

Figure 2-6. Schematic of X-ray scattering in a crystalline lattice with spacing d and incident angle θ . It is explicit from geometrical considerations that the difference in optical path is $2d \sin\theta$. ____ 38

Figure 2-7. Equivalent circuit used to fit IS response in the following chapters. _____ 42

Figure 3-1. Temperature dependence of the field effect mobility extracted from saturated regime in DPP(TBFu)₂ OFET (channel length of 20 μm) as-cast and annealed at 90 °C, 130 °C and 170 °C for 1 hour and corresponding fit using equation (3.11) developed in this work. Black dashed lines indicate typical power law decay with exponent -0.5 (top) and -2 (bottom), typical range for transport governed by band or transient localization theory. _____ 48

Figure 3-2. Field dependence of the mobility extracted from saturated regime in FET (channel length of 10 μm) measured at different temperature for (a) as-cast devices and annealed at (b) 90 °C, (c) 130 °C and (d) 170 °C. _____ 50

Figure 3-3. (a) Out-of-plane grazing incidence wide angle X-ray scattering of as-cast DPP(TBFu)₂ and annealed at 90 °C, 130 °C and 170 °C. (b) density of state calculated using cyclic voltammetry data and (c) using chemical capacitance extracted from impedance spectroscopy of as-cast devices annealed at 90 °C, 130 °C and 170 °C. _____ 52

Figure 3-4. Atomic force microscopy height images (scale bar 100 nm) and corresponding distribution of the Young modulus of the SiO₂/DPP(TBFu)₂ interface measured on DPP(TBFu)₂ delaminated films as-cast and previously annealed at 90 °C, 130 °C and 170 °C. Dashed lines in the histogram correspond to Gaussian fit of the Young modulus distribution of as-cast (blue) annealed at 90 °C (green), 130 °C (orange) and 170 °C (red). _____ 53

Figure 3-5. (a) UV-vis spectrum of DPP(TBFu)₂ in solution (CHCl₃) and thin films as-cast and annealed at 90 °C, 130 °C and 170 °C and measured at RT as well as molten (~300 °C). (b - d) Relative differential absorption (spectrum at 300 K as baseline) at different temperature for thin films as-cast and annealed at 90 °C, 130 °C and 170 °C. _____ 54

Figure 3-6. Schematic of the energy landscape as function of molar volume for a 1st order reversible transition between initial state A and transition state B. Crystallization can then happen from the high energy transition state B to crystalline state C. Black dot represent the actual state of a molecule. _____ 58

Figure 3-7. Temperature dependence of the field effect mobility extracted from saturated regime in DPP(TBFu)₂ OFET (channel length of 20 μm) as-cast and annealed at 90 $^{\circ}\text{C}$, 130 $^{\circ}\text{C}$ and 170 $^{\circ}\text{C}$ for 1 hour and corresponding fit using equation (3.11) developed in this work. **Erreur ! Signet non défini.**

Figure 3-8. Schematic of the 3 phases present in the film as expected from AFM measurement. As-cast (left) present only a poorly crystalline phase, A, which is in equilibrium with the transition phase B. Respective population of these two phase is temperature dependent. After annealing at 90 $^{\circ}\text{C}$ and 130 $^{\circ}\text{C}$ a crystalline phase appears, though no percolation pathway through this crystalline phase exist. Then mobility remains highly affected by the equilibrium between phase A and B. When annealed at 170 $^{\circ}\text{C}$, direct percolation pathway starts to form through the crystalline channel, limiting the effect of equilibrium between phase A and B on the mobility. _____ 62

Figure 3-9. Integrated young modulus distribution presented in **Figure 3-4** of as-cast sample and annealed at 90 $^{\circ}\text{C}$, 130 $^{\circ}\text{C}$ and 170 $^{\circ}\text{C}$. Blue dashed-line represents the threshold defining the overlap with YM of as-cast sample. Green and orange dashed line indicates the fraction of poorly crystalline regions obtained by from the model for sample annealed at respectively 90 $^{\circ}\text{C}$ and 130 $^{\circ}\text{C}$. _____ 64

Figure 4-1. Chemical structures and synthetic strategy of the novel DPP(TBFu)₂ based dimers, V-(DPP)₂ and H-(DPP)₂. _____ 73

Figure 4-2. UV-vis and crystallographic characterization. The normalized optical absorption spectra measured in chloroform solution (a) and in solid-state thin films (b) are shown for the parent M-DPP, and the two dimers H-(DPP)₂ and V-(DPP)₂. (c) Out-of-plane grazing incidence X-ray diffractograms of M-DPP, H-(DPP)₂ and V-(DPP)₂ obtained from chlorobenzene drop-casted films. _____ 74

Figure 4-3. Differential scanning calorimetry of the dimer materials. (a) shows the second heating and cooling (10 $^{\circ}\text{C min}^{-1}$) scans of M-DPP, V-(DPP)₂, H-(DPP)₂ (the broken line in represents the first heating scan from a drop-cast sample), 10 wt% V-(DPP)₂ in M-DPP and 10 wt% H-(DPP)₂ in M-DPP. (b) shows the second cooling only curves for blend samples of M-DPP:H-(DPP)₂ in wt. ratios as indicated (where 0:1 represents pure dimer). _____ 77

Figure 4-4. Average hole mobility (μ_h) extracted from saturated regime in OFET devices prepared with pure M-DPP (blue markers) and M-DPP blended with the dimer molecules H-(DPP)₂ (green markers) and V-(DPP)₂ (red markers). Circle markers represent values from as-cast thin films while triangles indicate values taken from devices annealed at 110 $^{\circ}\text{C}$ for 10 min. _____ 80

Figure 4-5. Atomic force microscopy height trace images (scale bars 2 μm) of annealed films containing M-DPP (a), and with 10 wt% addition of (b) H-(DPP)₂ and (c) V-(DPP)₂. _____ 81

Figure 4-6. AFM height images of (a) neat H-(DPP)₂ and (b) M-DPP. _____ 82

Figure 4-7. (a) J-V curves of photovoltaic devices based on bulk heterojunction Donor:PC₆₁BM at a weight ratio of 6:4. The donor component consists of M-DPP with added dimer as indicated. Devices were annealed at 110 °C. (b) J-V curves of (as-cast, unannealed) photovoltaic devices based on bulk heterojunction Donor:PC₆₁BM at a weight ratio of 6:4. The donor component consists of M-DPP with added dimer as indicated. _____ 83

Figure 4-8. Heating curves measured by differential scanning calorimetry for a) different ratios of H-(DPP)₂:PCBM blends and b) M-DPP:PCBM (6:4) on first heating (solid line) and second heating (dashed line). (exothermic down) _____ 84

Figure 4-9. Optical microscopy images of thermally annealed (5h 100°C) M-DPP:PCBM bulk-heterojunction thin films (a) without added dimer and (b) with 10 % wt. H-(DPP)₂ and (c) with 10 wt% V-(DPP)₂ included in the blend. _____ 85

Figure 4-10. The OPV power conversion efficiency of M-DPP:PCBM devices with and without 10 wt% H-(DPP)₂ as a function of the active layer annealing time at 100 °C. The inset shows J-V curves for M-DPP:PCBM for devices annealed for 10 min (solid lines) and 5 h (broken lines) with (green) and without (blue) addition of 10 wt% H-(DPP)₂. _____ 86

Figure 5-1. Chemical structure of the ternary small molecules used in this work (a) SF-(DPP)₄ with R₁ = 2-ethylhexyl and (b) SF-(PDI)₄ with R₂ = 2-hexyldecyl. (c) Energy levels and band gap of the active molecules used in this work. (d) cyclic voltammetry of drop casted films over a platinum working electrode. (e) UV-vis absorption spectra of SF-(DPP)₄ and SF-(PDI)₄ in CHCl₃ (dotted lines) and in solid-state thin films (solid lines). _____ 96

Figure 5-2. (a) differential scanning calorimetry second heating and cooling curves of drop casted SF-(DPP)₄ and SF-(PDI)₄ from dichlorobenzene at 80 °C with a scan rate of 10 °C min⁻¹. Black arrows indicate scan direction. (b) Out-of-plane grazing incident wide angle X-ray diffraction of neat SF-(DPP)₄ and SF-(PDI)₄ thin films. _____ 97

Figure 5-3. (a) differential scanning calorimetry second heating curves of neat P3HT, neat PCBM and with varying amount of SF-(DPP)₄ (solid lines) and SF-(PDI)₄ (dotted lines). Scale bars represent 0.2 mW g⁻¹. (b) relative crystallinity (based on melting enthalpies) of PCBM (dots) and P3HT (triangles) as a function of additive content. _____ 98

Figure 5-4. Full width at half maximum of PCBM (right axis) and P3HT (left axis) diffraction peaks as a function of SF-(DPP)₄ content. _____ 99

Figure 5-5. Photovoltaic device performance with added amorphous cascade molecules. (a) and (b) shows typical J-V curves with varying amount of SF-(DPP)₄ and SF-(PDI)₄, respectively. (c) average figures of merit (PCE, J_{SC}, V_{OC} and FF) as a function of SF-(DPP)₄ (blue) and SF-(PDI)₄ (green) content in P3HT:PCBM BHJ OPVs. _____ 101

Figure 5-6. (a) External and (c) internal quantum efficiency of the host blend and containing 1, 2.5 and 10 wt% SF-(DPP)4. (b) shows the corresponding UV-vis data. (d) recombination lifetime obtained from fitting (solid lines, inset) the impedance spectroscopy response (dots, inset) at open circuit under 1 sun for increasing content of SF-(DPP)4 (0, 1, 2.5, 5, 10 wt%). _____ 102

Figure 5-7. Kelvin probe force microscopy images of thermally-driven phase segregated sample measured at domains interface with varying amount of additives. Top images (black) shows KPFM measured under dark conditions while bottom images (red) shows surface photovoltage built-up images obtained by subtracting KPFM unde light and dark conditions. Scale bar 2 μm . _____ 104

Figure 5-8. (a, b) Short circuit current as function of light intensity expressed in sun (1 sun = 100 W cm^{-2}) for varying loadings of either additives. (c) Schematic depicting limitations of this approach due to isolation of crydstalline domains in the BHJ. _____ 105

Figure 6-1. Analytical gel permeation chromatograms of selected a) PBTTT and b) PDPP4T-TT fractions separated by prep-GPC are shown as the normalized detector response versus elution volume of the mobile phase. The gray line represents the crude polymerization chromatograph. The reported M_n and \bar{D}_M values for each fraction are versus polystyrene standards. For clarity, not all fractions employed in subsequent analysis are shown here. _____ 111

Figure 6-2. J-V characteristics of PDPP4T-TT:PCBM BHJ solar cells using different polymer M_n . Polymer fraction with high polydispersity is shown in grey dashed line. _____ 113

Figure 6-3. Tapping-mode atomic force microscopy images of the surface morphology of spin-casted thin films of PDPP4T-TT at (a) 9 kDa, (b) 30 kDa, (c) 70 kDa and (d) large \bar{D}_M fractions. _____ 114

Figure 6-4. Young modulus mapping images of 9 kDa (a), 30 kDa (b) and 70 kDa (c) PDPP4T-TT:PCBM thin films. _____ 115

Figure 6-5. J-V characteristics of PBTTT:PCBM solar cells at different M_n . Polymer fraction with high polydispersity is shown in grey dashed line. _____ 116

Figure 6-6. Tapping-mode atomic force microscopy images of the surface morphology of spin-casted thin films of PBTTT at (a) 10 kDa, (b) 35 kDa, (c) 80 kDa and (d) large \bar{D}_M fractions. ____ 117

Table 3-1. Thermodynamic parameters describing the temperature dependent behaviour of the hole mobility in OFET for different annealing temperatures according to the isodesmic self-assembly model. _____ 61

Table 4-1. Average hole mobility (μ_h) extracted from saturated and linear regime, on/off ratio and threshold voltage of the different OFET devices presented in this study in annealed conditions. Parameters for as-cast devices are given in parenthesis. _____ 79

Table 6-1. Average figures of merit calculated from at least four devices for PBTTT:PCBM and PDPP4T-TT:PCBM devices with different polymer MW. _____ 112

List of abbreviations & symbols

<i>1D</i>	<i>1 dimensional</i>
<i>2D</i>	<i>2 dimensional</i>
A_c	<i>Contact area</i>
<i>AC</i>	<i>Alternative current</i>
<i>AFM</i>	<i>Atomic force microscopy</i>
<i>Ag</i>	<i>Silver</i>
<i>AM</i>	<i>Air mass</i>
<i>APCE</i>	<i>Absorbed photon-to-electron conversion efficiency</i>
a	<i>Average hopping distance</i>
<i>BHJ</i>	<i>Bulkheterojunction</i>
<i>BTBT</i>	<i>benzothienobenzothiophene</i>
C_μ	<i>Chemical capacitance</i>
<i>CB</i>	<i>Chlorobenzene</i>
<i>CCL</i>	<i>Crystal correlation length</i>
<i>CHCl₃</i>	<i>Chloroform</i>
C_i	<i>Gate dielectric capacitance</i>
<i>cm</i>	<i>Centimeter</i>
C_n	<i>Aliphatic chain with n carbon</i>
<i>CV</i>	<i>Cyclic voltammetry</i>
<i>C</i>	<i>Capacitance</i>
<i>CPE</i>	<i>Constant phase element</i>
<i>c</i>	<i>Speed of light</i>
<i>D-A</i>	<i>Donor-acceptor</i>
<i>DC</i>	<i>Direct current</i>
\bar{M}	<i>Molar mass dispersity</i>
<i>DMT</i>	<i>Derjaguin-Muller-Toporov</i>
<i>DOS</i>	<i>Density of state</i>
<i>DPP</i>	<i>Diketopyrrolopyrrole</i>
<i>DPP(TBFu)₂</i>	<i>6-bis(5-(benzofuran-2-yl) thiophen-2-yl)-2, 5-bis (2-ethylhexyl) pyrrolo [3, 4-c] pyrrole-1, 4-dione</i>
<i>DSC</i>	<i>Differential scanning calorimetry</i>
<i>D</i>	<i>Diffusion coefficient</i>
<i>d</i>	<i>Optical path length</i>
d_i	<i>Interplanar distance</i>
<i>E</i>	<i>Field</i>
E^*	<i>Reduced young modulus</i>
ϵ_0	<i>Vacuum permittivity</i>
<i>E_g</i>	<i>Band gap</i>
<i>EQE</i>	<i>External quantum efficiency</i>
<i>e</i>	<i>Elementary charge</i>

ε	<i>Dielectric constant</i>
$\varepsilon(\lambda)$	<i>Extinction coefficient</i>
F	<i>Force</i>
FET	<i>Field effect transistor</i>
FF	<i>Fill factor</i>
$FWHM$	<i>Full width at half maximum</i>
Φ	<i>Work function</i>
ΔG^0	<i>Variation in Gibbs free energy</i>
GDM	<i>Gaussian disorder model</i>
$GIXRD$	<i>Grazing incidence X-ray spectroscopy</i>
GPC	<i>Gel permeation chromatography</i>
$g(E_F)$	<i>Density of state</i>
h	<i>Planck constant</i>
\hbar	<i>Reduced Planck constant</i>
$H-(DPP)_2$	<i>Horizontal DPP(TBFu)₂ dimer</i>
ΔH	<i>Enthalpy variation</i>
$HOMO$	<i>Highest occupied molecular orbital</i>
Hz	<i>Hertz</i>
I_{DS}	<i>Source-drain current</i>
I_{ON}/I_{OFF}	<i>On/off current ratio</i>
$IPCE$	<i>Incident photon-to-electron conversion efficiency</i>
IQE	<i>Internal quantum efficiency</i>
IS	<i>Impedance spectroscopy</i>
ITO	<i>Indium-doped tin oxide</i>
J	<i>Transfer integral</i>
J_{sc}	<i>Short circuit current</i>
$J-V$	<i>Current density as function of voltage</i>
K	<i>Kelvin</i>
K_{ET}	<i>Charge transfer rate constant</i>
k_B	<i>Boltzman constant</i>
$KPFM$	<i>Kelvin probe force microscopy</i>
K	<i>Combined reduced young modulus</i>
L	<i>Tranistor channel length</i>
$LUMO$	<i>Lowest unoccupied molecular orbital</i>
m	<i>Meter</i>
M	<i>Molar</i>
$M-DPP$	<i>Monomeric DPP(TBFu)₂</i>
meV	<i>Millielectronvolt</i>
min	<i>minute</i>
M_n	<i>Molecular weight</i>
MO	<i>Molecular orbital</i>
Mo	<i>Molybdenum</i>
NBS	<i>N-Bromosuccinimide</i>
N_{CC}	<i>Density of collected charge carriers</i>

N_{ph}	<i>Density of incident photons</i>
η_{Col}	<i>Charge carrier collection efficiency</i>
η_{ES}	<i>Exciton splitting efficiency</i>
η_{LH}	<i>Light harvesting efficiency</i>
η	<i>Power conversion efficiency</i>
O	<i>Oxygen</i>
$OFET$	<i>Organic field effect transistor</i>
$OLED$	<i>Organic light emitting diode</i>
OPV	<i>Organic photovoltaic</i>
OS	<i>Organic semiconductors</i>
OTS	<i>octadecyltrichlorosilane</i>
P	<i>Power</i>
P_i	<i>Probability</i>
P_{IN}	<i>Incident power</i>
$P3HT$	<i>Poly-3-hexylthiophene</i>
$PBTtT$	<i>poly(2,5-bis(3-alkylthiophen-2-yl)thieno[3,2-b]thiophene)</i>
$PCBM$	<i>[6,6]-phenyl-C₆₀-butyric acid methyl ester</i>
PCE	<i>Power conversion efficiency</i>
PDI	<i>Perylene diimide</i>
$PEDOT:PSS$	<i>Poly(3,4-ethylenedioxythiophene):polystyrene sulfonate</i>
PF	<i>Poole-Frenkel</i>
P_{max}	<i>Maximum power point</i>
Pt	<i>Platinum</i>
q	<i>q vector</i>
R_s	<i>Series resistance</i>
R_{rec}	<i>Recombination resistance</i>
RT	<i>Room temperature</i>
R_c	<i>Combined curvature radius of the contact</i>
R	<i>The gas constant</i>
s	<i>Scan speed</i>
$SCLC$	<i>Space charge limited current</i>
Si	<i>Silicon</i>
t	<i>Time</i>
T_m	<i>Transition phase temperature</i>
Ti	<i>Titanium</i>
$TIPS$	<i>triisopropyl-silyl ethynyl</i>
T	<i>Temperature</i>
UV	<i>Ultraviolet</i>
$UV-vis$	<i>Ultraviolet-visible</i>
$V-(DPP)_2$	<i>Vertical DPP(TBFu)₂ dimer</i>
V_{CPD}	<i>Contact potential difference</i>
V_{ph}	<i>Photovoltage</i>
ν_0	<i>attempt-to-escape frequency</i>
V_{DS}	<i>Source-drain bias</i>

V_{GS}	<i>Source-gate bias</i>
V_{oc}	<i>Open circuit voltage</i>
VRH	<i>Variable range hopping</i>
V_{th}	<i>Threshold voltage</i>
W	<i>Transistor channel width</i>
$wt.$	<i>Weight</i>
Xe	<i>Xenon</i>
YM	<i>Young modulus</i>
Zn	<i>Zinc</i>
Z	<i>Impedance</i>
Z'	<i>Real part impedance</i>
Z''	<i>Imaginary part impedance</i>
α	<i>Degree of aggregation</i>
γ	<i>Work</i>
δ	<i>Inverse localization length</i>
θ	<i>Scattering angle</i>
λ	<i>Wavelength</i>
λ_0	<i>Reorganization energy</i>
μ	<i>Mobility</i>
μ_{lin}	<i>Mobility extracted from linear regime</i>
μ_{sat}	<i>Mobility extracted from saturated regime</i>
σ	<i>Gaussian distribution width for the energy</i>
τ	<i>Lifetime</i>
φ	<i>Phase shift</i>
ω	<i>Frequency</i>



Chapter 1 Introduction

Since the discovery of semiconducting behaviour in polyacetylene in 1977,¹ which earned Heeger, MacDiarmid and Shirakawa the Nobel prize, the field of organic semiconductors (OS) has attracted a tremendous interest from research and industry. Despite their rather poor performances, as compared to inorganic semiconductors, OS represent a unique alternative given their potential low cost roll-to-roll processing as well as their outstanding mechanical resistance, paving the road for flexible electronics.

Main applications using organic semiconductors encompass not only electronic application but also lighting and energy conversion from solar energy. The latter was introduced by Tang in 1986, demonstrating the first example of a flat heterojunction organic photovoltaic (OPV).² One year later, Tang et al. reported the first example of organic light emitting diode (OLED);³ A technology routinely used in smartphone's screens. In the meantime, the first example of organic field effect transistor (OFET) is developed by Koezuka and coworkers.⁴ Thirty years later, improving performances, stability and overall cost but also understanding the underlying physical processes remain key challenges in the field of OS.

1.1 Organic semiconductors

In a general sense, semiconductors are isolating materials that under certain circumstances can exhibit charge transport properties. As a matter of fact, semiconducting behaviour arises only when charge carriers are present in the active material, which can be induced by photon absorption, doping or injection of free charges. In this respect, organic semiconductors are carbon-based small molecules or polymers that can reversibly accommodate charge carriers, as holes or electrons, onto their π -conjugated backbone. This extended π -electrons system arises from the occupation of overlapping p_z orbitals arising from sp^2 hybridization with electron distribution reaching out perpendicularly to the molecular plane.⁵ These molecular orbitals (MO) are responsible for the molecule optoelectronic

properties as they constitute the highest occupied molecular orbital (HOMO) and the lowest unoccupied molecular orbital (LUMO). The difference between LUMO and HOMO energy levels – called band gap (E_g) – defines the minimum energy required for electronic excitation from the ground state to the excited state.

While, for a given molecule in vacuum, the HOMO and LUMO have well defined energy levels as predicted by Hückel MO theory, this is not the case in thin films where the relative molecular orientations will give rise to a distribution of states. Indeed, quadrupoles inherent to the negatively charged π -orbitals extending out of the molecular plane in combination with dipoles arising from the presence of heteroatoms in some molecular structures are well known to affect the energetics of surrounding molecules.⁶ This effect can be limited in single crystal where a finite number of packing conformations exist. Nonetheless, in thin films the paracrystalline nature (*e.g.* lack of long range order) as well as polymorphisms, common for organic materials, leads to a tremendous amount of possible conformations within the film and hence broad energy distribution of the HOMO and LUMO levels. In addition, electronic coupling between neighbouring molecules leads to extension of the π -conjugation and induces narrower E_g in thin films than in vacuum.⁷

1.1.1 Transport in organic semiconductors

The typical metric describing transport in semiconductors is the charge carrier mobility, which directly relates the drift velocity of the charge carriers in the material to the applied electric field. At the state-of-the-art, charge carrier mobility in OS have been reported to exceed $10 \text{ cm}^2 \text{ V}^{-1} \text{ s}^{-1}$.^{8–10} While this is impressive for the field, it remains several orders of magnitude lower than inorganic semiconductors such as silicon, which exhibits charge carrier mobilities about 2 orders of magnitude higher.¹¹ The main reason behind this stark difference in performances is attributed to the much weaker Van der Waals intermolecular interactions in OS as compared to the strong covalent bonds in Si.¹² This leads to larger intermolecular distances (*e.g.* several Angstroms) and weak electronic coupling that impedes delocalization of the charge carriers over significant distances as generally found in inorganic semiconductors.¹³ In addition, charge carriers in OS generate a lattice distortion leading to significant phonon coupling as encompassed in red in **figure 1-1** for poly-3-hexylthiophene (P3HT).¹⁴ Quasi-particles which encompass the charge carrier as well as the structural deformation are called polarons.

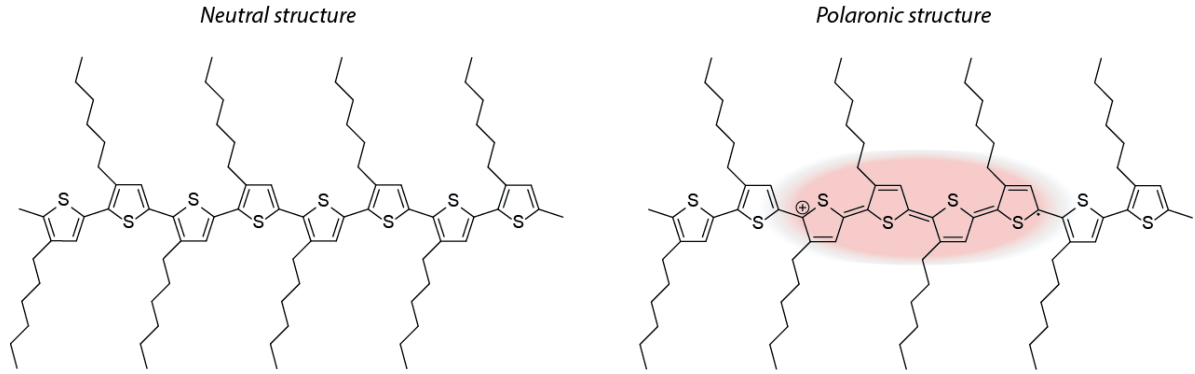


Figure 1-1. Neutral (left) and polaronic (right) structures of poly-3-hexylthiophene as reported in Ref 14.

Polaron being in most cases localized on a single molecule transport in thin films occurs *via* series of hop from one molecule to another. Intermolecular charge transfer *via* hopping can be described either by Miller-Abrahams or Marcus equations for charge transfer rate. The former is a simplified model considering activation energy to be non-zero only if hop from a state i to a state j is upward in energy. It can be expressed as,¹⁵

$$k_{ET} = \begin{cases} v_0 \exp(-\delta r_{ij}) \exp\left(-\frac{E_j - E_i}{k_B T}\right) & \text{if } E_j - E_i > 0 \\ v_0 \exp(-\delta r_{ij}) & \text{if } E_j - E_i \leq 0 \end{cases} \quad (1.1)$$

Where v_0 is the attempt-to-escape frequency, δ the inverse localization length, r_{ij} the distance between the two states and E the energy of the respective states i and j . The rate constant for electron transfer can then be related to the mobility using Einstein relation as,¹⁶

$$\mu = \frac{eD}{k_B T} = \frac{ea^2}{k_B T} k_{ET} \quad (1.2)$$

With D the diffusion coefficient and a an average hopping distance which would be equal to the lattice constant if mobility was measured over a dimer.¹⁷ This equation has been successfully used to predict the mobility of organic semiconductors through the Gaussian disorder model (GDM) developed by Bässler¹⁸ or variable range hopping model (VRH).¹⁹ Nonetheless, Miller-Abrahams equation

completely neglects any reorganizational energy during the charge transfer, inherent to polarons present in OS. Such polaronic behaviour can be accounted for using Marcus equation which can be written as,²⁰

$$k_{ET} = \frac{2\pi}{\hbar} J^2 \sqrt{\frac{1}{4\pi\lambda_0 k_B T}} \exp\left(-\frac{(\lambda_0 + \Delta G^0)^2}{4\lambda_0 k_B T}\right) \quad (1.3)$$

With J is the transfer integral, λ_0 the reorganization energy and ΔG^0 the variation in Gibbs free energy (note that $\Delta G^0 = 0$ in a homogenous film). In the case of OS this equation is of crucial importance in the experimental field as it allows to easily extract physically significant parameters as reorganizational energy from temperature dependent data. It is interesting to note that while polaronic nature of OS has been experimentally demonstrated, VRH models based on Miller-Abrahams hopping are nowadays better at simulating mobility in OS.²¹ In any case, choice of the adapted hopping model can be done considering disorder and temperature of the system. Indeed, close to 0 K lattice vibration and thus polaronic behaviour is reduced, favouring Miller-Abrahams type of hopping. Also, in case of high energetic disorder the GDM should be used. In contrast, close to room temperature (RT) and in presence of significant crystallinity, Marcus equation should be considered.

Notable exceptions have nonetheless observed band-like transport mechanism in OS – where band-like refers to charge carriers delocalized over a small number of sites as opposed to band transport. Signature of this band transport is generally seen as a negative temperature dependency of mobility as opposed to thermally activated mechanism (*e.g.* hopping) aforementioned. Indeed, theory for band transport predicts a power law decay of the mobility with temperature of the form $\mu \propto T^{-\alpha}$, with α depending on the phonon scattering mechanism.²² Handful of groups have supported their findings with hall effect measurements and other techniques.^{10,23–25} Despite these reports, band-like transport mechanism remains controversial, especially given that mobilities in OS are flirting with the Mott-Ioffe-Regel limit, predicting a minimum mobility around $1 \text{ cm}^2 \text{ V}^{-1} \text{ s}^{-1}$ for viable band transport.^{26,27} Moreover, negative mobility dependence on temperature should not be routinely assigned as a signature of band-like transport in OS given that it can also arise from weak intermolecular Van der Waals interactions as will be discussed in chapter 3.

To conclude the discussion on transport in OS, it is important to not only consider polaron transfer between neighboring molecules, but also how morphology in thin films – as opposed to single crystals

– will affect the overall mobility. Indeed, structural defects and paracrystallinity in thin films results in a rough energy landscape as mentioned above, which can lead to molecules with deeper LUMO or higher HOMO levels than their surroundings. Such energy wells, called trap states, can greatly affect the mobility if the charge carrier density and applied electric field are not high enough to balance them. These trap states are especially present at interfaces, as air or substrate interfaces, but also at the interface in between crystalline domains at the grain boundaries. The latter is well known to limit the mobility within the bulk of the thin film acting as a structural defect with weak electronic coupling and significant offset in HOMO levels, leading to either trap state or energy barrier. This kind of limitation is understood in term of percolation pathways and emphasize the critical role of self-assembly in thin film.²⁸

1.1.2 Self-assembly and molecular engineering

Processing techniques as vapour phase deposition can be used to manufacture highly ordered thin films of OS (*e.g.* single crystals) as commonly done in the field of inorganic semiconductors. However, one of the main advantage of OS is their potential to be solution-processed from ink using techniques such as spin-, bar-, spray-, drop- or dip-coating, paving the way for low cost applications. While the method of choice for processing organic thin films is certainly bar-coating – or similar meniscus coating techniques – given its compatibility with roll-to-roll process, spin-coating is routinely used in research to manufacture small scale devices, despite the poor temperature control it offers, unfortunately affecting reproducibility. This choice is mainly motivated by the inherent kinetic aspect of spin-coating which allows trapping metastable morphologies for high-performance devices.²⁹ Such example illustrates well the key role of the supramolecular assembly on device performance, underlining the importance of understanding and controlling the thin film growth. Nonetheless, despite the tremendous amount of efforts invested by the community, it remains challenging to predict the self-assembly. Already in vacuum, organic molecules possess orientational as well as rotational degrees of freedom which introduce a new level of complexity over the supramolecular assembly as compared to inorganic semiconductors.⁶ Moreover, OS are paracrystalline materials generally lacking long range order mainly because of their weak intermolecular Van der Waals interactions as π - π stacking, H-bonding, and so on. When solution-processed, several strategies and tools have been developed over the years to affect and regulate OS self-assembly but current understanding is limited to systematic studies which can hardly be generalized.

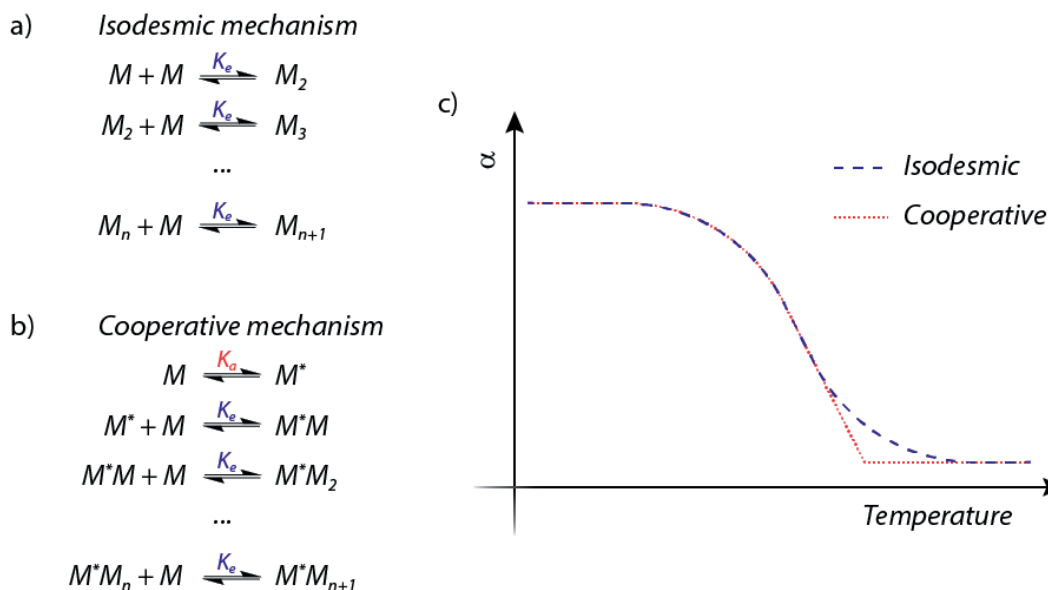


Figure 1-2. Self-assembly mechanism of OS either (a) isodesmic (elongation with a single equilibrium constant) and (b) cooperative (activation step followed by elongation). (c) schematic representation of the degree of aggregation as function of temperature for the respective mechanisms.

Two main mechanism can be seen for film growth from solution, either isodesmic or cooperative (depicted on **Figure 1-2**).³⁰ The former implies that the rate of self-assembly is independent whether a molecule assembles with an aggregate or a single molecule. On the other hand, cooperative mechanism refers to a nucleation and growth process where self-assembly between single molecules is limiting the overall process. Solution-processed crystalline OS are usually seen to follow a cooperative mechanism.²⁹ Hence, self-assembly can be separated in two main steps: nucleation and growth. Nucleation being a stochastic process, it is especially difficult to control. Nonetheless, several studies have demonstrated the key aspect of solvent evaporation rate as well as the solvent-solute interactions.^{31,32} Indeed, nucleation will happen upon saturation of the solution which is determined by the solubility of the molecule in solution and the temperature. Another common strategy to control nucleation is the use of additives acting as nucleation inducing agents which lower the activation energy for nucleation.^{33,34} In contrast, crystal growth offers a wide range of opportunities for fine control of the morphology. Indeed, the kinetic nature of the process allows catching some metastable states and to regulate crystal domain size. Post-annealing, either solvent or thermal, is likely the most used strategy to manage crystal growth.^{35,36} Solvent annealing consist of having the solid film in contact with a solvent saturated atmosphere which helps diffusion and rearrangement of molecules in solid-state.³⁷ Thermal annealing is only different in the sense that it uses thermal energy instead of solvent vapour

to trigger molecular reorganization inside the film.³⁸ Affecting crystal growth during the processing is also possible for example using high boiling point solvent additive such as diiodooctane (DIO).³⁹ Researchers have also reported the possibility to induce crystal domain alignment in thin films, mostly using a shearing strategy but also *via* additional forces during processing as gravitational or centrifugal forces or even using pre-patterned substrate to induce the directionality.²⁹

While these strategies constitute a potent toolbox for controlling the supramolecular assembly of a given OS, the ease of molecular engineering remains one of the most powerful feature of OS. Indeed, current synthetic knowledge allows rational design as well as fine tuning of the molecules opto-electronic properties; A strategy also widely used to investigate the impact of the supramolecular assembly in thin film over the performances. As aforementioned, OS by definition is composed of a conjugated core which is responsible for the optoelectronic properties of the molecule. However, the conjugated core by itself usually exhibits poor solubility and requires additional solubilizing alkyl chains to be amenable for solution process. Engineering of these side chains has been extensively explored as a way to control the self-assembly without affecting optoelectronics properties.⁴⁰ Unfortunately, it requires case to case optimization and, hence, significant synthetic efforts. In this respect, a new class of flexibly linked materials – where conjugated cores are tethered together *via* an aliphatic linker – is emerging as a powerful tool to subtly control the supramolecular assembly, with a direct strain over the conjugated core though without affecting the optoelectronic properties itself.^{41–44} This family of flexibly linked molecule will be further discussed in chapter 4.

Finally, it should be noted that while small-molecules have well defined chemical structure, it is not the case of polymer OS, which have to be described by an average molecular weight (M_n) in combination with a molar mass dispersity (D_M). Several works (*vide infra*) have demonstrated the importance of M_n on self-assembly. As a general rule, it seems that increasing the polymer chain length is beneficial for the performances up to a certain threshold where polymer chain entanglement starts to limit the performances as typically seen by Gasperini et. al. for poly(2,5-bis(3-alkylthiophen-2-yl)thieno[3,2-b]thiophene) (PBTtT).⁴⁵

1.2 Organic field effect transistor

Among the many applications for OS, OFET has attracted a lot of scientific attention. Underlying reasons of this success are multiple. On one hand its impressive potential in the ever growing market

of everyday electronics, development of the internet of things and sensor application makes this technology economically appealing. In particular, its mechanical resistance defies competition for the field of flexible electronics as electronic skin or paper. On the other hand, the simple structure of the device offers unique opportunity to measure materials charge carrier mobility and understand the underlying physical processes involved in polaronic transport.

1.2.1 Working principle

Field effect transistor is a three-probe device which is essential for logic circuit in electronic applications as microprocessors. It is composed of two electrodes in Ohmic contact with the active layer and a gate electrode separated from each other by a dielectric layer as schematized in **Figure 1-3**. The principle of a FET is to turn on or off the current flowing in between the source and drain electrodes by applying a bias in between source and gate electrodes, resulting in a logic response.

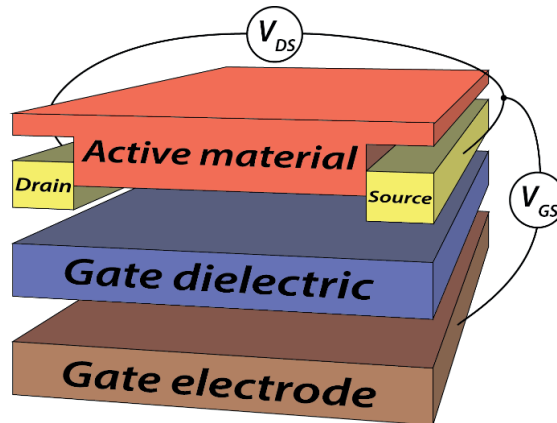


Figure 1-3. Schematic of a bottom-gate, bottom-contacts OFET. Architecture can also vary with for example top-contact and/or top gate electrodes.

The source-gate bias (V_{GS}) induces the presence of charge carriers at the gate dielectric interfaces, as schematized on **Figure 1-4**. In the case where intrinsic charge carrier concentration of the OS is negligible, no field effect transport will be seen at $V_{GS} = 0$ V. If $V_{GS} < 0$ V, then the active material at the gate dielectric interface will form a hole accumulation (electron depletion) layer where hole transport will take place for p-type materials (materials which exhibit hole mobility). In contrast, at positive V_{GS} , a hole depletion (electron accumulation) layer will form, favouring electron transport in n-type material (materials which exhibit electron mobility). Materials which exhibit both electron and hole mobilities are called ambipolar materials and will generate current at both positive and negative V_{GS} .

In addition to the charge carrier mobility, the current ratio between on and off states (I_{ON}/I_{OFF}) as well as the threshold voltage (V_{th}) constitute the three main figures of merit of FET. The latter defines the minimum V_{GS} required to create a conductive path which is often related to density of trap state present in the conductive layer. Early reports have actually shown that surface dipoles at the SiO_2 dielectric interface attributed to silanol groups can generate trap-states.⁴⁶ Such dipoles can be removed by fonctionnalizing the interface with a self-assembled monolayer (e.g. using octadecyltrichlorosilane (OTS)); A strategy commonly used to influence the active interface. On the other hand, I_{ON}/I_{OFF} gives a measure of the signal to noise ratio.

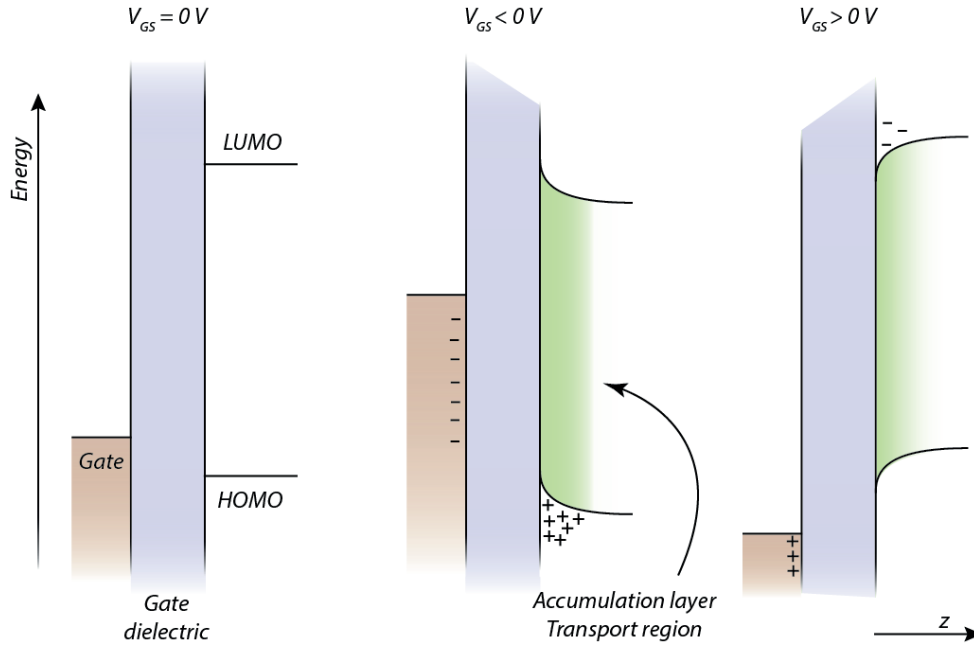


Figure 1-4. Schematic of the gate / gate dielectric / active material junctions when (a) no gate bias is applied and under (b) negative gate bias and (c) positive gate bias.

In addition to commercial applications, OFET offer a convenient way to selectively measure hole or electron mobility of OS simply by regulating V_{GS} . Indeed, the FET current response as function of the source-drain voltage (V_{DS}) can be simplified by considering two distinct regimes. At low V_{DS} the source-drain current (I_{DS}) will increase linearly with V_{DS} , while at high V_{DS} , I_{DS} tend toward a plateau.

This consideration leads to the following expressions for I_{DS} , from which it is trivial to extract mobility:

$$I_{DS} = \mu_{lin} C_i \frac{W}{L} (V_{GS} - V_T) V_{DS} \quad V_{DS} \ll (V_{GS} - V_T) \quad (1.4)$$

$$I_{DS} = \mu_{sat} C_i \frac{W}{2L} (V_{GS} - V_T)^2 \quad V_{DS} > (V_{GS} - V_T) \quad (1.5)$$

Where, C_i is the gate dielectric capacitance, W the channel width, L the channel length. Mobility being strongly dependent on temperature, it is conventionally measured at RT.

1.2.2 Recent advances and challenges in OFET

OFET application for full organic displays implies structural constraints in order to achieve a good display resolution and brightness, leading to a minimum mobility about $1.5 \text{ cm}^2 \text{ V}^{-1} \text{ s}^{-1}$.⁴⁷ Recent advances in OFET, through molecular and supramolecular engineering as to minimize energetic disorder and reorganizational energy while maximizing the transfer integral, have led to mobilities exceeding this threshold. Historically, material-based on highly crystalline small molecules have reached higher mobilities than polymers. This class of small molecules mainly consist of acenes and heteroacenes, pentacene probably being one of the most popular member. Nevertheless, in most cases these acene cores suffer from poor solubility given their strong intermolecular π - π stacking and require additional solubilizing groups, such as triisopropyl-silylethynyl (TIPS), to be solution-processed. Anthony et al. first developed spin-coated TIPS-pentacene OFET that resulted in mobilities above $1 \text{ cm}^2 \text{ V}^{-1} \text{ s}^{-1}$ with a cofacial π - π stacking allowing strong electronic coupling as well as 2D transport (preferable to 1D type of transport).^{48,49} Notably, by blade coating TIPS-pentacene Diao and coworkers achieved mobilities up to $11 \text{ cm}^2 \text{ V}^{-1} \text{ s}^{-1}$ through shearing process that favour a non-equilibrium polymorphic structure with better transport properties.⁵⁰ Another example of well-performing highly crystalline small molecule is alkyl substituted benzothienobenzothiophene (C_n -BTBT) which can achieve ground-breaking mobilities up to $31 \text{ cm}^2 \text{ V}^{-1} \text{ s}^{-1}$ using advanced printing technique where formation of a single crystal is triggered by diffusion of an antisolvent.⁵¹

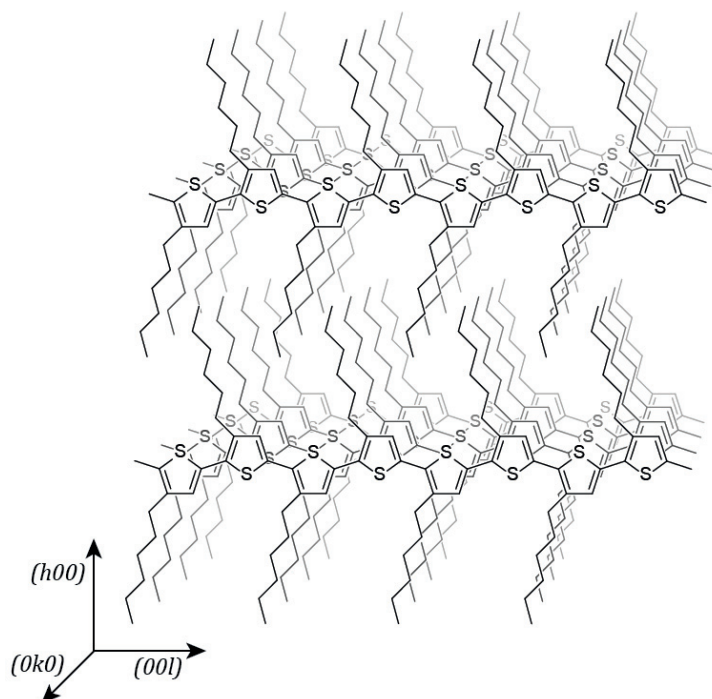


Figure 1-5. Schematic of the lamellar 2D paracrystalline packing structure of P3HT.

In stark contrast, polymers do not exhibit a similar level of crystallinity mainly because of their molecular weight distribution leading to a paracrystalline behaviour. Nonetheless, fully amorphous polymers with limited energetic disorder mobilities can still achieve reasonable mobilities up to $10^{-2} \text{ cm}^2 \text{ V}^{-1} \text{ s}^{-1}$,^{52,53} which is about two orders of magnitude higher than mobilities observed in amorphous small molecule based OFET.⁵⁴ Despite the poor intermolecular coupling expected for amorphous materials, in polymers, polarons can still be efficiently transported along the backbone through intramolecular transport reducing the number of hops required to cross the channel.⁵⁵ In semicrystalline polymers such as the archetypal P3HT, where supramolecular assembly consists of a lamellar structure with layers of π - π stacked conjugated backbone separated by aliphatic chains (**Figure 1-5**), mobility essentially arises from a combination of intra- and intermolecular transport in 2D, the aliphatic chains acting as an insulating layer in between the planes. One of the key aspect to obtain this semicrystalline lamellar morphology has been to use regioregular P3HT, with monomeric units always attached together through the 2- and 5-positions (head to tail) leading to equally spaced aliphatic chains along the backbone, as shown by Bao and coworkers.⁵⁶ The importance of the supramolecular domain orientation was demonstrated by Sirringhaus et al., which reported that having the (010)-axis oriented parallel to the substrate (edge-on) and not perpendicular (face-on) is essential for efficient

charge transport along the plane.⁵⁷ The effect of molecular weight on the microstructure has also been widely investigated, especially the work from Brinkmann et al. which highlighted the highly crystalline nature of low M_n (<7 kDa) which form fibrillary structure in contrast to the semicrystalline nature of high M_n (>19 kDa).⁵⁸ Using solvent fractionation, the former was found to be detrimental for hole mobility.⁵⁹

One of the most astonishing polymers in terms of its self-assembly was discovered by McCulloch et al. by coupling a fused thienothiophene with a thiophene monomer, leading to poly(2,5-bis(3-alkylthiophen-2-yl)thieno[3,2-b]thiophene) (PBTtT).^{60,61} The more rigid conjugated backbone in combination with the sparser alkyl solubilizing groups offers a unique highly ordered edge-on lamellar structure resulting in terraces like structure observable by atomic force microscopy corresponding to the interplanar spacing. This polymer has led to mobilities about $1 \text{ cm}^2 \text{ V}^{-1} \text{ s}^{-1}$, 2 orders of magnitude higher than for P3HT. Recent studies from Gasperini et al. on the effect of M_n have shown that, in contrast to P3HT, PBTtT exhibit 3 different morphologies upon increasing the M_n .⁴⁵ A similar fibrillar structure below 20 kDa is replaced by the terraces structure from 20 to 50 kDa which in turn disappear for an entangled structure above 50 kDa. The terraces structure at this medium M_n exhibited the best transport properties, underlining the importance of the self-assembly. Gasperini and coworkers further demonstrated the crucial role of the supramolecular assembly over intramolecular transport by synthesizing a PBTtT based polymer consisting of 8 kDa molecule tethered together through an aliphatic linker.⁴³ This new flexibly linked polymer exhibited terraces like structure as well as enhanced mobility while intramolecular transport is left unaffected through the isolating aliphatic chains.

Another class of polymers, named donor-acceptor (D-A) polymer, consist of alternating electron deficient and electron rich units in order to reduce the bandgap. While this strategy is extremely attractive for solar energy conversion application, optical properties of the polymer have no direct incidence on the performances in OFET. Nonetheless, it seems that the strong Van der Waals interactions between donor and acceptor units might lead to smaller intermolecular distances and hence better transfer integral, favourable for transport.⁶² Among D-A polymers, a family based on diketopyrrolopyrrole (DPP) as the electron deficient unit and thiophene-based electron rich unit has appeared as promising high mobility ambipolar materials with both hole and electrons mobilities exceeding $1 \text{ cm}^2 \text{ V}^{-1} \text{ s}^{-1}$.⁶³ Increasing the molecular weight has even lead to mobilities exceeding $10 \text{ cm}^2 \text{ V}^{-1} \text{ s}^{-1}$.⁶⁴ Many other D-A polymers with high mobilities have been reported, but will not be presented here. It is worth

noting that the supramolecular assembly of these polymers do not follow the same trend than thiophene-based polymers where well-ordered lamellar structure is beneficial for good transport properties. In contrast, D-A polymers exhibit higher mobilities despite their poorly ordered structure as observed by X-ray diffraction and even thin films exhibiting preferential face-on orientation.⁴⁷ This brings into debate the understanding and design rules for charge transport, demonstrating that highly ordered systems is not required for high mobility. Actually, Noriega et al. proposed a unified explanation where only short range crystalline domains would provide good intermolecular transport while connection in between these disordered aggregate would be provided *via* intramolecular pathways (see **Figure 1-6**).⁶⁵ Recently published results from Son et al. have shown using a thiophene based random copolymer that in spite of the decreased crystallinity as compared to P3HT, mobilities in the order of $1 \text{ cm}^2 \text{ V}^{-1} \text{ s}^{-1}$ are achievable.⁶⁶ The lower energy barrier they observed is consistent with the idea that small yet well dispersed aggregate are sufficient to provide good intermolecular transport in polymer while large crystals as in P3HT often exhibits high resistance in between aggregates.

Overall, this short survey of the literature underlines the importance of self-assembly for high mobility OFET as well as the singular complexity of the structural transport mechanism. Simple strategies to generally address and increase control over supramolecular assembly is thereof critical for the field.

1.3 Organic photovoltaic

Substituting limited energy resources as fossil fuels by renewable energy resources while facing a growing energy demand is a major challenge of the century. Moreover, reducing greenhouse gas emission in the atmosphere through carbon-free energy resources is critical to prevent drastic climate change. Among the many renewable energy sources (i.e. wind, biomass and so on...), the solar energy is one of the most promising candidate given the tremendous raw power reaching the earth surface estimated about 184 W m^{-2} .⁶⁷ Assuming a power conversion efficiency for photons to electricity of 15 % and based on a world energy consumption in 2015 about 17.5 TW,⁶⁸ less than 0.13 % of the earth surface would provide enough energy for humanity. As a benchmark, urban areas covers about 0.9 % of the earth surface including more than 0.13 % of impervious surface⁶⁹ which means that integrating photovoltaic modules in architectural components as roofs, walls, roads and so on... can potentially meet the global energy demand. Nonetheless, two major challenges remain to be solved for this technology to be competitive on the energy market. As a matter of fact, solar energy production is subject to great variability during day time and seasons, requiring an adequate technology for

safe and large scale energy storage. In addition, the levelized cost of solar energy production is still high as compared to fossil fuels, nuclear or even wind energies. Such cost results from a balance between the actual production cost of the device, its power conversion efficiency (PCE) and its life-time. While crystalline silicon p-n junction is the most mature technology reaching PCE close to the theoretical limit proposed by Shockley and Queisser,⁷⁰ the high production cost drastically limits its applications. To address this issue, a whole new class of low-cost photovoltaic technology has been developed, among which photovoltaics based on organic semiconductors.

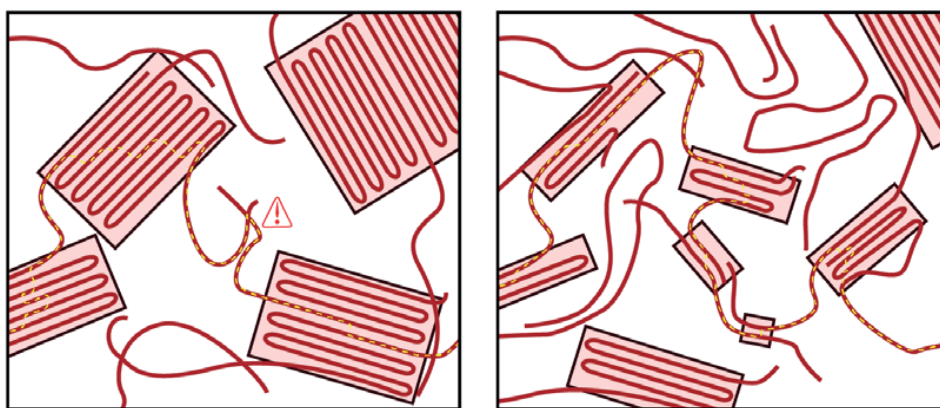


Figure 1-6. Schematic of the transport mechanism in polymer. On the left, highly crystalline blend with transport limited at the grain boundaries. On the right, poorly crystalline polymer with numerous small aggregation sites yielding a good balance between inter- and intramolecular transport.

1.3.1 Working principle

Organic photovoltaics essentially consist of a photoactive layer sandwiched in between two electrodes as schematized in **Figure 1-7**. Careful optimization of the electrodes work functions is necessary to guarantee charge carrier selectivity at the contact, typical choices are low work function metals as aluminium for the cathode and high work function materials as gold or silver for the anode. It is common to use interlayers to improve charge carrier selectivity and contact energy at the interface such as poly(3,4-ethylenedioxythiophene):polystyrene sulfonate (PEDOT:PSS) or MoO₃ and ZnO or TiO_x at the anode and cathode respectively.⁷¹ Indium-doped tin oxide (ITO) is routinely used as a transparent bottom electrode with small surface roughness.

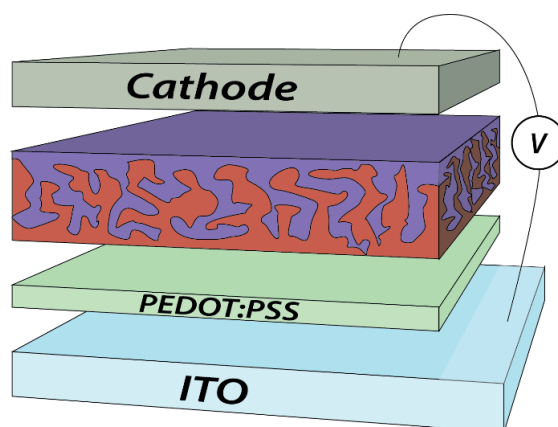


Figure 1-7. Schematic of a typical bulk heterojunction solar cell architecture.

In contrast to OFET devices, OS for applications in OPV do not require exceptionally high charge carrier mobilities (typical mobilities are in the range of 10^{-5} - 10^{-3} $\text{cm}^2 \text{V}^{-1} \text{s}^{-1}$),⁷² a consequence of the small active layer thickness (about 100-200 nm). However, the optical property of the active layer which is mainly defined by the band gap of its molecular constituents, is primordial for maximizing photon harvesting from sunlight. In order to generate free charge carriers, the photoactive layer consists of a heterojunction between at least two organic materials, an electron donor and an electron acceptor. Indeed, upon light absorption, the low dielectric constant characteristic of OS ($\epsilon_r \approx 3$) leads to significant Coulomb attraction between the photoexcited electron and hole, leading to the formation of a Frenkel exciton with binding energy in the range of 100 – 500 meV that is much higher than thermal energy (**Figure 1-8, i**).⁵ The additional driving force to split such exciton must hence be provided by the energy difference between the LUMO (if the exciton is generated on the donor molecule) or the HOMO (if the exciton is generated on the acceptor molecule) levels of the donor and acceptor molecules (**Figure 1-8, iii**). Therefore, the interface is a key aspect of the active layer, as exciton generated further away from the interface than their corresponding diffusion length (typically 10–20 nm) will recombine to the ground state (**Figure 1-8, D**). This consideration leads to a first design rule for optimum morphology which is that the domain size for donor or acceptor molecule should not exceed the exciton diffusion length (**Figure 1-8, ii**). Moreover, to optimize the charge generation, the interfacial area between donor and acceptor should be maximized.

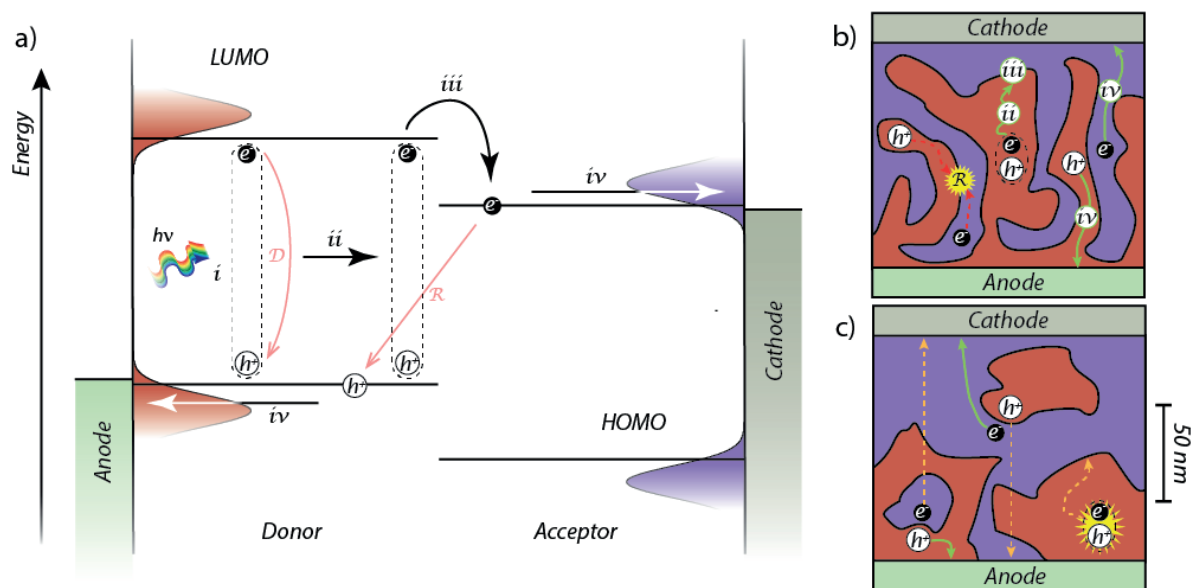


Figure 1-8. (a) schematic depicting the main physical processes involved in solar to current energy conversion (i-iv) and the main competing detrimental mechanisms (D and R). HOMO and LUMO levels are drawn as well defined energy levels for simplicity, though an equivalent Gaussian distribution is shown as reminder that they actually consist of a distribution of energy levels. (i) absorption of light leading to the formation of a Frenkel exciton. (ii) Diffusion of the exciton to the donor-acceptor interface. (iii) Electron transfer to the acceptor allowing formation free charge carriers. (iv) Free charge carrier transport to the interface. (D) Excitonic decay. (R) Charge carrier recombination. (b) schematic representing an ideal donor (red) and acceptor (purple) intermixed morphology. Processes contributing to current generation are shown in green while potential detrimental process (R) is shown in red dashed line. (c) schematic of a non ideal morphology presenting isolated domains without percolation pathway to electrodes as well as large domains in which exciton decay before reaching the interface.

Once free charge carriers have been generated, electrons and holes still have to be transported *via* diffusion or drift to the respective electrodes (**Figure 1-8**, iv). For that to be possible, it is critical that percolation pathways to the contacts exist for virtually every donor and acceptor molecules in the active layer so that the free charge carriers generated do not end up spatially trapped in an energy well (as depicted in **Figure 1-8c**). Finally, free charge carrier extraction mechanism is in direct competition with recombination processes (**Figure 1-8**, R). As the latter takes place at the interface between donor and acceptor, it implies that the donor-acceptor interfacial area should be minimized to favour charge extraction. In summary, in addition to engineering of the donor and acceptor optoelectronic properties, the active layer requires a careful balance of the donor-acceptor interfacial area as well as their respective domain size and percolation pathways.

Solar cells electrical characteristics depend on light as well as the load applied between the electrodes. One can distinguish three main cases as depicted on **Figure 1-9**. (I) When no load is applied on the external circuit, charge carriers are free to move from one electrode to another so that Fermi levels are

at equilibrium in the device and no power is generated. In such short-circuited configuration, bimolecular recombination is normally negligible and the current density (J_{sc}) should be representative of the number of generated free charge carrier inside the device. It is therefore strongly affected by the optical characteristic of the blend. (2) When the load applied on the external circuit is infinite, then free charge carriers cannot be extracted at electrodes and must recombine through bimolecular recombination. Generated free electrons and holes will then accumulate in the active layer until reaching a steady state where recombination and generation fluxes for free charge carriers are equal. That leads to a potential build-up (V_{oc}) between the two electrodes at open circuit. Even though no power can be extracted as no current flows in the electrical circuit, the V_{oc} is representative of the maximum work that can be extracted from a single charge carrier. It is mainly dependent on the difference between the HOMO level of the donor and the LUMO level of the acceptor as well as energetic disorder within the film.⁷³ (3) The operation regime of the solar cell is found in between J_{sc} and V_{oc} , in this range the power – defined as $P = JV$ – will reach a maximum value (P_{max}) at the singular point (V_{max} , J_{max}), where operation of the solar cell is optimum. From these value one can define the fill factor (FF) of the solar cell as,

$$FF = \frac{P_{max}}{J_{sc}V_{oc}} = \frac{J_{max}V_{max}}{J_{sc}V_{oc}} \quad (1.6)$$

The PCE of the solar cell can then be defined as,

$$\eta = \frac{P_{max}}{P_{in}} = \frac{J_{sc}V_{oc}FF}{P_{in}} \quad (1.7)$$

Where P_{in} is the incident light power density. These four parameters (J_{sc} , V_{oc} , FF and η) are the key figures of merit of any solar cells upon given light intensity. Conventionally, characterization of a solar cell is performed at an irradiance P_{in} of 1000 W m^{-2} using the Air Mass 1.5 standard terrestrial solar spectral irradiance distribution.

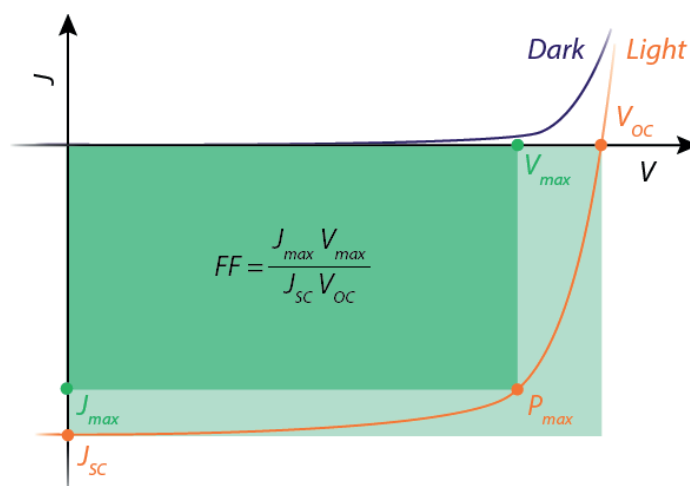


Figure 1-9. Typical J - V characteristic of a photovoltaic device under dark and light conditions and the main figures of merit.

1.3.2 Recent advances and challenges in OPV

Originally, OPV were first conceived as flat heterojunction by depositing sequentially the donor and the acceptor materials which strongly limited the interfacial area. A turning point was the discovery of the bulkheterojunction (BHJ), obtained from single-step deposition of the active layer using a blend solution of donor and acceptor. The resulting morphology presents high interfacial area leading to enhanced J_{sc} .^{74,75} Even though such processing technique provides limited control – mainly through processing conditions or post-treatment (see section 1.1.2) – over the self-assembly, it is routinely used in state-of-the-art devices to reach the optimized morphology for high PCE. Further progress in regard of the PCE has mainly been achieved through molecular engineering, which will shortly be discussed thereafter.

From a historical perspective, electron accepting materials have been mainly dominated by fullerene derivatives, in particular the family of [6,6]-phenyl- C_{60} -butyric acid methyl ester (PCBM), despite difficult synthesis and purification. Physical reasons behind such hegemony are numerous; One can cite their good electron mobility, low reorganizational energy, relatively high dielectric constant (*ca.* 4.4) or even beneficial entropy effect for charge separation ensuing from their central symmetry which provides 3D transport.^{76,77} Nevertheless, in recent years alternative materials presenting high efficiencies have started to arise,⁷⁸ notably through imposing a twist between conjugated planes of perylene diimide (PDI) or DPP-based molecules.^{79–81} State-of-the-art devices based on 3,9-bis(2-methylene-(3-(1,1-dicyanomethylene)-indanone))-5,5,11,11-tetrakis(4-hexylphenyl)-dithieno[2,3-

d:2',3'-d']-s-indaceno[1,2-b:5,6-b']dithiophene (ITIC) small molecules as electron acceptor and reaching up to 13 % have recently been demonstrated.⁸²

In contrast, electron donating materials are generally polymer-based, the typical example being of course P3HT which combined with PCBM yields PCE in the 3-4 % range.⁸³ It is worth noting here that while PBTTT represents a step forward for OFET devices, PCE observed in OPV are actually lower. The underlying reason for this loss in performance is the unique ability for PBTTT and PCBM to form a co-crystal impeding the good charge collection efficiency in the system.^{84,85} A clear limitation to P3HT-based solar cell is its large bandgap ($E_g = 2$ eV) which cannot convert the red part of the solar spectrum. In this respect, the class of D-A alternating polymer with narrower band gap has paved the way for high efficiencies reaching beyond 10 % PCE. Hendriks et al. reported DPP-based polymers that have reached close to 8 % PCE.⁸⁶ Another subclass of high efficiency D-A polymers consist of thienothiophene and benzodithiophene units (PTB) among which a specific polymer coded PTB7 has been repeatedly reported with PCE exceeding 10 %.⁸⁷⁻⁸⁹ High crystallinity being more of a drawback in BHJ OPV – as it favours large scale phase segregation of the donor and acceptor material, reducing the interface – development of small molecule for p-type materials has attracted less attention than polymer, in spite of their well-defined electronic structure. One of the model material for small molecule OPV is a D-A-D symmetrical DPP derivative, 6-bis(5-(benzofuran-2-yl)thiophen-2-yl)-2, 5-bis (2-ethylhexyl) pyrrolo [3, 4-c] pyrrole-1, 4-dione (DPP(TBFu)₂) introduced by Walker et al. in 2009 and reaching over 3 %.⁹⁰ State-of-the-art small molecule devices nowadays reach over 9 % efficiency.^{91,92}

In order to further improve performances of the active layer, a common strategy is to add in a third molecular component within the blend, a strategy globally referred to as ternary OPV.⁹³⁻⁹⁵ This is widely used to improve light absorption of the active layer through co-donor or co-acceptor solar cells adding molecules with complementary absorption spectra⁹⁶⁻⁹⁸ and is also a powerful tool to tune the open circuit voltage in the cell through formation of an organic alloy.⁹⁹ In flat junctions, presence of a material with narrow E_g at the interface can drastically increase the exciton diffusion length through long range energy transfer processes as Förster resonance energy transfer.¹⁰⁰ Moreover, integrating a ternary compound with intermediate HOMO and LUMO levels at the donor acceptor interface is a well-known strategy to reduce recombination, the ternary molecule acting as a depletion region which forces electrons and holes apart.¹⁰¹⁻¹⁰³ Finally, wide range of ternary additives have been developed to help controlling self-assembly and stability of the BHJ.^{104,105}

1.4 Stability of organic semiconductor based technology

Long term stability is essential for commercial application of organic semiconductors and remain a critical challenge to address. Estimating lifetime of a device is simply done by measuring performance over time. Lifetime required for application being about several years, investigation of stability is performed under accelerated aging process by increasing the temperature (conventionally to 80 °C). Instability in OS based technology can be either of chemical (*e.g.* stability of the molecule itself) or physical (*e.g.* stability of the supramolecular assembly) nature. Most organic semiconductors suffer from poor chemical stability in air. That is a direct consequence of their LUMO levels lying relatively high in energy (in the range of 3-4 eV *vs* vacuum) which permits direct reduction of water and oxygen, producing persistent radical cations on the structure and bleaching of the polymer.¹⁰⁶ Two main strategies exist to remedy this issue. Device can be encapsulated to limit contact of the OS with air, though this strategy requires the processing of the device to take place under inert atmosphere.^{107,108} On the other hand, significant effort have been invested on designing materials with lower LUMO levels that would have improved stability in air.¹⁰⁹

Physical instability encompasses morphological change of the active layer as well as diffusion of electrodes within the active layer, impeding the performances.¹⁰⁶ The former is especially challenging in OPV where, in most cases, the optimal BHJ supramolecular assembly corresponds to a thermodynamical metastable state resulting from kinetic constraints during processing. Therefore, with time, the morphology of the blend will tend to change toward a thermodynamic equilibrium different from the optimum structure, resulting in performance losses. Strategies to solve this intrinsic instability can be distinguished in two categories; the ones addressing the kinetic stability of the blend by slowing down the degradation process and the ones focusing on the thermodynamic aspect of the blend by trying to overlap the optimum morphology with the thermodynamic equilibrium. The former essentially consists in crosslinking the active layer to limit the phase segregation.¹¹⁰ It relies on the presence of functional groups (*e.g.* azide) within the blend that will react upon UV exposure or heating to form intermolecular covalent bond, freezing the morphology. Its main drawback is the stochastic nature of the reaction which can modify the conjugated backbone of the active molecules. In contrast to such brutal concepts, elegantly addressing thermodynamics of the blend seems more promising. Visionary work from Siuvala et al. reported a novel amphiphilic molecule to attend to the intrinsic phase segregation of P3HT:PCBM blends, ultimately obtaining stable PCE for 10 h.¹⁰⁵ More recently, Schroeder et al. synthesized a PCBM dumbbell which was found to improve the thermal stability of

the blend.⁴² In addition, Gasperini et al. have showed that adding only 1 wt.% of a flexibly linked polymer inside a DPP(TBFu)₂:PCBM blend can significantly improve the stability of the device.⁴¹ All these publications have in common that they address the crystallinity of the BHJ to avoid large scale phase segregation through crystallization. In this respect, designing a single material that would self-assemble into an optimal configuration through crystallization would be ideal. Guo et al. has reported a photovoltaic device with 3 % PCE solely based on a conjugated blockcopolymer satisfying those requirements.¹¹¹ However, rational design of the polymer to further improve PCE is yet limited by the living polymerization synthetic method, even though promising results of novel coupling method have recently been reported.¹¹²

1.5 References

- (1) Shirakawa, H.; Louis, E. J.; MacDiarmid, A. G.; Chiang, C. K.; Heeger, A. J. *J. Chem. Soc. Chem. Commun.* **1977**, No. 16, 578.
- (2) Tang, C. W. *Appl. Phys. Lett.* **1986**, *48* (2), 183.
- (3) Tang, C. W.; VanSlyke, S. A. *Appl. Phys. Lett.* **1987**, *51* (12), 913.
- (4) Koezuka, H.; Tsumura, A.; Ando, T. *Synth. Met.* **1987**, *18* (1), 699.
- (5) Clarke, T. M.; Durrant, J. R. *Chem. Rev.* **2010**, *110* (11), 6736.
- (6) Koch, N. In *Physics of Organic Semiconductors*; Brütting, W., Adachi, C., Eds.; Wiley-VCH Verlag GmbH & Co. KGaA, 2012; pp 35–63.
- (7) Ueno, N. In *Physics of Organic Semiconductors*; Brütting, W., Adachi, C., Eds.; Wiley-VCH Verlag GmbH & Co. KGaA, 2012; pp 65–89.
- (8) Kim, G.; Kang, S.-J.; Dutta, G. K.; Han, Y.-K.; Shin, T. J.; Noh, Y.-Y.; Yang, C. *J. Am. Chem. Soc.* **2014**, *136* (26), 9477.
- (9) Xu, X.; Yao, Y.; Shan, B.; Gu, X.; Liu, D.; Liu, J.; Xu, J.; Zhao, N.; Hu, W.; Miao, Q. *Adv. Mater.* **2016**, *28* (26), 5276.
- (10) Yamashita, Y.; Hinkel, F.; Marszalek, T.; Zajackowski, W.; Pisula, W.; Baumgarten, M.; Matsui, H.; Müllen, K.; Takeya, J. *Chem. Mater.* **2016**, *28* (2), 420.
- (11) Li, S. S.; Thurber, W. R. *Solid-State Electron.* **1977**, *20* (7), 609.
- (12) Bässler, H.; Köhler, A. In *Unimolecular and Supramolecular Electronics I*; Metzger, R. M., Ed.; Topics in Current Chemistry; Springer Berlin Heidelberg, 2011; pp 1–65.
- (13) Mladenović, M.; Vukmirović, N. *Adv. Funct. Mater.* **2015**, *25* (13), 1915.
- (14) Yamamoto, J.; Furukawa, Y. *J. Phys. Chem. B* **2015**, *119* (13), 4788.
- (15) Miller, A.; Abrahams, E. *Phys. Rev.* **1960**, *120* (3), 745.
- (16) Schein, L. B.; McGhie, A. R. *Phys. Rev. B* **1979**, *20* (4), 1631.
- (17) Shuai, Z.; Wang, L.; Song, C. In *Theory of Charge Transport in Carbon Electronic Materials*; SpringerBriefs in Molecular Science; Springer Berlin Heidelberg, 2012; pp 7–41.
- (18) Bässler, H. *Phys. Status Solidi B* **1993**, *175* (1), 15.
- (19) Lu, N.; Li, L.; Banerjee, W.; Sun, P.; Gao, N.; Liu, M. *J. Appl. Phys.* **2015**, *118* (4), 045701.
- (20) Marcus, R. A.; Sutin, N. *Biochim. Biophys. Acta BBA - Rev. Bioenerg.* **1985**, *811* (3), 265.

-
- (21) Nenashev, A. V.; Oelerich, J. O.; Baranovskii, S. D. *J. Phys. Condens. Matter* **2015**, *27* (9), 093201.
- (22) Sootsman, J. R.; Kong, H.; Uher, C.; D'Angelo, J. J.; Wu, C.-I.; Hogan, T. P.; Caillat, T.; Kanatzidis, M. G. *Angew. Chem.* **2008**, *120* (45), 8746.
- (23) Minder, N. A.; Ono, S.; Chen, Z.; Facchetti, A.; Morpurgo, A. F. *Adv. Mater.* **2012**, *24* (4), 503.
- (24) Yamashita, Y.; Tsurumi, J.; Hinkel, F.; Okada, Y.; Soeda, J.; Zajaczkowski, W.; Baumgarten, M.; Pisula, W.; Matsui, H.; Müllen, K.; Takeya, J. *Adv. Mater.* **2014**, *26* (48), 8169.
- (25) Senanayak, S. P.; Ashar, A. Z.; Kanimozhi, C.; Patil, S.; Narayan, K. S. *Phys. Rev. B* **2015**, *91* (11), 115302.
- (26) Glarum, S. H. *J. Phys. Chem. Solids* **1963**, *24* (12), 1577.
- (27) Fratini, S.; Ciuchi, S. *Phys. Rev. Lett.* **2009**, *103* (26), 266601.
- (28) Smith, J.; Hamilton, R.; Qi, Y.; Kahn, A.; Bradley, D. D. C.; Heeney, M.; McCulloch, I.; Anthopoulos, T. D. *Adv. Funct. Mater.* **2010**, *20* (14), 2330.
- (29) Diao, Y.; Shaw, L.; Bao, Z.; B. Mannsfeld, S. C. *Energy Environ. Sci.* **2014**, *7* (7), 2145.
- (30) Smulders, M. M. J.; Nieuwenhuizen, M. M. L.; de Greef, T. F. A.; van der Schoot, P.; Schenning, A. P. H. J.; Meijer, E. W. *Chem. – Eur. J.* **2010**, *16* (1), 362.
- (31) Machui, F.; Langner, S.; Zhu, X.; Abbott, S.; Brabec, C. J. *Sol. Energy Mater. Sol. Cells* **2012**, *100*, 138.
- (32) Walker, B.; Tamayo, A.; Duong, D. T.; Dang, X.-D.; Kim, C.; Granstrom, J.; Nguyen, T.-Q. *Adv. Energy Mater.* **2011**, *1* (2), 221.
- (33) Treat, N. D.; Nekuda Malik, J. A.; Reid, O.; Yu, L.; Shuttle, C. G.; Rumbles, G.; Hawker, C. J.; Chabinyc, M. L.; Smith, P.; Stingelin, N. *Nat. Mater.* **2013**, *12* (7), 628.
- (34) Sharenko, A.; Treat, N. D.; Love, J. A.; Toney, M. F.; Stingelin, N.; Nguyen, T.-Q. *J. Mater. Chem. A* **2014**, *2* (38), 15717.
- (35) Wang, J.-L.; Liu, K.-K.; Yan, J.; Wu, Z.; Liu, F.; Xiao, F.; Chang, Z.-F.; Wu, H.-B.; Cao, Y.; Russell, T. P. *J. Am. Chem. Soc.* **2016**, *138* (24), 7687.
- (36) Yuan, Y.; Giri, G.; Ayzner, A. L.; Zoombelt, A. P.; Mannsfeld, S. C. B.; Chen, J.; Nordlund, D.; Toney, M. F.; Huang, J.; Bao, Z. *Nat. Commun.* **2014**, *5*, 3005.
- (37) Sun, K.; Xiao, Z.; Lu, S.; Zajaczkowski, W.; Pisula, W.; Hanssen, E.; White, J. M.; Williamson, R. M.; Subbiah, J.; Ouyang, J.; Holmes, A. B.; Wong, W. W. H.; Jones, D. J. *Nat. Commun.* **2015**, *6*, 6013.
- (38) Tamayo, A.; Kent, T.; Tantitiwat, M.; A. Dante, M.; Rogers, J.; Nguyen, T.-Q. *Energy Environ. Sci.* **2009**, *2* (11), 1180.
- (39) Sun, Y.; Welch, G. C.; Leong, W. L.; Takacs, C. J.; Bazan, G. C.; Heeger, A. J. *Nat. Mater.* **2012**, *11* (1), 44.
- (40) Mei, J.; Bao, Z. *Chem. Mater.* **2014**, *26* (1), 604.
- (41) Gasperini, A.; Jeanbourquin, X. A.; Rahmanudin, A.; Yu, X.; Sivula, K. *Adv. Mater.* **2015**, *27* (37), 5541.
- (42) Schroeder, B. C.; Li, Z.; Brady, M. A.; Faria, G. C.; Ashraf, R. S.; Takacs, C. J.; Cowart, J. S.; Duong, D. T.; Chiu, K. H.; Tan, C.-H.; Cabral, J. T.; Salleo, A.; Chabinyc, M. L.; Durrant, J. R.; McCulloch, I. *Angew. Chem. Int. Ed.* **2014**, *53* (47), 12870.
- (43) Gasperini, A.; Bivaud, S.; Sivula, K. *Chem. Sci.* **2014**, *5* (12), 4922.
- (44) Schroeder, B. C.; Chiu, Y.-C.; Gu, X.; Zhou, Y.; Xu, J.; Lopez, J.; Lu, C.; Toney, M. F.; Bao, Z. *Adv. Electron. Mater.* **2016**, *2* (7), 1600104.
- (45) Gasperini, A.; Sivula, K. *Macromolecules* **2013**, *46* (23), 9349.
- (46) Yagi, I.; Tsukagoshi, K.; Aoyagi, Y. *Appl. Phys. Lett.* **2005**, *86* (10), 103502.
- (47) Sirringhaus, H. *Adv. Mater.* **2014**, *26* (9), 1319.

- (48) Anthony, J. E.; Brooks, J. S.; Eaton, D. L.; Parkin, S. R. *J. Am. Chem. Soc.* **2001**, *123* (38), 9482.
- (49) Payne, M. M.; Parkin, S. R.; Anthony, J. E.; Kuo, C.-C.; Jackson, T. N. *J. Am. Chem. Soc.* **2005**, *127* (14), 4986.
- (50) Diao, Y.; Tee, B. C.-K.; Giri, G.; Xu, J.; Kim, D. H.; Becerril, H. A.; Stoltenberg, R. M.; Lee, T. H.; Xue, G.; Mannsfeld, S. C. B.; Bao, Z. *Nat. Mater.* **2013**, *12* (7), 665.
- (51) Minemawari, H.; Yamada, T.; Matsui, H.; Tsutsumi, J.; Haas, S.; Chiba, R.; Kumai, R.; Hasegawa, T. *Nature* **2011**, *475* (7356), 364.
- (52) Gasperini, A.; Jeanbourquin, X. A.; Sivula, K. *J. Polym. Sci. Part B Polym. Phys.* **2016**, n/a.
- (53) Veres, J.; Ogier, S. d.; Leeming, S. w.; Cupertino, D. c.; Mohialdin Khaffaf, S. *Adv. Funct. Mater.* **2003**, *13* (3), 199.
- (54) Ono, L. K.; Schulz, P.; Endres, J. J.; Nikiforov, G. O.; Kato, Y.; Kahn, A.; Qi, Y. *J. Phys. Chem. Lett.* **2014**, *5* (8), 1374.
- (55) Grozema, F. C.; van Duijnen, P. T.; Berlin, Y. A.; Ratner, M. A.; Siebbeles, L. D. A. *J. Phys. Chem. B* **2002**, *106* (32), 7791.
- (56) Bao, Z.; Dodabalapur, A.; Lovinger, A. J. *Appl. Phys. Lett.* **1996**, *69* (26), 4108.
- (57) Sirringhaus, H.; Brown, P. J.; Friend, R. H.; Nielsen, M. M.; Bechgaard, K.; Langeveld-Voss, B. M. W.; Spiering, A. J. H.; Janssen, R. a. J.; Meijer, E. W.; Herwig, P.; Leeuw, D. M. de. *Nature* **1999**, 401.
- (58) Brinkmann, M.; Rannou, P. *Adv. Funct. Mater.* **2007**, *17* (1), 101.
- (59) Zen, A.; Pflaum, J.; Hirschmann, S.; Zhuang, W.; Jaiser, F.; Asawapirom, U.; Rabe, J. P.; Scherf, U.; Neher, D. *Adv. Funct. Mater.* **2004**, *14* (8), 757.
- (60) McCulloch, I.; Heeney, M.; Bailey, C.; Genevicius, K.; MacDonald, I.; Shkunov, M.; Sparrowe, D.; Tierney, S.; Wagner, R.; Zhang, W.; Chabiny, M. L.; Kline, R. J.; McGehee, M. D.; Toney, M. F. *Nat. Mater.* **2006**, *5* (4), 328.
- (61) McCulloch, I.; Heeney, M.; Chabiny, M. L.; DeLongchamp, D.; Kline, R. J.; Cölle, M.; Duffy, W.; Fischer, D.; Gundlach, D.; Hamadani, B.; Hamilton, R.; Richter, L.; Salleo, A.; Shkunov, M.; Sparrowe, D.; Tierney, S.; Zhang, W. *Adv. Mater.* **2009**, *21* (10–11), 1091.
- (62) Tsao, H. N.; Cho, D. M.; Park, I.; Hansen, M. R.; Mavrinskiy, A.; Yoon, D. Y.; Graf, R.; Pisula, W.; Spiess, H. W.; Müllen, K. *J. Am. Chem. Soc.* **2011**, *133* (8), 2605.
- (63) Chen, Z.; Lee, M. J.; Shahid Ashraf, R.; Gu, Y.; Albert-Seifried, S.; Meedom Nielsen, M.; Schroeder, B.; Anthopoulos, T. D.; Heeney, M.; McCulloch, I.; Sirringhaus, H. *Adv. Mater.* **2012**, *24* (5), 647.
- (64) Li, J.; Zhao, Y.; Tan, H. S.; Guo, Y.; Di, C.-A.; Yu, G.; Liu, Y.; Lin, M.; Lim, S. H.; Zhou, Y.; Su, H.; Ong, B. S. *Sci. Rep.* **2012**, *2*, 754.
- (65) Noriega, R.; Rivnay, J.; Vandewal, K.; Koch, F. P. V.; Stingelin, N.; Smith, P.; Toney, M. F.; Salleo, A. *Nat. Mater.* **2013**, *12* (11), 1038.
- (66) Son, S. Y.; Kim, Y.; Lee, J.; Lee, G.-Y.; Park, W.-T.; Noh, Y.-Y.; Park, C. E.; Park, T. *J. Am. Chem. Soc.* **2016**, *138* (26), 8096.
- (67) Trenberth, K. E.; Fasullo, J. T.; Kiehl, J. *Bull. Am. Meteorol. Soc.* **2009**, *90* (3), 311.
- (68) Statistical Review of World Energy | Energy economics | BP Global <http://www.bp.com/en/global/corporate/energy-economics/statistical-review-of-world-energy.html> (accessed May 28, 2017).
- (69) Liu, Z.; He, C.; Zhou, Y.; Wu, J. *Landsc. Ecol.* **2014**, *29* (5), 763.
- (70) Shockley, W.; Queisser, H. J. *J. Appl. Phys.* **1961**, *32* (3), 510.
- (71) Lai, T.-H.; Tsang, S.-W.; Manders, J. R.; Chen, S.; So, F. *Mater. Today* **2013**, *16* (11), 424.
- (72) Proctor, C. M.; Kher, A. S.; Love, J. A.; Huang, Y.; Sharenko, A.; Bazan, G. C.; Nguyen, T.-Q. *Adv. Energy Mater.* **2016**, 1502285.

- (73) Collins, S. D.; Proctor, C. M.; Ran, N. A.; Nguyen, T.-Q. *Adv. Energy Mater.* **2016**, 6 (4), 1501721.
- (74) Yu, G.; Heeger, A. J. *J. Appl. Phys.* **1995**, 78 (7), 4510.
- (75) Spanggaard, H.; Krebs, F. C. *Sol. Energy Mater. Sol. Cells* **2004**, 83 (2–3), 125.
- (76) Sieval, A. B.; Hummelen, J. C. In *Organic Photovoltaics*; Brabec, C., Scherf, U., Dyakonov, V., Eds.; Wiley-VCH Verlag GmbH & Co. KGaA, 2014; pp 209–238.
- (77) Gregg, B. A. *J. Phys. Chem. Lett.* **2011**, 2 (24), 3013.
- (78) Nielsen, C. B.; Holliday, S.; Chen, H.-Y.; Cryer, S. J.; McCulloch, I. *Acc. Chem. Res.* **2015**, 48 (11), 2803.
- (79) Li, S.; Liu, W.; Shi, M.; Mai, J.; Lau, T.-K.; Wan, J.; Lu, X.; Li, C.-Z.; Chen, H. *Energy Environ. Sci.* **2016**, 9 (2), 604.
- (80) Yi, J.; Wang, Y.; Luo, Q.; Lin, Y.; Tan, H.; Wang, H.; Ma, C.-Q. *Chem. Commun.* **2016**, 52 (8), 1649.
- (81) Liu, T.; Meng, D.; Cai, Y.; Sun, X.; Li, Y.; Huo, L.; Liu, F.; Wang, Z.; Russell, T. P.; Sun, Y. *Adv. Sci.* **2016**, 3 (9), 1600117.
- (82) Zhao, W.; Li, S.; Yao, H.; Zhang, S.; Zhang, Y.; Yang, B.; Hou, J. *J. Am. Chem. Soc.* **2017**.
- (83) Dang, M. T.; Hirsch, L.; Wantz, G. *Adv. Mater.* **2011**, 23 (31), 3597.
- (84) Mayer, A. C.; Toney, M. F.; Scully, S. R.; Rivnay, J.; Brabec, C. J.; Scharber, M.; Koppe, M.; Heeney, M.; McCulloch, I.; McGehee, M. D. *Adv. Funct. Mater.* **2009**, 19 (8), 1173.
- (85) Causa', M.; Jonghe-Risse, J. D.; Scarongella, M.; Brauer, J. C.; Buchaca-Domingo, E.; Moser, J.-E.; Stingelin, N.; Banerji, N. *Nat. Commun.* **2016**, 7, 12556.
- (86) Hendriks, K. H.; Heintges, G. H. L.; Gevaerts, V. S.; Wienk, M. M.; Janssen, R. A. J. *Angew. Chem. Int. Ed.* **2013**, 52 (32), 8341.
- (87) Liang, Y.; Xu, Z.; Xia, J.; Tsai, S.-T.; Wu, Y.; Li, G.; Ray, C.; Yu, L. *Adv. Mater.* **2010**, 22 (20), E135.
- (88) He, Z.; Xiao, B.; Liu, F.; Wu, H.; Yang, Y.; Xiao, S.; Wang, C.; Russell, T. P.; Cao, Y. *Nat. Photonics* **2015**, 9 (3), 174.
- (89) Liu, C.; Yi, C.; Wang, K.; Yang, Y.; Bhatta, R. S.; Tsige, M.; Xiao, S.; Gong, X. *ACS Appl. Mater. Interfaces* **2015**, 7 (8), 4928.
- (90) Walker, B.; Tamayo, A. B.; Dang, X.-D.; Zalar, P.; Seo, J. H.; Garcia, A.; Tantiwiwat, M.; Nguyen, T.-Q. *Adv. Funct. Mater.* **2009**, 19 (19), 3063.
- (91) Bin, H.; Yang, Y.; Zhang, Z.-G.; Ye, L.; Ghasemi, M.; Chen, S.; Zhang, Y.; Zhang, C.; Sun, C.; Xue, L.; Yang, C.; Ade, H.; Li, Y. *J. Am. Chem. Soc.* **2017**, 139 (14), 5085.
- (92) Zhang, Q.; Kan, B.; Liu, F.; Long, G.; Wan, X.; Chen, X.; Zuo, Y.; Ni, W.; Zhang, H.; Li, M.; Hu, Z.; Huang, F.; Cao, Y.; Liang, Z.; Zhang, M.; Russell, T. P.; Chen, Y. *Nat. Photonics* **2015**, 9 (1), 35.
- (93) Lu, L.; Kelly, M. A.; You, W.; Yu, L. *Nat. Photonics* **2015**, 9 (8), 491.
- (94) Goubard, F.; Wantz, G. *Polym. Int.* **2014**, 63 (8), 1362.
- (95) Savoie, B. M.; Dunaisky, S.; Marks, T. J.; Ratner, M. A. *Adv. Energy Mater.* **2015**, 5 (3), 1400891.
- (96) Lim, B.; Bloking, J. T.; Poncec, A.; McGehee, M. D.; Sellinger, A. *ACS Appl. Mater. Interfaces* **2014**, 6 (9), 6905.
- (97) Yang, Y. (Michael); Chen, W.; Dou, L.; Chang, W.-H.; Duan, H.-S.; Bob, B.; Li, G.; Yang, Y. *Nat. Photonics* **2015**, 9 (3), 190.
- (98) Bi, P.-Q.; Wu, B.; Zheng, F.; Xu, W.-L.; Yang, X.-Y.; Feng, L.; Zhu, F.; Hao, X.-T. *ACS Appl. Mater. Interfaces* **2016**, 8 (35), 23212.
- (99) Street, R. A.; Davies, D.; Khlyabich, P. P.; Burkhart, B.; Thompson, B. C. *J. Am. Chem. Soc.* **2013**, 135 (3), 986.
- (100) Cnops, K.; Rand, B. P.; Cheyns, D.; Verreert, B.; Empl, M. A.; Heremans, P. *Nat. Commun.* **2014**, 5, 3406.
- (101) Lu, L.; Xu, T.; Chen, W.; Landry, E. S.; Yu, L. *Nat. Photonics* **2014**, 8 (9), 716.

- (102) Zhang, Y.; Deng, D.; Lu, K.; Zhang, J.; Xia, B.; Zhao, Y.; Fang, J.; Wei, Z. *Adv. Mater.* **2015**, 27 (6), 1071.
- (103) Kipp, D.; Ganesan, V. *Macromolecules* **2016**, 49 (14), 5137.
- (104) Liao, H.-C.; Chen, P.-H.; Chang, R. P. H.; Su, W.-F. *Polymers* **2014**, 6 (11), 2784.
- (105) Sivula, K.; Ball, Z. T.; Watanabe, N.; Fréchet, J. M. J. *Adv. Mater.* **2006**, 18 (2), 206.
- (106) Cheng, P.; Zhan, X. *Chem. Soc. Rev.* **2016**, 45 (9), 2544.
- (107) Adams, J.; Salvador, M.; Lucera, L.; Langner, S.; Spyropoulos, G. D.; Fecher, F. W.; Voigt, M. M.; Dowland, S. A.; Osvet, A.; Egelhaaf, H.-J.; Brabec, C. J. *Adv. Energy Mater.* **2015**, 5 (20), 1601065.
- (108) Carlé, J. E.; Helgesen, M.; Madsen, M. V.; Bundgaard, E.; Krebs, F. C. *J. Mater. Chem. C* **2014**, 2 (7), 1290.
- (109) Zhao, Z.; Yin, Z.; Chen, H.; Guo, Y.; Tang, Q.; Liu, Y. *J. Mater. Chem. C* **2017**, 5 (11), 2892.
- (110) Rumer, J. W.; McCulloch, I. *Mater. Today* **2015**, 18 (8), 425.
- (111) Guo, C.; Lin, Y.-H.; Witman, M. D.; Smith, K. A.; Wang, C.; Hexemer, A.; Strzalka, J.; Gomez, E. D.; Verduzco, R. *Nano Lett.* **2013**, 13 (6), 2957.
- (112) Gasperini, A.; Johnson, M.; Jeanbourquin, X.; Yao, L.; Rahmanudin, A.; Guijarro, N.; Sivula, K. *Polym. Chem.* **2017**, 8 (5), 824.



Chapter 2 Experimental methods

Complete experimental methods used to fabricate and characterize materials and devices presented in chapter 3 to 6 are discussed in this section. Given that this thesis mainly focuses on physical aspect of the materials, synthetic routes and full characterization of organic semiconductors that have been synthesized for the next chapters are presented in the appendix.

2.1 Purification technique

2.1.1 *Size exclusion chromatography*

Size exclusion chromatography also known as gel permeation chromatography (GPC) is an entropically driven separation technique in which molecules can be separated based on their hydrodynamic volume.¹ It simply consists of stacked porous beads in a chromatography column (as represented in green, **Figure 2-1**). Upon injection of a polymer with large D_M , small polymer chains will interact with the pores, leading to long travel time through the column while the long polymer chains, not able to enter the pores, will flow straight through the column. It ensues that high M_n fractions can be collected in the early time after injection while low M_n is collected lastly. GPC is equipped with a simple UV-vis absorption detector at the output in order to monitor accurately the elution time of the polymer fraction. In analytical configuration, GPC can only be used as a relative technique that relies on column calibration, for example using tagged polystyrene with known M_n as references. It can also be used as a preparatory technique to fractionate a crude polymer (large D_M) into fractions with varying M_n and narrower D_M .

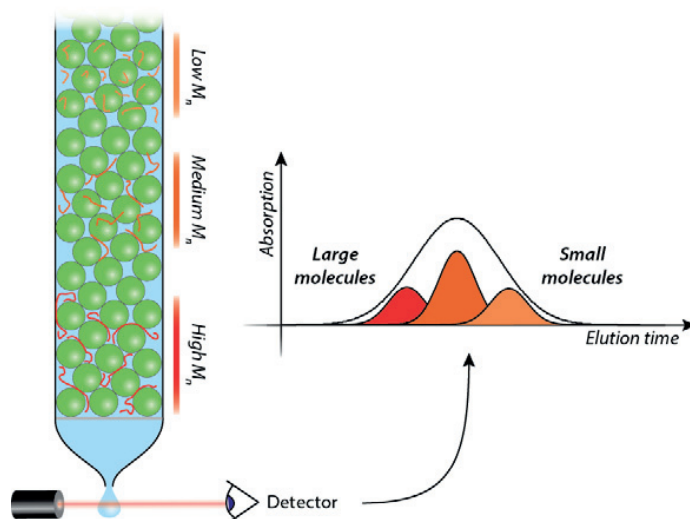


Figure 2-1. Schematic of a GPC setup with porous beads in green. The polymer is represented in red with long chains migrating faster than short chains due to difference in interaction with the porous beads. Absorption is measured in function of time at a selected wavelength resulting in a typical Gaussian distribution.

In this work analytical GPC (Shimadzu) was performed using a PSS SDV analytical linear M column ($8 \times 250 \text{ mm}^2$) with a mobile phase consisting of chlorobenzene (CB) at 80°C at 1 mL min^{-1} using polystyrene fluorescein labelled standards (PSS) as reference. Preparatory GPC (Shimadzu) was carried out by injecting the polymer sample at a concentration of 5 mg mL^{-1} in a PSS SDV preparative linear M column ($40 \times 250 \text{ mm}^2$) with chlorobenzene at 80°C as mobile phase at a constant elution flow of 10 mL min^{-1} . Fraction collection was carried out every 20 s. Single fractions were then analysed through the analytical size exclusion column as described above. The CB was removed, and the samples were stored in an argon glovebox until further use.

2.2 Opto-electronic properties characterization

2.2.1 Cyclic voltammetry

Cyclic voltammetry (CV) is a three electrodes technique which relies on a reference electrode to quantify the absolute potential at which electrochemical processes take place. It is of critical importance for OS characterization as it allows to accurately measure HOMO and LUMO onset position. In addition to the reference electrode, the setup consists of a working electrode that is a conductive substrate onto which the active component is casted and a counter electrode, such as a Pt wire. The three electrodes are then placed in an electrolyte (to provide conductivity) and connected through

a potentiostat. In this configuration, the potentiostat can apply a bias on the working electrode relative to the fixed potential of the reference electrode, while measuring the current flowing between the working and counter electrode. Before testing any material, it is important to measure a baseline without active material to make sure that no parasitic processes occurs within the potential window under consideration (*e.g.* water reduction). When the OS is present, an associated reductive peak (negative current) and oxidative peak (positive current) will appear corresponding respectively to the LUMO and HOMO of the material. The onset is extracted as the intersection between the tangent to the peak and the baseline. It is worth noting that most OS are not stable through these redox processes. Hence the sample must be changed after each measurement. Moreover, high lying LUMO and deep HOMO levels as for P3HT and PCBM respectively are out of the potential window and must be inferred from the bandgap of the material.

CV was performed on drop-casted films over a platinum working electrode (if not specified otherwise) within a 0.5 M tetrabutylammonium hexafluorophosphate solution in acetonitrile at a sweeping rate of 50 mV s⁻¹ vs. an Ag/Ag⁺ reference electrode and using a SP-300 potentiostat from biologic.

2.2.2 Ultraviolet-visible spectroscopy

Ultraviolet-visible spectroscopy (UV-vis) is a technique which characterize light-induced electronic transition within a material. A monochromatic light with intensity I_0 (measured *via* a reference) is shined through a sample and on a detector which measures the intensity I after the sample. The loss in intensity through the sample can be expressed as $I_0 = I + I_a + I_r$, with I_a the amount of light absorbed by the material and I_r the light lost by diffuse and direct reflection. The ratio I/I_0 is defined as the transmittance of the sample, while the absorbance can be expressed according to Beer-Lambert law as,

$$A(\lambda) = -\log\left(\frac{I}{I_0}\right) = \varepsilon(\lambda) d \quad (2.1)$$

Where $\varepsilon(\lambda)$ is the extinction coefficient and d is the optical path length through the sample (ideally the thickness of the sample). It is clear that this expression only holds while reflective contributions are negligible as compared to absorption. Even though this consideration is generally true in thin film OS, some sensitive calculations, as internal quantum efficiency which will be discussed later, require the exact total absorption of the film. Such measurement is achieved using an integrating sphere to collect all photons not absorbed by the sample.

Absorption spectra were recorded with a UV-vis-NIR UV-3600 spectrophotometer from Shimadzu. Temperature-dependent absorption spectra were measured using a custom-made heater for the solid-state samples. In order to calculate the internal quantum efficiency, total absorbance was measured using an integration sphere.

2.3 Supramolecular assembly characterization

2.3.1 *Differential scanning calorimetry*

Differential scanning calorimetry (DSC) is an analytical technique measuring the energy required to heat up a sample relative to a reference at a controlled rate in $^{\circ}\text{C min}^{-1}$ and under inert atmosphere to limit oxidation. It results in a linear behaviour with a slope corresponding to the specific heat capacity of the sample. Deviation from the linear behaviour indicates that the sample undergoes a phase transition which can be of either first or second order. The former is a thermodynamical transition which by definition will be associated with a latent heat as crystallisation, melting and so on. Hence they can be described by an onset temperature at which phase transition occurs and an enthalpy (ΔH) obtained by integrating the peak corresponding to the transition (as depicted on **Figure 2-2**). Transition from an initial phase to a final phase can either release or absorb energy, respectively exothermic ($\Delta H < 0$) or endothermic ($\Delta H > 0$), depending on which of the initial or final state in thermodynamically favourable. Enthalpy of melting is of peculiar interest in this work as it conveys the total energy required to break all Van der Waals interactions within the crystal structure, which are crucial to assessing crystallinity of the solid phase. In contrast, second order transitions do not involve a change in thermodynamic state but a vibrational excitation of the same thermodynamic state, hence they are not associated with a latent heat. A typical example in semiconducting polymer is the glass transition which conveys a change in viscosity of the material associated with a change in specific heat capacity that can be detected by DSC. It arises from an increase in degrees of freedom with the same packing structure caused by thermal expansion and/or vibration. It is important to understand that the glass transition temperature depends on the scan rate and thereof cannot be considered a physical constant. Altogether, these first and second order transitions are critical to the understanding of the packing structure evolution with temperature and hence to assess thermal stability.²

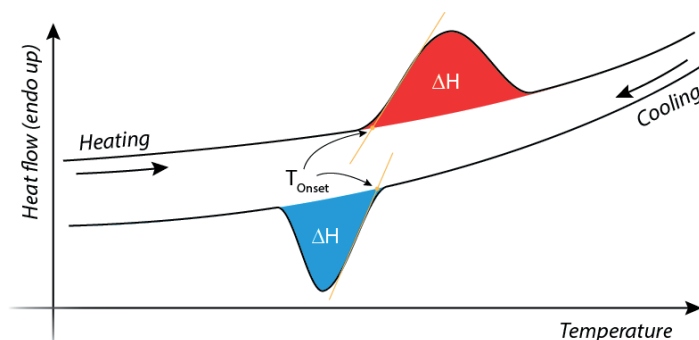


Figure 2-2. Schematic of a 1st order phase transition with position of onset temperature and the associated enthalpy.

Differential scanning calorimetry was performed using a Perkin-Elmer DSC8000 calibrated with indium and zinc at a scanning rate of 10 °C min⁻¹. Samples were prepared by drop-casting from a precursor solution and evaporation of the solvent under argon atmosphere at RT (unless specified otherwise). The samples were then dried under vacuum. Enthalpies were calculated by integrating over the phase transition.

2.3.2 Atomic force microscopy

Atomic force microscopy (AFM) is a powerful technique to probe a sample surface with nanometric resolution relying on forces arising between the sample surface and a sharp tip mounted on a cantilever. These forces encompass Van der Waals forces, electrostatic interactions, contact forces and so on. AFM presents several advantages over popular electron microscopy techniques with comparable high resolution. On one hand, it returns information over the z-direction with a resolution over a few Angstrom. On the other hand, while AFM is mainly used to measure topography of the surface, it can also be used in a variety of other modes, even allowing to manipulate single molecules on a surface. The three main modes that will be used in this work are tapping mode, Young modulus (YM) mapping and Kelvin probe force microscopy (KPFM), all performed in air. A brief review of these techniques is proposed in the next three paragraphs.

a) Tapping mode

Tapping mode is an AFM technique where the cantilever is excited to a resonance frequency using a dither piezo. It is preferred to the normal contact mode given that the oscillation of the tip in the z-direction provides a more secure approach on the surface during scanning in the xy-direction. The surface is then located through minimizing the force exerting on the cantilever by varying the position of the sample using a feedback loop. In addition to the height, tapping mode returns two other key

figures which are the amplitude and phase of the cantilever oscillation. Change in the former should simply be minimized as in example a reduction in amplitude could result from a tip hitting too hard on the surface. The phase however is extremely interesting as it can convey very small change in Van der Waals forces, in example arising from a change in chemical structure on the surface, which are too weak to be addressed by the feedback loop. Hence the phase can potentially indicate change in composition of the surface (*e.g.* as reported by Gasperini et al.).³

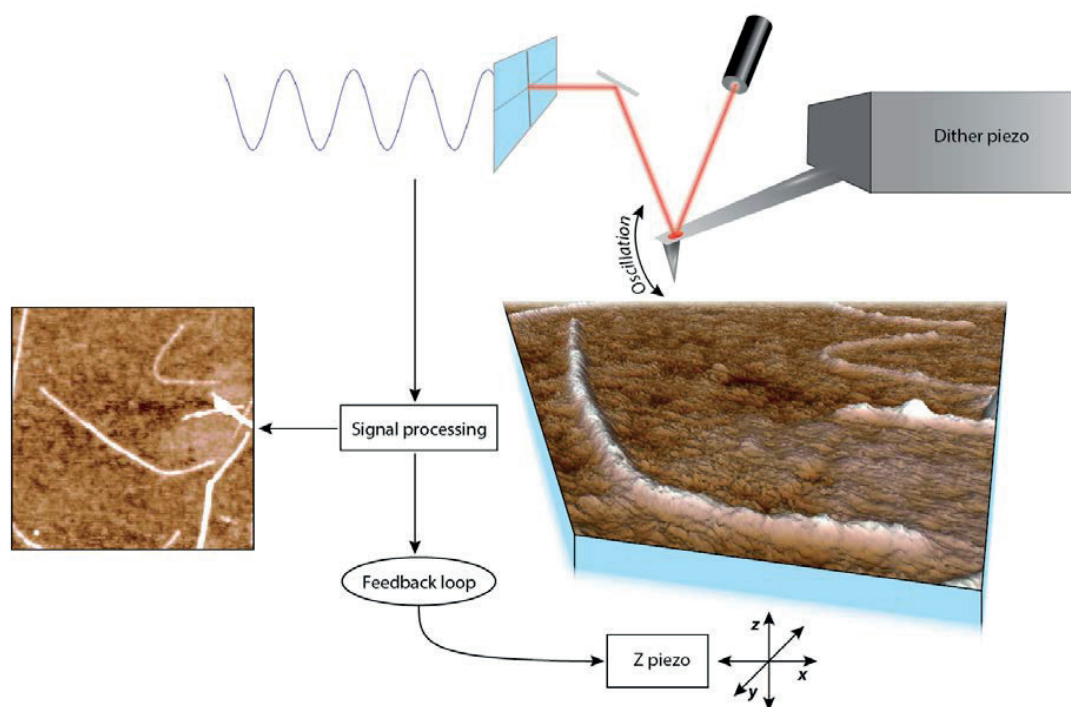


Figure 2-3. Schematic of atomic force microscopy operating in tapping mode to scan the surface profile. The surface presents DNA-wrapped carbon nanotubes.

b) Force curve mode

Young modulus mapping simply consists in an array of force curves each measured by pressing the tip against the sample while measuring deflection of the cantilever. A typical force curve for organic semiconductor is depicted in **Figure 2-4**. During the approach of the surface no bending of the cantilever occurs. Once close to the surface, attraction forces will deflect the cantilever downward and as the tip start pushing on the surface, repulsive forces will deflect the cantilever upward. Converting deflection to the force exerted on the cantilever requires the inverse optical lever sensitivity obtained by thermal calibration of the cantilever. Force measurement requires a typical indentation of the surface about 5 nm, in order to have enough contact data to extract the YM. In general, with OS, there exist a slight hysteresis between approach and retraction force curves, suggesting that tip induces deformation with relaxation time longer than measurement time (>0.5 s). The YM can then be extracted by fitting the force curve using an appropriate model. Given the adhesion characteristic of OS, the Derjaguin-Muller-Toporov (DMT) model is used as to account for attractive forces between tip and surface, leading to the following expression:⁴

$$A_c = \pi \frac{R^{2/3}}{K^{2/3}} (F + 2\pi\gamma R_c)^{2/3} \quad (2.2)$$

Where A_c is the contact area with the surface similar to indentation distance, F is the repulsive force exerted on the tip, γ is the work per unit area required to balance attractive forces, R is the combined curvature radius of the contact and K is the combined reduced young modulus of the different materials i (E_i^*) expressed as,

$$K = \frac{4}{3} \left(\sum_i \frac{1}{E_i^*} \right)^{-1} \quad (2.3)$$

Knowing the young modulus of the cantilever through thermal calibration, the YM of the surface can then be calculated for each force curves and plotted as function of xy-position or as a distribution of YM.^{5,6}

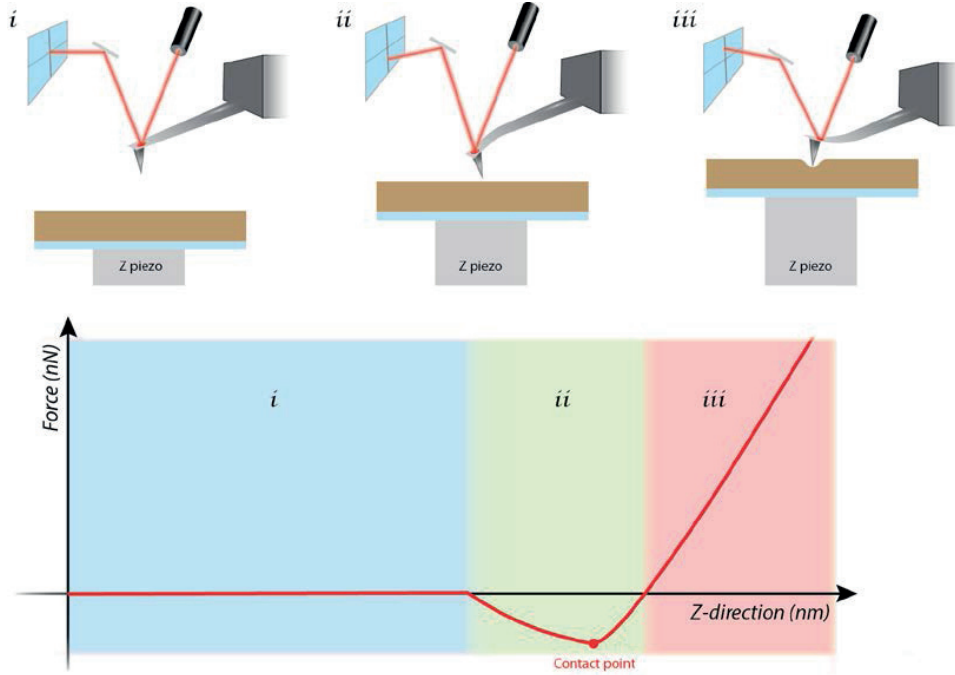


Figure 2-4. Schematic of force curve measurements with the 3 main regions: (i) non-contact, (ii) attractive force bend the tip downwards and (iii) repulsive forces bend the tip upwards.

c) Kelvin probe mode

Kelvin probe force microscopy is based on electrostatic forces exerting on the tip when it is close to the surface. In this method, each line of the image needs to be scanned twice. The first pass is done in normal tapping mode with a mechanical excitation in order to measure the surface profile. In the second pass, the probe is maintained at a distance Δh (inversely proportional to the lateral resolution) above the surface while following its profile. During this scan the conductive tip is no more excited mechanically but electrically by applying an AC bias (V_{AC}) on it. The electrostatic force acting on the tip during this pass can be expressed in term of a parallel plates capacitor with $F \propto V^2$.⁷ The voltage difference between the tip and the surface can be written as $V = (V_{DC} - V_{CPD}) + V_{AC}\sin(\omega t)$ with V_{CPD} being the contact potential difference, V_{DC} any external bias applied on the tip or sample and ω the frequency of the electrical excitation. From this expression it is clear that V will reach a minimum when $V_{DC} = V_{CPD}$. Hence, the force acting on the cantilever will be minimized when an additional

direct bias equal to the contact potential difference is applied on the tip. This is achieved by varying the V_{DC} through a feedback loop. This technique can also be explained in term of energy diagram as schematized on **Figure 2-5**. When tip and surface are at electrical equilibrium, a force is generated in between surface and tip, the air acting as a dielectric. By applying an external bias on the tip, the potential diagram can be shifted back to its original position before electrical equilibrium, cancelling the force on the cantilever. From the diagram in **Figure 2-5**, it is clear that the applied DC potential required to cancel the force on the cantilever can be define by the difference between the respective work function (Φ) of the the tip and surface as $V_{CPD} = \frac{1}{e}(\Phi_{Surface} - \Phi_{Tip})$. Hence, if the work function of the tip is known, this method can be used to quantitatively measure the work function of a surface on the nanometric scale. It should be noted however that quantitative measurements should only be performed under inert environment to limit oxidation or adsorption of chemicals as water on the surface which will affect the absolute work function. In addition, etching of the tip during height measurements can significantly affect its work function and thus the absolute result. Therefore, this method is more suited to extract relative informations. An extension of KPFM is the surface photovoltage measurement which is obtained from a difference between measurement in dark condition and under illumination as,

$$V_{ph} = V_{CPD}^{Light} - V_{CPD}^{Dark} \cong \frac{1}{e}(\Phi_{Surface}^{Light} - \Phi_{Surface}^{Dark}) \quad (2.4)$$

Which gives information on the photoinduced variation of the surface work function, assuming that the tip work function remains unaffected under light. This method gives useful insight over the photogenerated holes or electrons accumulation near the surface.⁸

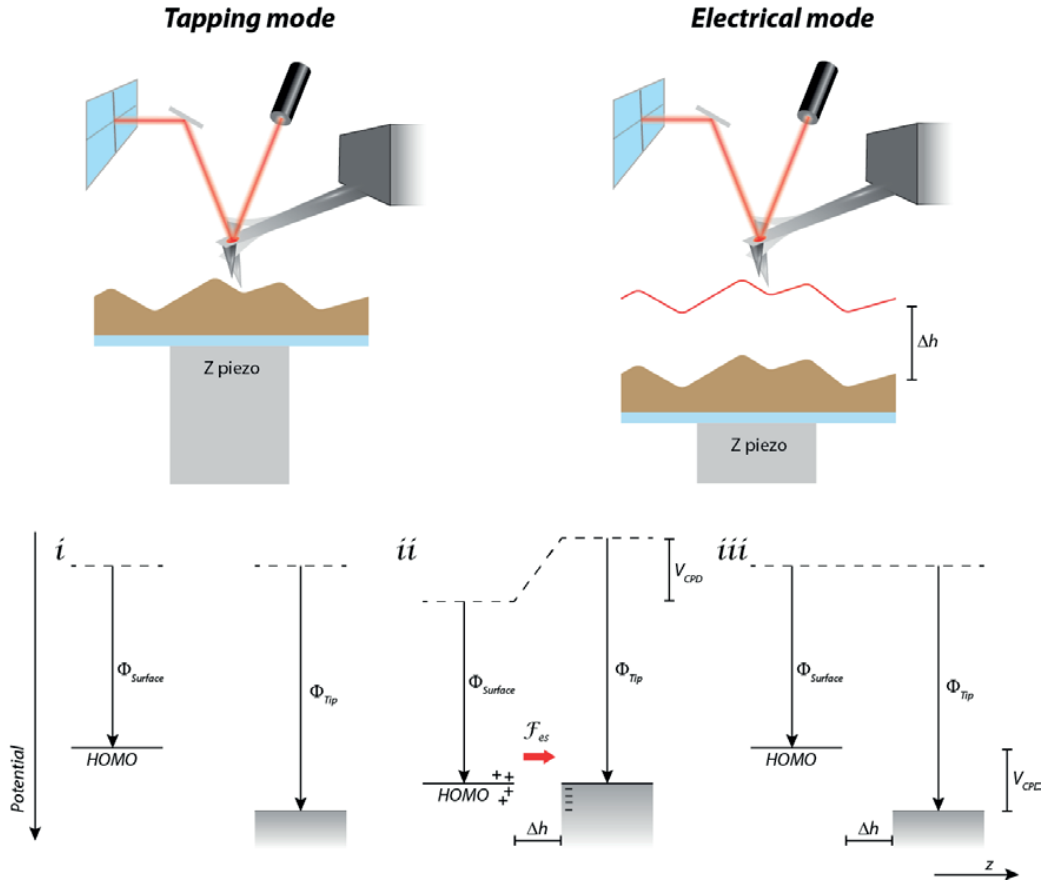


Figure 2-5. (Top) schematic depicting the 2 pass working principle of KPFM in tapping and electrical mode. (bottom) energy level schematic of the surface and tip (i) before electrical contact, (ii) after electrical contact but without any DC bias so that the presence of a dielectric layer between the tip and surface leads to a force bending the tip and (iii) in electrical contact after the force exerted on tip has been cancelled by a DC bias.

d) Experimental details

AFM characterization were carried out on an Asylum Research Cypher S using Atomic Force AC240TS cantilever in tapping mode, AC240TS and AC160TS for force curve measurement and AC240TM as conductive tips for KPFM measurements (all cantilever manufactured by Olympus). In all cases AFM is measured directly on the sample surface in air and at room temperature except in chapter 3 where samples were delaminated from an OTS-treated substrate using UV-cured adhesive (Nordland) prior to measuring AFM at the interface. Light source for KPFM measurements under illumination was provided by white LEDs situated above the sample and cantilever.

2.3.3 X-ray spectroscopy

Grazing incidence X-ray spectroscopy (GIXRD) data relates directly to the crystal structure of the sample. When an incident X-ray beam is scattered by particles in a sample, resulting waves will either have constructive or desctructive interactions. According to Bragg's law, coherent scattering will only be found when the following expression is verified.

$$2d_i \sin(\theta) = n\lambda \quad (2.5)$$

Where d_i is the interplanar distance, θ the scattering angle, n is a positive integer related to the order of reflection and λ the wavelength of the incident X-ray. The first term in this equation, $2d_i \sin(\theta)$, refers to the difference in optical path of photons scattered on neighbouring planes (see **Figure 2-6**). Hence, Bragg's law states that constructive interactions will only arise when the wavelength is an integer of this optical path difference. The experiment then consists of varying the angle of the incident X-ray beam and detecting any constructive signal that is diffracted of the surface. Data can then be presented as function of 2θ or q_z (q_{xy}) vector for out-of-plane (in-plane) diffraction. The use of q_z vector is preferred as it is independent of the light source wavelength and hence more prone to direct data comparison in the field, in contrast to 2θ . This q vector is defined in reciprocal space as the difference between incident and scattered light vectors and can be expressed as,

$$q = \frac{2\pi}{d_i} \quad (2.6)$$

Most GIXRD data presented in this work will be as function of q_z . Crystal correlation length (CCL) can then be obtained using Scherrer's equation:

$$CCL = \frac{2\pi}{FWHM} \quad (2.7)$$

Where FWHM is the full width at half maximum obtained by fitting the diffracted peak as function of q_z with a Pseudo-Voigt equation. Hence, sharpness of the diffracted peak can be associated to the crystallite perfection and/or size.⁹

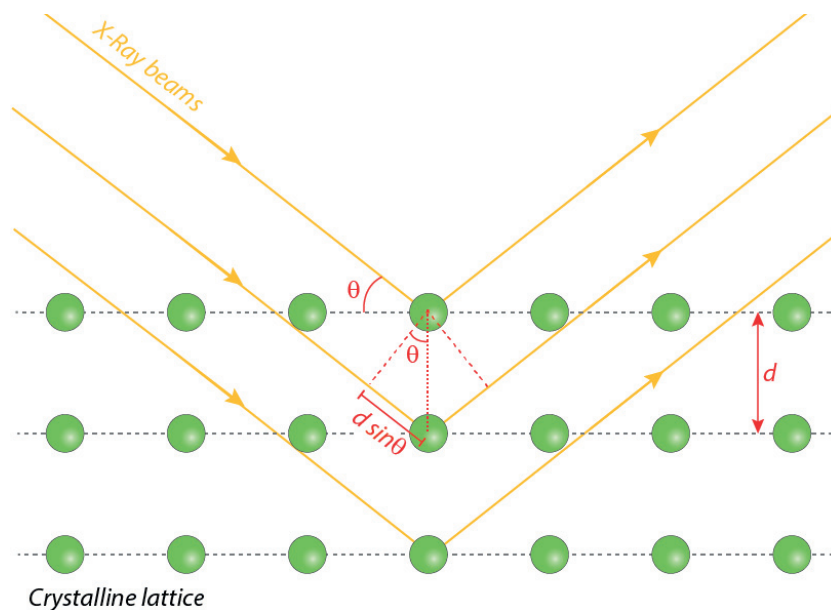


Figure 2-6. Schematic of X-ray scattering in a crystalline lattice with spacing d and incident angle θ . It is explicit from geometrical considerations that the difference in optical path is $2d \sin(\theta)$.

Grazing incidence X-ray diffraction was measured with a D8 Discovery (Bruker) diffractometer using Cu K α radiation source ($\lambda = 0.15418$ nm) and a Ni β -filter. During measurements incident beam angle was kept at a constant angle of 0.2° while detector was rotating with a scan rate of $0.05^\circ \text{ min}^{-1}$ and a step width of 0.01° .

2.4 Electrical characterization

2.4.1 Organic field effect transistor

As the working principle of OFET has already been covered in the previous chapter, this section will only discuss the experimental details for fabrication and characterization of OFET.

Bottom-gate, bottom-contact FETs were fabricated using pre-patterned test substrates (Fraunhofer Institute for Photonic Microsystems) whose source and drain contacts were composed of a 30 nm thick gold layer on top of a 10 nm thick titanium adhesion layer. A 230 nm thick silicon oxide layer was used as gate dielectric and n-doped silicon wafer as the substrate and gate electrode. The channel width was 1 cm and the length either 10 or 20 μm as specified in the work. The transistor substrates

were cleaned by sequentially rinsing with acetone, deionized water, and isopropyl alcohol. After drying under nitrogen, the substrates were subsequently exposed to a nitrogen plasma for 15 min. If specified, substrates were soaked in a 10 mM octadecyltrichlorosilane (OTS, Acros organics) solution in toluene for 15 min at 80 °C under argon prior to rinsing with toluene and drying. The active material was spin-coated from 10 mg mL⁻¹ precursor solution, generally resulting in *ca.* 50 nm thick films, as measured by profilometry. All solutions and films were prepared under argon atmosphere and the former were allowed to stir under heating overnight.

Electronic testing of the FETs was carried out in a nitrogen atmosphere at RT, if not specified otherwise, using a custom-built probe station and a Keithley 2612A dual-channel source measure unit. Temperature control of the probe station was performed using a multistage thermoelectric cooler (Thermonamic) for temperature below RT and a custom-made hotplate for temperatures above RT. The field-effect mobility was extracted from the saturation region as presented in section 1.2.1.

2.4.2 *Organic photovoltaic*

As already mentioned for OFET, working principle of OPV has been discussed in the previous chapter. Therefore, this section will only cover the experimental details for fabrication and characterization of OPV.

Solar cells were fabricated on a glass substrate patterned with 300 nm of ITO. A 40 nm layer of PEDOT:PSS (Ossilla M121 Al 4083) was first spin-coated at 3000 rpm for 1 min prior to annealing at 130 °C in air. The BHJ active layer was then spin-casted from the adequate precursor solution. An 80 nm thick aluminium cathode was deposited (area 16 mm²) by thermal evaporation (Kurt J. Lesker Mini-SPECTROS). Prior to testing, samples underwent post annealing treatment as specified in the work.

Electronic characterization was performed under simulated AM1.5G irradiation from a 300 W Xe arc lamp set to 100 mW cm⁻² with a calibrated Si photodiode (ThorLabs). Current–voltage curves were obtained with a Keithley 2401 source measure unit. Device fabrication was performed under an argon atmosphere and testing was performed under nitrogen atmosphere.

2.4.3 *Space charge limited current*

Space charge limited current (SCLC) measurements is a powerful technique to extract charge carrier mobility of a material. It requires fabrication of specific device architecture similar to OPV but with relatively thick active layer (>200 nm) and selective contacts for either hole-only (*e.g.* PEDOT:PSS

or MoO_x / Au or Ag) or electron-only (e.g. ZnO or TiO_x / Al) diodes. The mobility can then be extracted using the Mott-Gurney law in the space charge limited regime,¹⁰

$$J = \frac{9\epsilon\epsilon_0\mu V^2}{8L^3} \quad (2.8)$$

Where J is the current density, ϵ the dielectric constant of the material, ϵ_0 is the vacuum permittivity, μ the charge carrier mobility, L the thickness of the device and V the applied bias.

Hole only diodes were fabricated on a glass substrate patterned with 300 nm of ITO. A 40 nm layer of PEDOT:PSS (Ossilla M121 Al 4083) was first spin-coated at 3000 rpm for 1 min prior to annealing at 130 °C in air. The active layer was then spin-casted under argon atmosphere at 3000 rpm from a chloroform solution at 30 mg mL⁻¹ (stirred overnight at 40 °C). A 4 nm thick MoO₃ interlayer was deposited prior to 80 nm thick silver top electrode by thermal evaporation (Kurt J. Lesker Mini-SPECTROS). Testing was performed under nitrogen atmosphere with a Keithley 2401 Sourcemeter.

2.4.4 Quantum efficiency

External quantum efficiency (EQE), also known as incident photon to electron conversion efficiency (IPCE), is a wavelength dependent measurements defined as the ratio between the density of incident photons (N_{ph}) and the density of collected charge carriers at the electrodes (N_{cc}). It is widely used to understand the spectral contribution of the blend to the observed current. The probability of photons to electrons conversion depends on the efficiency of 3 main physical processes in the active blend as,

$$EQE(\lambda) = \frac{N_{cc}(\lambda)}{N_{ph}(\lambda)} = \eta_{LH}(\lambda) \eta_{ES}(\lambda) \eta_{col} \quad (2.9)$$

Where η_{LH} is the light harvesting efficiency, η_{ES} is the exciton splitting efficiency and η_{col} is the free charge carrier collection efficiency. The latter should normally not be dependent on the wavelength of the original photon. The measurement setup requires a tuneable monochromatic light source to illuminate the device while measuring the current output. In order to calculate N_{ph} , the power density of the incident light (P_{in}) must be measured through a calibrated diode. N_{ph} can then be expressed per unit of time as,

$$N_{ph}(\lambda) = P_{in}(\lambda) \frac{\lambda}{hc} \quad (2.10)$$

With h as Planck constant, c as light speed and $\frac{hc}{\lambda}$ the energy contained in one photon according to Planck's relation. Finally, from the current density output J , N_{cc} can be expressed per unit of time as,

$$N_{cc}(\lambda) = -\frac{J(\lambda)}{e} \quad (2.11)$$

EQE is then obtained by substituting expressions for N_{ph} and N_{cc} inside equation (2.9). The internal quantum efficiency (IQE), also known as absorbed photon to electron conversion efficiency (APCE), consist in accounting for η_{LH} and can be expressed as,

$$IQE(\lambda) = \frac{EQE(\lambda)}{\eta_{LH}(\lambda)} = \eta_{ES}(\lambda) \eta_{Col} \quad (2.12)$$

Indeed, η_{LH} can be measured by UV-vis spectroscopy as the total absorption of the sample at each wavelength. EQE can then be corrected to reflect only losses associated with excitons or free charge carriers recombination. IPCE was performed using a 75 W Xe arc lamp light source and a monochromator (from optical building block). A calibrated photodiode was used to measure the incident number of photons at each wavelength.

2.4.5 Impedance spectroscopy

Impedance spectroscopy (IS) is an advanced electrical characterization technique which involves measuring a current response to a small sinusoidal voltage perturbation with varying the frequency. Potential (E_t) can be expressed as,

$$E_t = E_{DC} + E_{AC} e^{i\omega t} \quad (2.13)$$

With E_{DC} the constant bias, E_{AC} the amplitude of the excitation bias, ω the frequency and t the time. As long as the amplitude of the perturbation is small enough, the system should react linearly. Hence, the current oscillation will exhibit the same frequency with a phase shift φ ,

$$I_t = I_{DC} + I_{AC} e^{i(\omega t - \varphi)} \quad (2.14)$$

With I_{DC} and I_{AC} the current response to the constant bias and the excitation bias respectively. The impedance of the sinusoidal component of the system can be expressed as,

$$Z = \frac{E_{AC} e^{i\omega t}}{I_{AC} e^{i(\omega t - \varphi)}} = Z_0 e^{i\varphi} \quad (2.15)$$

Finally, using Euler relationship, equation (2.13) can be rewritten as a real and imaginary part, Z' and Z'' respectively, both depending on the phase shift.

$$Z = Z_0 [\cos(\varphi) + i \sin(\varphi)] \quad \begin{cases} Z' = Z_0 \cos(\varphi) \\ Z'' = Z_0 \sin(\varphi) \end{cases} \quad (2.16)$$

Data is then presented as a Nyquist plot with $Z'' = f(Z')$ or as a Bode plot (Z and φ vs. $\log(\omega)$). In order to relate such data to physically relevant parameters, models based on equivalent circuit are used to fit IS data. Typical model used in this work is shown in **Figure 2-7**.

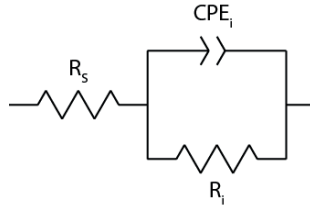


Figure 2-7. Equivalent circuit used to fit IS response in the following chapters.

With R_s the series resistance, R_i and CPE_i the resistance and the constant phase element associated with the process i respectively. This equivalent circuit is well suited to model Nyquist plots exhibiting a single semicircle with an eventual slightly flattened shape. The equivalent capacitance of the constant phase element (C) can be calculated as function of its time and phase constant (respectively Q and n) using the following expression:

$$C = \frac{(Q R)^{1/n}}{R} \quad (2.17)$$

With R is the parallel resistance and $0 < n \leq 1$. It ensues from this expression that if $n = 1$ the constant phase element behaves as an ideal capacitor. It is important that equation (2.17) is only valid for a CPE in parallel to a charge transfer resistance. Finally, the lifetime of the process can be calculated as,

$$\tau_i = R_i C_i \quad (2.18)$$

Impedance spectroscopy was carried out under inert atmosphere using a SP-300 potentiostat at frequencies ranging from 1 MHz up to 1 Hz. Fitting of the data was performed using Zview software.

2.5 References

- (1) Barth, H. G.; Jackson, C.; Boyes, B. E. *Anal. Chem.* **1994**, *66* (12), 595R.
- (2) Müller, C. *Chem. Mater.* **2015**, *27* (8), 2740.
- (3) Gasperini, A.; Johnson, M.; Jeanbourquin, X.; Yao, L.; Rahmanudin, A.; Guijarro, N.; Sivula, K. *Polym. Chem.* **2017**, *8* (5), 824.
- (4) Roa, J. J.; Oncins, G.; Diaz, J.; Sanz, F.; Segarra, M. *Recent Pat. Nanotechnol.* **2011**, *5* (1), 27.
- (5) Wang, D.; Russell, T. P.; Nishi, T.; Nakajima, K. *ACS Macro Lett.* **2013**, *2* (8), 757.
- (6) Gasperini, A.; Jeanbourquin, X. A.; Rahmanudin, A.; Yu, X.; Sivula, K. *Adv. Mater.* **2015**, *27* (37), 5541.
- (7) Melitz, W.; Shen, J.; Kummel, A. C.; Lee, S. *Surf. Sci. Rep.* **2011**, *66* (1), 1.
- (8) Spadafora, E. J.; Demadrille, R.; Ratier, B.; Grévin, B. *Nano Lett.* **2010**, *10* (9), 3337.
- (9) Proctor, C. M.; Kher, A. S.; Love, J. A.; Huang, Y.; Sharenko, A.; Bazan, G. C.; Nguyen, T.-Q. *Adv. Energy Mater.* **2016**, 1502285.
- (10) Kokil, A.; Yang, K.; Kumar, J. J. *Polym. Sci. Part B Polym. Phys.* **2012**, *50* (15), 1130.



Chapter 3 Observation of bell-shaped temperature dependence of hole mobility in hopping regime

Interpretation of the charge carrier mobility temperature dependence in organic semiconductors which deviates from the expected thermally-activated mechanism is subject to strong controversy in the field. Indeed, many examples of organic materials exhibiting apparent band-like behaviour have been reported to date, despite the intrinsic small charge carrier delocalization compared to the molecule size.

In this work, a bell-shaped temperature dependence of the hole mobility extracted from field effect transistor devices based on a DPP(TBFu)₂ small molecule is reported. The low mobility inherent to DPP(TBFu)₂ solution-processed thin films exclude the possibility of significant delocalization and band-like transport as a potential explanation, making it a unique system to understand deviation from standard thermally activated regime. The bell-shape temperature dependent mobility, as observed, is found to be strongly affected by annealing steps and crystallization of the DPP(TBFu)₂ as found by GIXRD. AFM images and Young modulus measurements reveals the presence of a poorly crystalline phase in the transport channel with appearance of crystalline platelets upon annealing.

Based on temperature dependent UV-vis measurements indicating a loss in intermolecular electronic coupling with increasing temperature, and the presence of isosbestic points, we hypothesize that the loss in mobility with temperature arises from the presence of a poorly aggregated meso-phase with high rotational and/or translational degree of freedom and poor transfer integral which is in equilibrium with the poorly crystalline phase. This equilibrium is then expressed as an isodesmic self-assembly which in turn leads to a model that effectively describes the observed mobility data. Thereof, we propose a new explanation for the negative mobility dependence on temperature in the frame of thermally-activated mechanism. More importantly, our result shows that mobility dependence over

temperature exhibiting a negative slope should not be accepted as a signature for band-like transport in organic devices

3.1 Introduction

The exact transport mechanism occurring in OFETs – especially in the state-of-the-art devices that deviate in behaviour from a thermally-activated transport mechanism – remains controversial. A clear understanding of the transport mechanism is however crucial for rationally improving mobility in organic semiconductors.¹ Therefore, unravelling the underlying physical processes that can lead to deviation from the expected hopping behaviour is an important and urgent goal of the field.

Large structural disorder in combination with the weak Van der Waals intermolecular interaction in organic semiconductors generally leads to localization of charge carriers on a single molecule at discrete energy levels. Diffusion then occurs via hopping between sites. In a hopping mechanism, the charge carrier mobility can either be expressed in term of Miller-Abrahams² or Marcus³ equations, as explained in chapter 1. A common aspect in both of these thermally-activated models is their positive charge carrier mobility dependence on temperature. In contrast, crystalline inorganic semiconductors normally exhibit carrier transport in continuous energy bands with charge carriers delocalized over distances several times the unit cell size. In such case, mobility is related to temperature through a power law such as $\mu \propto T^{-\alpha}$, with α depending on the scattering mechanism.⁴ Accordingly, this band-type transport mechanism results in a negative charge carrier mobility dependence on temperature – the opposite of a typical organic semiconductor.

Interestingly, a handful of reports focusing on transport in organic semiconductors have observed negative slopes in Arrhenius plots, which are commonly interpreted as a signature of delocalization of charge carriers and band-like transport mechanism within the film. Here, band-like refers to delocalization occurring over a small number of sites only, as opposed to band transport. In 2004, Podzorov et al. and, later, several other groups, reported such behaviour for crystalline small molecules.^{5–9} In the last decade, a handful of reports have claimed to identify a transition temperature from hopping to band-like transport further supporting their findings by measuring the mobility via the Hall effect.^{10–13} Based on these initial works, several more recent works reported band-like transport in OFET solely based on the mobility dependence with temperature.^{14–18} However, mobilities measured in these works (in the range of 1–10 cm² V⁻¹ s⁻¹ at RT) are close to the Mott-Ioffe-Regel limit stating

that the minimum mobility for considering a valid band transport mechanism is *ca.* $1 \text{ cm}^2 \text{ V}^{-1} \text{ s}^{-1}$ assuming a reasonable lattice spacing of 2.5 \AA .^{19,20} This limit leads to a strong controversy within the field as to whether a band-type transport mechanism actually occurs in organic semiconductors. Hence researchers have been looking for alternative explanations. Notably, in 2010, Sakanoue et al. reported a band-like temperature dependence which they attributed to thermal lattice fluctuation rather than fully delocalized charge carriers.²¹ This theory considers the diffusion of charge carriers to be limited by transient localization events arising from the large intermolecular lattice vibrations, in turn leading to dynamic fluctuations in the transfer integral.²² In contrast, non-linear charge transport behaviour with bias or temperature, suspected to be fingerprints of Luttinger liquid behavior²³ (1D metallic transport), have recently been accounted for simply using a VRH model with field-assisted hopping.²⁴ Moreover, it appears that negative charge carrier mobility dependence on temperature could exceptionally arise from a hopping mechanism. As a matter of fact, such inversions in temperature dependence have been previously reported while studying intramolecular charge transfer of dyads in solution. This unexpected behaviour was found to arise from additional temperature-dependence of the reorganizational energy,²⁵ transfer integral²⁶ or even from complex kinetics²⁷ resulting in bell-shaped Arrhenius plots.

Overall, it seems that – even though some organic semiconductors seem to indeed exhibit band-like transport – in some cases mobility *vs.* temperature data might be misinterpreted and could also well be explained in term of hopping mechanism. In this respect, our work aims at undermining the routine interpretation of negative dependence for charge carrier mobility as function of temperature as a signature of band transport mechanism.

Herein we investigate the transport mechanism relevant to DPP(TBFu)₂, a fruit fly material among small molecule semiconductors. We report a bell-shaped Arrhenius plot for the hole mobility for DPP(TBFu)₂ small molecule based OFET. Hole mobilities being well below the Mott-Ioffe-Regel limit, a band transport mechanism cannot be considered as a viable explanation. Strong field dependence and presence of trap states are investigated as potential causes for deviation from thermally activated regime. However, the inverted region is found to originate from a breakdown in transfer integrals in poorly crystalline regions with increasing temperature, ultimately leading to a loss in mobility. We show that this phenomenon can be modelled considering temperature dependent equilibrium between two populations with distinct electronic coupling.

3.2 Results

3.2.1 Temperature dependent FET measurements

The effect of temperature on charge transport properties of DPP(TBFu)₂ was investigated for devices as-cast from chlorobenzene and subsequently thermally annealed at 90 °C, 130 °C and 170 °C. For all conditions, output curves exhibit clear linear and saturated behaviour with weak non linearity at the onset, consistent with a small contact resistance (see appendix, Figure A-1 to A-4).¹⁸ Saturated hole mobilities, extracted from the corresponding transfer curves (see appendix, Figure A-5) are found to be in good agreement with hole mobilities extracted from linear regime (see appendix, Figure A-6). Varying the FET channel direction or length did not impact in any significant way over the OFET results.

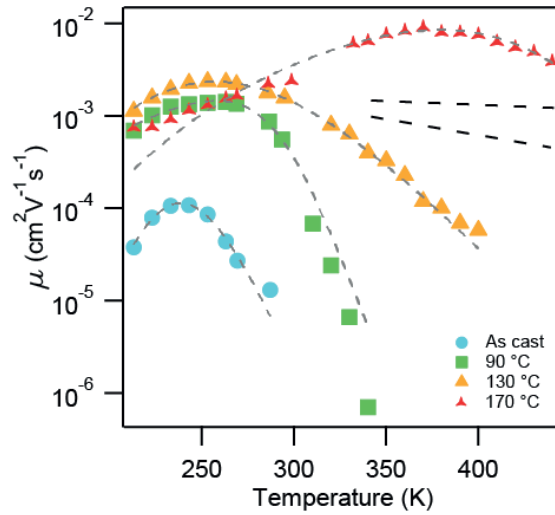


Figure 3-1. Temperature dependence of the field effect mobility extracted from saturated regime in DPP(TBFu)₂ OFET (channel length of 20 μm) as-cast and annealed at 90 °C, 130 °C and 170 °C for 1 hour and corresponding fit using equation (3.11) developed in this work. Black dashed lines indicate typical power law decay with exponent -0.5 (top) and -2 (bottom), typical range for transport governed by band or transient localization theory.

Figure 3-1 shows the hole mobility of DPP(TBFu)₂ spin-casted thin films extracted from the OFET saturation regime (plain symbols) and hole-only diodes in space charge limited current devices (open circles) as a function of temperature. At temperatures lower than 243 K, the FET mobility for as-cast DPP(TBFu)₂ (solid circles, **Figure 3-1**) increases with temperature as expected from thermally activated transport mechanism. In stark contrast, the mobility is found to deteriorate with temperature above 243 K, resulting in a bell-shaped temperature dependence. After annealing the device at 90 °C

for 1h (solid squares, **Figure 3-1**) FET mobility is found to increase by 1 order of magnitude. However, the bell-shape dependence is still present, with an inversion at *ca.* 253 K. Notably, above 340 K the current drops down below setup sensitivity, suggesting almost non-existent hole mobilities. Similar behaviour is found after further annealing the device at 130 °C (solid triangle, **Figure 3-1**) with a slight increase in the temperature at which maximum hole mobility is found to *ca.* 263 K. Finally, device annealed at 170 °C (solid star, **Figure 3-1**) exhibits a linear trend close to RT, even though a negative slope is still present at much higher temperature (*ca.* 370 K). This bell-shape behaviour in FET is found to be in good correlation with the I_{ON}/I_{OFF} ratio, further supporting that the loss in mobility at high temperature is real and does not arise from an artefact in the output curve (see appendix, Figure A-7). Indeed, optimum values for the I_{ON}/I_{OFF} ratio are found at temperatures similar to where optimum hole mobilities are measured, consistent with the higher I_{ON} . In addition, it is consistent with the trend observed in the threshold voltage (see appendix, Figure A-7), where the threshold voltage decreases with increasing temperature – as expected from the smaller amount of trapped charges at high temperature. Notable exception are found in the case of as-cast FET and annealed at 90 °C, where the threshold voltage is found to increase back up again close to RT, suggesting the formation of new hole-trapping states with increasing temperature.

In order to study the interface, SiO₂ substrates were functionalized with a monolayer of octadecyltrichlorosilane (OTS). Hole mobilities measured from OTS functionalized DPP(TBFu)₂ FET (see appendix, Figure A-8) are found to be in the same order of magnitude than non-functionalized FET. Moreover, the bell-shape dependence is still present, indicating that the SiO₂ surface it-self is not responsible for the inversion.

As the DPP(TBFu)₂ is well-known to irreversibly self-assemble into crystalline domains upon thermal annealing, we investigated the reversibility of the temperature dependent measurement. Mobility in as-cast DPP(TBFu)₂ was measured while cooling down from RT and heating back up again to RT (see appendix, Figure A-9a). A slight hysteresis can be found at low temperature, probably caused by the strong temperature gradient. Nonetheless, the bell-shape mobility dependence is present either when cooling or heating the FET. The good agreement between mobilities measured at RT before and after the cycle demonstrate that no irreversible modification of the film occurs during the experiment. A similar experiment was performed on DPP(TBFu)₂ annealed at 90 °C for temperature ranges above RT (see appendix, Figure A-9b). The hole mobility at RT is found to improve by 3-fold after the heating-cooling cycle, certainly caused by a thermal annealing effect inherent to the measurement

inducing irreversible crystallisation. While this annealing effect is not negligible, it remains much smaller than the actual drop in hole mobility observed upon increasing temperature.

Field dependence of the hole mobility was investigated as a possible cause for the inversion behaviour observed in **Figure 3-1**, given that the Poole-Frenkel (PF) relationship ($\mu \propto \exp(\sqrt{E}/T^{1.5})$), predicts a negative slope with temperature (assuming the PF term dominates the mobility). Hole mobilities measured at different temperatures for as-cast and annealed samples are shown in **Figure 3-2** according to the PF relation. The field was assumed to be directly proportional to the applied source-drain voltage V_{DS} as $E = V_{DS}/L$ with L the channel length. For all samples, the logarithmic mobility as function of square root of field are seen to be fairly linear, in agreement with a PF behaviour. For as-cast FETs and the FET annealed at 90 °C, the mobility exhibits negligible dependence on the electric field at high temperature only (e.g. 300 K and 286 K), corresponding to the deep inverted region in **Figure 3-1**. Notably, the increasing field dependence at lower temperature suggests that, at very low field, the hole mobility might be increasing with temperature even for samples not annealed at 170 °C as expected for a thermally activated mechanism. This eventuality will be further discussed below in section 3.3.2.

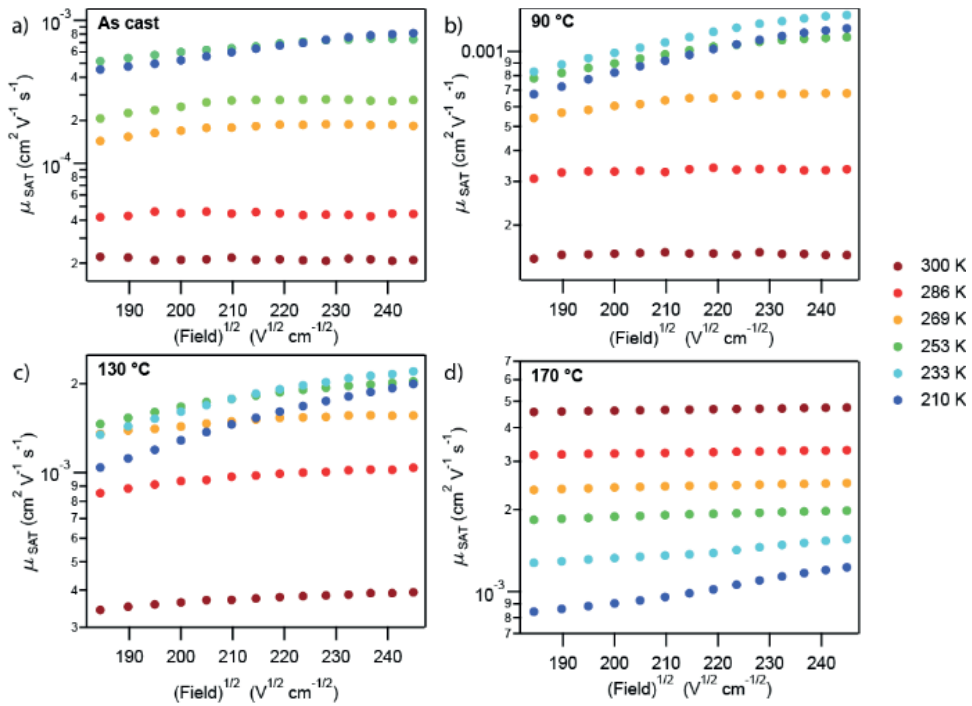


Figure 3-2. Field dependence of the mobility extracted from saturated regime in FET (channel length of 10 μm) measured at different temperature for (a) as-cast devices and annealed at (b) 90 °C, (c) 130 °C and (d) 170 °C.

3.2.2 Effect of annealing on the supramolecular assembly

All the temperature dependent mobility data presented above exhibit a critical effect of the thermal annealing step temperature. In this section we scrutinise the effect of thermal annealing over the supramolecular assembly, crystallinity and energetics of DPP(TBFu)₂ in thin film. First, the curing effect of the annealing step was investigated by GIXRD as presented on **Figure 3-3a**. In all cases, a strong out-of-plane diffraction peak at 2Θ of 6° can be seen which corresponds to the (020) reflection induced by layers of π - π stacked DPP(TBFu)₂ separated by alkyl chains.²⁸ Despite the similar thicknesses of the all the samples (*ca.* 50 nm) the scattering intensity is found to significantly increase upon annealing. Furthermore, the FWHM, which is inversely proportional to crystallite size and perfection through Scherrer's equation,²⁹ clearly decreases with annealing temperature. Overall, these two results demonstrate that the main effect of the annealing step is an improved crystallinity. It is important to note that this crystallization process is essentially irreversible upon cooling and does not correlate with the reversible change in mobility. However, it suggests that poorly crystalline domains gradually disappear with annealing. These amorphous domains could be critical to understand the hole mobility behaviour with temperature.

Generally, such poorly crystalline domains are characterized by rough energetic landscape. Hence we examine the presence of trap states within the film by cyclic voltammetry (CV). **Figure 3-3b** shows the CV results of the first oxidation scan for as-cast and annealed films (30 nm thick) on FTO substrates. The measured current density can be related to the density of state (DOS) as $J = dse^2g(E_F)$, assuming negligible porosity, where d is the thickness of the layer, s the scan speed and $g(E_F)$ the DOS at given energy level.³⁰ A main oxidation peak can be seen at -5.4 eV with an onset at *ca.* -5.2 eV which can be attributed to the HOMO energy level of DPP(TBFu)₂. This is in good agreement with HOMO level reported in previous work.³¹ Interestingly, the DOS above the HOMO level decreases significantly with annealing, revealing potential hole trapping states which seems to be partially cured by annealing. The presence of these states was further confirmed by impedance spectroscopy performed on hole-only diode in dark conditions and presented in **Figure 3-3c**. The chemical capacitance C_μ was extracted from the impedance response by fitting with a single semi-circle (see appendix, Figure A-10). The DOS can then be obtained using the trivial relation $C_\mu = e^2g(E_F)$.³⁰ At low applied voltage (*ca.* 0.5 V), a small DOS peak appears for samples as-cast and annealed at 90 °C. These peaks disappear on samples annealed at 130 °C and 170 °C. The exponential increase observed at higher voltage for all samples is attributed to the HOMO level. Overall, this result seems to confirm the presence of hole trapping states above the HOMO level which are suppressed with annealing. It

is worth noting that, lacking a reference electrode in this solid-state configuration, the energy axis is given relative to the fermi level of the counter electrode. Thus, unnatural broadness of the peak originates from the floating counter electrode fermi level upon applied voltage.

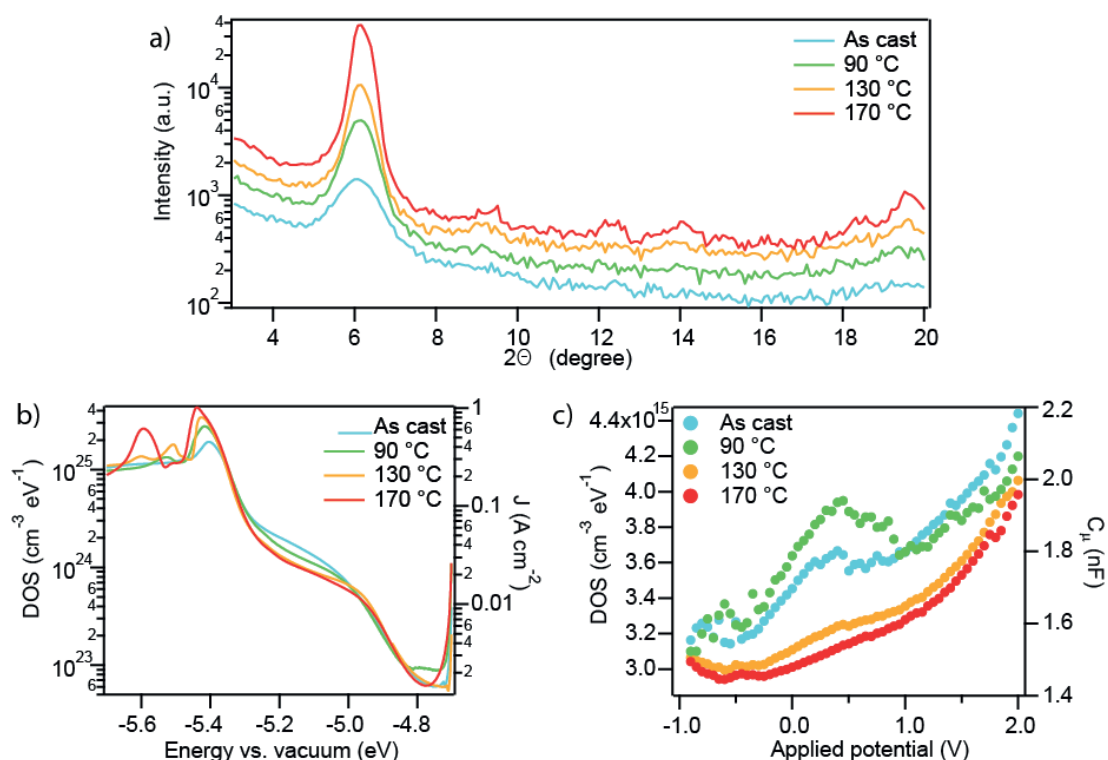


Figure 3-3. (a) Out-of-plane grazing incidence wide angle X-ray scattering of as-cast DPP(TBFu)₂ and annealed at 90 °C, 130 °C and 170 °C. (b) density of state calculated using cyclic voltammetry data and (c) using chemical capacitance extracted from impedance spectroscopy for as-cast devices annealed at 90 °C, 130 °C and 170 °C.

The change in crystallinity was further investigated by imaging the active layer interface in contact with SiO₂ where the transport occurs. This was achieved by delaminating the DPP(TBFu)₂ layer from the OTS functionalized SiO₂ substrate and imaging the morphology at RT in air by atomic force microscopy tapping mode. Data, presented in **Figure 3-4**, shows the evolution of the morphology with annealing. The as-cast sample exhibits uncorrelated features, typical of an amorphous or poorly crystalline interfacial layer (here the term interfacial layer refers to the DPP(TBFu)₂ at the SiO₂ interface only, in contrast with the bulk of the film which can exhibit stark differences in morphology). Upon annealing at 90 °C, 130 °C and 170 °C, platelet features progressively appear, consistent with an increasing crystallinity of the interfacial layer. Furthermore, the YM distribution corresponding to these images was extracted by fitting the force curve with a DMT model accounting

for adhesion (see chapter 2).³² It can be seen that the mean YM increases from *ca.* 80 MPa to *ca.* 120 MPa for samples as-cast and annealed at 170 °C respectively, consistent with a tighter packing induced by crystallization. It is worth noting that the as-cast layer exhibits a sharp YM distribution, in contrast to annealed films which exhibit broader distributions. The significant YM distribution overlap in between samples as-cast and annealed at 90 °C or even 130 °C indicates a heterogeneous composition of this surface layer after mild annealing, which likely consists of different degree of crystalline and amorphous regions. Finally we note that only the YM distribution of the sample annealed at 170 °C does not overlap the as-cast one, indicating that poorly crystalline domains are smaller than tip resolution (< 9 nm).

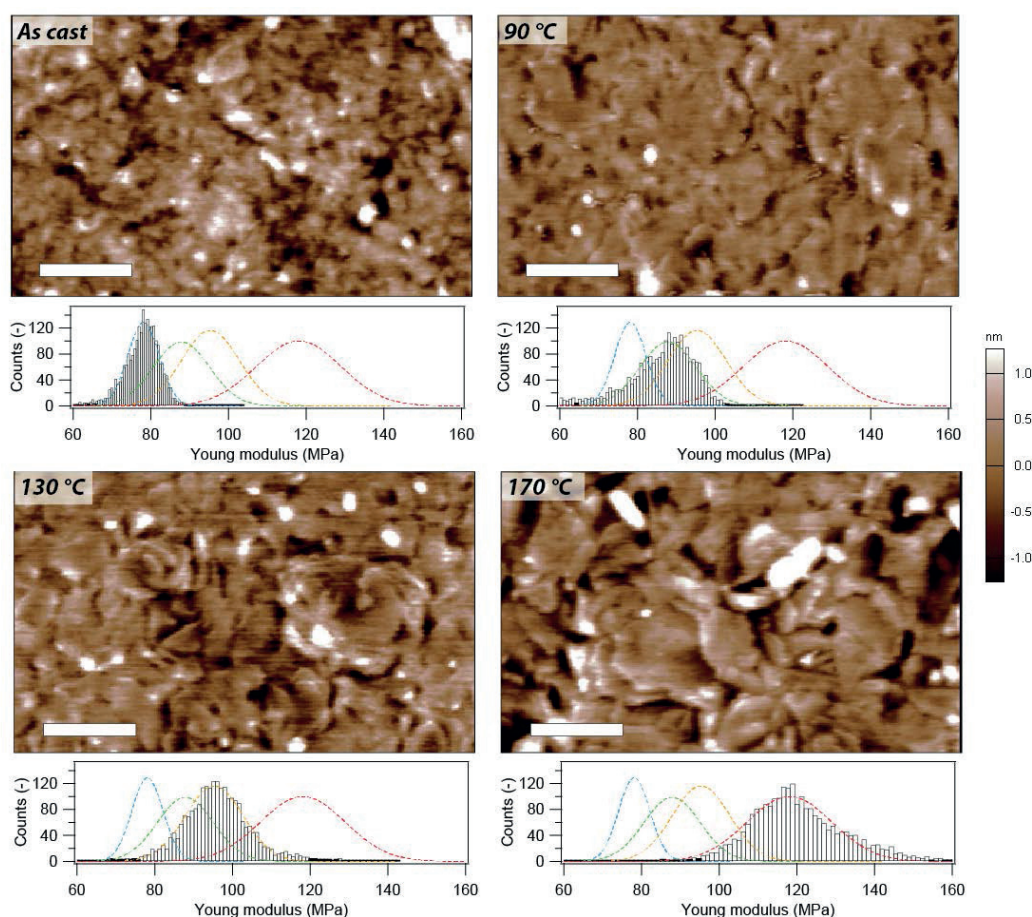


Figure 3-4. Atomic force microscopy height images (scale bar 100 nm) and corresponding distribution of the Young modulus of the $\text{SiO}_2/\text{DPP}(\text{TBFu})_2$ interface measured on $\text{DPP}(\text{TBFu})_2$ delaminated films as-cast and previously annealed at 90 °C, 130 °C and 170 °C. Dashed lines in the histogram correspond to Gaussian fit of the Young modulus distribution for as-cast (blue) annealed at 90 °C (green), 130 °C (orange) and 170 °C (red).

3.2.3 Insight into the degree of aggregation by temperature dependent UV-vis

Finally, the change in aggregation was studied by UV-vis spectroscopy as function of temperature. As it can be seen on **Figure 3-5a**, in the solid-state at RT, DPP(TBFu)₂ exhibits 3 main spectroscopic transitions at *ca.* 557, 599 and 670 nm. The latter is well-known to be related to disorder within the film, as it strongly decreases upon annealing.³¹ However, in earlier work, we reported that this transition does not simply scale with a relative loss in melting enthalpy of DPP(TBFu)₂ but rather originates from a specific type of slip-stack π - π stacking similar to J-aggregation.³³ We note that, while annealed samples all exhibit similar spectral shape, the absorption intensity increases with annealing temperature. Given that films all have similar thicknesses (*ca.* 50 nm) this suggests a stronger extinction coefficient.

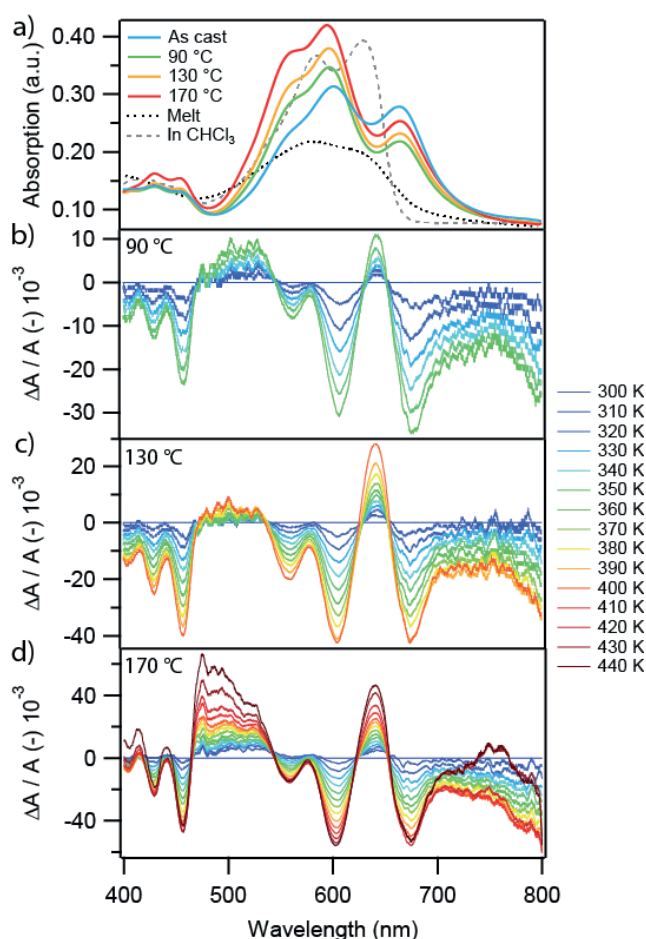


Figure 3-5. (a) UV-vis spectrum of DPP(TBFu)₂ in solution (CHCl₃) and thin films as-cast and annealed at 90 °C, 130 °C and 170 °C and measured at RT as well as molten (~300 °C). (b - d) Relative differential absorption (spectrum at 300 K as baseline) at different temperature for thin films as-cast and annealed at 90 °C, 130 °C and 170 °C.

In order to follow the evolution of the spectra with varying temperature, relative differential absorption with respect to spectrum at RT for samples annealed at 90 °C, 130 °C and 170 °C is presented in **Figure 3-5c-d**. Data were measured while cooling down the sample as to reduce potential contribution from the annealing effect inherent to the measurement on the results, though we note that observations were found to be reversible upon reheating. For all annealed samples, the three peaks exhibit a loss in intensity with increasing temperature, consistent with decreased extinction coefficient. The intensity loss is similar for the three peaks, with exception for the sample annealed at 90 °C where low energy peaks exhibit greater loss in intensity on similar temperature range. It is worth noting that peak positions obtained by deconvolution of the spectrum using a linear combination of three Lorentzians peaks (see appendix, Figure A-11 and Figure A-12) all undergo a linear hypsochromic shift upon increasing temperature ranging from 0.1 to 0.2 nm per decade. Moreover, looking at the 670 nm peak, a stronger shift is found for samples annealed at 90 °C than 130 and 170 °C with respective slopes of 0.2, 0.14 and 0.11 nm per decade.

Finally, an obvious key feature in the relative differential absorption data is the presence of 4 isosbestic points. Isosbestic points are commonly attributed to an equilibrium between two species with distinct absorption spectra.^{34,35} **Figure 3-5a** also present the absorption spectrum of non-aggregated DPP(TBFu)₂, either dissolved in CHCl₃ or molten at 300 °C (importantly, these two spectra are only qualitative as there is no correlation with the aforementioned thin films thicknesses). Nonetheless, both spectra are characterized by a significant bathochromic shift as compared to the solid-state. This leads to a transition peak around 630 nm for monomers which is in very good agreement with the spectral region that exhibit an increase in extinction coefficient with temperature in **Figure 3-5c-d**. Overall, it supports the idea that a reversible equilibrium is present within the film between two phases that could be associated with aggregated and non-aggregated molecules. It is worth recalling that the formation of the crystalline phase with increasing temperature is not reversible and hence should not be associated with the aforementioned phases in equilibrium.

3.3 Discussion

3.3.1 Beyond band theory

While the bell-shaped dependence presented in **Figure 3-1** is often explained as a transition from hopping to band-like transport (*e.g.* as reported by Yamashita and co-workers),¹¹ the low hole mobilities characteristic of DPP(TBFu)₂ ($< 10^{-2} \text{ cm}^2 \text{ V}^{-1} \text{ s}^{-1}$, well below the Mott-Ioffe-Regel limit), suggest

that charges are localized on single molecules rather than delocalized. DPP(TBFu)₂ being a small molecule, potential contribution from charges delocalized along the backbone on significant distances can be excluded. In addition, the sharp breakdown in hole mobility observed for FET annealed at 90 °C does not match a power law typically expected for band transport or even transient localization theories. Altogether, these elements refute band transport mechanism as a plausible explanation for the observed negative dependence of hole mobility on temperature. Rather, charge carriers in DPP(TBFu)₂ are expected to be localized on a single molecule and follow a hopping mechanism. Given the relatively high temperature range (close to RT) studied in this work as well as the crystalline nature of DPP(TBFu)₂, we actually expect the hopping mechanism to be better described by Marcus equation rather than the GDM model. Using Einstein relation, the charge carrier mobility can be expressed from the Marcus equation as,³⁶

$$\mu = \frac{ea^2}{k_B T} \frac{2\pi}{\hbar} J^2 \sqrt{\frac{1}{4\pi\lambda_0 k_B T}} \exp\left(-\frac{E_a}{k_B T}\right) \quad (3.1)$$

Where μ is the charge carrier mobility, a the hopping distance, J the overlap integral and λ_0 the reorganization energy for an average hop (see section 1.1.1). Then, a main issue remains: how can theory for thermally activated transport mechanism account for the bell-shape temperature dependence of hole mobility observed in this work?

3.3.2 Exploring field dependence of the mobility

A transport pathway with both crystalline and amorphous domains including the presence of trapping sites must exhibit rough energetic landscape (*e.g.* potential trap states) which can lead to a strong field dependence of the mobility. Indeed, previous work from Li et al. suggested that field dependence of the mobility in the context of VRH model could account for non-linear transport.²⁴ Indeed, the temperature dependence of the mobility observed in this work can be fit fairly well using a general expression of the form proposed by Parris et al.,³⁷

$$\mu = \mu_0 \exp\left(-\frac{E_a}{k_B T} - A_1 \left(\frac{\sigma}{k_B T}\right)^2 + A_2 \left[\left(\frac{\sigma}{k_B T}\right)^{\frac{3}{2}} - A_3 \right] \sqrt{\frac{eaE}{\sigma}}\right) \quad (3.2)$$

With μ_0 an exponential prefactor, σ the Gaussian distribution width for the energy, E the electric field and A_i are fitting parameters. As the first and second term represent polaronic behaviour and GDM respectively, the third term describes the empirically defined field dependence of mobility following a PF relationship, as mentioned above. From equation (3.2), it is trivial that if mobility gets dominated

by the PF term, a negative dependence of the mobility on the temperature would arise. We exclude this possibility given that the experimentally determined mobility field-dependence is not strong enough to fully account for the inversion. Indeed, the fitting parameter for the field dependence can be extracted out of the field dependent mobility data presented in **Figure 3-2**. As mobility follows a PF relationship then data in **Figure 3-2** result as a straight line with slope,

$$\frac{\partial \ln(\mu)}{\partial \sqrt{E}} = A_2 \left[\left(\frac{\sigma}{k_B T} \right)^{\frac{3}{2}} - A_3 \right] \sqrt{\frac{ea}{\sigma}} \quad (3.3)$$

From the temperature dependence of this slope, one can trivially obtain the fitting prefactor of the PF temperature dependent term corresponding to $A_2 \sqrt{\frac{ea}{\sigma}} \left(\frac{\sigma}{k_B} \right)^{\frac{3}{2}}$ (see appendix, Figure A-13). Knowing the field, we experimentally obtain a typical PF prefactor in the order of $10^4 \text{ K}^{1.5}$, while a good fit of the data would require a prefactor more than 1 order of magnitude higher. Hence field dependence of the hole mobility fails to fully explain the observed bell-shape behaviour observed in **Figure 3-1**.

3.3.3 Exploring transfer integral variation with temperature

Another possibility for the bell-shaped mobility is the eventuality of the intermolecular transfer integral collapsing with increasing temperature. In a way, this idea of a transfer integral strongly dependent on temperature was already reported by Davis et al. who observed a bell-shaped Arrhenius plot that they ascribed to a complex torsional motion dependent on temperature within dyads in solution which in turn affects the transfer integral.²⁶ While this exact mechanism is intrinsic to the specific dyad molecules used in that work and cannot be extended to DPP(TBFu)₂ in the solid-state, variation in intermolecular electronic coupling with temperature is strongly suggested by the UV-vis data. Indeed, the decreasing intensity of the respective electronic transitions with temperature indicates a decreased absorption coefficient within the film, under the reasonable assumption – given the low incident monochromatic light intensity – that the sample is not saturated by photons (in which case the lower intensity would naturally arise from broadening of the peak). The hypsochromic shift observed with increasing temperature further supports the notion of a deterioration of the π - π stacking upon increasing temperature. The stronger intensity loss, as well as hypsochromic shift, observed on sample annealed at 90 °C as compared to samples annealed at 130 °C and 170 °C is consistent with the presence of poorly crystalline regions and structural defects (aforementioned in section 3.3.1). Indeed, weak π - π interactions are more prone to deteriorate with increasing temperature.

3.3.4 Theory and modelling behind variation in electronic coupling

In general, the transfer integral associated with a structural conformation is considered to only change marginally with temperature.³⁸ Thereof, the development of a reasonable model for such a loss in electronic coupling with increasing temperature must rely on a change in packing structure exhibiting different electronic coupling. That is supported by the presence of isosbestic points in **Figure 3-5** that confirms the existence of two phases (A and B) in equilibrium with high temperature, seemingly favouring a poorly or even non-aggregated phase (B). In addition, Sharenko et al. have reported that solution-processed thin films of DPP(TBFu)₂ exhibit a cold crystallization at temperatures (T_C) as low as 323 K.³⁹ Hence, for cooperative crystallization to take place at T_C , reorganization of DPP(TBFu)₂ molecules must be facilitated by significant rotational and/or translational modes of motion.⁴⁰ The latter can originate from phase transitions from an initial phase (A) to a transition state (B) (higher in energy) from which it can reorganize as a crystalline phase (C), as depicted in **Figure 3-6**.

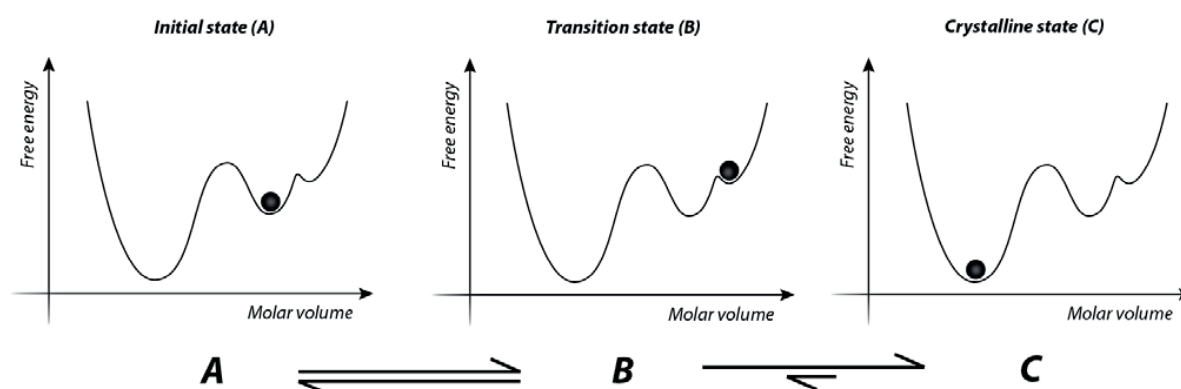


Figure 3-6. Schematic of the energy landscape as function of molar volume for a 1st order reversible transition between initial state A and transition state B. Crystallization can then happen from the high energy transition state B to crystalline state C. Black dot represent the actual state of a molecule.

Transition from phase A to phase B would then be the origin of the change in intermolecular electronic coupling with temperature. In this respect, we postulate that phase B must exhibit a significantly reduced intermolecular transfer integral relative to phase A, which is the very basis of the model. Moreover, molecules in phase B – being characterized by a significant loss in aggregation (*vide supra*) – will be assimilated to monomers. That, the self-assembly mechanism from non-aggregated state B to aggregated state A will define how the population in state A and B will evolve with temperature. In order to simplify the treatment, we will not consider the presence of the third phase

C in the blend but just an equilibrium between phase A and B. The underlying reason is that the inhomogeneous distribution of phase C within phase A (in equilibrium with phase B) leads to complex percolation considerations which greatly complicate the model development. However, the assumption behind the fact that no phase C is present nor generated during the mobility measurements is that mobility can be defined by transport only through phase A and B. While this might hold for as-cast FET, it is certainly not true for annealed sample as we will discuss below.

Let us then consider a solid solution of phases A and B. The evolution of the number of molecules in state A vs. state B will depend on the kind of mechanism governing self-assembly which could be cooperative or isodesmic. The clear sigmoidal trend present in **Figure 3-7** of the mobility at high temperature suggests that an isodesmic mechanism will be more appropriate to model the data and will thus be considered in this work. Even though, we note that a posteriori using a cooperative model such as the one describe by Smulders et al.⁴¹ for self-assembly is also possible and does not limit the model as expected from the marginal difference between the two trends. Considering isodesmic self-assembly, the fraction of molecules in state A can then be described in function of temperature as,^{42,43}

$$\alpha = \frac{N_A}{N_A + N_B} \cong \frac{1}{1 + \exp\left(-\Delta H \frac{T - T_m}{RT_m^2}\right)} \quad (3.4)$$

Where α is the degree of aggregation, N_A and N_B are the number of molecules in state A and B respectively, R the gas constant, ΔH the enthalpy and T_m the temperature where $\alpha = 0.5$ associated with the phase transition from B to A. Notably, equation (3.2) is popular to model the thermodynamic excitations of glass forming liquids.⁴³ The stochastic nature of an isodesmic process – as no specific nucleation centres are present – consequently leads to a homogenous mixture of A and B phases on the molecular scale. As defined above, phase A and B essentially differ by their intermolecular interactions. Let us then define their respective transfer integral J_A and J_B , which will be assumed as temperature independent and wich satisfies the relation $J_A \gg J_B$. The probability for a hole to hop between two molecules with electronic coupling J_A can then be expressed as,

$$P_A = \frac{N_A k_A}{N_A k_A + N_B k_B} \quad (3.5)$$

Where k_A and k_B are rate constant for hole transfer in state A and B respectively. Assuming that reorganizational energy is the same for state A and B, then equation (3.5) can be rewritten as,

$$P_A = \frac{N_A J_A^2}{N_A J_A^2 + N_B J_B^2} \quad (3.6)$$

Similarly, the probability for a hop to occur in between two molecules with intermolecular coupling J_B can be expressed:

$$P_B = \frac{N_B J_B^2}{N_A J_A^2 + N_B J_B^2} \quad (3.7)$$

We can then express the mean transfer integral experienced by a hole while hopping through this system by taking the geometrical average of the transfer integral for each hop (J_i) over a number of hops n as,

$$\bar{J} = \lim_{n \rightarrow \infty} \left(\prod_i^n J_i \right)^{1/n} \quad (3.8)$$

As in this model, J_i can only take two values (e.g. J_A and J_B), equation (3.8) can be rewritten for a large number of hops as,

$$\bar{J} = J_A^{P_A} J_B^{P_B} = \exp[P_A \ln(J_A) + P_B \ln(J_B)] \quad (3.9)$$

Finally, by substituting equation (3.6) and (3.7), we get:

$$\bar{J} = \exp \left[\frac{\alpha J_A^2 \ln(J_A) + (1 - \alpha) J_B^2 \ln(J_B)}{\alpha J_A^2 + (1 - \alpha) J_B^2} \right] \quad (3.10)$$

One can then express the mobility as to account for variation in transfer integral with temperature by substituting J within equation (3.1) by equation (3.10) as,

$$\mu = \frac{e a^2}{k_B T} \frac{2\pi}{\hbar} \sqrt{\frac{1}{4\pi\lambda_0 k_B T}} \exp\left(-\frac{E_a}{k_B T}\right) \exp\left[2 \frac{\alpha J_A^2 \ln(J_A) + (1 - \alpha) J_B^2 \ln(J_B)}{\alpha J_A^2 + (1 - \alpha) J_B^2}\right] \quad (3.11)$$

With E_a approximated as $E_a = \frac{\lambda_0}{4}$ (see equation (1.3)).

Table 3-1. Thermodynamic parameters describing the temperature dependent behaviour of the hole mobility in OFET for different annealing temperatures according to the isodesmic self-assembly model.

Annealing	λ_0 [meV]	J_a [meV]	J_b [meV]	T_m [K]	ΔH [kJ/mol]
As-	629.9	30.0	2×10^{-7}	206.3	-
90	516.7	54.5	0.1	209.8	-
130	556.2	107.0	0.4	201.8	-
170	883.1	275.5	41.5	373.6	-

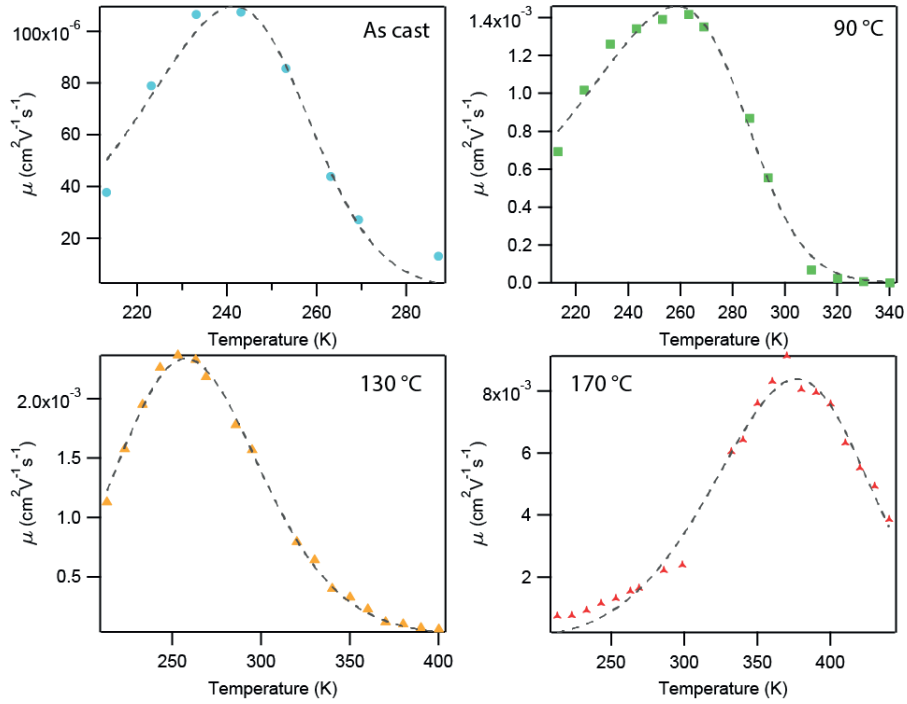


Figure 3-7. Temperature dependence of the field effect mobility extracted from saturated regime in DPP(TBFu)2 OFET (channel length of 20 μm) as-cast and annealed at 90 °C, 130 °C and 170 °C for 1 hour and corresponding fit using equation (3.11) developed in this work.

3.3.5 Application of the isodesmic model

Data presented in **Figure 3-1** can now be fit using equation (3.11) (also shown in **Figure 3-7**). In particular, the absence of crystalline domains in the as-cast sample – strongly suggested by the AFM data measured at the buried interface – makes it an ideal dataset to apply the model. The latter successfully fits as-cast FET mobility as function of temperature, returning physically significant parameters (summarized in **Table 3-1**). As a matter of fact, $J_A \gg J_B$ is verified, the former exhibiting an electronic coupling about 30 meV which is physically relevant. The parameter T_m is found to be around 206 K, that is about 30 K lower than the observed inversion, which makes sense as when $\alpha = 0.5$, the mean transfer integral can be approximated as $\bar{J} \approx J_A$. In addition, the enthalpy associated with this transition is lower than that measured for the melting of DPP(TBFu)₂ (*ca.* 40 kJ mol⁻¹).³³ Finally, the reorganization energy is found to be *ca.* 630 meV – corresponding to an activation energy of *ca.* 158 meV – which is higher than previously reported values for other organic system usually closer to 100 meV.^{44,45} While this is consistent with the lower hole mobilities measured in this work, it is important to also note that the temperature dependence of the exponential prefactor is routinely neglected in the literature when extracting E_a , which can lead to significant underestimation of E_a . Overall, our simple model demonstrates that a phase transition occurring within the transport channel can physically account for the inverted temperature dependence of the mobility observed in this work, while remaining in the frame of hopping theory.

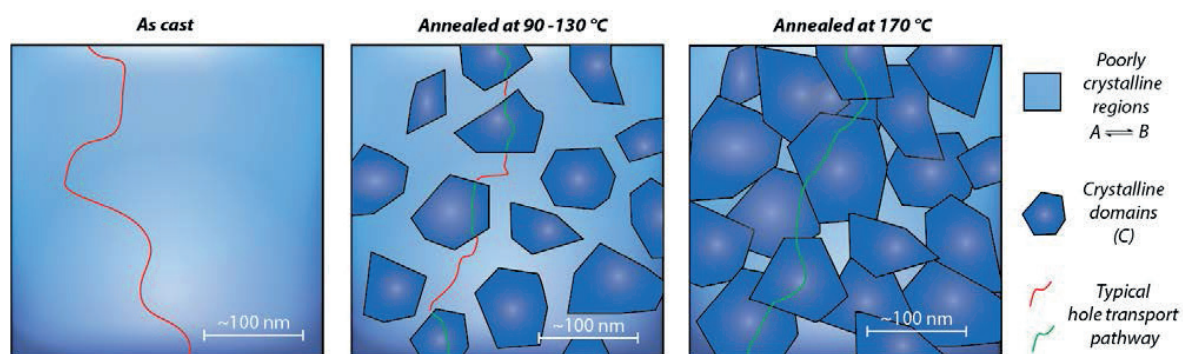


Figure 3-7. Schematic of the 3 phases present in the film as expected from AFM measurement. As-cast (left) present only a poorly crystalline phase, A, which is in equilibrium with the transition phase B. Respective population of these two phases is temperature dependent. After annealing at 90 °C and 130 °C a crystalline phase appears, though no percolation pathway through this crystalline phase exist. Then mobility remains highly affected by the equilibrium between phase A and B. When annealed at 170 °C, direct percolation pathway starts to form through the crystalline channel, limiting the effect of equilibrium between phase A and B on the mobility.

As previously mentioned, the model considers no crystalline phases and should therefore only be used to fit the as-cast data unless taking into account a third phase C in combination with complex percolation criteria. However, we found that the model can still fit temperature-dependent mobility data of FET annealed at 90 °C and 130 °C (and even at 170 °C as will be discussed later). Indeed, very similar reorganization energy and transition temperature are obtained, respectively 596 ± 80 meV and 208 ± 5 K. Hence, it suggests that the FET devices annealed at 90 and 130 °C are still limited by the same phase transition as the as-cast FET despite the presence of crystalline domains. This can easily be rationalized if crystalline domains are isolated from each other by a poorly crystalline phase (equivalent to a blend of A and B phases). As illustrated in **Figure 3-8**, hole transport will then be largely affected by the population ratio of phase A and B and thereof, by temperature. This is in good agreement with AFM data where platelets are visible (suggesting crystalline regions) while YM distribution strongly overlap the as-cast one (suggesting remaining poorly crystalline regions). In terms of fitting parameters, the main effect of annealing arises from an increase in transfer integral and a decrease in the enthalpy of the transition. Indeed, the presence of crystalline domains are expected to increase the mean transfer integral. As the model does not consider an electronic coupling for the crystalline phase C (J_C), the enhanced mean electronic coupling is reflected on J_A and J_B . The loss in enthalpy associated with the transition from phase A to B can also be rationalized given that crystalline phases do not undergo this phase transition. Thereof, as we do not account for this third population, which is not participating to the enthalpy, the overall molar enthalpy of the system must decrease according to $\Delta H^i = \beta \Delta H^0$, where ΔH^0 is the real molar enthalpy of the A to B transition as extracted from the as-cast sample and β is the poorly crystalline fraction composed of phases A and B (expressed as $\beta = 1 - \frac{N_C}{N_A + N_B + N_C}$ with N_C the number of molecules in state C). Consequently, in samples annealed at 90 °C and 130 °C, β can be calculated from the enthalpy ratio relative to as-cast conditions, which yields respectively *ca.* 58 % and 29 % of poorly crystalline regions. Interestingly, the degree of poorly crystalline regions can also be assessed by integrating the YM distribution as shown in **Figure 3-9**. The overlap fraction between YM of annealed samples and as-cast sample can be extracted as the y-value at the crossing point between the integral curve and the vertical blue dashed line marking the YM threshold below which domains are supposed to be poorly crystalline. It can be seen that values of β obtained with the model for samples annealed at 90 °C and 130 °C (see green dashed line and orange dashed line) are in very good agreement with the as-cast YM overlapping fraction. This strongly supports the validity of our approach even when the crystalline phase is present.

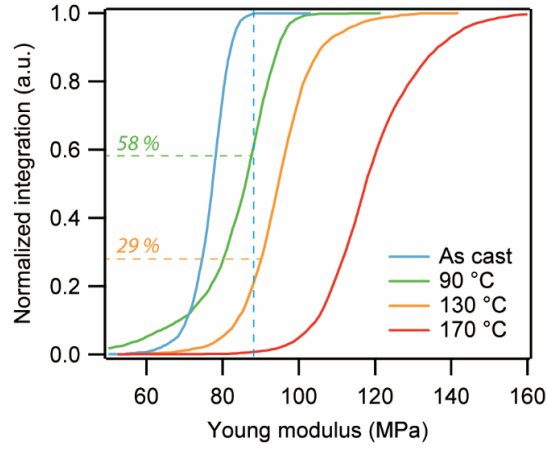


Figure 3-8. Integrated Young modulus distribution presented in **Figure 3-4** of as-cast sample and annealed at 90 °C, 130 °C and 170 °C. Blue dashed-line represents the threshold defining the overlap with YM of as-cast sample. Green and orange dashed lines indicates the fraction of poorly crystalline regions obtained from the model for samples annealed at respectively 90 °C and 130 °C.

Finally, it can be seen from **Figure 3-7** that the inversion of the mobility temperature dependence in FET annealed at 170 °C can still be fairly well fit using equation (3.11). However, the resulting T_m (ca. 373 K) strongly differs from the T_m obtained for samples annealed at lower temperature which was around 210 K. This strongly suggests that the mobility is not limited by transport within poorly crystalline region as transport pathways mainly through crystalline domains exist (as illustrated in **Figure 3-8** and supported by AFM and YM data). Before further discussing the new origin for the inversion in this last sample, it is important to keep in mind that the morphology of the active layer is largely beyond our initial assumption for the model where no crystalline phase is present. Indeed, the AFM image in combination with YM distribution suggests that it is mainly composed of crystalline platelets. Therefore, we will first discuss the origin of the inverted trend for the mobility in the frame of our model and then focus on alternative eventualities. In the former case, mobility would simply be limited by a new transition state that is in equilibrium with the crystalline phase around 373 K. In other words, at this high temperature phase C undergoes a transition to a fourth phase, D, which is an excited state of C with lower electronic coupling. Hence, we are back to our original assumption considering only two phases in equilibrium but with a distinct phase transition. Alternatively, the mobility loss with temperature could arise from a breakdown in percolation pathway at the grain boundaries. This would likely be caused by the presence of a thin layer (<9 nm) of phases A/B in between crystalline domains. As such percolation argument is not taken into account by equation

(3.11), it cannot fit the data with reasonable physical parameters. Finally, we cannot exclude that strong thermal lattice fluctuations (in the frame of transient localization theory) could limit the transport given the high temperature and reasonable mobility. However, it is important to note that the previously reported power law dependence $\mu \propto T^{-2}$ for transient localization is not strong enough to account for the loss in mobility observed in this work.²²

Further establishing our hypothesis of self-assembly governing the temperature dependence of the mobility through calculation of the transfer integrals in play would require a complex simulation study of DPP(TBFu)₂ molecular packing which is beyond the scope of the current work. Nonetheless, it is well-known that the transfer integral is highly affected by the relative orientation of the neighbouring molecules. Though no calculation were made for DPP(TBFu)₂ itself in the literature, it is sound to consider that conformational change between the two phases could lead to drastic change in the charge transfer rate as reported for other organic molecules.⁴⁶ Indeed, in the case of our model applied to DPP(TBFu)₂, it only supposes a change in transfer integral about 2 order of magnitude. This seems reasonable when comparing to the transfer integral dependency over angle and distance reported for neighbouring pentacene or hexabenzocoronene.⁴⁷ Nonetheless, DPP(TBFu)₂ itself would need to be studied using similar computational method for conclusive proof of this hypothesis.

3.4 Conclusions

We report a bell-shaped hole mobility dependence on temperature for DPP(TBFu)₂ FET, with hole mobilities well below the Mott-Ioffe-Regel limit, excluding significant charge delocalization. Rather, our hypothesis invokes a thermally activated transport mechanism where the inverted region arises from a collapse of the transfer integral in poorly crystalline regions present at the SiO₂/DPP(TBFu)₂ interface. These poorly crystalline regions are already known to crystallize at temperature as low as 320 K and hence to undergo a phase transition toward a poorly aggregated meso-phase below this temperature. The latter is expected to greatly impact the transfer integral between neighbouring molecules and in turn the mobility. In addition, we bring the breakdown in aggregation and electronic coupling in relation with an isodesmic self-assembly mechanism which successfully models the data, resulting in physically significant parameters. Most importantly, this work demonstrates that mobility dependence over temperature exhibiting a negative slope should not be accepted as a signature for band-like transport in organic devices, but also considered in term of hopping transport.

3.5 References

- (1) Sirringhaus, H. *Adv. Mater.* **2014**, 26 (9), 1319.
- (2) Miller, A.; Abrahams, E. *Phys. Rev.* **1960**, 120 (3), 745.
- (3) Marcus, R. A.; Sutin, N. *Biochim. Biophys. Acta BBA - Rev. Bioenerg.* **1985**, 811 (3), 265.
- (4) Sootsman, J. R.; Kong, H.; Uher, C.; D'Angelo, J. J.; Wu, C.-I.; Hogan, T. P.; Caillat, T.; Kanatzidis, M. G. *Angew. Chem.* **2008**, 120 (45), 8746.
- (5) Podzorov, V.; Menard, E.; Borissov, A.; Kiryukhin, V.; Rogers, J. A.; Gershenson, M. E. *Phys. Rev. Lett.* **2004**, 93 (8), 086602.
- (6) Uemura, T.; Nakayama, K.; Hirose, Y.; Soeda, J.; Uno, M.; Li, W.; Yamagishi, M.; Okada, Y.; Takeya, J. *Curr. Appl. Phys.* **2012**, 12, Supplement 3, S87.
- (7) Cho, J.; Mori, T. *Phys. Rev. Appl.* **2016**, 5 (6), 064017.
- (8) Mitsui, C.; Okamoto, T.; Yamagishi, M.; Tsurumi, J.; Yoshimoto, K.; Nakahara, K.; Soeda, J.; Hirose, Y.; Sato, H.; Yamano, A.; Uemura, T.; Takeya, J. *Adv. Mater.* **2014**, 26 (26), 4546.
- (9) Matsubara, K.; Manaka, T.; Iwamoto, M. *Appl. Phys. Express* **2015**, 8 (4), 041601.
- (10) Minder, N. A.; Ono, S.; Chen, Z.; Facchetti, A.; Morpurgo, A. F. *Adv. Mater.* **2012**, 24 (4), 503.
- (11) Yamashita, Y.; Tsurumi, J.; Hinkel, F.; Okada, Y.; Soeda, J.; Zajaczkowski, W.; Baumgarten, M.; Pisula, W.; Matsui, H.; Müllen, K.; Takeya, J. *Adv. Mater.* **2014**, 26 (48), 8169.
- (12) Yamashita, Y.; Hinkel, F.; Marszalek, T.; Zajaczkowski, W.; Pisula, W.; Baumgarten, M.; Matsui, H.; Müllen, K.; Takeya, J. *Chem. Mater.* **2016**, 28 (2), 420.
- (13) Senanayak, S. P.; Ashar, A. Z.; Kanimozhi, C.; Patil, S.; Narayan, K. S. *Phys. Rev. B* **2015**, 91 (11), 115302.
- (14) Lee, J.; Chung, J. W.; Kim, D. H.; Lee, B.-L.; Park, J.-I.; Lee, S.; Häusermann, R.; Batlogg, B.; Lee, S.-S.; Choi, I.; Kim, I. W.; Kang, M. S. *J. Am. Chem. Soc.* **2015**, 137 (25), 7990.
- (15) Cho, J.; Higashino, T.; Mori, T. *Appl. Phys. Lett.* **2015**, 106 (19), 193303.
- (16) Xu, X.; Yao, Y.; Shan, B.; Gu, X.; Liu, D.; Liu, J.; Xu, J.; Zhao, N.; Hu, W.; Miao, Q. *Adv. Mater.* **2016**, 28 (26), 5276.
- (17) Krupskaya, Y.; Gibertini, M.; Marzari, N.; Morpurgo, A. F. *Adv. Mater.* **2015**, 27 (15), 2453.
- (18) Schott, S.; Gann, E.; Thomsen, L.; Jung, S.-H.; Lee, J.-K.; McNeill, C. R.; Sirringhaus, H. *Adv. Mater.* **2015**, 27 (45), 7356.
- (19) Glarum, S. H. *J. Phys. Chem. Solids* **1963**, 24 (12), 1577.
- (20) Fratini, S.; Ciuchi, S. *Phys. Rev. Lett.* **2009**, 103 (26), 266601.
- (21) Sakanoue, T.; Sirringhaus, H. *Nat. Mater.* **2010**, 9 (9), 736.
- (22) Fratini, S.; Mayou, D.; Ciuchi, S. *Adv. Funct. Mater.* **2016**, 26 (14), 2292.
- (23) Yuen, J. D.; Menon, R.; Coates, N. E.; Namdas, E. B.; Cho, S.; Hannahs, S. T.; Moses, D.; Heeger, A. J. *Nat. Mater.* **2009**, 8 (7), 572.
- (24) Li, L.; Lu, N.; Liu, M. *J. Appl. Phys.* **2014**, 116 (16), 164504.
- (25) Waskasi, M. M.; Kodis, G.; Moore, A. L.; Moore, T. A.; Gust, D.; Matyushov, D. V. *J. Am. Chem. Soc.* **2016**, 138 (29), 9251.
- (26) Davis, W. B.; Ratner, M. A.; Wasielewski, M. R. *J. Am. Chem. Soc.* **2001**, 123 (32), 7877.
- (27) Kim, H. B.; Kitamura, N.; Kawanishi, Y.; Tazuke, S. *J. Am. Chem. Soc.* **1987**, 109 (8), 2506.
- (28) Viterisi, A.; Gispert-Guirado, F.; Ryan, J. W.; Palomares, E. *J. Mater. Chem.* **2012**, 22 (30), 15175.
- (29) Proctor, C. M.; Kher, A. S.; Love, J. A.; Huang, Y.; Sharenko, A.; Bazan, G. C.; Nguyen, T.-Q. *Adv. Energy Mater.* **2016**, 1502285.

- (30) Bisquert, J.; Fabregat-Santiago, F.; Mora-Seró, I.; Garcia-Belmonte, G.; Barea, E. M.; Palomares, E. *Inorganica Chim. Acta* **2008**, *361* (3), 684.
- (31) Walker, B.; Tamayo, A. B.; Dang, X.-D.; Zalar, P.; Seo, J. H.; Garcia, A.; Tantiwiwat, M.; Nguyen, T.-Q. *Adv. Funct. Mater.* **2009**, *19* (19), 3063.
- (32) Gasperini, A.; Jeanbourquin, X. A.; Rahmanudin, A.; Yu, X.; Sivula, K. *Adv. Mater.* **2015**, *27* (37), 5541.
- (33) Jeanbourquin, X. A.; Rahmanudin, A.; Gasperini, A.; Ripaud, E.; Yu, X.; Johnson, M.; Guijarro, N.; Sivula, K. *J. Mater. Chem. A* **2017**, *5* (21), 10526.
- (34) Scharsich, C.; Fischer, F. S. U.; Wilma, K.; Hildner, R.; Ludwigs, S.; Köhler, A. *J. Polym. Sci. Part B Polym. Phys.* **2015**, *53* (20), 1416.
- (35) Reish, M. E.; Huff, G. S.; Lee, W.; Uddin, M. A.; Barker, A. J.; Gallaher, J. K.; Hodgkiss, J. M.; Woo, H. Y.; Gordon, K. C. *Chem. Mater.* **2015**, *27* (8), 2770.
- (36) Duhm, S.; Xin, Q.; Hosoumi, S.; Fukagawa, H.; Sato, K.; Ueno, N.; Kera, S. *Adv. Mater.* **2012**, *24* (7), 901.
- (37) Parris, P. E.; Kenkre, V. M.; Dunlap, D. H. *Phys. Rev. Lett.* **2001**, *87* (12), 126601.
- (38) Shuai, Z.; Wang, L.; Song, C. In *Theory of Charge Transport in Carbon Electronic Materials*; SpringerBriefs in Molecular Science; Springer Berlin Heidelberg, **2012**; pp 7–41.
- (39) Sharenko, A.; Kuik, M.; Toney, M. F.; Nguyen, T.-Q. *Adv. Funct. Mater.* **2014**, *24* (23), 3543.
- (40) Müller, C. *Chem. Mater.* **2015**, *27* (8), 2740.
- (41) Smulders, M. M. J.; Schenning, A. P. H. J.; Meijer, E. W. *J. Am. Chem. Soc.* **2008**, *130* (2), 606.
- (42) Smulders, M. M. J.; Nieuwenhuizen, M. M. L.; de Greef, T. F. A.; van der Schoot, P.; Schenning, A. P. H. J.; Meijer, E. W. *Chem. – Eur. J.* **2010**, *16* (1), 362.
- (43) Douglas, J. F.; Dudowicz, J.; Freed, K. F. *J. Chem. Phys.* **2008**, *128* (22), 224901.
- (44) Son, S. Y.; Kim, Y.; Lee, J.; Lee, G.-Y.; Park, W.-T.; Noh, Y.-Y.; Park, C. E.; Park, T. *J. Am. Chem. Soc.* **2016**, *138* (26), 8096.
- (45) Khim, D.; Xu, Y.; Baeg, K.-J.; Kang, M.; Park, W.-T.; Lee, S.-H.; Kim, I.-B.; Kim, J.; Kim, D.-Y.; Liu, C.; Noh, Y.-Y. *Adv. Mater.* **2016**, *28* (3), 518.
- (46) Huang, J.; Kertesz, M. *J. Chem. Phys.* **2005**, *122* (23), 234707.
- (47) Kirkpatrick, J. *Int. J. Quantum Chem.* **2008**, *108* (1), 51.



Chapter 4 Engineering the self-assembly of diketopyrrolopyrrole-based molecular semiconductors via an aliphatic linker strategy

Elemental solid-state self-assembly of molecular semiconductors is a key aspect for controlling the optoelectronic properties of organic electronic materials. Herein, we investigate the use of a flexible linker strategy to control the self-assembly of a solution-processable diketopyrrolopyrrole semiconductor coded as DPP(TBFu)₂. Two distinct dimers—prepared with varied linker position relative to the orientation of the conjugated core—reveal the effect of connectivity on the solid-state self-assembly and optoelectronic properties—favoring either H- or J-type aggregation. The dimer with a “vertical” linker orientation exhibits a poor crystallinity in neat films, but improves hole mobility in OFETs by 10-fold, reaching $3.0 \times 10^{-3} \text{ cm}^2 \text{V}^{-1} \text{s}^{-1}$ when used as an additive in with DPP(TBFu)₂. Distinctively, the dimer with a “horizontal” linker orientation does not enhance charge carrier transport, but is found to affect the thermal stability of donor:acceptor blends in OPVs with PCBM. Devices retain 90% of their initial conversion efficiency after 5 hours of thermal stress, compared to only 45% for control devices. Thermodynamic and kinetic rationale further suggest that this flexible linker strategy represents a powerful tool to control supramolecular assembly in molecular semiconductors without altering the nature of the core conjugated segment.

*This chapter has been adapted from “Engineering the self-assembly of diketopyrrolopyrrole-based molecular semiconductors via an aliphatic linker strategy” (Jeanbourquin, X. A.; Rahmanudin, A.; Gasperini, A.; Ripaud, E.; Yu, X.; Johnson, M.; Guijarro, N.; Sivula, K., J. Mater. Chem. A, **2017**, 5, 10526-10536)*

4.1 Introduction

As demonstrated in the previous chapter, the ultimate optoelectronic performance of molecular semiconductor-based device is severely dictated by its supramolecular self-assembly in the solid-state, which in turn is strongly influenced by π - π interactions between the conjugated segments. These intermolecular interactions have proved quite challenging to predict¹ and to control² without altering the semiconductor core properties. Moreover, phenomena such as structural polymorphism,^{3–5} defects formation,^{6–8} strain,⁹ and domain orientation/grain boundaries^{10–13} have been identified as additional complications that confound the rational engineering of molecular semiconductors. Thus developing generalizable tools to improve our understanding and ability to control the supramolecular self-assembly of organic semiconductors independently of altering the core π -conjugated unit is an important goal.^{14,15}

Previous investigations have already begun to address this objective using process engineering based techniques¹⁶ such as forcing directionality and/or spatial confinement during solution casting, which can influence polymorphism^{17–19} and the crystal domain size/orientation.^{16,20} Processing additives such as inert polymers or small molecule nucleation promoters have also been shown to influence the self-assembly of molecular semiconductors.²¹ While these processing-based techniques have shown an encouraging level of control, they are essentially extrinsic, i.e. they can be greatly affected by external factors such as substrate, solvent, evaporation rate, and are not generalizable towards arbitrary molecular structures. In contrast, routes for controlling molecular self-assembly by engineering the solubilizing side chains can preserve the electronics of the semiconducting core.²² This route has been widely investigated for π -conjugated polymers,^{23–28} and to a lesser extent for small molecule organic semiconductors.^{29–31} Indeed, since the self-assembly of a typical molecular semiconductor with standard aliphatic solubilizing chains is dominated by π - π interactions, side chain engineering offers limited control. Including heteroatoms to promote hydrogen bonding, ionic coordination, or other specific interactions can offer increased influence over the self-assembly, but can also alter the electronic properties potentially leading to the introduction of trapping states.²²

Recently, a promising strategy to control supramolecular assembly without altering the semiconducting core has been suggested via the covalent tethering of conjugated segments with flexible non-conjugated chains.^{32–35} Indeed, employing flexible linkers in conjugated polymer systems—which break continuous backbone conjugation—have already shown promising effects by easing chain rigidity, increasing processability, and offering unique self-assembly motifs.^{36–43} In contrast, when

flexibly linking small molecule semiconductors, π - π stacking can be hindered due to the conformational restrictions, which can alter crystal domains size leading to more isotropic charge transport, and increased thermal stability of the solid-state morphology.³² Melt processing was even recently demonstrated with this approach.⁴⁴ Despite these encouraging results employing the flexible linker approach, a clear understanding of the mechanism by which these flexibly-linked molecular systems affect intermolecular self-assembly is lacking. Thus, in order to develop this approach towards a functional tool to control supramolecular assembly in molecular semiconductors, more insight into the additive effect is needed. Herein we employ a model molecular semiconductor system and different linking strategies to prepare two distinct dimers with the same conjugated core. The effect of the linker positions on the optoelectronic properties and self-assembly are scrutinized from both thermodynamic and kinetic perspectives.

4.2 Results and Discussion

To investigate the effects of the covalent linking strategy for controlling the self-assembly of solution-processable molecular semiconductors, we choose DPP(TBFu)₂ as the model π -conjugated unit. DPP-based small-molecules, especially DPP(TBFu)₂, have been reported as promising electron donor molecules for organic photovoltaics when used in combination with PCBM as electron acceptor,⁴⁵ and their self-assembly into well-ordered crystalline domains is known to have an important effect on the device performance⁴⁶ as seen in chapter 3.

Two dimers based on DPP(TBFu)₂ were synthesized using an unbranched aliphatic chain as a linker between the two conjugated segments. A horizontally linked dimer, coded H-(DPP)₂, was connected at the 5-benzofuran position, while a vertical connection in the dimer coded V-(DPP)₂ is placed at the imide position where the branched solubilizing chain normally resides. **Figure 4-1** shows the structure and synthetic strategy to prepare the two dimers. H-(DPP)₂ was synthesized based on a modified procedure from previous work on an aliphatically-linked DPP(TBFu)₂ polymer.³³ For the coupling of one benzofuran group onto the dibromominated DPP(T)₂ core (**1**), we found that the typical Suzuki coupling conditions strongly favoured the di-functionalized DPP(TBFu)₂ even when only one equivalent of the borylated benzofuran was used.⁴⁷ However, using a Stille coupling method with polar aprotic DMF as a solvent instead of the conventional non-polar toluene together with the stannylated benzofuran (**2**), gave high yield of the mono-benzofuranated product, likely due to the role of DMF as a catalytic inhibitor.⁴⁸ The subsequent symmetric coupling of this mono-functionalized DPP with 1,6-bis(2-(trimethylstannyl)benzofuran-5-yl)hexane (**3**) gave the H-(DPP)₂ dimer (**4**). On the other hand, the V-(DPP)₂ dimer was synthesized by first linking two mono-alkylated DPP(T)₂ (**5**) units via an alkylation with a C₁₀ aliphatic chain at the imide position. The product was subsequently coupled using a Suzuki coupling with excess borylated benzofuran (**6**) to give the vertically linked V-(DPP)₂ (**7**). Full synthetic details are available in appendix B.

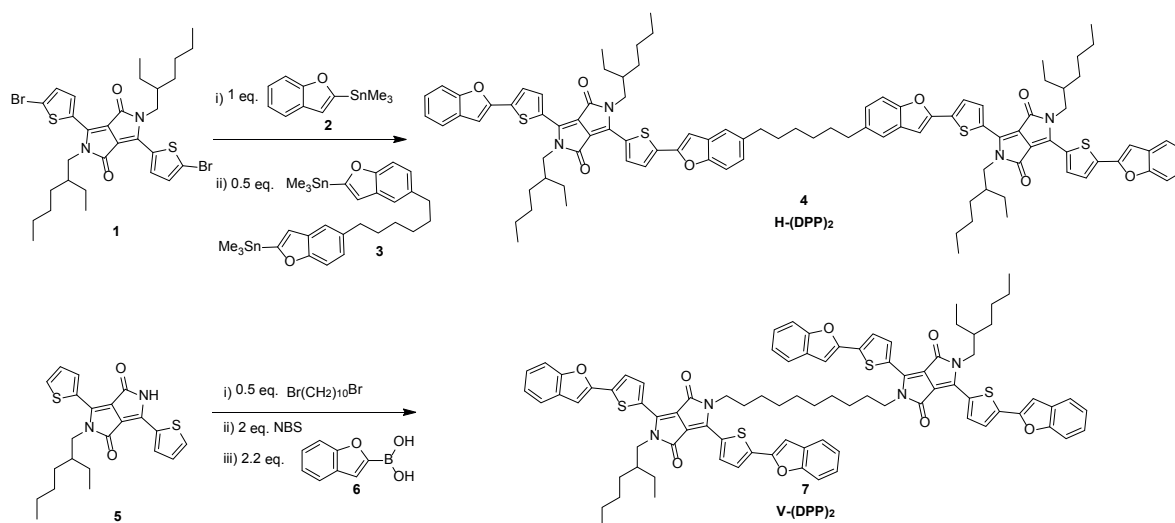


Figure 4-1. Chemical structures and synthetic strategy of the novel DPP(TBFu)₂ based dimers, V-(DPP)₂ and H-(DPP)₂.

4.2.1 Impact of the flexible linker on the supramolecular assembly

Normalized UV-vis absorption spectra of the two dimers as well as the parent monomeric DPP(TBFu)₂ (coded as M-DPP in this chapter) dissolved in chloroform are shown in **Figure 4-2a**. The three molecules have identical absorption spectra in solution, which is in good agreement with previously published data for the parent M-DPP.⁴⁵ Indeed, aliphatic substituents are not expected to greatly affect the electron density of the conjugated core. In the solid-state UV-vis of the dimers cast from chloroform into thin films, the V-(DPP)₂ dimer exhibits a spectrum qualitatively similar to the M-DPP (see normalized spectra **Figure 4-2b**). However, we note the presence of an increased background signal and broader peaks—likely stemming from poor film formation of the V-(DPP)₂ which is due to its relatively low solubility (*ca.* 1 mg mL⁻¹, compared to >20 mg mL⁻¹ for the horizontally-linked dimer or M-DPP), resulting in the presence of aggregates in the film. Considering the horizontally-linked dimer, while the absorption peaks of H-(DPP)₂ in the solid-state appear at similar wavelengths and with similar peak widths compared to M-DPP, a clear change in the relative peak intensities is evidenced. The peak at 560 nm of H-(DPP)₂ shows a relative decrease in intensity compared to M-DPP, whereas the peak at 665 nm exhibits an increased relative intensity. This change in solid-state absorption between M-DPP and H-(DPP)₂ suggests a possible difference in the solid-state self-assembly motif.

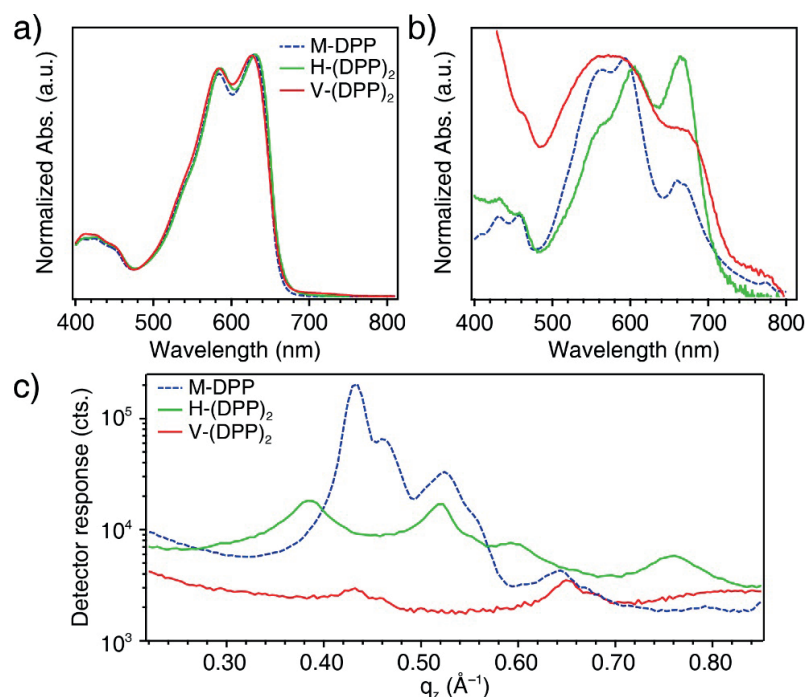


Figure 4-2. UV-vis and crystallographic characterization. The normalized optical absorption spectra measured in chloroform solution (a) and in solid-state thin films (b) are shown for the parent M-DPP, and the two dimers H-(DPP)₂ and V-(DPP)₂. (c) Out-of-plane grazing incidence X-ray diffractograms of M-DPP, H-(DPP)₂ and V-(DPP)₂ obtained from chlorobenzene drop-casted films.

In order to further investigate a possible change in self-assembly or crystal packing of the dimer molecules compared to the parent M-DPP, grazing incidence X-ray diffraction (GIXRD) was performed on solid-state thin films prepared by drop-casting. The resulting out-of-plane diffractograms are shown in **Figure 4-2c** where M-DPP exhibits a primary peak at a scattering vector value of $q_z = 0.435 \text{ \AA}^{-1}$, which is in good agreement with previous reports.⁵⁰ This primary peak has been assigned to the (020) reflection corresponding to a stacking distance of 14.4 \AA between layers of overlapped (π - π stacked) M-DPP molecules separated by solubilizing alkyl chains.⁵¹ We note that the scattering peak for the reported π - π stacking distance (*ca.* 3.5 \AA) is typically not sufficiently intense to be observed in thin film XRD measurements. The V-(DPP)₂ dimer exhibits a peak at a similar q_z value compared to the primary M-DPP peak, suggesting that the vertical linking strategy does not affect the interplanar stacking distance. However, we observe a drastically smaller scattering intensity by almost two orders of magnitude despite similar film thickness, implying a significantly reduced crystallinity. An interplanar stacking peak is also observed for the H-(DPP)₂ dimer, however, at a lower q_z value of 0.39 \AA^{-1} (stacking distance of 16.1 \AA). This larger interplanar stacking distance is surprising given that the solubilizing alkyl chains are identical in the M-DPP and the H-(DPP)₂. However,

this difference together with the additional peaks at $q_z = 0.60$ and 0.76 \AA^{-1} support the notion of a unique molecular self-assembly in the H-(DPP)₂ dimer thin film. We note that the intensity of the scattering was also one order of magnitude lower than the M-DPP, suggesting a decrease in crystallinity similarly with the V-(DPP)₂ dimer.

The different supramolecular self-assembly of the H-(DPP)₂ dimer implied by the GIXRD results, is consistent with the solid-state UV-vis results, considering previous studies of M-DPP and similar molecules. Indeed, previous work from Nguyen and co-workers suggests that the relative magnitude of the 665 nm optical absorption peak is inversely correlated to the amount of intermolecular π - π stacking interactions in M-DPP films (since this peak decreased with annealing temperature relative to the peak at 590 nm).⁴⁵ Moreover, previous work with a set of similar (monomeric) DPP-based molecules with varying units substituting the benzofuran (*e.g.* triphenyl amine or pyrene) reported a similar trend in the UV-vis data compared to our H-(DPP)₂ dimer.⁵² A pyrene-functionalized DPP molecule in that work exhibited a very strong self-assembly due to its planarity, while the more bulky structure of a triphenyl amine derivative was suggested to hinder the π - π stacking. Interestingly, their optical absorption data indicate the presence of a strong peak around 650 nm for the triphenyl amine derivative, whereas this peak is negligible in the case of the pyrene-substituted DPP. This observation further reinforces the view that the presence of the UV-vis peak at 665 nm is either due to a decreased amount of π - π stacking or to an increased π - π stacking distance. However, if this peak only was attributed to a larger disorder within the film (decreased amount of π - π stacking), we would expect the V-(DPP)₂ dimer to exhibit a stronger relative absorption at 665 nm compared to H-(DPP)₂ due to its drastically lower crystallinity implied by the GIXRD results. As this is not the case, an altered π - π stacking of the H-(DPP)₂ dimer is thus likely the cause of the altered UV-vis spectrum. More specifically, the H-(DPP)₂ dimer reasonably self-assembles with a different overlap of the π -conjugated cores compared to M-DPP. Indeed, other DPP-based molecules have been reported to self-assemble with varying amounts of co-existing H-aggregate and J-aggregate character within the structure, which strongly affects their optical absorption properties.⁵³

The hypsochromic shift observed in M-DPP when going from solution to solid-state (*e.g.* from 580 nm to 560 nm) is typically ascribed to the direct overlap of the π -conjugated cores (H-aggregation). On the other hand, the bathochromic shift leading to the peak at 665 nm in solid-state is characteristic of staggered overlap (J-aggregation). Therefore, even though both the M-DPP and H-(DPP)₂ exhibit combined H- and J-aggregate character, the self-assembly of H-(DPP)₂ likely consists of more stag-

gered overlapping nature compared to the parent M-DPP, which would explain both the reduced absorption at 560 nm and the strong peak at 665 nm. We note that while it is common for J-aggregates to exhibit a narrower absorption peak with higher extinction coefficient and smaller Stokes shift compared to H-aggregates, the apparent broadness of the peak at 665 nm is caused by the overlap of transitions that can be resolved by deconvolution (see appendix B, Figure B-1). Moreover, a smaller Stokes shift observed in fluorescence emission measurements in H-(DPP)₂ films compared to M-DPP films (100 nm vs 145 nm) corroborates the self-assembly hypothesis (see appendix B, Figure B-1c).

A possible origin for the different solid-state behaviour of the H-(DPP)₂ dimer could be due to intramolecular interactions between the two conjugated cores of the H-(DPP)₂ dimer, (*e.g.* folding on itself). To investigate this possibility, we measured the UV-vis spectrum of H-(DPP)₂ in solution with increasing amounts of a non-solvent (MeOH) at very low concentrations to promote intramolecular self-assembly. The UV-Vis data (see appendix, Figure B-2) shows that the intensity of the peak at 665 nm increases with the H-(DPP)₂ concentration, suggesting that this peak arises from intermolecular rather than intramolecular self-assembly. Moreover, insight into the self-assembly mechanism of H-(DPP)₂ in methanol can be obtained by plotting the aggregation fraction in function of the concentration as previously reported.⁵⁴ This data shows that the self-assembly follows a cooperative mechanism as opposed to an isodesmic model, indicating a nucleation and growth mechanism.

To further investigate the different solid-state behaviour of the dimers relative to the parent M-DPP, we next examined the compounds by differential scanning calorimetry (DSC). **Figure 4-3a** shows the second heating and cooling curves of the pure materials as well as blends of M-DPP containing different ratios of the dimers. The parent M-DPP exhibits an endothermic transition onset at 224 °C when heating at 10 °C min⁻¹ while an exothermic transition begins at 206 °C during cooling, attributed to, respectively, melting and crystallization. Scans of the vertically linked dimer show no detectable thermal transitions, consistent with a poor crystallinity suggested by the GIXRD results, and suggests that the vertically linking strategy prevents the conjugated core self-assembly in the solid-state leaving only an amorphous film. In contrast, we did observe phase transitions with the horizontally linked dimer. The first heating scan of H-(DPP)₂ (**Figure 4-3a**, broken line) after preparing the sample via drop casting from chloroform shows an endothermic transition at 186 °C, considerably lower than M-DPP (note that no difference in melting temperature was noted in M-DPP between the first and second scans). Upon cooling, a weak exothermic transition was observed at 147 °C. The subsequent (2nd) heating scan (solid line) exhibited an exothermic transition starting at 121 °C followed by an

endothermic transition at a temperature of 165°C. This behaviour suggests that a kinetically limited crystallization occurs when cooling the melt at 10°C min⁻¹.

Indeed, upon increasing the cooling rate from 1 to 100°C min⁻¹, the subsequent heating scan shows an increase in the enthalpy of the exothermic transition (see appendix, Figure B-3) confirming this view. However, the melting temperature remains constant at *ca.* 165°C regardless of the cooling rate indicating the formation of a consistent crystalline phase distinct from the M-DPP. Moreover, the enthalpy for the melting phase transition of H-(DPP)₂ is similar to that of M-DPP (35 J g⁻¹ and 50 J g⁻¹ respectively), which, contrary to the disparate scattering intensity observed by GIXRD, suggests that the horizontal linking strategy does not drastically reduce the crystallinity of the material. The different behaviour during the first heating scan is likely due to the effect of casting the materials from solvent, which results in a different self-assembly compared to freezing the melt with potentially solvent residues. Indeed, polymorph formation has been observed⁵¹ in this class of materials even without flexible linker.

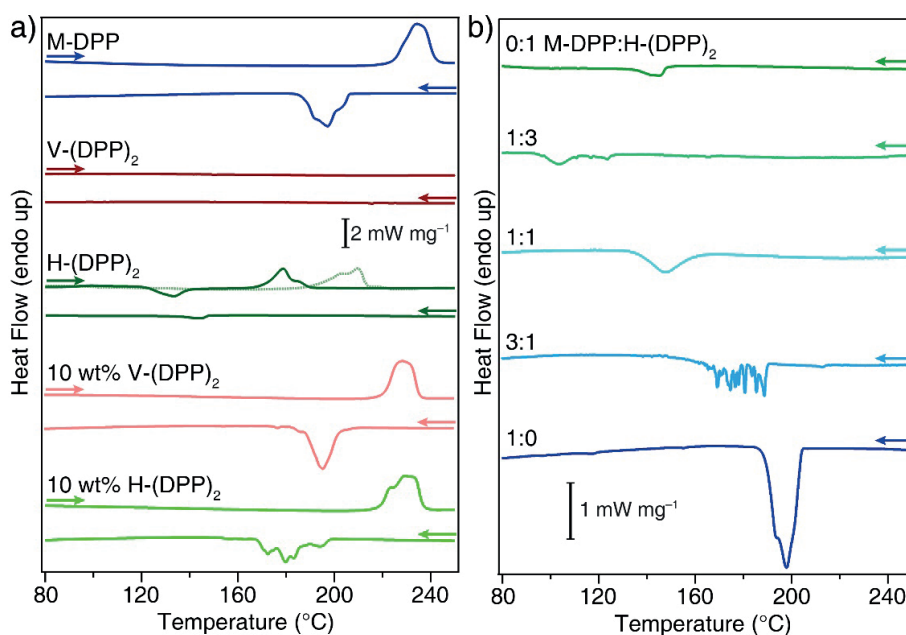


Figure 4-3. Differential scanning calorimetry of the dimer materials. (a) shows the second heating and cooling (10 °C min⁻¹) scans of M-DPP, V-(DPP)₂, H-(DPP)₂ (the broken line in represents the first heating scan from a drop-cast sample), 10 wt% V-(DPP)₂ in M-DPP and 10 wt% H-(DPP)₂ in M-DPP. (b) shows the second cooling only curves for blend samples of M-DPP:H-(DPP)₂ in wt. ratios as indicated (where 0:1 represents pure dimer).

The different solid-state self-assembly of the two dimers compared to the parent molecule was next further probed by blending 10 wt% of each dimer into M-DPP and examining the DSC response. The second heating and cooling scans are shown in **Figure 4-3a** for 10 wt% V-(DPP)₂ and 10 wt% H-(DPP)₂. The effect of blending the vertically-linked dimer into M-DPP was minor: a slight melting point depression of 4°C to 220°C is noted, and the crystallization began 2°C earlier at 208°C. However, the blend with H-(DPP)₂ exhibited a significant freezing point depression of *ca.* 10°C and a complex supercooling behaviour.

The effect of blending the H-(DPP)₂ and M-DPP on the crystallization was further investigated by combining these two materials at different weight ratios. The second cooling scan is reported in **Figure 4-3b** for each indicated M-DPP:H-(DPP)₂ ratio. Interestingly, addition of 25 wt% of M-DPP within H-(DPP)₂ (*e.g.* a ratio of 1:3) also results in a depression in crystallization temperature of about 40 °C. Taking all of the blend ratio results of **Figure 4-3b** together shows that M-DPP suppresses the crystallization of H-(DPP)₂ while H-(DPP)₂ also suppresses the crystallization of M-DPP. Such a behaviour can not be rationalized with the view that both compounds solidify in the same crystal structure with different degrees in supercooling caused by kinetic limitations, as in such case the crystallization temperature would be expected to increase with the addition of M-DPP into the dimer matrix. Indeed, the observed behaviour is consistent with colligative properties indicating that M-DPP and H-(DPP)₂ form a solid solution upon blending with $\Delta H^{\text{mix}} > 0$ and implying that pure H-(DPP)₂ and M-DPP self-assemble with different stacking motifs. Confirmation of the different crystal structure of H-(DPP)₂ was next sought by preparing single crystals of H-(DPP)₂ via the vapour diffusion crystal growth method. However, we were unable to form single crystals sufficiently large for X-ray analysis. Nonetheless, given the complexity of self-assembly in solution-processed films (as indicated by the difference between the first and second heating scans of the H-(DPP)₂), a single crystal sample would likely not be representative of the structures relevant to thin film charge transport.

Nevertheless, the UV-vis, GIXRD, and DSC results data taken together provide a clear picture that the horizontal linking strategy in the H-(DPP)₂ dimer effectively achieves the goal of the study: to modulate the molecular self-assembly without changing the conjugated core elements of the semiconducting molecule. In contrast, the vertical linking strategy leads to a dimer with poor solubility and a drastically reduced self-assembly in the solid-state.

4.2.2 Effect on the charge carrier mobility

To understand the effect of the molecular self-assembly on the electronic performance of the materials, charge transport in solution-processed thin films was measured by fabricating bottom-gate bottom-contact organic field effect transistors (OFETs). **Table 4-1** summarizes the main transistors characteristics, while device output characteristics and transfer curves are given in appendix, Figure B-4 and Figure B-5. As-cast M-DPP thin films gave hole mobility extracted from saturated regime (μ_h) values similar to previously reported work ($10^{-5} \text{ cm}^2 \text{ V}^{-1} \text{ s}^{-1}$),³³ while μ_h in pure H-(DPP)₂ films was found to be only slightly lower (**Table 4-1**). However, after thermally annealing at 110 °C, the μ_h for M-DPP increased by one order of magnitude, while μ_h for H-(DPP)₂ was only enhanced by a factor of two. The increase in charge transport in M-DPP has been explained by Viterisi et al. who showed that strong intermolecular π - π interactions at the benzofuran moiety act as a driving force for crystallization upon annealing.⁵⁰ Reasonably, the aliphatic linker on the benzofuran moiety in H-(DPP)₂ can kinetically hinder this π - π stacking leading to a hole mobility which is less affected by thermal annealing. Neat V-(DPP)₂ thin films exhibited a hole mobility lower than $10^{-6} \text{ cm}^2 \text{ V}^{-1} \text{ s}^{-1}$, which was attributed to poor self-assembly of the resulting in ineffective intermolecular charge transport. Indeed, in previous studies of a flexibly-linked polymeric M-DPP, the absence of thin film self-assembly was also correlated to a poor OFET mobility.³³ In addition the poor solubility of the V-(DPP)₂ and the resulting poor thin film formation is also likely a factor in the poor mobility.

Table 4-1. Average hole mobility (μ_h) extracted from saturated and linear regime, on/off ratio and threshold voltage of the different OFET devices presented in this study in annealed conditions. Parameters for as-cast devices are given in parenthesis.

Active layer	Content (wt. %)	μ_{sat} ($\text{cm}^2 \text{ V}^{-1} \text{ s}^{-1}$)	μ_{lin} ($\text{cm}^2 \text{ V}^{-1} \text{ s}^{-1}$)	On/off ratio	V_T (V)
Neat M-DPP	-	6.5×10^{-4} (3.0×10^{-5})	2.2×10^{-4}	7.0×10^2 (85.2)	-10 (-11)
Neat H-(DPP) ₂	-	2.4×10^{-5} (1.1×10^{-5})	9.7×10^{-6}	1.0×10^2 (38)	-5 (-10)
Neat V-(DPP) ₂	-	$< 1 \times 10^{-6}$	$< 1 \times 10^{-6}$	< 10	-10
Blend M-DPP:H-(DPP) ₂	1	7.9×10^{-4} (1.7×10^{-5})	4.1×10^{-4}	1.7×10^3 (85.5)	-11 (-15)
	5	8.3×10^{-4} (1.7×10^{-5})	3.9×10^{-4}	3.0×10^3 (5.1×10^2)	-6 (-11)
	10	1.1×10^{-3} (1.7×10^{-5})	4.8×10^{-4}	3.4×10^3 (1.2×10^2)	-5 (-10)
	25	7.9×10^{-5} (1.3×10^{-5})	-	3.9×10^2 (76)	-20 (-30)
Blend M-DPP:V-(DPP) ₂	1	1.6×10^{-3} (1.5×10^{-5})	6.4×10^{-4}	4.7×10^3 (61)	-6 (-25)
	5	2.0×10^{-3} (3.0×10^{-5})	7.7×10^{-4}	2.6×10^3 (45)	-7 (-17)
	10	3.0×10^{-3} (1.7×10^{-4})	9.2×10^{-4}	6.4×10^3 (4.7×10^2)	-9 (-13)
	25	1.6×10^{-4} (2.4×10^{-5})	-	1.1×10^3 (1.3×10^2)	-8 (-12)

As distinct behaviour of the of H- and V-(DPP)₂ dimers was observed by DSC when blending with M-DPP, we next sought to understand how this behaviour translates into altering charge transport characteristics. **Figure 4-4** shows μ_h as a function of the amount of dimer blended within films of M-DPP with as-cast and annealed devices. The values for the pure M-DPP are also shown (blue markers at 0 wt%). Despite the established different self-assembly of the horizontally-linker dimer, its addition up to 10 wt% does not significantly alter μ_h . However, upon the addition of 25 wt%, the annealed devices exhibit a reduced μ_h approaching that of the pure (annealed) H-(DPP)₂. In contrast, V-(DPP)₂ addition up to 10 wt% results in an order of magnitude increase in μ_h for both film conditions. Unfortunately, further increasing the amount of V-(DPP)₂ resulted in a decrease in μ_h which is attributed to the aforementioned poor crystallinity and film formation of the vertically-linked dimer.

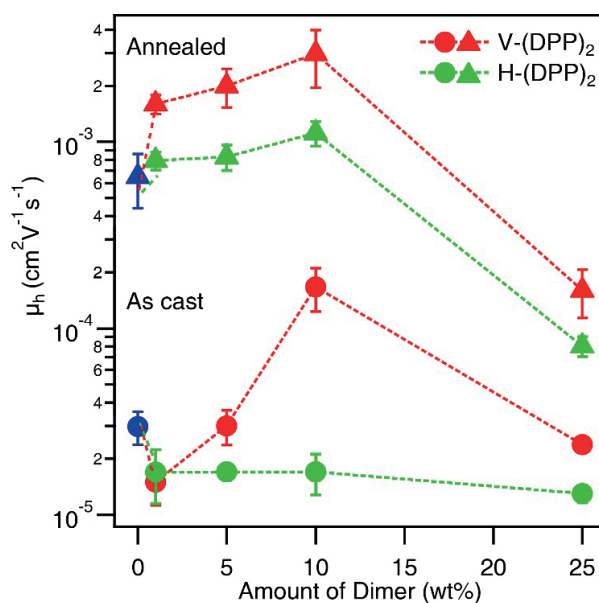


Figure 4-4. Average hole mobility (μ_h) extracted from saturated regime in OFET devices prepared with pure M-DPP (blue markers) and M-DPP blended with the dimer molecules H-(DPP)₂ (green markers) and V-(DPP)₂ (red markers). Circle markers represent values from as-cast thin films while triangles indicate values taken from devices annealed at 110 °C for 10 min.

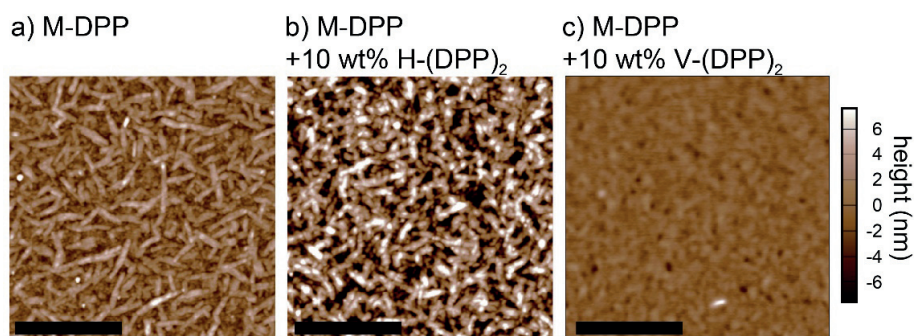


Figure 4-5. Atomic force microscopy height trace images (scale bars 2 μm) of annealed films containing M-DPP (a), and with 10 wt% addition of (b) H-(DPP)₂ and (c) V-(DPP)₂.

Topographical analysis of the OFET thin films by AFM (**Figure 4-5**), gives a plausible explanation for the behaviour of μ_{h} with respect to the addition of the dimer molecules. While we note that AFM gives an impression of the morphology at the semiconductor/air interface, and not the structure of the buried semiconductor/dielectric interface (where charge transport occurs in the OFET device structure employed in this work), comparisons between morphology and charge transport are routine and can offer useful insight. In our case, the thin film morphology of the pure M-DPP film (**Figure 4-5a**) exhibits the expected haystack morphology with needle-like features *ca.* 1 μm in length and 100 nm in width corresponding to crystal domains.³³ The thin film with 10 wt% H-(DPP)₂, shown in **Figure 4-5b**, shows similarly sized features and an increase in RMS roughness from 2.25 nm (pure M-DPP) to 4.38 nm (10 wt% H-(DPP)). In contrast, the film with added V-(DPP)₂ exhibits a much smoother surface (RMS 0.79 nm) without needle-shaped domains (**Figure 4-5c**). Since grain-boundaries and void spaces between crystals grains are known to limit charge carrier transport through thin films,⁵⁵ the reduced presence of grain boundaries in the film with the vertical dimer could reasonably explain the higher mobility, which is observed at optimum loading before the self-assembly is perturbed too much by the poorly crystalline dimer. Indeed, the DSC data of the M-DPP with 10 wt% V-(DPP)₂ (**Figure 4-3a**) does show a sharper crystallization peak compared to the neat M-DPP, and a slightly earlier onset of crystallization. These features suggest that V-(DPP)₂ may act as nucleation promotor, inducing a more homogeneous crystallization of the film, which is consistent with AFM topography results. For the horizontally-linked dimer, we note that the topography of the pure H-(DPP)₂ film (**Figure 4-6a**) shows a much smaller grain size (but does reveal features consistent with a semicrystalline film). The increased presence of grain boundaries in this case reasonably explains its lower mobility despite the substantial crystallinity. However, we cannot discount a reduced transfer integral

(electronic coupling)⁵⁶ for intermolecular charge transfer that may result from the different molecular self-assembly.

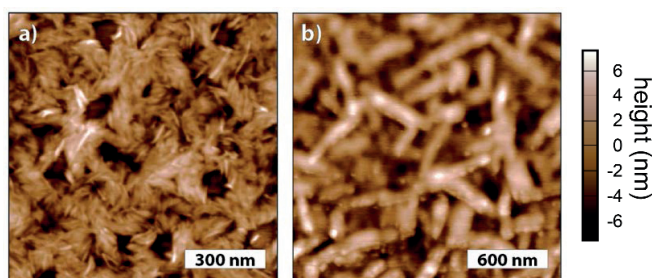


Figure 4-6. AFM height images of (a) neat $H-(DPP)_2$ and (b) $M-DPP$.

4.2.3 Structural stability enhancement of the bulkheterojunction

Given the interesting behaviour of the dimers in OFET devices, we next sought to investigate their performance in bulk heterojunction OPVs. Devices were fabricated with $PC_{61}BM$ as the electron acceptor and a donor:acceptor ratio of 6:4. Current-voltage curves for representative devices after a standard annealing treatment (110 °C for 10 min) are shown in **Figure 4-7**. We note that all as-cast devices (tested before thermal annealing) performed poorly with short circuit current densities (J_{sc}) of *ca.* 1-2 $mA\ cm^{-2}$ (see J-V curves of as-cast devices in **Figure 4-7b**), similar to previously reported performances.⁴⁵ The standard $M-DPP:PC_{61}BM$ 6:4 device (dark blue curve, **Figure 4-7**) reached a J_{sc} of 9 $mA\ cm^{-2}$ and a power conversion efficiency (PCE) of *ca.* 3.5 % after the annealing treatment. We note that the state-of-the-art efficiency for this system has been reported above 4 % using $M-DPP$, and the lower performances observed here can be attributed to the use of $PC_{61}BM$ instead of $PC_{71}BM$. Generally in the $M-DPP:PCBM$ system, the performance enhancement upon annealing is known to be caused by a phase segregation of the donor and acceptor phases driven by the crystallization of the $M-DPP$.⁴⁶ Optimum demixing results from this crystallization and creates a BHJ with a high interfacial surface area to afford high free charge carrier generation but also continuous donor and acceptor phases for effective charge carrier transport. Adding a small amount (10 wt%) of either of the dimers into the donor component in the BHJ did not significantly affect the J-V behaviour in our case as seen by the light blue and red J-V curves in **Figure 4-7** (corresponding to $H-(DPP)_2$ and $V-(DPP)_2$ addition, respectively). This is in contrast to the OFET results where the 10 wt% of $V-$

(DPP)₂ produced a change in thin film morphology and a large increase in charge carrier mobility after annealing. The different distances required for charge carrier transport (100 nm in OPV vs. 20 μm for OFET) is likely the cause for this absence of any effect of the V-(DPP)₂ addition. Indeed, grain-boundary limited charge transport is less likely to constrain the performance of the OPV given the thin active layer thickness.

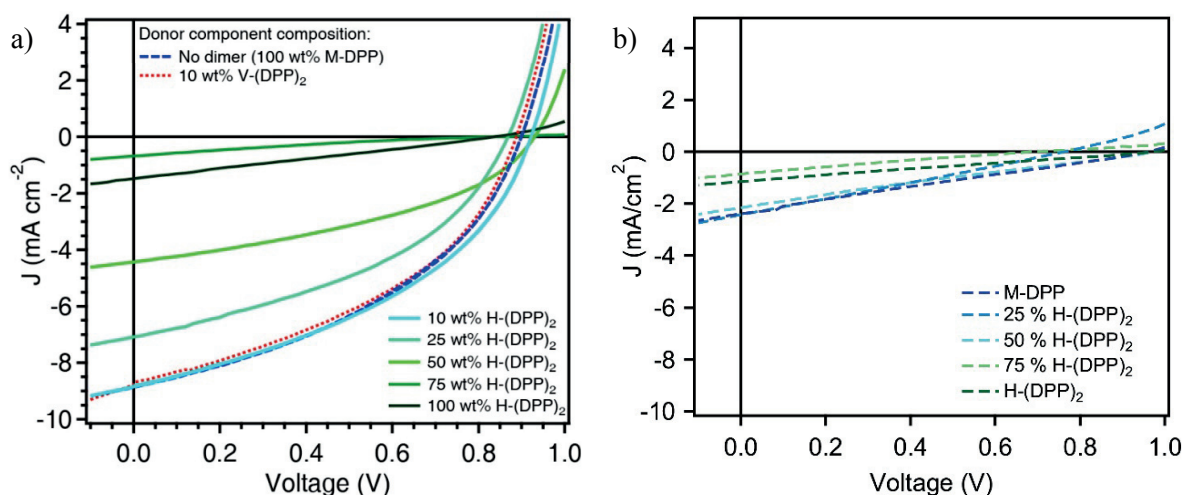


Figure 4-7. (a) J - V curves of photovoltaic devices based on bulk heterojunction Donor:PC₆₁BM at a weight ratio of 6:4. The donor component consists of M-DPP with added dimer as indicated. Devices were annealed at 110 °C. (b) J - V curves of (as-cast, unannealed) photovoltaic devices based on bulk heterojunction Donor:PC₆₁BM at a weight ratio of 6:4. The donor component consists of M-DPP with added dimer as indicated.

Due to the poor solubility of the vertically linked dimer, OPV devices with higher fraction of V-(DPP)₂ as additive were not considered, however blends with increasing amounts of the horizontally linked dimer were tested. In the case of the OPV device with pure H-(DPP)₂ as the donor phase (dark green curve in **Figure 4-7**) we found that the annealing step did not significantly affect the J - V -curve and the J_{sc} remained at the low as-cast value of 1.5 mA cm^{-2} . A small J_{sc} which does not change upon annealing can either be due to a large degree of phase segregation in the as-cast device (which limits free charge carrier generation), or to the lack of crystallization of the H-(DPP)₂ during the annealing conditions, leaving the blend in a well-mixed state which enhances charge carrier recombination. Since no large-scale phase segregation was observed in the film prepared with H-(DPP)₂ (*vide infra*) the latter explanation is most reasonable. Indeed, blending of H-(DPP)₂ into M-DPP in the donor

component of the BHJ exhibited intermediate J_{sc} 's after annealing, as shown in **Figure 4-7**, suggesting a tunable degree of phase segregation in the films is present after the thermal annealing. It is worth noting that the trend of the annealed J_{sc} in function of the H-(DPP)₂ content corresponds well with the trend observed in **Figure 4-3b** for the DSC crystallization temperature. Indeed, the smallest J_{sc} in the OPV devices is found to be at 75 wt% H-(DPP)₂ (1:3 monomer to dimer), which also corresponds to the DSC curve showing the lowest crystallization temperature. The lower driving force for crystallization implied by the behaviour of this composition in the DSC characteristics suggests that the J_{sc} is the lowest in this device as the PCBM forms a well-mixed (non-phase segregated) active layer. To confirm the differing phase segregation in H-(DPP)₂:PCBM blends, solvent cast BHJs were further studied by DSC. Differences between the first and second heating scan from solvent cast BHJs heating past the melting transitions are shown in **Figure 4-8**. Interestingly, when H-(DPP)₂ is blended with PCBM over a wide range of composition, the donor melting transition is present on the first heating scan but disappears on the second heating. This is in contrast to M-DPP:PCBM blends where the melting transition is present also on the second heating scan, and thus indicates that the H-(DPP)₂ has a relatively increased interaction with PCBM.

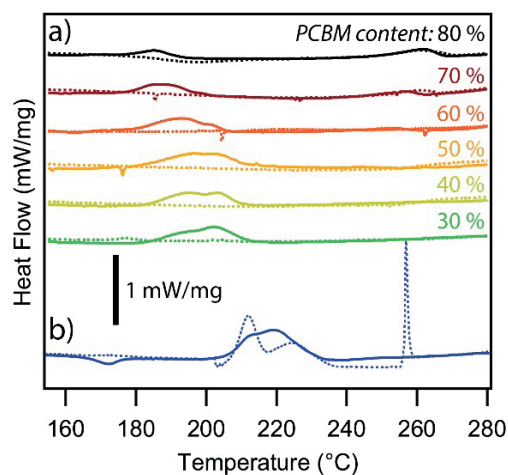


Figure 4-8. Heating curves measured by differential scanning calorimetry for a) different ratios of H-(DPP)₂:PCBM blends and b) M-DPP:PCBM (6:4) on first heating (solid line) and second heating (dashed line). (exothermic down)

Even though phase segregation control using the H-(DPP)₂ as additive offers no improvement of the PCE in this system since an ideal BHJ can already be realized with the known optimized annealing treatment, it remains a potential tool to affect the thermodynamic equilibrium of the BHJ. Indeed, upon long thermal treatments the standard M-DPP:PCBM BHJ is known to further phase segregate, expelling the PCBM and leading to a drop in PCE.³³ Moreover, the general lack of a detectable glass transition temperature in small molecule semiconductors⁵⁷ means that the “cold crystallization” and continued phase segregation can occur at temperatures lower than the annealing temperature⁴⁶ albeit at lower rates. This inherent morphological instability remains a key issue for the long-term stability of OPVs based on crystalline molecules.⁵⁸

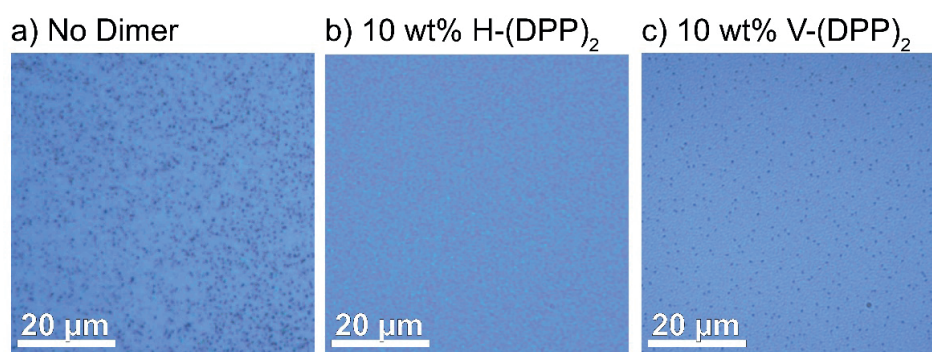


Figure 4-9. Optical microscopy images of thermally annealed (5 h 100 °C) M-DPP:PCBM bulk-heterojunction thin films (a) without added dimer and (b) with 10 wt% H-(DPP)₂ and (c) with 10 wt% V-(DPP)₂ included in the blend.

In initial experiments of the long-term annealing of BHJs with added dimers, we noticed a significant qualitative difference in the morphology. Optical micrographs of the BHJs after annealing for 5 hours at 100°C with or without 10 wt% of either dimer are shown in **Figure 4-9**. Indeed, the neat film of M-DPP:PCBM exhibits dark aggregates that have previously been identified as phase-segregated PCBM domains.²¹ The BHJ prepared with 10 wt% of the V-(DPP)₂ in the donor component phase also showed segregation under the same annealing conditions (**Figure 4-9c**); However, the effect was slightly attenuated. Surprisingly, the H-(DPP)₂ dimer showed no indication of any large-scale phase segregation (**Figure 4-9b**), suggesting an improved BHJ thermal stability. It is worth noting that 10 wt% H-(DPP)₂ offers a more stable BHJ than 10 wt% V-(DPP)₂ despite its higher degree of crystallinity as observed from GIXRD and DSC data. This observation suggests an important role of the molecular packing of H-(DPP)₂ for engineering the BHJ stability.

OPV devices prepared with 10 wt% of either dimer and annealed after deposition of the top electrode did not show significant difference in performance upon long-term annealing (data not shown). In all cases a significant decrease in PCE at short annealing times was observed with or without the dimer present. This decrease can be attributed to chemical degradation within the active layer due to reaction with the aluminium cathode.⁵⁹ In order to decouple morphology changes from possible chemical instability in presence of the cathode, thermal annealing was performed prior to aluminium deposition for BHJs with 10 wt% H-(DPP)₂ dimer as the behaviour of this blend was found to be more promising in the optical micrographs presented in **Figure 4-9**. The PCE as a function of the active layer annealing time is presented in **Figure 4-10**.

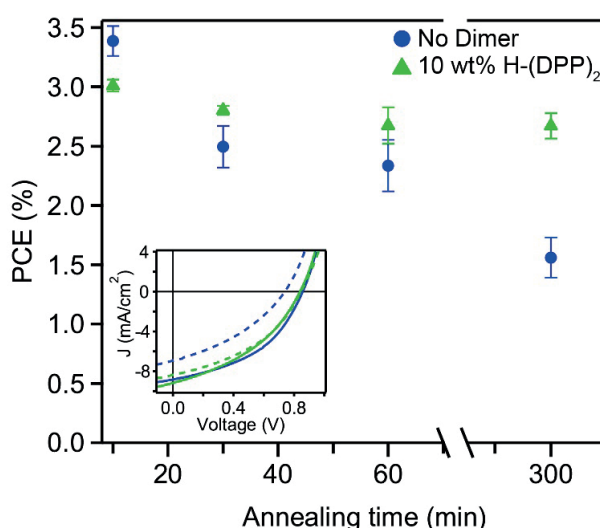


Figure 4-10. The OPV power conversion efficiency of M-DPP:PCBM devices with and without 10 wt% H-(DPP)₂ as a function of the active layer annealing time at 100 °C. The inset shows J-V curves for M-DPP:PCBM for devices annealed for 10 min (solid lines) and 5 h (broken lines) with (green) and without (blue) addition of 10 wt% H-(DPP)₂.

As expected, the data demonstrate a faster as well as greater PCE loss for the OPV device prepared without the dimer, losing more than 50 % of its original performance after 5 hours of annealing. However, devices containing 10 wt% H-(DPP)₂ exhibit only a slight loss in performance (about 10 %) after 5 h of annealing, retaining a PCE of 2.7 %. J-V curves corresponding to the devices are shown in the inset of **Figure 4-10**. As expected upon annealing, the change in PCE is correlated with a decrease in J_{sc} . This can be rationalized as a larger phase segregation leads to a smaller electron

donor/acceptor interface possibly leading to larger exciton recombination. For BHJs without the dimer additive, a significant drop in V_{oc} also appears upon annealing. While a change in V_{oc} is generally attributed to change in recombination pathways, in this case, the V_{oc} decrease is more likely caused by a smaller shunt resistance caused by the large phase segregation. This is supported by the dark J-V curves (see appendix, Figure B-6) which clearly indicated a smaller resistance near short-circuit conditions. Overall, these OPV device results demonstrate the advantage of morphological control over the BHJ via the H-(DPP)₂ additive.

Altogether, the different behaviours of the dimers as additives in BHJ OPVs can be rationalized by their different interactions with the parent M-DPP. The aforementioned nucleation promoting effects of the V-(DPP)₂ dimer do not offer any significant improvement over the BHJ morphology obtained by optimized thermal annealing of the as-cast blend, and since this dimer at 10 wt% loading does not significantly hinder the ability of the M-DPP to crystallize, no apparent changes in OPV device performance are evidenced. On the other hand, from the DSC results the horizontally-linked dimer has a clear thermodynamic influence on the self-assembly of the M-DPP to crystallize. This effect reasonably translates into a reduced interaction parameter between the donor and acceptor in the blend⁶⁰ and thus a reduced phase separation during annealing. While this does lead to a more stable bulk-heterojunction when 10 wt% of the H-(DPP)₂ dimer is used in the donor phase, we note that an increased miscibility of the donor and acceptor is not necessarily beneficial for OPV operation. Indeed, the benefit of improved carriers charge separation implied with a well-mixed blend is offset by an increase in charge trapping,⁶¹ as previously mentioned, which reasonably explains the poor behaviour of the OPVs when the H-(DPP)₂ dimer is purely used as the donor.

4.3 Conclusion

In this work we present a strategy directed toward increasing understanding of the effects of self-assembly in solution-processed molecular semiconductors on their optoelectronic properties. We designed two novel DPP(TBFu)₂-based dimers using an aliphatic linker approach that allows retaining a well-defined conjugated core while also controlling the interactions and self-assembly of the semiconducting moiety. The “vertically-linked” V-(DPP)₂, and the “horizontally-linked” H-(DPP)₂, dimers were found to retain the optical band-gap of the parent DPP(TBFu)₂ molecule, but exhibit very different self-assembly properties. For H-(DPP)₂, solid-state UV-vis, GIXRD and DSC data suggest the aliphatic linker partially lowers Van der Waals interaction between neighbouring conjugated cores while DSC data show only a slightly reduced melting enthalpy and a positive enthalpy of mixing

between the horizontal dimer and the parent molecule, confirming a different solid-state self-assembly. In contrast the vertically-linked dimer was poorly crystalline and likely acted as a nucleation promoter for the parent DPP(TBFu)₂. Both dimers maintained ability to transport charge in OFET devices, although at a reduced hole mobility. Blends of V-(DPP)₂ and the parent DPP(TBFu)₂ showed an enhanced mobility by a factor of 5-10 in annealed and as-cast films, respectively, up to $3.0 \times 10^{-3} \text{ cm}^2 \text{ V}^{-1} \text{ s}^{-1}$ in the bottom-contact bottom-gate configuration. This increase was correlated to a change in thin film morphology, caused by the potential nucleation promotion effect of the dimer, where fewer large charge-trapping grain boundaries are observed but the crystallinity of the DPP(TBFu)₂ in the thin film remains present. In contrast, blends of H-(DPP)₂ and the parent DPP(TBFu)₂, did not show a significant increase in hole mobility, but OPV devices including 10 wt% of H-(DPP)₂ in the donor phase yielded a significant increase in device stability under thermal stress (retaining 90 % of the initial PCE after 5 hours compared to only 45 % for the control). In this case, the increased thermodynamic miscibility between the donor and acceptor phases when including the H-(DPP)₂ prevents large scale phase segregation.

Overall, this work demonstrates that linking conjugated segments into dimers with a flexible aliphatic chain is a promising approach to control molecular self-assembly without changing the nature of the semiconducting molecular core. The linker position has a significant effect on the self-assembly of the resulting dimer, which in turn alters the optoelectronic properties in the solid-state and gives insight into the effects of self-assembly apart from other factors. We demonstrate that by using dimers as additives in functional devices, either kinetic (*e.g.* nucleation promotion by the vertically-linker dimer) or thermodynamic (*e.g.* controlling the interactions of mixing with the horizontally-linker dimer) aspects of the molecular self-assembly can be tuned to offer unique control over the thin film morphology and device performance. Since our flexibly-linked dimer strategy is easily generalizable to a large set of solution processable molecular semiconductors (given the ubiquitous present of aliphatic solubilizing chains), the extension of this concept to other systems will likely lead to an increased understanding of the important relation between molecular self-assembly and the performance of organic electronic devices.

4.4 References

- (1) L. Price, S. *Chem. Soc. Rev.* **2014**, 43 (7), 2098.
- (2) Huang, C.-F.; Wu, S.-L.; Huang, Y.-F.; Chen, Y.-C.; Chang, S.-T.; Wu, T.-Y.; Wu, K.-Y.; Chuang, W.-T.; Wang, C.-L. *Chem. Mater.* **2016**, 28 (15), 5175.

- (3) Jones, A. O. F.; Chattopadhyay, B.; Geerts, Y. H.; Resel, R. *Adv. Funct. Mater.* **2016**, 26 (14), 2233.
- (4) Wombacher, T.; Gassmann, A.; Foro, S.; von Seggern, H.; Schneider, J. J. *Angew. Chem.* **2016**, 128 (20), 6145.
- (5) Stolte, M.; Suraru, S.-L.; Diemer, P.; He, T.; Burschka, C.; Zschieschang, U.; Klauk, H.; Würthner, F. *Adv. Funct. Mater.* **2016**, 26 (41), 7415.
- (6) Lee, B.; Chen, Y.; Fu, D.; Yi, H. T.; Czelen, K.; Najafov, H.; Podzorov, V. *Nat. Mater.* **2013**, 12 (12), 1125.
- (7) Mikhnenko, O. V.; Kuik, M.; Lin, J.; van der Kaap, N.; Nguyen, T.-Q.; Blom, P. W. M. *Adv. Mater.* **2014**, 26 (12), 1912.
- (8) Liscio, F.; Albonetti, C.; Broch, K.; Shehu, A.; Quiroga, S. D.; Ferlauto, L.; Frank, C.; Kowarik, S.; Nervo, R.; Gerlach, A.; Milita, S.; Schreiber, F.; Biscarini, F. *ACS Nano* **2013**, 7 (2), 1257.
- (9) Wu, Y.; Chew, A. R.; Rojas, G. A.; Sini, G.; Haugstad, G.; Belianinov, A.; Kalinin, S. V.; Li, H.; Risko, C.; Brédas, J.-L.; Salleo, A.; Frisbie, C. D. *Nat. Commun.* **2016**, 7, 10270.
- (10) Rivnay, J.; Jimison, L. H.; Northrup, J. E.; Toney, M. F.; Noriega, R.; Lu, S.; Marks, T. J.; Facchetti, A.; Salleo, A. *Nat. Mater.* **2009**, 8 (12), 952.
- (11) Dong, H.; Fu, X.; Liu, J.; Wang, Z.; Hu, W. *Adv. Mater.* **2013**, 25 (43), 6158.
- (12) Rivnay, J.; Mannsfeld, S. C. B.; Miller, C. E.; Salleo, A.; Toney, M. F. *Chem. Rev.* **2012**, 112 (10), 5488.
- (13) Chen, W.; P. Nikiforov, M.; B. Darling, S. *Energy Environ. Sci.* **2012**, 5 (8), 8045.
- (14) Lee, C.-H.; Lee, G.-H.; van der Zande, A. M.; Chen, W.; Li, Y.; Han, M.; Cui, X.; Arefe, G.; Nuckolls, C.; Heinz, T. F.; Guo, J.; Hone, J.; Kim, P. *Nat. Nanotechnol.* **2014**, 9 (9), 676.
- (15) Mei, J.; Diao, Y.; Appleton, A. L.; Fang, L.; Bao, Z. *J. Am. Chem. Soc.* **2013**, 135 (18), 6724.
- (16) Diao, Y.; Tee, B. C.-K.; Giri, G.; Xu, J.; Kim, D. H.; Becerril, H. A.; Stoltenberg, R. M.; Lee, T. H.; Xue, G.; Mannsfeld, S. C. B.; Bao, Z. *Nat. Mater.* **2013**, 12 (7), 665.
- (17) Giri, G.; Park, S.; Vosgueritchian, M.; Shulaker, M. M.; Bao, Z. *Adv. Mater.* **2014**, 26 (3), 487.
- (18) Giri, G.; Li, R.; Smilgies, D.-M.; Li, E. Q.; Diao, Y.; Lenn, K. M.; Chiu, M.; Lin, D. W.; Allen, R.; Reinspach, J.; Mannsfeld, S. C. B.; Thoroddsen, S. T.; Clancy, P.; Bao, Z.; Amassian, A. *Nat. Commun.* **2014**, 5, 3573.
- (19) Luo, C.; Kyaw, A. K. K.; Perez, L. A.; Patel, S.; Wang, M.; Grimm, B.; Bazan, G. C.; Kramer, E. J.; Heeger, A. J. *Nano Lett.* **2014**, 14 (5), 2764.
- (20) Yuan, Y.; Giri, G.; Ayzner, A. L.; Zoombelt, A. P.; Mannsfeld, S. C. B.; Chen, J.; Nordlund, D.; Toney, M. F.; Huang, J.; Bao, Z. *Nat. Commun.* **2014**, 5, 3005.
- (21) Niazi, M. R.; Li, R.; Li, E. Q.; Kirmani, A. R.; Abdelsamie, M.; Wang, Q.; Pan, W.; Payne, M. M.; Anthony, J. E.; Smilgies, D.-M.; Thoroddsen, S. T.; Giannelis, E. P.; Amassian, A. *Nat. Commun.* **2015**, 6, 8598.
- (22) Mei, J.; Bao, Z. *Chem. Mater.* **2014**, 26 (1), 604.
- (23) Back, J. Y.; Yu, H.; Song, I.; Kang, I.; Ahn, H.; Shin, T. J.; Kwon, S.-K.; Oh, J. H.; Kim, Y.-H. *Chem. Mater.* **2015**, 27 (5), 1732.
- (24) Kang, I.; Yun, H.-J.; Chung, D. S.; Kwon, S.-K.; Kim, Y.-H. *J. Am. Chem. Soc.* **2013**, 135 (40), 14896.
- (25) Lee, J.; Han, A.-R.; Yu, H.; Shin, T. J.; Yang, C.; Oh, J. H. *J. Am. Chem. Soc.* **2013**, 135 (25), 9540.
- (26) Fang, L.; Zhou, Y.; Yao, Y.-X.; Diao, Y.; Lee, W.-Y.; Appleton, A. L.; Allen, R.; Reinspach, J.; Mannsfeld, S. C. B.; Bao, Z. *Chem. Mater.* **2013**, 25 (24), 4874.
- (27) Wang, Y.; Liu, Y.; Chen, S.; Peng, R.; Ge, Z. *Chem. Mater.* **2013**, 25 (15), 3196.
- (28) Sun, Y.; Zhang, C.; Dai, B.; Lin, B.; Yang, H.; Zhang, X.; Guo, L.; Liu, Y. *J. Polym. Sci. Part Polym. Chem.* **2015**, 53 (16), 1915.

- (29) Balakrishnan, K.; Datar, A.; Naddo, T.; Huang, J.; Oitker, R.; Yen, M.; Zhao, J.; Zang, L. *J. Am. Chem. Soc.* **2006**, *128* (22), 7390.
- (30) Wang, C.; Qin, Y.; Sun, Y.; Guan, Y.-S.; Xu, W.; Zhu, D. *ACS Appl. Mater. Interfaces* **2015**, *7* (29), 15978.
- (31) Hartnett, P. E.; Margulies, E. A.; Matte, H. S. S. R.; Hersam, M. C.; Marks, T. J.; Wasielewski, M. R. *Chem. Mater.* **2016**, *28* (11), 3928.
- (32) Schroeder, B. C.; Li, Z.; Brady, M. A.; Faria, G. C.; Ashraf, R. S.; Takacs, C. J.; Cowart, J. S.; Duong, D. T.; Chiu, K. H.; Tan, C.-H.; Cabral, J. T.; Salleo, A.; Chabinyc, M. L.; Durrant, J. R.; McCulloch, I. *Angew. Chem. Int. Ed.* **2014**, *53* (47), 12870.
- (33) Gasperini, A.; Jeanbourquin, X. A.; Rahmanudin, A.; Yu, X.; Sivula, K. *Adv. Mater.* **2015**, *27* (37), 5541.
- (34) Xiang, X.; Shao, W.; Liang, L.; Chen, X.-Q.; Zhao, F.-G.; Lu, Z.; Wang, W.; Li, J.; Li, W.-S. *RSC Adv.* **2016**, *6* (28), 23300.
- (35) Liang, Z.; Cormier, R. A.; Nardes, A. M.; Gregg, B. A. *Synth. Met.* **2011**, *161* (11–12), 1014.
- (36) Zhu, X.; Traub, M. C.; Vanden Bout, D. A.; Plunkett, K. N. *Macromolecules* **2012**, *45* (12), 5051.
- (37) Lin, X.; Hirono, M.; Seki, T.; Kurata, H.; Karatsu, T.; Kitamura, A.; Kuzuhara, D.; Yamada, H.; Ohba, T.; Saeki, A.; Seki, S.; Yagai, S. *Chem. – Eur. J.* **2013**, *19* (21), 6561.
- (38) Gasperini, A.; Bivaud, S.; Sivula, K. *Chem. Sci.* **2014**, *5* (12), 4922.
- (39) Shao, W.; Liang, L.; Xiang, X.; Li, H.; Zhao, F.; Li, W. *Chin. J. Chem.* **2015**, *33* (8), 847.
- (40) Schroeder, B. C.; Chiu, Y.-C.; Gu, X.; Zhou, Y.; Xu, J.; Lopez, J.; Lu, C.; Toney, M. F.; Bao, Z. *Adv. Electron. Mater.* **2016**, *2* (7), 1600104.
- (41) Zhao, Y.; Zhao, X.; Zang, Y.; Di, C.; Diao, Y.; Mei, J. *Macromolecules* **2015**, *48* (7), 2048.
- (42) Ding, L.; Li, H.-B.; Lei, T.; Ying, H.-Z.; Wang, R.-B.; Zhou, Y.; Su, Z.-M.; Pei, J. *Chem. Mater.* **2012**, *24* (10), 1944.
- (43) Zhao, X.; Zhao, Y.; Ge, Q.; Butrouna, K.; Diao, Y.; Graham, K. R.; Mei, J. *Macromolecules* **2016**, *49* (7), 2601.
- (44) Zhao, Y.; Zhao, X.; Roders, M.; Gumyusenge, A.; Ayzner, A. L.; Mei, J. *Adv. Mater.* **2017**, *29* (6), 1605056.
- (45) Walker, B.; Tamayo, A. B.; Dang, X.-D.; Zalar, P.; Seo, J. H.; Garcia, A.; Tantiwiwat, M.; Nguyen, T.-Q. *Adv. Funct. Mater.* **2009**, *19* (19), 3063.
- (46) Sharenko, A.; Kuik, M.; Toney, M. F.; Nguyen, T.-Q. *Adv. Funct. Mater.* **2014**, *24* (23), 3543.
- (47) Li, W.; Kelchtermans, M.; M. Wienk, M.; J. Janssen, R. A. *J. Mater. Chem. A* **2013**, *1* (47), 15150.
- (48) Proutiere, F.; Schoenebeck, F. *Angew. Chem. Int. Ed.* **2011**, *50* (35), 8192.
- (49) Jeanbourquin, X. A.; Rahmanudin, A.; Gasperini, A.; Ripaud, E.; Yu, X.; Johnson, M.; Guijarro, N.; Sivula, K. *J. Mater. Chem. A* **2017**, *5* (21), 10526.
- (50) Viterisi, A.; Gispert-Guirado, F.; Ryan, J. W.; Palomares, E. *J. Mater. Chem.* **2012**, *22* (30), 15175.
- (51) Liu, J.; Walker, B.; Tamayo, A.; Zhang, Y.; Nguyen, T.-Q. *Adv. Funct. Mater.* **2013**, *23* (1), 47.
- (52) Lee, O. P.; Yiu, A. T.; Beaujuge, P. M.; Woo, C. H.; Holcombe, T. W.; Millstone, J. E.; Douglas, J. D.; Chen, M. S.; Fréchet, J. M. J. *Adv. Mater.* **2011**, *23* (45), 5359.
- (53) Kirkus, M.; Wang, L.; Mothy, S.; Beljonne, D.; Cornil, J.; Janssen, R. A. J.; Meskers, S. C. J. *J. Phys. Chem. A* **2012**, *116* (30), 7927.
- (54) Smulders, M. M. J.; Nieuwenhuizen, M. M. L.; de Greef, T. F. A.; van der Schoot, P.; Schenning, A. P. H. J.; Meijer, E. W. *Chem. Eur. J.* **2010**, *16* (1), 362.
- (55) Klauk, H. *Chem. Soc. Rev.* **2010**, *39* (7), 2643.
- (56) J. Thorley, K.; Risko, C. *J. Mater. Chem. C* **2016**, *4* (17), 3825.

- (57) Rodriquez, D.; Savagatrup, S.; Valle, E.; Proctor, C. M.; McDowell, C.; Bazan, G. C.; Nguyen, T.-Q.; Lipomi, D. J. *ACS Appl. Mater. Interfaces* **2016**, 8 (18), 11649.
- (58) Cardinaletti, I.; Kesters, J.; Bertho, S.; Conings, B.; Piersimoni, F.; D'Haen, J.; Lutsen, L.; Nesladek, M.; Van Mele, B.; Van Assche, G.; Vandewal, K.; Salleo, A.; Vanderzande, D.; Maes, W.; Manca, J. V. *J. Photonics Energy* **2014**, 4 (1), 040997.
- (59) Wang, M.; Xie, F.; Du, J.; Tang, Q.; Zheng, S.; Miao, Q.; Chen, J.; Zhao, N.; Xu, J. B. *Sol. Energy Mater. Sol. Cells* **2011**, 95 (12), 3303.
- (60) Kim, C. S.; Tinker, L. L.; DiSalle, B. F.; Gomez, E. D.; Lee, S.; Bernhard, S.; Loo, Y.-L. *Adv. Mater.* **2009**, 21 (30), 3110.
- (61) P. Lyons, B.; Clarke, N.; Groves, C. *Energy Environ. Sci.* **2012**, 5 (6), 7657.



Chapter 5 Amorphous ternary energy cascade molecules for bulk heterojunction photovoltaics

Ternary bulk heterojunctions with cascade-type energy level configurations are of significant interest for further improving the power conversion efficiency of organic solar cells. However, controlling the self-assembly in solution-processed ternary blends remains a key challenge. Herein, we leverage the ability to control the crystallinity of molecular semiconductors via a Spiro-linker to demonstrate a simple strategy to induce the self-assembly of an ideal energy cascade morphology. Spiro-bifluorene (SF) derivatives with optimized energy levels from diketopyrrolopyrrole (DPP) or perylene diimide (PDI) components, coded as SF-(DPP)₄ and SF-(PDI)₄, are synthesized and investigated for application as ternary components in the host blend of P3HT:PCBM. Differential scanning calorimetry and x-ray/electron diffraction studies suggest that at low loadings (up to 5 wt%) the ternary component does not perturb the crystallization of the donor:acceptor host blend. In photovoltaic devices, up to 36 % improvement in power conversion is found when adding 1 wt% of either SF-(DPP)₄ or SF-(PDI)₄ and is attributed to an increase in fill factor and open circuit voltage, while at higher loadings PCE decreased due to lower short circuit current density. Comparing quantum efficiency measurements (where light absorption of the SF-(DPP)₄ was found to give up to 95 % internal conversion) suggests that improvement due to enhanced light absorption or to better exciton harvesting via resonance energy transfer are unlikely, supporting the conclusion that the SF-compounds are excluded to the donor:acceptor interface by crystallization of the host blend.

This chapter has been adapted from “Amorphous ternary energy cascade molecules for bulk heterojunction photovoltaics” (Jeanbourquin, X. A.; Rahmanudin, A.; Yu, X.; Johnson, M.; Guijarro, N.; Liang, Y.; Sivula, K., ACS Appl. Mater. Interfaces, 2017, under review)

5.1 Introduction

The use of a ternary BHJ (*e.g.* including a third active component in the donor:acceptor BHJ) has recently been established as a powerful approach to engineer high efficiency OPVs.^{3–6} Blending multiple donor molecules to extend the absorption spectrum^{7–10} or using additives to control morphology¹¹ or doping,¹² as well as a cascade strategy^{13–17} exemplify the advantages of ternary systems. Energy cascade ternaries, in particular, represent an elegant and versatile way to mitigate bimolecular recombination in OPVs. This approach consists of including a tertiary molecule with intermediate energy levels ideally at the interface between donor and acceptor domains so that free photogenerated holes and electrons accumulate on the donor and acceptor materials, respectively, and are spatially separated by the cascade molecule. Several reports even show the possibility to enlarge the exciton harvesting distance through long range energy transfer from the donor to the cascade material, provided that the donor has a larger band gap.^{9,18,19} These two considerations lead to well-known design rules for the energetics of cascade molecules: HOMO and LUMO energy levels must be in between those of the donor and acceptor while retaining a narrow absorption band gap. Molecules matching these properties have been successfully used in planar junction devices with the ternary compound selectively placed at the interface, reaching over 8 % PCE.¹⁸ In BHJ OPV, PCE over 11 % has been recently reported.²⁰

Despite these encouraging results, the relative improvement in performance when applying the ternary cascade approach to the BHJ remains inferior to the planar junction configuration in part due to the inherent morphological complexity of the BHJ active layer. Indeed, controlling the self-assembly of a ternary BHJ into the ideal cascade morphology—especially driving the cascade compound to the donor:acceptor interface—remains a key challenge. Concrete efforts to prepare ternary blends with one component at the interface of the other two have been reported by Honda et al. using a silicon phthalocyanine derivative in a P3HT:PCBM host blend.²¹ The self-assembly of that system was later ascribed to surface energy differences in between the three materials,²² which limits the chemical nature of the cascade material. Moreover, engineering surface energies in the BHJ blend remains non-trivial. Alternatively, Gu et al. have recently reported the formation of a multi-length-scale ternary morphology attributed to crystallization of P3HT, allowing the formation of two distinct donor phases working as sub-cells in parallel.²³ Even though this system does not form an ideal cascade structure, the use of the host blend crystallization as a driving force for the self-assembly is a promising and simple strategy to engineer ternary morphology. Inspired by recent work employing a spiro linker^{24–26} to control the 3D self-assembly and crystallinity in materials for organic electronics, herein we

demonstrate that controlling crystallinity can be used for efficient self-assembly of cascade BHJ towards formation of an ideal cascade structure. Specifically by using an non-crystalline “amorphous” cascade molecule as the ternary component and by tuning the crystallinity of the electron donor and acceptor phases thereby driving ternary molecule to the interface leads to a maximum 36 % improvement in PCE of a P3HT:PCBM solar cell.

5.2 Results and discussion

5.2.1 Optoelectronic and packing properties of the ternary molecules

In order to demonstrate the self-assembly of an ideal cascade morphology using an amorphous ternary additive, two molecules (**Figure 5-1**) were synthesized *via* the Suzuki coupling reaction between functionalized conjugated aryl groups and a spiro-core. The spiro-core is chosen to discourage long-range pi-pi stacking in the material, while perylene diimide derivative, commonly coded as PDI, and a diketopyrrolopyrrole derivative, coded as DPP, are used as aryl groups, in order to tune the energy levels of the molecule. The PDI aryl group yields the molecule here coded as SF-(PDI)₄, which was recently reported as an electron acceptor for OPV^{25,26} and alternatively coupling the DPP yields a novel molecule coded SF-(DPP)₄. Full synthetic information are given in appendix C. Electrochemical properties of both molecules were measured by CV in order to position their respective HOMO levels. As it can be seen on **Figure 5-1d**, two irreversible oxidation waves at -5.4 eV and -6.0 eV *vs* vacuum are present for SF-(DPP)₄ and SF-(PDI)₄ respectively, which we attributed to the HOMO levels of the molecules. The LUMO position was then inferred from the optical properties of both molecules measured by UV-vis spectroscopy (**Figure 5-1e**). The bandgap for SF-(DPP)₄ and SF-(PDI)₄, estimated from onset absorption, are found to be 1.7 eV and 2.05 eV respectively. Energy levels are summarized in **Figure 5-1c** together with the host blend components. The optoelectronic properties of SF-(DPP)₄ and SF-(PDI)₄ are similar to those reported for parent DPP(TBFu)₂ and PDI derivatives^{27,28} supporting the notion that the band gap and energy levels of the overall spiro molecule can be effectively engineered by varying the aryl groups. It can be seen that the P3HT:PCBM system accommodates well both spiro derivatives as potential cascade molecules given their intermediate highest occupied and lowest unoccupied molecular orbital (HOMO and LUMO respectively) energy levels. Therefore, this classic system was chosen as the host blend to test our new ternary materials.

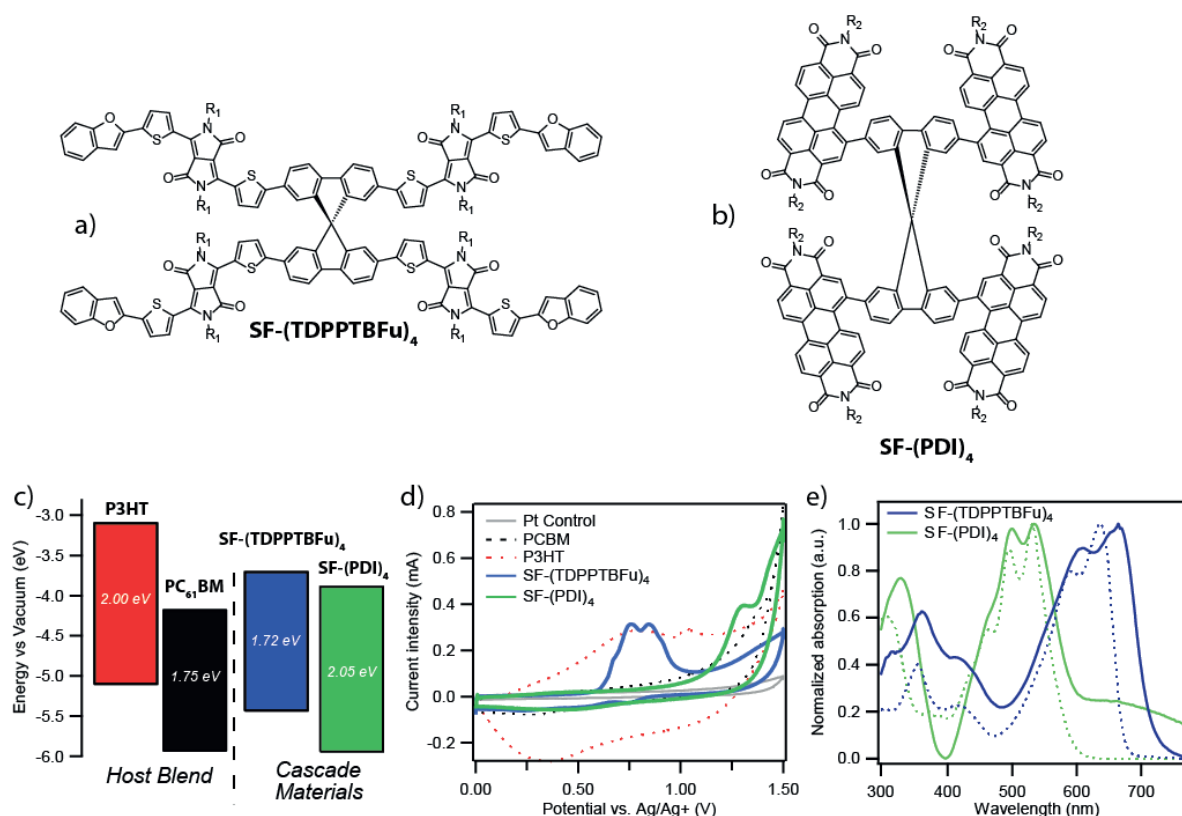


Figure 5-1. Chemical structure of the ternary small molecules used in this work (a) $SF-(DPP)_{4}$ with $R_1 = 2$ -ethylhexyl and (b) $SF-(PDI)_{4}$ with $R_2 = 2$ -hexyldecyl. (c) Energy levels and band gap of the active molecules used in this work. (d) cyclic voltammetry of drop casted films over a platinum working electrode. (e) UV-vis absorption spectra of $SF-(DPP)_{4}$ and $SF-(PDI)_{4}$ in $CHCl_3$ (dotted lines) and in solid-state thin films (solid lines).

DSC measurements of pure $SF-(DPP)_{4}$ and $SF-(PDI)_{4}$ did not exhibit any indication of crystallinity. In the thermograms of the pure materials (**Figure 5-2a**) no particular melting or crystallization peaks are seen, strongly suggesting that both compounds lack crystalline ordering in the solid-state. This is supported by GIXRD data measured on spin-coated films (**Figure 5-2b**) where no out-of-plane diffraction peak can be seen for either molecules.

5.2.2 Exclusion of ternary molecules from crystalline phases

In order to examine the mixing behavior of the spiro derivatives in the presence of P3HT and PCBM, DSC measurements of pure P3HT or PCBM as well as blends with 10 or 25 wt% of either ternary component were performed. The (second) heating scans are shown in **Figure 5-3a** with the solid and broken lines, respectively representing the addition of $SF-(DPP)_{4}$ and $SF-(PDI)_{4}$. It can be seen that pure P3HT (red trace) exhibits an endothermic melting transition at *ca.* 234 °C. This peak remains

present after addition of either spiro additive up to 25 wt%. A sharp endothermic (melting) transition is also seen for pure PCBM (black trace) at *ca.* 282 °C. Similarly to the P3HT, the addition of SF-(PDI)₄ does not significantly affect the melting transition of PCBM. However, when blending the SF-(DPP)₄, the PCBM melting transition strongly decreases in intensity and melting temperature (down to 266 °C for 25 wt%). Interestingly, a small exothermic transition appears at *ca.* 182 °C which likely originates from the crystallization of a kinetically frustrated mixture created during cooling of the melt.

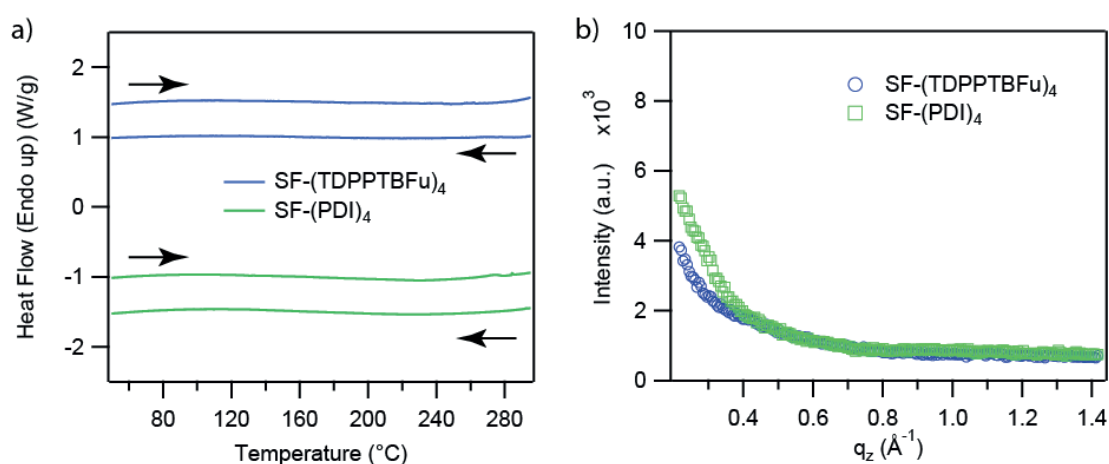


Figure 5-2. (a) differential scanning calorimetry second heating and cooling curves of drop casted SF-(DPP)₄ and SF-(PDI)₄ from dichlorobenzene at 80 °C with a scan rate of 10 °C min⁻¹. Black arrows indicate scan direction. (b) Out-of-plane grazing incident wide angle X-ray diffraction of neat SF-(DPP)₄ and SF-(PDI)₄ thin films.

The melting enthalpy extracted from the DSC data allows the estimation of the relative crystallinity of the donor or acceptor component in the blends with the ternary component (**Figure 5-3b**).²⁹ In the case of P3HT, the relative crystallinity only slightly decreases upon addition of both additives and never drops below 95 %, supporting the notion that SF-(DPP)₄ and SF-(PDI)₄ do not disrupt significantly the crystallinity of P3HT and are excluded from the pristine crystalline P3HT domains. In contrast, the PCBM shows a significant decrease in relative crystallinity with about 38 % loss when 25 wt% of the SF-(DPP)₄ additive is included. This suggests that the additive mixes with the PCBM and limits its crystallization to some extent. Nonetheless we note that at 1 wt% of the additive the relative PCBM crystallinity remains 94 %. On the other hand, the PCBM phase exhibits a relative

crystallinity higher than 88 % at 25 wt% SF-(PDI)₄ content, suggesting this additive mixes less with the PCBM.

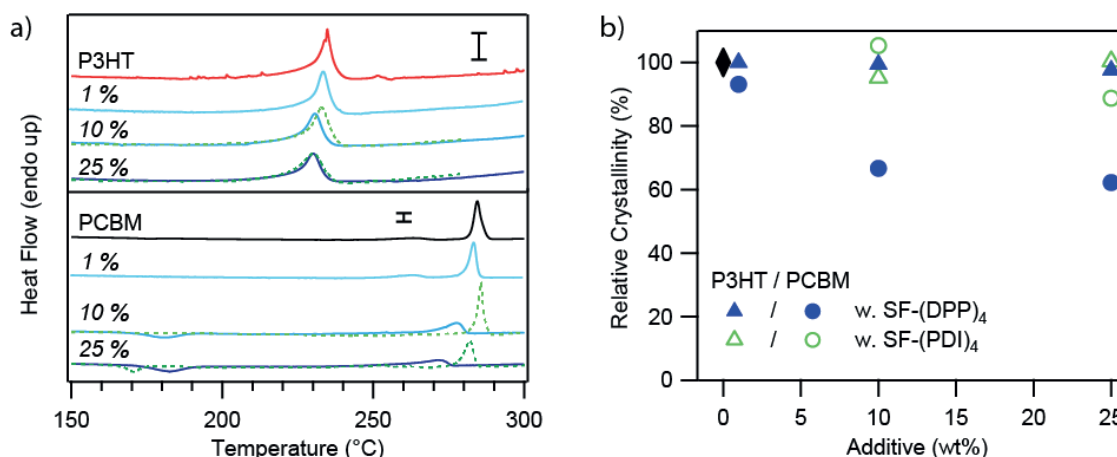


Figure 5-3. (a) differential scanning calorimetry second heating curves of neat P3HT, neat PCBM and with varying amount of SF-(DPP)₄ (solid lines) and SF-(PDI)₄ (dotted lines). Scale bars represent 0.2 mW g⁻¹. (b) relative crystallinity (based on melting enthalpies) of PCBM (dots) and P3HT (triangles) as a function of additive content.

While the melting transition behavior gives an indication of the mixing of the additives with host donor and acceptor in the solid-state, the DSC measurement conditions are significantly different than the conditions that occur during solution processing the BHJ into a thin film. Thus, further investigation over the crystallinity of P3HT or PCBM blended with one of the additives, SF-(DPP)₄, in thin films spin casted from dichlorobenzene and annealed at 140 °C for 10 min were performed using GIXRD (out-of-plane) and electron diffraction, respectively, to assess the crystallinity of P3HT and PCBM (see appendix, Figure C-1 and Figure C-2). The FWHM (**Figure 5-4**) of the diffraction peaks is well-known to be inversely proportional to crystallite size and quality in paracrystalline materials according to Scherrer's equation (see section 2.3.3).^{30,31} Pristine P3HT is found to have a FWHM of *ca.* 0.55 nm⁻¹ corresponding to a crystal coherence length (CCL) of 11.4 nm. Further addition of SF-(DPP)₄ does not significantly affect the FWHM for P3HT, as blend of 25 wt% SF-(DPP)₄ still exhibits a FWHM of *ca.* 0.56 nm⁻¹. In the case of pristine PCBM, a much larger FWHM of 3.52 nm⁻¹ is calculated, as expected from its lower crystallinity. Upon addition of 1, 10 and 25 wt% SF-(DPP)₄,

the FWHM increases only slightly to *ca.* 3.71, 3.81, 4.18 nm⁻¹ respectively, which is in good agreement with the aforementioned DSC results and supports the view that the SF-(DPP)₄ additive does not form a co-crystal with the P3HT or PCBM nor does it significantly affect the crystallinity of the pure donor and acceptor components. We note that no meaningful CCL can be extracted for FWHM data from the electron diffraction of PCBM.³²

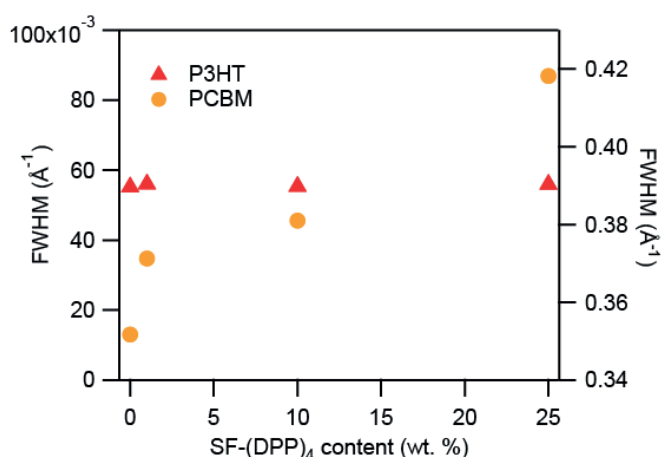


Figure 5-4. Full width at half maximum of PCBM (right axis) and P3HT (left axis) diffraction peaks as a function of SF-(DPP)₄ content.

5.2.3 Effect of the ternary molecules in OPV

The application of the ternary additives in BHJ OPV devices was next investigated in optimized P3HT:PCBM host blend BHJs. We note that the PCE observed at the optimized 6:4 ratio (see appendix, Figure C-3) under the best conditions without any ternary additive (*ca.* 2.5 %) is slightly lower than the average PCE reported of 3.0 %³³ due to the relatively large device area used (0.16 cm²) and the fact that PC₇₁BM and Ca (as a cathode interlayer) were not employed in this study. We also established that, upon addition of 5 wt% SF-(DPP)₄ to the host blend, no change in optimal P3HT:PCBM blending ratio was found (see appendix, Figure C-4). Atomic force microscopy height images of film surface, shown in appendix Figure C-5, further confirm that the bulk heterojunction morphology remains largely unaffected by addition of SF-(DPP)₄.

The effect of varying the content of SF-(DPP)₄ or SF-(PDI)₄ on the performance was then investigated by fabricating devices containing 0, 1, 2.5, 5 and 10 wt% of the ternary additive. The device figures of merit (averaged over at least 4 different devices) are plotted on **Figure 5-5** as a function of additive

concentration with the corresponding J-V curves. It can be seen that addition of 1 wt% SF-(DPP)₄ results in an increased PCE up to 3.2 % compared to the 2.5 % of the control blend (about 28 % improvement). This increase can be mainly attributed to the enhancement in fill factor (FF) (14 %), which improves from 0.43 to 0.49 upon SF-(DPP)₄ addition. The open circuit voltage (V_{OC}) also increases by 20 mV. Taken together, the V_{OC} and FF improvements suggest a reduced recombination within the BHJ. Partially due to the extended absorption spectrum of the SF-(DPP)₄ compared to the host blend, a slight improvement in short circuit current (J_{SC}) is also observed. Further addition of SF-(DPP)₄ seems to deteriorate the device performance as both J_{SC} and FF decrease. In contrast, the V_{OC} continues to improve gradually from 0.52 V up to 0.67 V upon addition of SF-(DPP)₄ up to 10 wt%. Similar enhancement in V_{OC} for ternary devices has been attributed to the additional density of states³⁴ as well as alloy formation,^{35,36} however these studies have only been demonstrated on miscible ternary blends, which is not the case of SF-(DPP)₄ reported here (as demonstrated by the DSC results). Rather the improvement in V_{OC} in our case could result from either a doping effect or mitigated recombination at open circuit and will be further discussed thereafter.

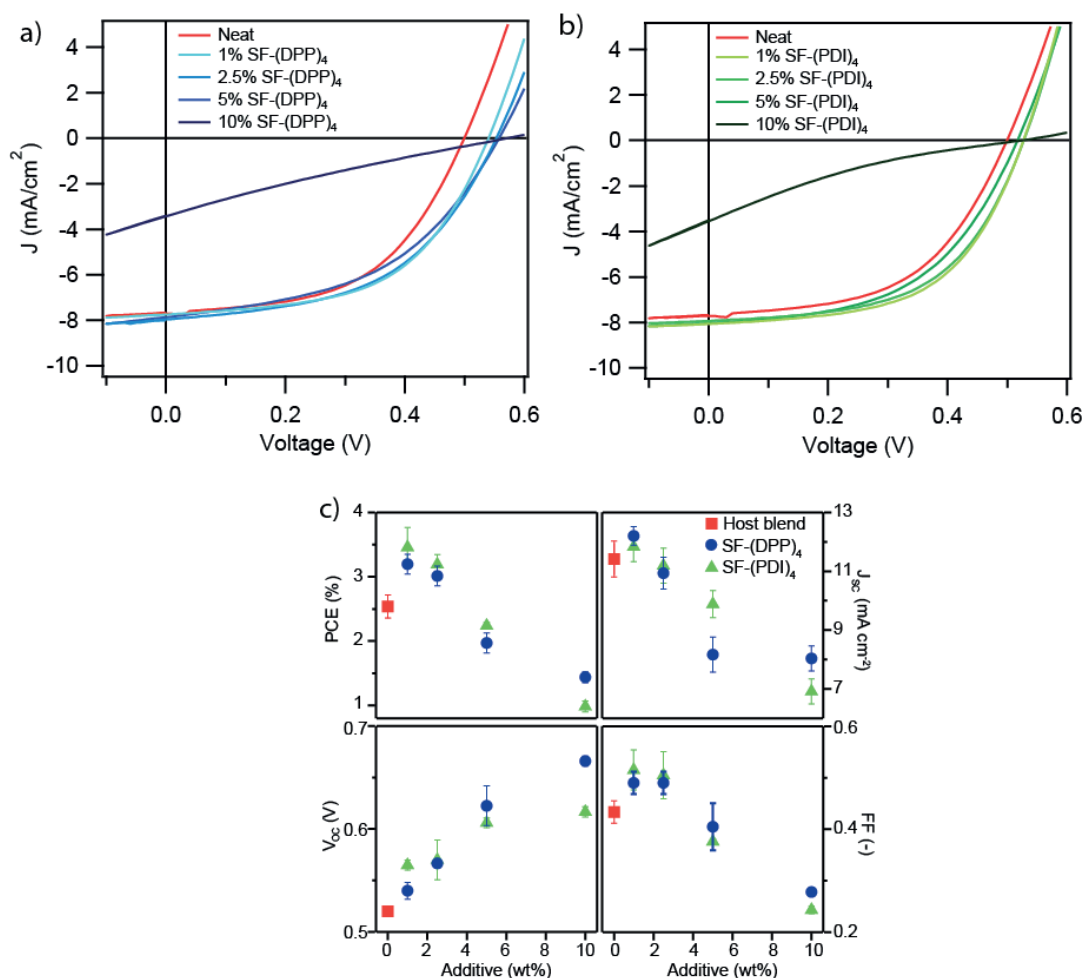


Figure 5-5. Photovoltaic device performance with added amorphous cascade molecules. (a) and (b) shows typical J - V curves with varying amount of SF-(DPP)₄ and SF-(PDI)₄, respectively. (c) average figures of merit (PCE, J_{sc} , V_{oc} and FF) as a function of SF-(DPP)₄ (blue) and SF-(PDI)₄ (green) content in P3HT:PCBM BHJ OPVs.

The SF-(PDI)₄ additive exhibits a very similar performance trend to SF-(DPP)₄, with a 36 % improvement in PCE at 1 wt% (due to increases in V_{oc} and FF) reaching an efficiency of *ca.* 3.5 %. Since SF-(PDI)₄ also improves the J_{sc} (to a lesser extent than SF-(DPP)₄) this suggests that the extended absorption spectrum is not the main origin for the device improvement. At higher content than 1 wt% of SF-(PDI)₄, except for the enhancement in V_{oc} , all the figures of merit are seen to decrease, similarly to SF-(DPP)₄. Taken together, the higher PCE for the SF-(PDI)₄ additive at 1 wt% as compared to SF-(DPP)₄ at the same concentration supports the conclusion that the role of extended absorption as well as any possible extended exciton harvesting distance in the SF-(DPP)₄ system are negligible. This is plausible given the intrinsic low optimum concentration of the additive and already optimized

morphology. In stark contrast, the addition of 9,9'-spirobifluorene (the unfunctionalized spiro-core molecule, with $E_g = 3.8$ eV) results in a loss in PCE at 1 wt% further supporting the cascade mechanism (see appendix, Figure C-6).

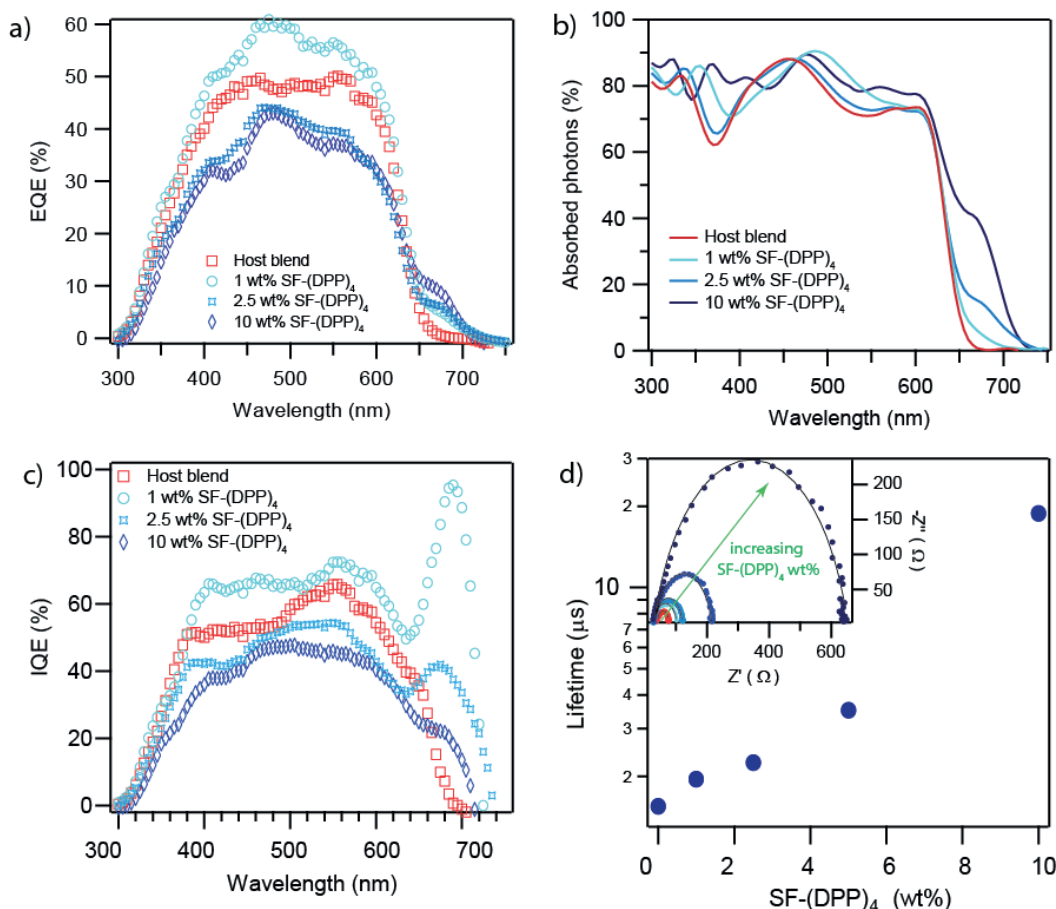


Figure 5-6. (a) External and (c) internal quantum efficiency of the host blend and containing 1, 2.5 and 10 wt% SF-(DPP)₄. (b) shows the corresponding UV-vis data. (d) recombination lifetime obtained from fitting (solid lines, inset) the impedance spectroscopy response (dots, inset) at open circuit under 1 sun for increasing content of SF-(DPP)₄ (0, 1, 2.5, 5, 10 wt%).

5.2.4 Confirming the ideal self-assembly

In order to gain further insight into the working mechanism the amorphous cascade additives, we next focused in detail on the effect of the SF-(DPP)₄ additive by estimating the internal quantum efficiency

(IQE) (**Figure 5-6c**) from external quantum efficiency and absorption data (**Figure 5-6a** and **b**). The host blend device exhibits IQE values close to 60 % (square markers in **Figure 5-6c**) in line with previous reports.³⁷ Adding 1 wt% SF-(DPP)₄ gives higher IQE values over the entire absorption range correlating well with the observed enhancement in J_{SC} (circle markers in **Figure 5-6c**). Strikingly, the photons absorbed by the SF-(DPP)₄ at 685 nm reach an IQE of 95 %, suggesting that essentially all excitons generated within SF-(DPP)₄ molecules are efficiently dissociated into free charge carriers and collected. This strongly supports the argument that SF-(DPP)₄ successfully self-assembles at the interface between P3HT and PCBM molecules, either in between crystalline domains or within amorphous domains, leading to an ideal cascade morphology. Further addition of SF-(DPP)₄ leads to an overall decrease in IQE, accounting for the loss in J_{SC} . It is worth noting that the IQE at 685 nm decreases significantly more than IQE within the P3HT absorption region, which translates into a loss in exciton splitting efficiency within the SF-(DPP)₄ phase. This loss could be attributed to SF-(DPP)₄ domains growing larger than exciton the diffusion length. However, one might also consider that the disrupted crystallinity of PCBM at high SF-(DPP)₄ content, as seen from DSC data, could account for a PCBM amorphous rich region at the interface, surrounding SF-(DPP)₄ molecules which leads to hole trapping state formation.

Charge carrier lifetimes were extracted from impedance spectroscopy (IS) data under 1 sun illumination at open circuit as this technique is well-known to provide useful insight into recombination losses.³⁸ The impedance response of the devices (see Nyquist plots inset **Figure 5-6b**) always exhibited a single semicircle at low frequency which was fit using a simple constant phase element (CPE) parallel to a resistance (R_{rec}). The latter, R_{rec} , which can be associated to the electrical resistance through recombination channels, is found to increase by more than one order of magnitude with addition of SF-(DPP)₄ (see appendix, Figure C-7). This supports the view that the recombination rate decreases in the presence of the amorphous cascade additive at the interface of the P3HT and PCBM. The trend in recombination life-time, shown in **Figure 5-6b** as a function of additive concentration, indicates a longer free charge carrier lifetime with increasing SF-(DPP)₄, and confirms that recombination is mitigated in presence of the ternary additive.

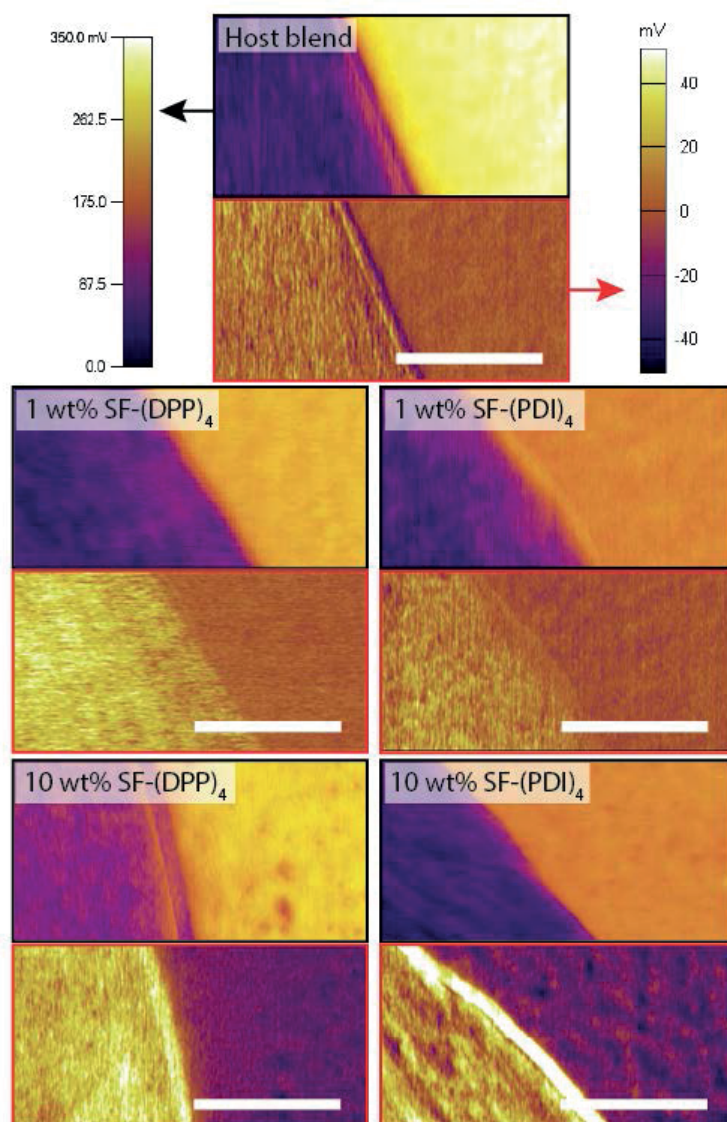


Figure 5-7. Kelvin probe force microscopy images of thermally-driven phase segregated sample measured at domains interface with varying amount of additives. Top images (black) shows KPFM measured under dark conditions while bottom images (red) shows surface photovoltage built-up images obtained by subtracting KPFM under light and dark conditions. Scale bar 2 μm .

Surface photovoltage built-up images, shown in **Figure 5-7**, further supports a mitigated recombination. Samples were thermally annealed at 150 $^{\circ}\text{C}$ for 5h to drive large scale phase segregation in order to have well distinct PCBM and P3HT phases. The phase exhibiting larger work function in dark condition (yellow phase, top images) can be attributed to PCBM due to its deeper HOMO level (phase on the right of the image). Consequently, P3HT should have lower work function and hence lower V_{CPD} which corresponds to the phase on the left of the images. While no major change in V_{CPD} can

be seen in the dark upon varying the additive content, the photovoltage built-up strongly increases with addition of either additive. Indeed, at 10 wt% additive content, work function of the P3HT region significantly increases while the work function of PCBM decreases under illumination. This clearly indicates accumulation of respectively holes and electrons on the PCBM and P3HT phases. In perspective, the host blend shows almost no photovoltage built-up, which confirms the cascade mechanism.

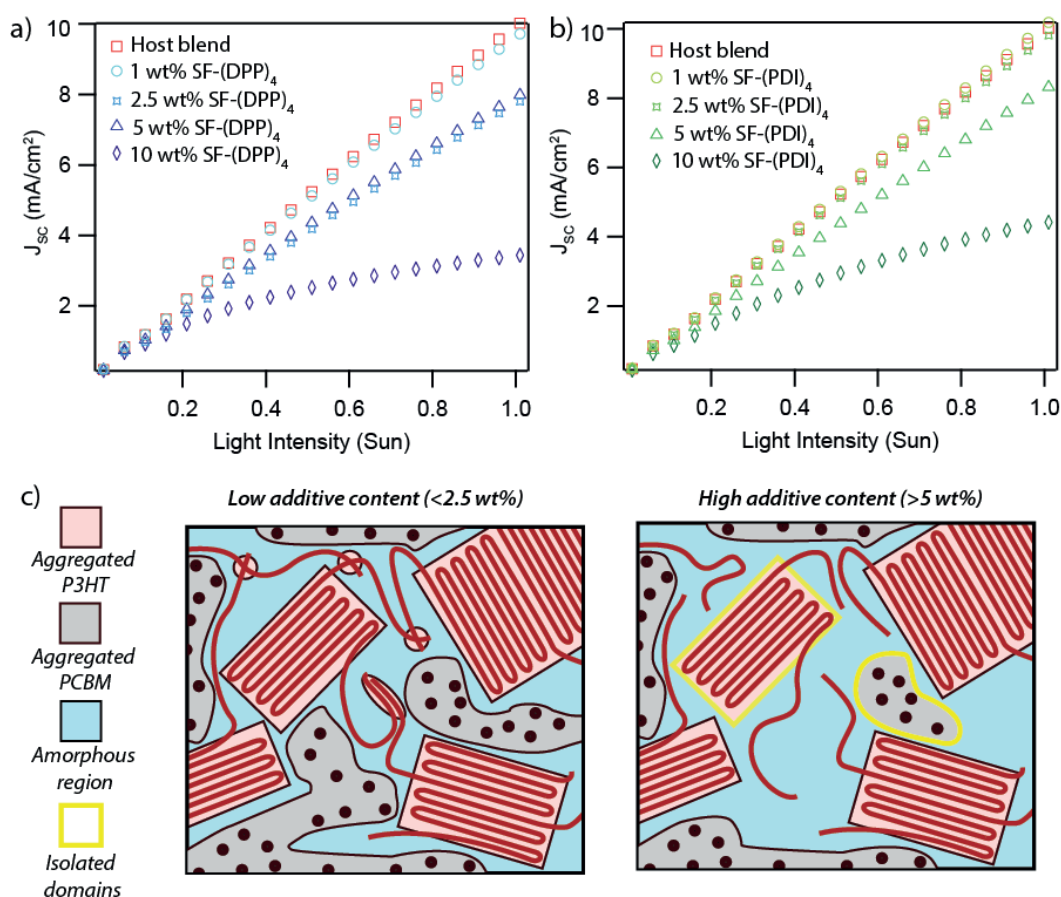


Figure 5-8. (a, b) Short circuit current as function of light intensity expressed in sun ($1 \text{ sun} = 100 \text{ W cm}^{-2}$) for varying loadings of either additives. (c) Schematic depicting limitations of this approach due to isolation of crystalline domains in the BHJ.

Interestingly, lifetimes (**Figure 5-6d**) are especially longer at high loadings (*e.g.* 5 and 10 wt%), despite their poor J-V performances. Actually, 5 and 10 wt% SF-(DPP)₄ or SF-(PDI)₄ devices both exhibit a sublinear dependence of the J_{sc} as a function of incident illumination intensity as seen on **Figure 5-8a** and **b**, which is typically characteristic of high recombination.³⁹ However, the aforementioned considerable increase in recombination lifetimes at higher loadings contrasts with this possibility. Rather, this sublinear behavior and loss in performance could reasonably be caused by the formation of a space charge layer,⁴⁰ or, less likely at open circuit, poor transport. Under the assumption that the amorphous additive is excluded from both the donor and acceptor phases at all loading concentrations, upon increasing the loading there reasonably must exist a loading limit above which amorphous region generated by the spiro additive would isolate some donor or acceptors domains, breaking down the percolation pathways and favoring the formation of a space charge layer within the BHJ (since isolated donor or acceptor domains will accumulate free charges upon light illumination) and deteriorating the transport. Such possibility is illustrated in **Figure 5-8c**. While the morphological verification of this condition is complicated by the optimal donor:acceptor domain size present in P3HT:PCBM BHJs (*ca.* 20 nm) and the similar chemical nature of the components, the experimentally demonstrated decrease in the OPV device performance at higher loadings reasonably demonstrates this fundamental drawback of the amorphous ternary cascade approach. Despite this, the increased performance of the control BHJ upon optimized loading of the amorphous ternary cascade molecules, observed in this work, gives promise for this approach to enhance the performance of high performance OPVs based on semi-crystalline materials.

5.3 Conclusions

In conclusion, in this work we have combined the aspects of the exclusion of an amorphous ternary additive from a crystalline donor:acceptor blend for BHJ OPVs with the energy cascade approach to establish a proof-of-concept of the amorphous ternary cascade approach. By employing DPP and PDI chromophores with the ideal energy levels to enhance the electron and hole separation in a P3HT:PCBM BHJ OPV and controlling the chromophore mixing with the P3HT and PCBM by using a spiro linking strategy, we demonstrated the successful exclusion of the ternary additives from the host blend using DSC and crystal domain size results. At optimized ternary loadings (*e.g.* 1 wt%) an improvement of up to 36 % relative to the host blend (from a PCE of 2.5 % to 3.5%) was found with the SF-(PDI)₄ additive while a similar improvement (28%) was also observed with the SF-(DPP)₄ additive. The change in the device performance metrics upon additive inclusion together with the

different UV-vis absorption properties of the two additive molecules and the quantum efficiency measures (which showed an impressive 95% IQE of the SF-(DPP)₄ in optimized blends) indicated that the improvement was not due to increased light absorption or by increasing the exciton harvesting distance through FRET. Further investigation by impedance spectroscopy supported the view that the improvement was due to a lower recombination within the active layer at optimized conditions, while at high additive loading (e.g. 5-10 wt%) a decrease in performance was reasonably attributed to formation of a space charge layer likely caused by the isolation of crystalline P3HT or PCBM domains by the ternary compound. The promising performance demonstrated and the simplicity of the strategy demonstrated herein could likely be extended to high efficiency paracrystalline blends to further increase the PCE without requiring a complex optimization, assuming that the segregation and interfacial properties are similar to the P3HT:PCBM system.

5.4 References

- (1) Zhao, W.; Li, S.; Zhang, S.; Liu, X.; Hou, J. *Adv. Mater.* **2017**, 29 (2), 1604059.
- (2) Kang, H.; Kim, G.; Kim, J.; Kwon, S.; Kim, H.; Lee, K. *Adv. Mater.* **2016**, 28 (36), 7821.
- (3) Lu, L.; Kelly, M. A.; You, W.; Yu, L. *Nat. Photonics* **2015**, 9 (8), 491.
- (4) Goubard, F.; Wantz, G. *Polym. Int.* **2014**, 63 (8), 1362.
- (5) Savoie, B. M.; Dunaisky, S.; Marks, T. J.; Ratner, M. A. *Adv. Energy Mater.* **2015**, 5 (3), 1400891.
- (6) Lu, L.; Chen, W.; Xu, T.; Yu, L. *Nat. Commun.* **2015**, 6, 7327.
- (7) Lim, B.; Bloking, J. T.; Ponec, A.; McGehee, M. D.; Sellinger, A. *ACS Appl. Mater. Interfaces* **2014**, 6 (9), 6905.
- (8) Yang, Y. (Michael); Chen, W.; Dou, L.; Chang, W.-H.; Duan, H.-S.; Bob, B.; Li, G.; Yang, Y. *Nat. Photonics* **2015**, 9 (3), 190.
- (9) Bi, P.-Q.; Wu, B.; Zheng, F.; Xu, W.-L.; Yang, X.-Y.; Feng, L.; Zhu, F.; Hao, X.-T. *ACS Appl. Mater. Interfaces* **2016**, 8 (35), 23212.
- (10) Barito, A.; Sykes, M. E.; Huang, B.; Bilby, D.; Frieberg, B.; Kim, J.; Green, P. F.; Shtein, M. *Adv. Energy Mater.* **2014**, 4 (13), 1400216.
- (11) Gasperini, A.; Jeanbourquin, X. A.; Rahmanudin, A.; Yu, X.; Sivula, K. *Adv. Mater.* **2015**, 27 (37), 5541.
- (12) Liu, C.; Jang, J.; Xu, Y.; Kim, H.-J.; Khim, D.; Park, W.-T.; Noh, Y.-Y.; Kim, J.-J. *Adv. Funct. Mater.* **2015**, 25 (5), 758.
- (13) Lu, L.; Xu, T.; Chen, W.; Landry, E. S.; Yu, L. *Nat. Photonics* **2014**, 8 (9), 716.
- (14) Zhang, Y.; Deng, D.; Lu, K.; Zhang, J.; Xia, B.; Zhao, Y.; Fang, J.; Wei, Z. *Adv. Mater.* **2015**, 27 (6), 1071.
- (15) Kipp, D.; Ganesan, V. *Macromolecules* **2016**, 49 (14), 5137.
- (16) Chen, M. C.; Liaw, D. J.; Huang, Y. C.; Wu, H. Y.; Tai, Y. *Sol. Energy Mater. Sol. Cells* **2011**, 95 (9), 2621.
- (17) Chen, M.-C.; Kar, S.; Liaw, D.-J.; Chen, W.-H.; Huang, Y.-C.; Tai, Y. *Org. Electron.* **2012**, 13 (11), 2702.

- (18) Cnops, K.; Rand, B. P.; Cheyins, D.; Verreert, B.; Empl, M. A.; Heremans, P. *Nat. Commun.* **2014**, *5*.
- (19) Zhao, F.; Li, Y.; Wang, Z.; Yang, Y.; Wang, Z.; He, G.; Zhang, J.; Jiang, L.; Wang, T.; Wei, Z.; Ma, W.; Li, B.; Xia, A.; Li, Y.; Wang, C. *Adv. Energy Mater.* **2017**, *7*, 1602552.
- (20) Nian, L.; Gao, K.; Liu, F.; Kan, Y.; Jiang, X.; Liu, L.; Xie, Z.; Peng, X.; Russell, T. P.; Ma, Y. *Adv. Mater.* **2016**, *28* (37), 8184.
- (21) Honda, S.; Nogami, T.; Ohkita, H.; Benten, H.; Ito, S. *ACS Appl. Mater. Interfaces* **2009**, *1* (4), 804.
- (22) Honda, S.; Ohkita, H.; Benten, H.; Ito, S. *Adv. Energy Mater.* **2011**, *1* (4), 588.
- (23) Gu, Y.; Wang, C.; Liu, F.; Chen, J.; E. Dyck, O.; Duscher, G.; P. Russell, T. *Energy Environ. Sci.* **2014**, *7* (11), 3782.
- (24) Li, S.; Liu, W.; Shi, M.; Mai, J.; Lau, T.-K.; Wan, J.; Lu, X.; Li, C.-Z.; Chen, H. *Energy Environ. Sci.* **2016**, *9* (2), 604.
- (25) Yi, J.; Wang, Y.; Luo, Q.; Lin, Y.; Tan, H.; Wang, H.; Ma, C.-Q. *Chem. Commun.* **2016**, *52* (8), 1649.
- (26) Lee, J.; Singh, R.; Sin, D. H.; Kim, H. G.; Song, K. C.; Cho, K. *Adv. Mater.* **2016**, *28* (1), 69.
- (27) Walker, B.; Tamayo, A. B.; Dang, X.-D.; Zalar, P.; Seo, J. H.; Garcia, A.; Tantiwiwat, M.; Nguyen, T.-Q. *Adv. Funct. Mater.* **2009**, *19* (19), 3063.
- (28) Sharenko, A.; Proctor, C. M.; van der Poll, T. S.; Henson, Z. B.; Nguyen, T.-Q.; Bazan, G. C. *Adv. Mater.* **2013**, *25* (32), 4403.
- (29) Chen, H.-L.; Hwang, J. C. *Polymer* **1995**, *36* (22), 4355.
- (30) Lilliu, S.; Agostinelli, T.; Pires, E.; Hampton, M.; Nelson, J.; Macdonald, J. E. *Macromolecules* **2011**, *44* (8), 2725.
- (31) Verploegen, E.; Mondal, R.; Bettinger, C. J.; Sok, S.; Toney, M. F.; Bao, Z. *Adv. Funct. Mater.* **2010**, *20* (20), 3519.
- (32) Berry, C. R. *Phys. Rev.* **1952**, *88* (3), 596.
- (33) Dang, M. T.; Hirsch, L.; Wantz, G. *Adv. Mater.* **2011**, *23* (31), 3597.
- (34) Felekidis, N.; Wang, E.; Kemerink, M. *Energy Environ. Sci.* **2016**, *9* (1), 257.
- (35) Street, R. A.; Davies, D.; Khlyabich, P. P.; Burkhart, B.; Thompson, B. C. *J. Am. Chem. Soc.* **2013**, *135* (3), 986.
- (36) Khlyabich, P. P.; Rudenko, A. E.; Thompson, B. C.; Loo, Y.-L. *Adv. Funct. Mater.* **2015**, *25* (34), 5557.
- (37) Yoshida, K.; Oku, T.; Suzuki, A.; Akiyama, T.; Yamasaki, Y. *Mater. Sci. Appl.* **2013**, *04* (04), 1.
- (38) Leever, B. J.; Bailey, C. A.; Marks, T. J.; Hersam, M. C.; Durstock, M. F. *Adv. Energy Mater.* **2012**, *2* (1), 120.
- (39) Marsh, R. A.; Groves, C.; Greenham, N. C.; *J. Appl. Phys.* **2007**, *101* (8), 083509.
- (40) Koster, L. J. A.; Mihailetschi, V. D.; Xie, H.; Blom, P. W. M. *Appl. Phys. Lett.* **2005**, *87* (20), 203502.



Chapter 6 Effect of molecular weight in diketopyrrolopyrrole-based and thienothiophene-based polymers for photovoltaic applications

Controlling the supramolecular self-assembly of organic molecules has been challenging the scientific community for decades. Indeed, the complex interplay of physical parameters governing this self-assembly confound a universal understanding, even more for BHJ.

In polymers, the intrinsic molecular weight distribution is known to strongly affect the macromolecular assembly. Herein, we investigate the effect of M_n on the performances of OPV devices containing a DPP-based polymer (PDPP4T-TT) or PBTTT polymer as donor and PCBM as acceptor. Using GPC fractionation, well defined polymer chain length with narrow polydispersity are obtained. PDPP4T-TT based solar cells are found to have an optimum PCE at high M_n , attributed to the change in solubility which affects the BHJ morphology during the initial casting of the active layer. In stark contrast, PBTTT based devices are found to reach an optimum performance at a medium M_n of 35 kDa, in agreement with a self-assembly very similar to that of the neat PBTTT. Overall, this chapter highlights the role of these two polymers M_n on the self-assembly of the active BHJ layer and the performances in OPV.

*This chapter was adapted from “Effect of Molecular Weight in Diketopyrrolopyrrole-Based Polymers in transistor and Photovoltaic Applications”, Gasperini, A.; Jeanbourquin, X. A.; Sivula, K., J. Polym. Sci., Part B: Polym. Phys. **2016**, 54, 2245–2253*

6.1 Introduction

In addition to cascade mechanism presented in the last chapter, molecular engineering has been widely used to enhance the PCE of organic solar cells. In that perspective, the donor-acceptor “push-pull” alternating co-polymer strategy has recently expanded the number of polymer structures giving outstanding performance in OPV. Copolymers based on diketopyrrolopyrroles^{1,2}, carbazoles³, indacenodithiophene^{4,5} and isoindigo⁶ acceptor moieties can be straightforwardly polymerized with donor groups (*e.g.* thiophene or benzothiadiazole) using step-growth polymerization chemistry based on robust carbon-carbon cross coupling reactions (*e.g.* Stille or Suzuki reactions). Interestingly, this new generation of semiconducting polymers often lacks the significant long-range solid-state crystallinity (based on π -stacking interactions) well-known in “first generation” model semiconducting polymers like regioregular P3HT⁷ and PBTTT⁸. An increased backbone rigidity has been identified as a reasonable explanation for superior semiconducting performance despite the lack of crystallinity.⁹ Indeed, recent studies on this new class of polymers suggest that in absence of extended π -stacking motifs in the solid-state, charge transport occurs mostly uni-dimensionally along the highly rigid conjugated backbone with occasional intermolecular hopping through sparse π -linkages present in stacked aggregates.^{9,10} This charge transport mechanism implies a significant importance of the effect of polymer chain length (as characterized by the polymer chain number average molecular weight, M_n) on the semiconducting performances. However, the study of the effect of polymer molecular weight and molecular weight distribution (or molar-mass dispersity, D_M) is confounded by the step-growth polymerization techniques used to prepare the materials, which lead to variable molecular weight and D_M often over 2 implying a wide variation of chain lengths in a single polymer sample.

Indeed while much is now known regarding the effects of M_n and D_M on the archetypal P3HT^{11,12} and PBTTT,^{13,14} much less is known about the new class of polymers synthesized using step-growth techniques. A few studies have recently suggested a strong link between M_n and device performance.^{15–20} However, the high D_M and relatively low range of molecular weights investigated in these works (Typically up to an M_n of about 50 to 80 kDa) renders precise conclusions on the effects of M_n and D_M weaker due to the considerable overlap among each MW distributions. Moreover it is not known whether the effects of chain entanglement^{13,21} are important for the highest molecular weight chains. In this respect, systematic studies like reported for OPV-based P3HT²² are needed to better elucidate the effects of M_n and D_M on the photovoltaic performance of this new class of donor-acceptor step-growth polymers.

In this work, we employ standard Stille coupling polymerizations and the subsequent fractionation by preparative GPC to precisely characterize the effect of M_n on the performance of a diketopyrrolopyrrole-thienothiophene copolymers, coded PDPP4T-TT, based solar cells using PCBM as an electron acceptor. We isolate fractions ranging from M_n of 6 kDa to 80 kDa with extremely low polydispersity ($\bar{D}_M < 1.3$) and characterize the OPV figures of merits and thin film molecular packing behaviour as function of M_n . Additionally, we extend our investigation into the effect of M_n on PBTTT when used as donor in BHJ photovoltaic devices. This approach highlights the stark difference in optimal supramolecular assembly between these two family of polymer, even in presence of an acceptor moiety.

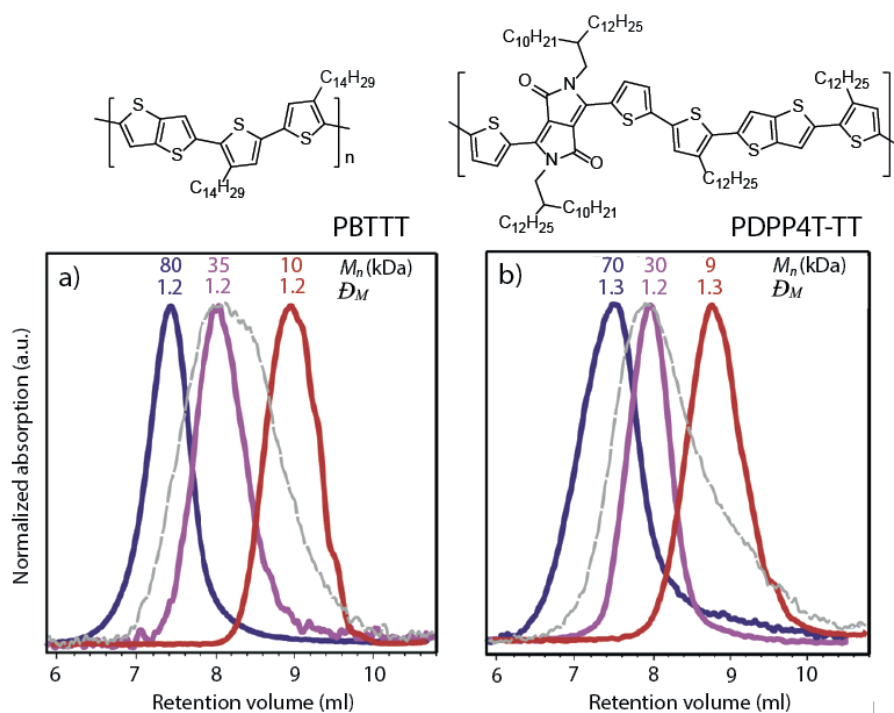


Figure 6-1. Analytical gel permeation chromatograms of selected a) PBTTT and b) PDPP4T-TT fractions separated by prep-GPC are shown as the normalized detector response versus elution volume of the mobile phase. The gray line represents the crude polymerization chromatograph. The reported M_n and \bar{D}_M values for each fraction are versus polystyrene standards. For clarity, not all fractions employed in subsequent analysis are shown here.

6.2 Results and discussion

6.2.1 Fractionation of the polymers

Stille coupling based step-growth polymerization used to obtain all the polymers investigated in this study produced batches with extremely high polydispersity indexes. To access samples with a defined M_n and a low D_M we employed a preparatory size exclusion chromatography column which affords separation of polymers chain length based on their characteristic hydrodynamic volume in solution. Starting from initial crude batches it was possible to afford separation of polymer chains lengths with M_n ranging from 9 to 80 kDa and narrow D_M (typically 1.1–1.3) as shown in the analytical GPC traces in **Figure 6-1**. To avoid aggregation and precipitation of longer polymer chains inside the column, the prep-GPC system was maintained at a relatively high temperature (80 °C), and low concentration of polymer was used in the mobile phase (chlorobenzene). Similarly to other reports molecular weights are calculated through a calibration curve based on poly(styrene) standards. We note that the actual polymer M_n can be slightly different from that estimated by PS standards due to a reported nonlinear relationship.²³ In addition, care must be taken to correlate M_n and chain length when comparing polymers with different repeating units. For this work, we note that the estimated length of a polymer repeat unit (based on standard bond lengths) divided by the molecular weight of the respective repeat unit gives values for PDPP4T-TT and PBTTT of respectively 1.5 and 1.8 nm kDa⁻¹. Thus, assuming that both polymer structures exhibit comparable hydrodynamic volumes as a function of chain length, at identical M_n , PBTTT will exhibit a polymer chain length about 1.2-fold longer.

Table 6-1. Average figures of merit calculated from at least four devices for PBTTT:PCBM and PDPP4T-TT:PCBM devices with different polymer MW.

	M_n (kDa)	D_M (-)	J_{sc} (mA/cm ²)	V_{oc} (V)	FF (-)	PCE (%)	R_{series} (Ω)
PDPP4T-TT	9	1.3	1.3 ± 0.1	0.62 ± 0.01	0.57 ± 0.01	0.44 ± 0.02	104 ± 2
	30	1.2	2.2 ± 0.2	0.62 ± 0.01	0.67 ± 0.03	0.89 ± 0.07	25 ± 1
	70	1.3	4.4 ± 0.1	0.60 ± 0.01	0.56 ± 0.02	1.41 ± 0.08	90 ± 1
	14	2.1	2.6 ± 0.1	0.62 ± 0.01	0.63 ± 0.02	0.94 ± 0.07	32 ± 1
PBTTT	10	1.2	2.9 ± 0.2	0.60 ± 0.01	0.37 ± 0.02	0.61 ± 0.05	298 ± 4
	16	1.2	3.2 ± 0.2	0.60 ± 0.01	0.46 ± 0.02	0.89 ± 0.05	201 ± 3
	35	1.2	4.3 ± 0.3	0.60 ± 0.01	0.45 ± 0.01	1.14 ± 0.07	176 ± 2
	80	1.2	3.2 ± 0.2	0.59 ± 0.01	0.36 ± 0.01	0.65 ± 0.04	563 ± 5
	26	2.0	3.7 ± 0.3	0.56 ± 0.01	0.53 ± 0.02	1.06 ± 0.06	56 ± 1

6.2.2 The effect of PDPP4T-TT's M_n on the photovoltaic performance

The BHJ between polymer and fullerene was optimized for PDPP4T-TT:PC₆₁BM blends and found to give the best performance at a weight ratio of 3:7 from CHCl₃ with a BHJ active layer thickness of *ca.* 150 nm, which is in agreement with previous publications on similar materials.¹⁰ No significant variations in optimal processing conditions were found with the different M_n fractions, allowing fair comparison of the performances. Figures of merit for PDPP4T-TT:PCBM solar cells at different M_n are summarized in **Table 6-1**, while typical J-V curves are shown on **Figure 6-2**. The open circuit voltage (V_{OC}) and fill factor (FF) of the PDPP4T-TT solar cells are similar to comparable materials.¹⁰ The higher short circuit current (J_{SC}) obtained in previous reports was afforded by using DIO as an additive optimize the morphology. Here, no DIO was used in order to avoid any other effect than the M_n on the morphology.

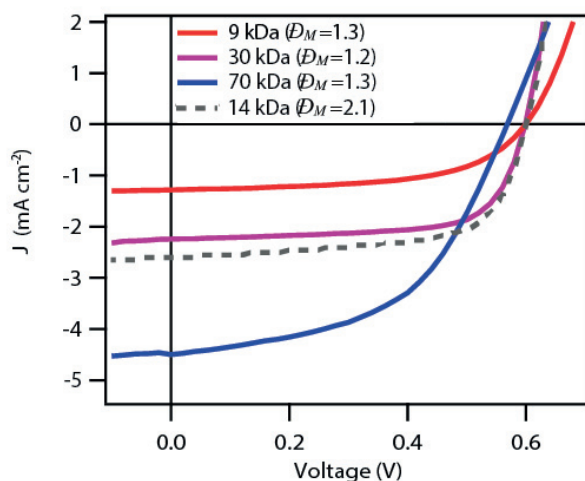


Figure 6-2. J-V characteristics of PDPP4T-TT:PCBM BHJ solar cells using different polymer M_n . Polymer fraction with high polydispersity is shown in grey dashed line.

Overall, the PCE increases with M_n resulting in a more than 3-fold enhancement when going from 9 kDa to 70 kDa. This improvement can be mainly attributed to the higher J_{SC} obtained at 70 kDa as the V_{OC} and FF remain almost unaffected. However, it is important to note that the FF is slightly improved at 30 kDa. Interestingly, the original fraction with large D_M does exhibit poor PCE as compared to the best performing high M_n fraction, demonstrating the beneficial effect of fractionation to isolate long polymer chains for optimum PCE in this system. Generally speaking, the observed trend

in PCE with M_n is in excellent agreement with reported OFET performances as function of M_n , where hole mobility increases until a plateau at high M_n .²⁴ Hence, a trivial rationalization for the improved PCE with M_n is the higher mobility in the donor phase which would favour collection efficiency of free charge carriers. However, increasing the active layer thickness from 150 nm to 200 nm results in similar enhancement for all M_n , suggesting that charge carrier collection is not a limiting factor. This is in good agreement with the higher series resistance measured in the high M_n fraction relative to the 30 kDa one (see **Table 6-1**). This indicates that the higher hole mobility expected in the device is not the main underlying reason for the better PCE.

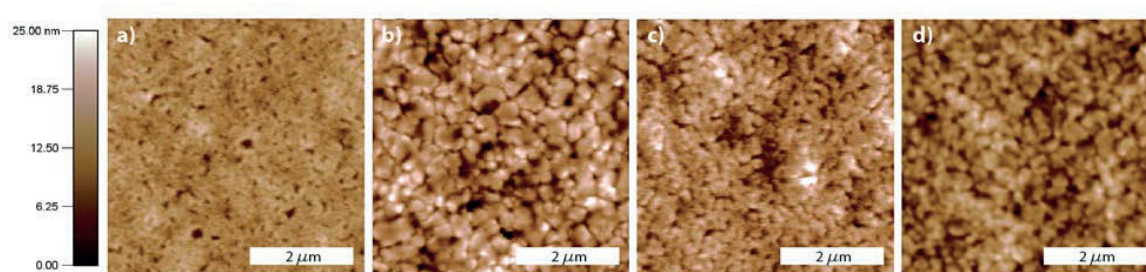


Figure 6-3. Tapping-mode atomic force microscopy images of the surface morphology of spin-casted thin films of PDPP4T-TT at (a) 9 kDa, (b) 30 kDa, (c) 70 kDa and (d) large \bar{D}_M fractions.

To gain further insight into the differences in device performance, the morphological characterization of the BHJ surface was performed by AFM (**Figure 6-3**). Interestingly, it can be seen that the 9 kDa BHJ film shows a smoother surface compared to the 30 kDa BHJ. While small features of around 50 and 100 nm, respectively, for low and high M_n can be observed. Surprisingly, at the medium M_n of 30 kDa, the BHJ forms a very different morphology with large domains of approximately 250–500 nm.

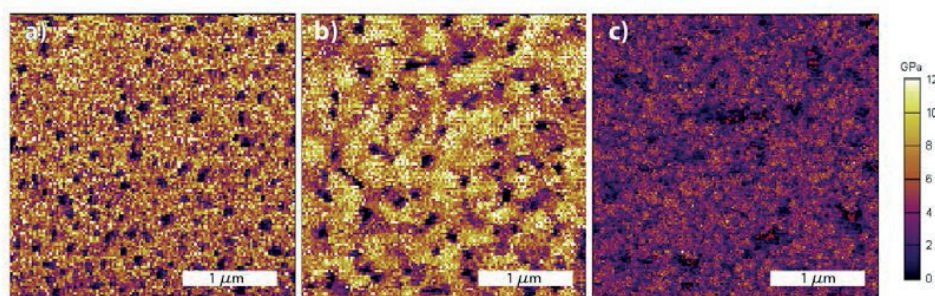


Figure 6-4. Young modulus mapping images of 9 kDa (a), 30 kDa (b) and 70 kDa (c) PDPP4T-TT:PCBM thin films.

Nanomechanical mapping, also shown in **Figure 6-4**, was used to identify the different phases present on the surface of the PDPP4T-TT:PC₆₁BM BHJs. This measurement allows calculating the Young Modulus (YM) of the indented surface and previous studies have shown that PCBM has a typical YM greater than 10 GPa, while polymers have relatively low YM (< 3 GPa).^{25–27} It can be seen that the large domains present on the surface of the 30 kDa BHJ film are mainly composed of PCBM as they present a YM larger than 10 GPa. Such a morphology strongly suggests the formation of a PCBM-rich surface due to a vertical segregation of the BHJ during spin casting.^{28,29} The presence of the PCBM-rich surface in contact with the Al top electrode may explain the smaller series resistance observed with this fraction of polymer. Indeed, the average YM of the surface of the BHJ prepared with the 9 kDa fraction is smaller and has an appearance suggesting that more intermixing of the components is present at the BHJ surface, and for the blend prepared with the 70 kDa polymer fraction, no regions with YM higher than 10 GPa are observed on the surface indicating that the PCBM in the film is likely well intermixed with the 70 kDa polymer. Although we cannot discount a vertical phase segregation of the film with the polymer at the surface in this case, this is unlikely given the relatively high J_{sc} observed.

As the devices shown in the present study for PDPP4T-TT do not undergo any annealing process, the nanoscopic morphology will be formed during drying of the precursor solution. In such case, the different phases present in the film are known to be determined by the demixing process occurring during the spin coating step.²⁹ Therefore, the difference in solvent interaction between the polymer and the PC₆₁BM plays a crucial role in this system. Indeed, the stark difference in surface BHJ morphology and composition demonstrates that the M_n critically affects the self-assembly, probably by affecting the solubility of the donor component. Thereof, decrease in solubility with M_n is likely to

cause the change in morphology and the enhanced device performance discovered in this work. Further study of the film formation process by in situ techniques³⁰ and of the resulting film by advanced TEM techniques³¹ may give important insights into the origin of the observed differences.

6.2.3 The effect of PBTTT's M_n on the photovoltaic performance

Further investigation over the effect of the M_n in PBTTT:PCBM BHJ photovoltaic devices will now be discussed. Indeed, as discussed in chapter 1, the outstanding performances of PBTTT in OFET starkly contrast with the poor PCE reported for OPV. Therefore, while the effect of M_n on OFET performance has already been the focus of many studies, it has never been extended to OPV.

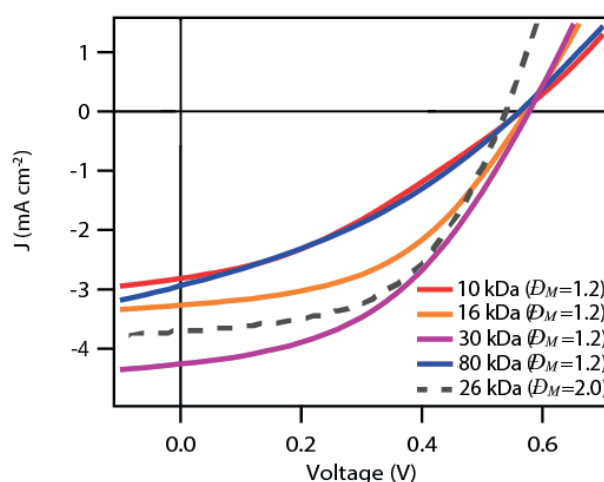


Figure 6-5. *J-V characteristics of PBTTT:PCBM solar cells at different M_n . Polymer fraction with high polydispersity is shown in grey dashed line.*

The PBTTT:PCBM BHJ was optimized for PBTTT:PC₆₁BM blends and found to give the best performances when processed at a weight ratio of 2:8 from DCB. Similarly to PDPP4T-TT, no significant variations in optimal processing conditions were found with the different M_n fractions. The best PCE obtained for these devices is similar to the previously reported values (around 2 % without additives).^{32–34} Overall, the PCE of PBTTT:PCBM solar cells is seen to increase significantly with M_n up to 30 kDa as can be seen on **Figure 6-5** and **Table 6-1**; In a first time, due to the enhancement of the FF and in a second time due to an increase in J_{sc} . However, further increase to 80 kDa results in a drastic loss in efficiency, back down to similar PCE as the low M_n fraction. Interestingly, the original fraction with large D_M exhibits an excellent PCE close to the best performing M_n fraction, which

demonstrate that fractionation of the M_n with low D_M is not required for optimal PCE. Once again, the trend observed in OPV is similar to the one previously reported for OFETs, with the 30 kDa giving the highest performances.¹³ However, in the case of PBTTT, the series resistances are depicting the opposite trend to PCE and mobility with the lowest R_s at medium M_n . Hence, the higher hole mobility of the 35 kDa PBTTT could be the origin of the enhanced performances in this film.

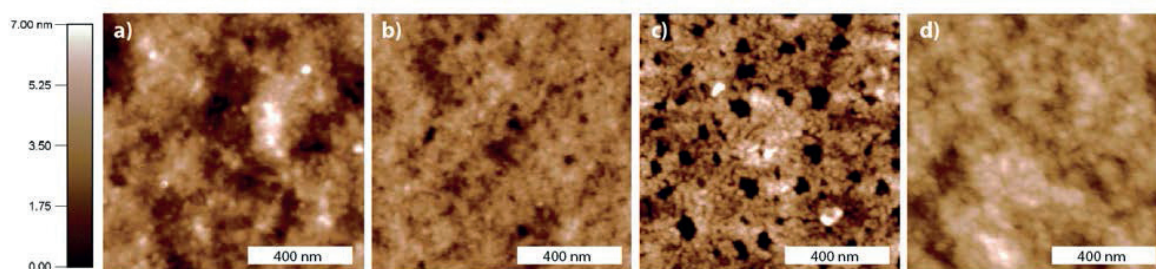


Figure 6-6. Tapping-mode atomic force microscopy images of the surface morphology of spin-casted thin films of PBTTT at (a) 10 kDa, (b) 35 kDa, (c) 80 kDa and (d) large D_M fractions.

To gain further insight, morphological characterization of the BHJ surface was performed by AFM. Height images of the 10, 35 and 80 kDa PBTTT films are shown in **Figure 6-6**. It can be seen that the low M_n fraction has a much rougher surface than the 35 kDa film which suggests a poorer film formation. In stark contrast, the high M_n PBTTT shows a surface morphology composed of small domains approximately 50 nm in size. The large amount of grain boundaries present in the 80 kDa film – probably originating from entanglement of the polymer chains – is likely to cause the decrease in both J_{sc} and FF observed.

Taken together, the optimum performance obtained at medium M_n is in good agreement with the co-crystal formation reported in PBTTT:PCBM blend. Indeed, the thin film morphology seems governed by the crystallization of the bimolecular crystal, instead of the solution demixing behavior aforementioned for PDPP4T-TT. Therefore, the self-assembly in PBTTT:PCBM BHJ blend or neat PBTTT behaves very similarly with no stark difference in optimum M_n .

6.3 Conclusion

The effect of polymeric donor's M_n on the performance of BHJ photovoltaic devices was investigated for PDPP4T-TT and PBTTT in combination with PCBM. The DPP-based polymer shows optimum PCE at high M_n , where previous work also reported the optimum mobility. Despite this obvious correlation, the enhancement in PCE is rather attributed to the stronger polymer demixing with PCBM during the processing, given the larger series resistance of the film in combination with the conspicuous surface morphology change. As the enhancement is seemingly caused by solubility parameter, optimum M_n might also depend on solubilizing group and processing conditions.

In stark contrast, PBTTT is found to behave very similarly than in OFET with a M_n fraction around 35 kDa that renders optimal performances. The formation of a cocrystal in presence of PCBM having very similar supramolecular assembly than the neat polymer it-self is consistent with this behaviour. This is supported by the series resistance drop at this medium M_n .

Overall, there is a clear breach between PBTTT and PDPP4T-TT concerning their optimum chain length for self-assembly in OPV. The characteristic paracrystallinity of PBTTT seems to govern the self-assembly in the blend, whereas the amorphous character of PDPP4T-TT leads to a self-assembly governed by the delicate balance of the donor and acceptor respective solubility. Such a strong dependence on processing condition is highly detrimental for large scale applications. Hence further work on understanding and controlling the self-assembly are greatly needed for this class of polymer. In addition, it ensues from the optimum high M_n of PDPP4T-TT that selecting this high M_n fraction with narrow D_M is highly beneficial for the PCE. In contrary, fractionation of the PBTTT M_n distribution does not result in significant improvement.

6.4 References

- (1) Ashraf, R. S.; Meager, I.; Nikolka, M.; Kirkus, M.; Planells, M.; Schroeder, B. C.; Holliday, S.; Hurhangee, M.; Nielsen, C. B.; Sirringhaus, H.; McCulloch, I. *J. Am. Chem. Soc.* **2015**, *137* (3), 1314.
- (2) Yi, Z.; Wang, S.; Liu, Y. *Adv. Mater.* **2015**, *27* (24), 3589.
- (3) Casey, A.; Ashraf, R. S.; Fei, Z.; Heeney, M. *Macromolecules* **2014**, *47* (7), 2279.
- (4) Zhang, W.; Han, Y.; Zhu, X.; Fei, Z.; Feng, Y.; Treat, N. D.; Faber, H.; Stingelin, N.; McCulloch, I.; Anthopoulos, T. D.; Heeney, M. *Adv. Mater.* **2016**, *28* (20), 3922.
- (5) Zhang, W.; Smith, J.; Watkins, S. E.; Gysel, R.; McGehee, M.; Salleo, A.; Kirkpatrick, J.; Ashraf, S.; Anthopoulos, T.; Heeney, M.; McCulloch, I. *J. Am. Chem. Soc.* **2010**, *132* (33), 11437.
- (6) Ho, C.-C.; Chen, C.-A.; Chang, C.-Y.; Darling, S. B.; Su, W.-F. *J. Mater. Chem. A* **2014**, *2* (21), 8026.

- (7) Joseph Kline, R.; McGehee, M. D.; Toney, M. F. *Nat. Mater.* **2006**, 5 (3), 222.
- (8) McCulloch, I.; Heeney, M.; Bailey, C.; Genevicius, K.; MacDonald, I.; Shkunov, M.; Sparrowe, D.; Tierney, S.; Wagner, R.; Zhang, W.; Chabiniy, M. L.; Kline, R. J.; McGehee, M. D.; Toney, M. F. *Nat. Mater.* **2006**, 5 (4), 328.
- (9) Zhang, X.; Bronstein, H.; Kronemeijer, A. J.; Smith, J.; Kim, Y.; Kline, R. J.; Richter, L. J.; Anthopoulos, T. D.; Sirringhaus, H.; Song, K.; Heeney, M.; Zhang, W.; McCulloch, I.; DeLongchamp, D. M. *Nat. Commun.* **2013**, 4, 2238.
- (10) Li, W.; Roelofs, W. S. C.; Wienk, M. M.; Janssen, R. A. J. *J. Am. Chem. Soc.* **2012**, 134 (33), 13787.
- (11) Koch, F. P. V.; Rivnay, J.; Foster, S.; Müller, C.; Downing, J. M.; Buchaca-Domingo, E.; Westcott, P.; Yu, L.; Yuan, M.; Baklar, M.; Fei, Z.; Luscombe, C.; McLachlan, M. A.; Heeney, M.; Rumbles, G.; Silva, C.; Salleo, A.; Nelson, J.; Smith, P.; Stingelin, N. *Prog. Polym. Sci.* **2013**, 38 (12), 1978.
- (12) Himmelberger, S.; Vandewal, K.; Fei, Z.; Heeney, M.; Salleo, A. *Macromolecules* **2014**, 47 (20), 7151.
- (13) Gasperini, A.; Sivula, K. *Macromolecules* **2013**, 46 (23), 9349.
- (14) Wang, L.; Zhang, X.; Zhang, J.; Tian, H.; Lu, Y.; Geng, Y.; Wang, F. *J. Mater. Chem. C* **2014**, 2 (46), 9978.
- (15) Tsao, H. N.; Cho, D. M.; Park, I.; Hansen, M. R.; Mavrinskiy, A.; Yoon, D. Y.; Graf, R.; Pisula, W.; Spiess, H. W.; Müllen, K. *J. Am. Chem. Soc.* **2011**, 133 (8), 2605.
- (16) Tong, M.; Cho, S.; Rogers, J. T.; Schmidt, K.; Hsu, B. B. Y.; Moses, D.; Coffin, R. C.; Kramer, E. J.; Bazan, G. C.; Heeger, A. J. *Adv. Funct. Mater.* **2010**, 20 (22), 3959.
- (17) Intemann, J. J.; Yao, K.; Yip, H.-L.; Xu, Y.-X.; Li, Y.-X.; Liang, P.-W.; Ding, F.-Z.; Li, X.; Jen, A. K.-Y. *Chem. Mater.* **2013**, 25 (15), 3188.
- (18) Mateker, W. R.; Douglas, J. D.; Cabanetos, C.; Sachs-Quintana, I. T.; Bartelt, J. A.; Hoke, E. T.; Labban, A. E.; Beaujuge, P. M.; Fréchet, J. M. J.; McGehee, M. D. *Energy Environ. Sci.* **2013**, 6 (8), 2529.
- (19) Huang, Z.; Fregoso, E. C.; Dimitrov, S.; Tuladhar, P. S.; Soon, Y. W.; Bronstein, H.; Meager, I.; Zhang, W.; McCulloch, I.; Durrant, J. R. *J. Mater. Chem. A* **2014**, 2 (45), 19282.
- (20) Vangerven, T.; Verstappen, P.; Drijkoningen, J.; Dierckx, W.; Himmelberger, S.; Salleo, A.; Vanderzande, D.; Maes, W.; Manca, J. V. *Chem. Mater.* **2015**, 27 (10), 3726.
- (21) Zhao, K.; Khan, H. U.; Li, R.; Su, Y.; Amassian, A. *Adv. Funct. Mater.* **2013**, 23 (48), 6024.
- (22) Schilinsky, P.; Asawapirom, U.; Scherf, U.; Biele, M.; Brabec, C. J. *Chem. Mater.* **2005**, 17 (8), 2175.
- (23) Wong, M.; Hollinger, J.; Kozycz, L. M.; McCormick, T. M.; Lu, Y.; Burns, D. C.; Seferos, D. S. *ACS Macro Lett.* **2012**, 1 (11), 1266.
- (24) Gasperini, A.; Jeanbourquin, X. A.; Sivula, K. *J. Polym. Sci. Part B Polym. Phys.* **2016**, 54 (21), 2245.
- (25) Wang, D.; Russell, T. P.; Nishi, T.; Nakajima, K. *ACS Macro Lett.* **2013**, 2 (8), 757.
- (26) Wang, D.; Liu, F.; Yagihashi, N.; Nakaya, M.; Ferdous, S.; Liang, X.; Muramatsu, A.; Nakajima, K.; Russell, T. P. *Nano Lett.* **2014**, 14 (10), 5727.
- (27) Gasperini, A.; Jeanbourquin, X. A.; Rahmanudin, A.; Yu, X.; Sivula, K. *Adv. Mater.* **2015**, 27 (37), 5541.
- (28) Campoy-Quiles, M.; Ferenczi, T.; Agostinelli, T.; Etchegoin, P. G.; Kim, Y.; Anthopoulos, T. D.; Stavrinou, P. N.; Bradley, D. D. C.; Nelson, J. *Nat. Mater.* **2008**, 7 (2), 158.
- (29) Kouijzer, S.; Michels, J. J.; van den Berg, M.; Gevaerts, V. S.; Turbiez, M.; Wienk, M. M.; Janssen, R. A. J. *J. Am. Chem. Soc.* **2013**, 135 (32), 12057.

- (30) Chou, K. W.; Yan, B.; Li, R.; Li, E. Q.; Zhao, K.; Anjum, D. H.; Alvarez, S.; Gassaway, R.; Biocca, A.; Thoroddsen, S. T.; Hexemer, A.; Amassian, A. *Adv. Mater.* **2013**, *25* (13), 1923.
- (31) Kozub, D. R.; Vakhshouri, K.; Orme, L. M.; Wang, C.; Hexemer, A.; Gomez, E. D. *Macromolecules* **2011**, *44* (14), 5722.
- (32) Parmer, J. E.; Mayer, A. C.; Hardin, B. E.; Scully, S. R.; McGehee, M. D.; Heeney, M.; McCulloch, I. *Appl. Phys. Lett.* **2008**, *92* (11), 113309.
- (33) Cates, N. C.; Gysel, R.; Beiley, Z.; Miller, C. E.; Toney, M. F.; Heeney, M.; McCulloch, I.; McGehee, M. D. *Nano Lett.* **2009**, *9* (12), 4153.
- (34) Buchaca-Domingo, E.; J. Ferguson, A.; C. Jamieson, F.; McCarthy-Ward, T.; Shoaee, S.; R. Tumbleston, J.; G. Reid, O.; Yu, L.; Madec, M.-B.; Pfannmöller, M.; Hermerschmidt, F.; R. Schröder, R.; E. Watkins, S.; Kopidakis, N.; Portale, G.; Amassian, A.; Heeney, M.; Ade, H.; Rumbles, G.; R. Durrant, J.; Stingelin, N. *Mater. Horiz.* **2014**, *1* (2), 270.



Chapter 7 Concluding remarks and perspectives

Efficient engineering of the supramolecular ordering of organic semiconductors is limited by the current understanding of the self-assembly event and available toolkit to control it. In the present thesis, we aim to address these two issues by unravelling the thermodynamic parameters that govern charge transport in molecular semiconductors and using them as a platform to develop new tools and strategies to efficiently control the morphology of active layers for OFET and OPV applications.

Chapter 3 reports a unique bell-shaped temperature dependence of the mobility in a range well below the Mott-Ioffe-Regel limit in OFET based on a DPP(TBFu)₂ small molecule. Surprisingly, these findings contrasted with the most extended transport theories in the field (*e.g.* band-like or hopping transport) bringing out a missing mechanism, key for broadening the understanding on the actual transport mechanisms in organic semiconductors. In conclusion, we propose a new theory where this anomalous mobility variation with temperature arises from a temperature dependent equilibrium in between polymorphic structures with stark differences in intermolecular electronic coupling, which can be successfully described with the help of an isodesmic self-assembly model. Overall, our work conciliates hopping transport mechanism with a negative temperature dependence of the mobility.

We next investigated the working mechanism whereby aliphatically-linked conjugated molecules control the self-assembly of organic semiconductors. More specifically, two novel DPP(TBFu)₂ dimers with distinct linking position, either on the DPP core or on the benzofurane position, were explored. The former was found to act as a nucleation promoter in presence of the monomer, ameliorating the charge transport in DPP(TBFu)₂ by reducing the amount of grain boundaries present in the film. In stark contrast, the other dimer was found to favour another polymorphic structure with reduced driving force for crystallization. When used as an additive, the dimers demonstrated an unparallel control on the thermodynamic of the DPP(TBFu)₂:PCBM phase segregation, ultimately leading to an enhanced stability of the PCE in OPV.

Finally, we discussed a simple strategy to engineer the self-assembly of charge transfer cascade solar cells based on crystallinity differences between host-blend and the ternary material. In this case, using amorphous spiro-based small molecules within P3HT:PCBM host blends was demonstrated to achieve PCE improvements about 30 %.

As a matter of fact, the self-assembly in BHJ is unquestionably more complex than for a neat material. In this respect, we investigated the effect of the polymer molecular weight on the self-assembly and performances of paracrystalline PBTTT and amorphous PDPP4T-TT-based solar cells. We found that while both exhibited optimum PCE in OPV at the same M_n observed for optimum mobility in OFET, the improvement in PDPP4T-TT OPV did not originate from enhanced mobility of the donor phase but rather from a more favourable intermixing with the fullerene phase.

This work raises two main future directions. On one hand, further demonstrating the critical role of phase transition on the electronic coupling and consequently the charge carrier mobility could be a stepping stone in understanding the controversial charge transport mechanism in OS. In this respect, in depth study of DPP(TBFu)₂ might reveal necessary. However, the inherent complexity of this unique system (*e.g.* the interfacial behaviour being very different than the bulk) makes it not well suited for studies. It might actually be easier to apply the model on another, more homogenous, system. For instance, PBTTT is well known to exhibit a liquid crystalline phase transition before melting, which can be tracked by DSC. Hence, applying our model in combination with experimentally measured enthalpy and transition temperature to fit a hypothetical deviation from Marcus equation in PBTTT hole mobility as function of temperature would represent a simple way to establish the viability of our approach.

On the other hand, providing evidence of the universality of the concepts investigated in chapter 4 and 6 by implementing them in state-of-the-art system would assess the actual benefits for commercial application. In particular, as demonstrated in this thesis the great potential of aliphatically linked molecules for controlling the thermodynamics of the BHJ morphology and packing structure of OS is not only limited to hypothetical commercial devices, but also has a direct impact in research to unravel the effect of supramolecular assembly on performances of any OS. In addition, this strategy has recently been proposed as an efficient way to lower the melting temperature of OS. This is highly relevant for moving towards the cheaper and greener melt processing techniques. Finally, it should be noted that the potential of these flexibly linked compounds as plasticizers to enhance the mechanical stability of the active layer remains in its infancy so far. In a more general vein, enlarging this

strategy to state-of-the-art materials seems a logical path, especially for molecules exhibiting high crystallinity (*e.g.* acenes, perylenes).

Appendix A

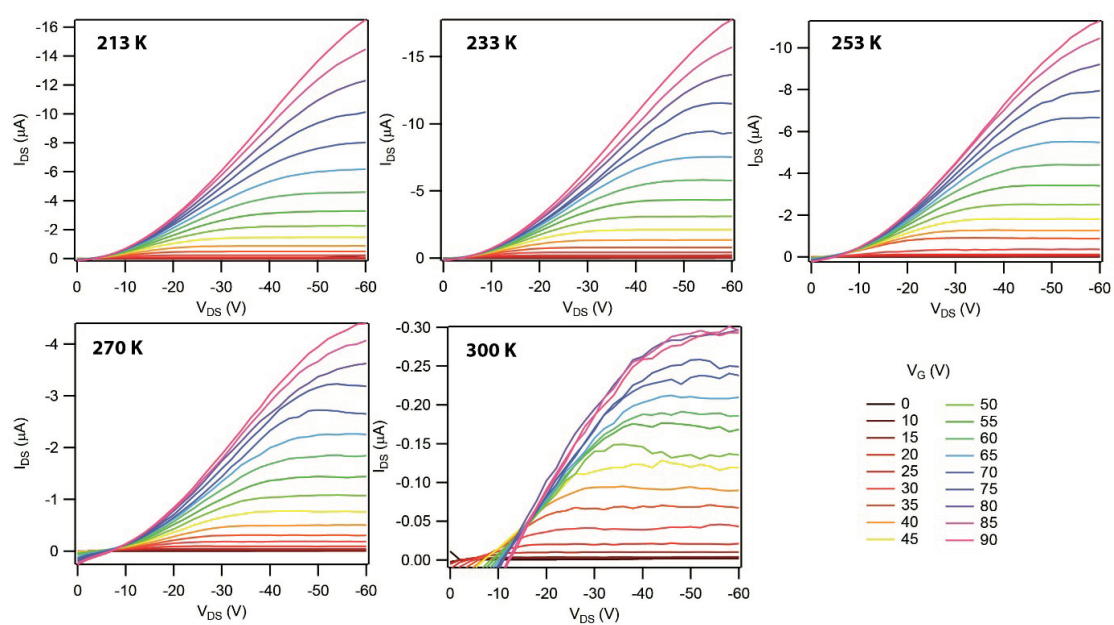


Figure A-1. As-cast DPP(TBFu)₂ FET output curves measured at specified temperatures at different gate voltages with channel length of 20 μm .

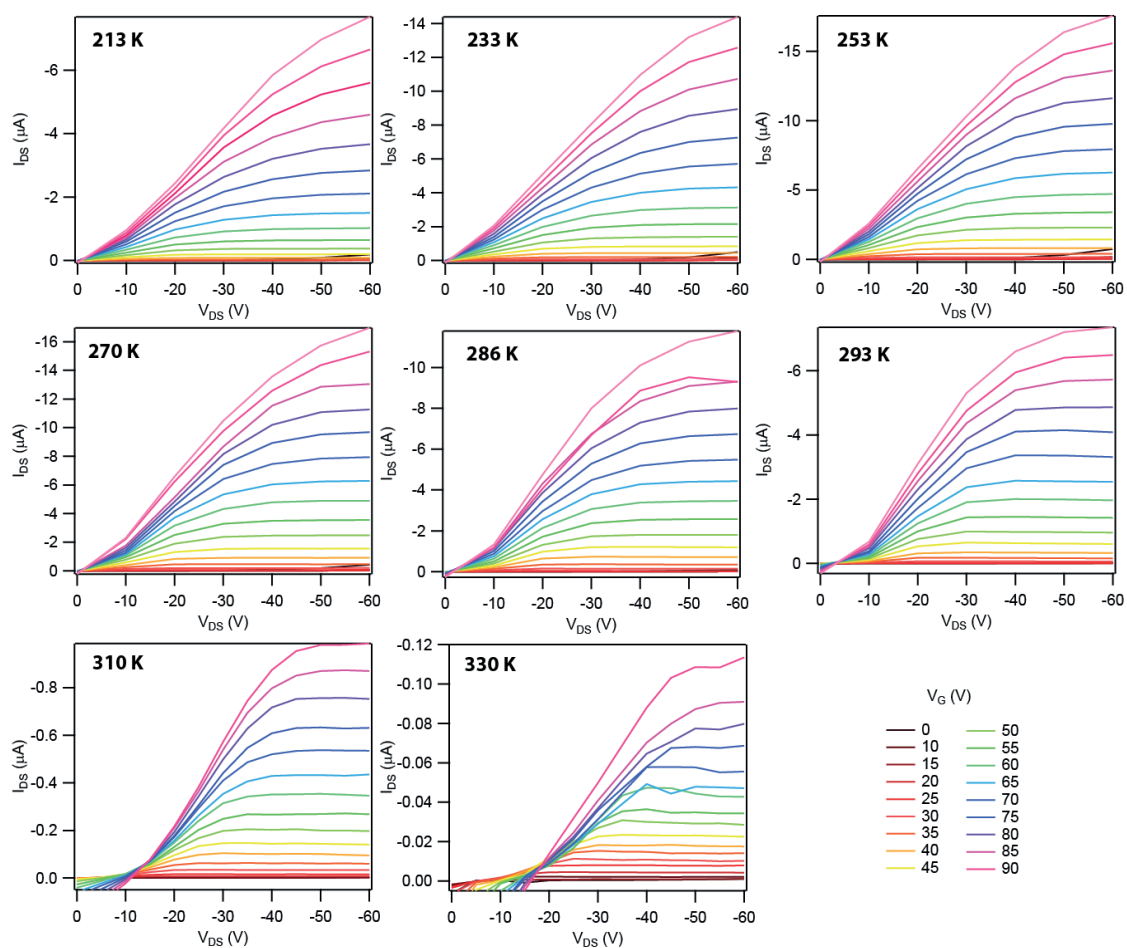


Figure A-2. Output curves measured at specified temperatures at different gate voltages for DPP(TBFu)₂ FET after annealing for 1h at 90 °C with channel length of 20 μm .

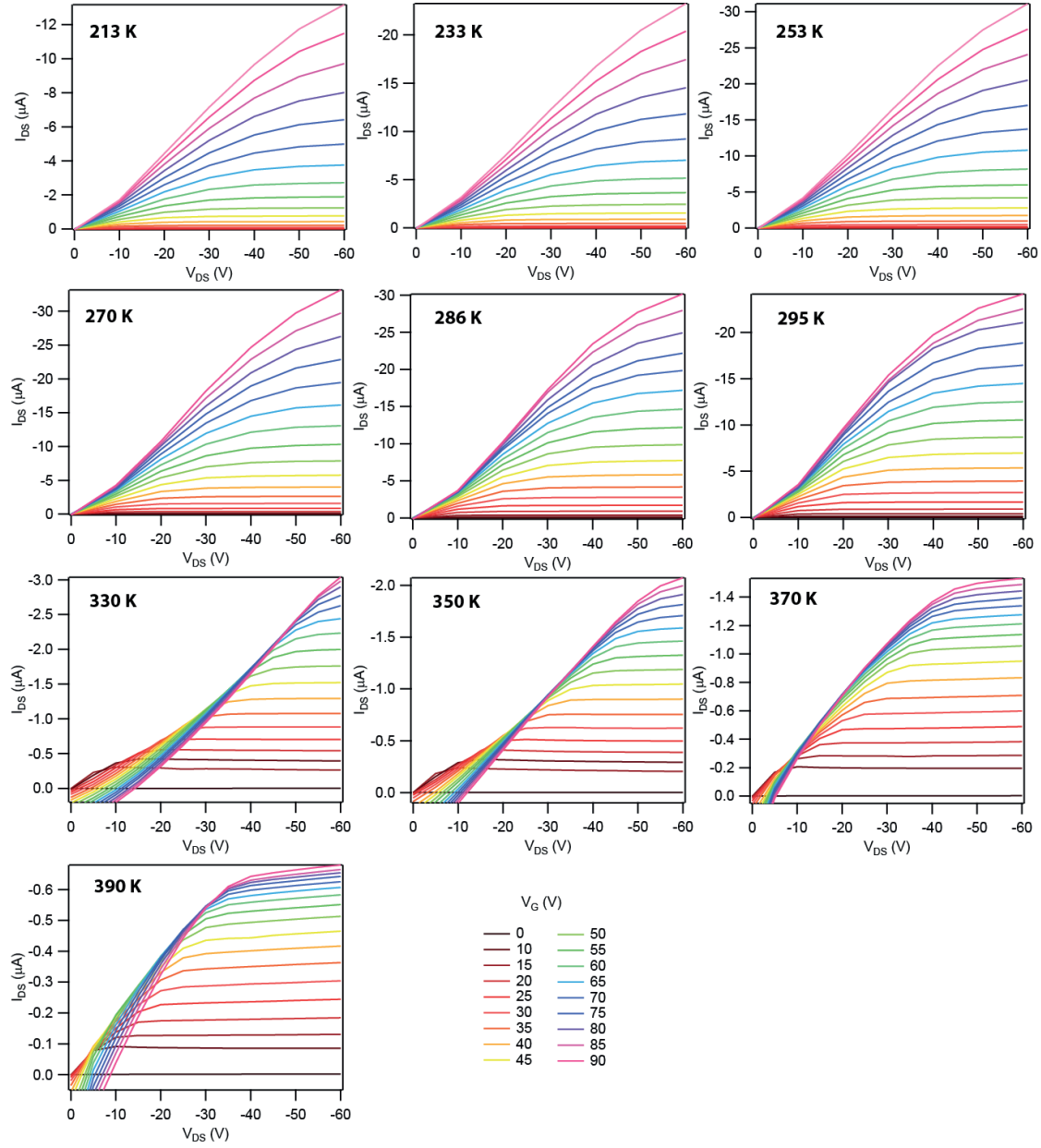


Figure A-3. Output curves measured at specified temperatures at different gate voltages for DPP(TBFu)₂ FET after annealing for 1 h at 130 °C with channel length of 20 μm .

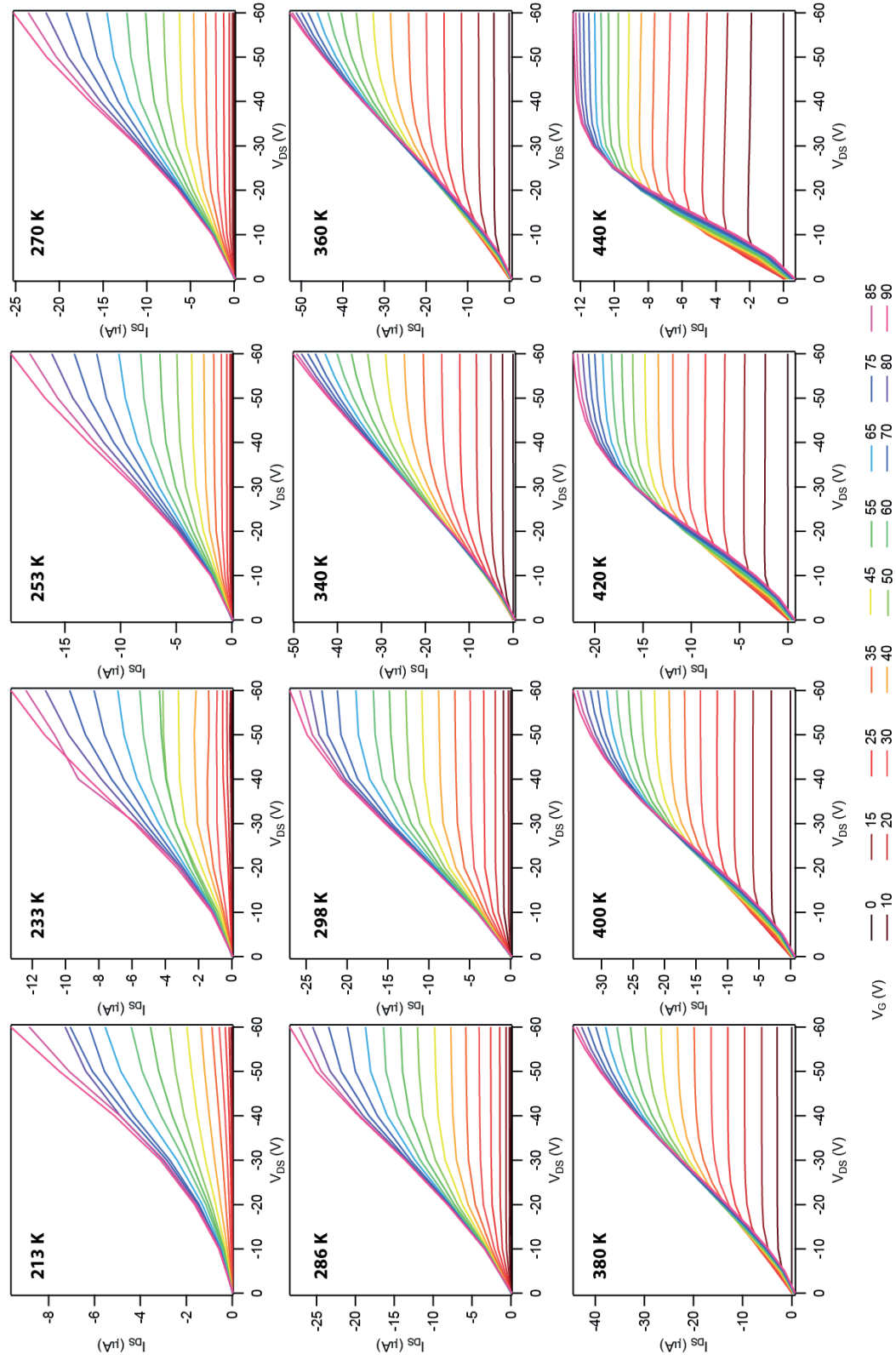


Figure A-4. Output curves measured at specified temperatures at different gate voltages for DPP(TBFD)₂ FET after annealing for 1h at 170 °C with channel length of 20 μ m.

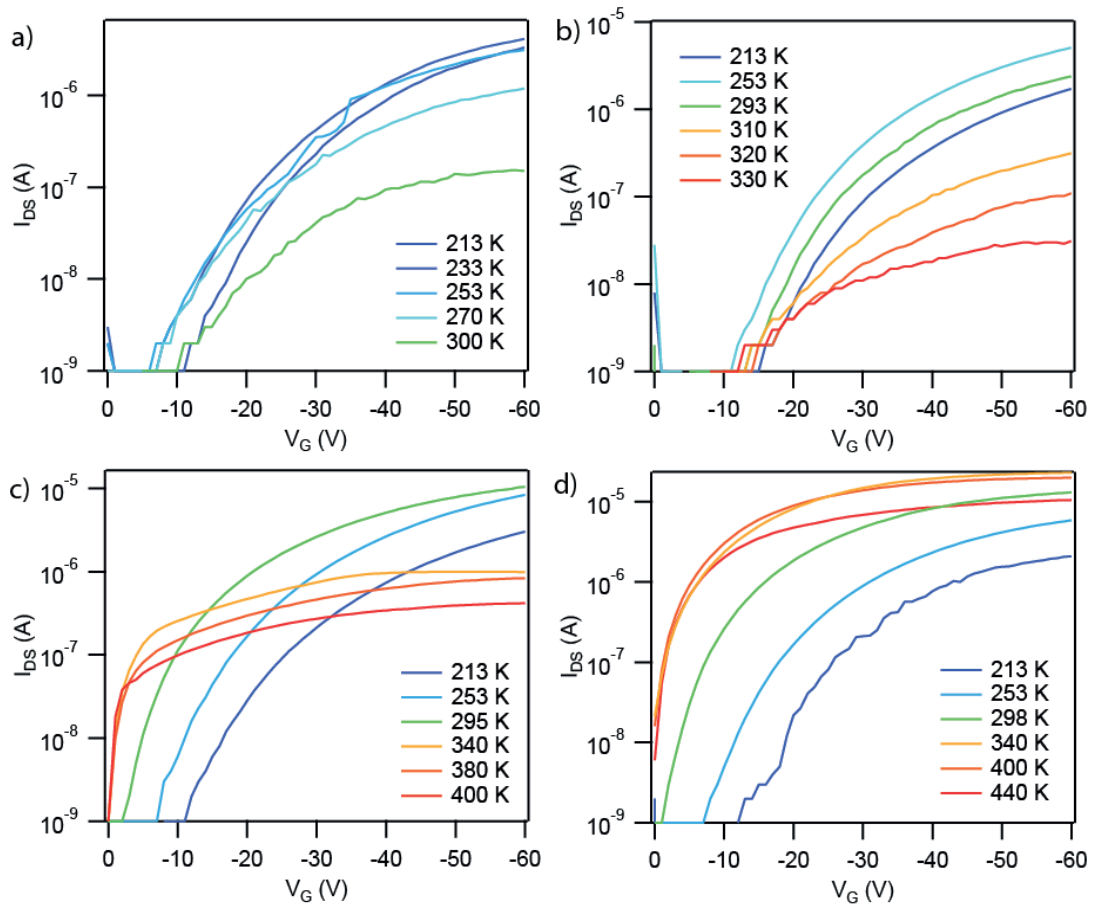


Figure A-5. Transfer curves measured at specified temperature with channel length of 20 μm of DPP(TBFu)₂ FET (a) as-cast and after annealing for 1h at (b) 90 $^{\circ}\text{C}$, (c) 130 $^{\circ}\text{C}$ and (d) 170 $^{\circ}\text{C}$.

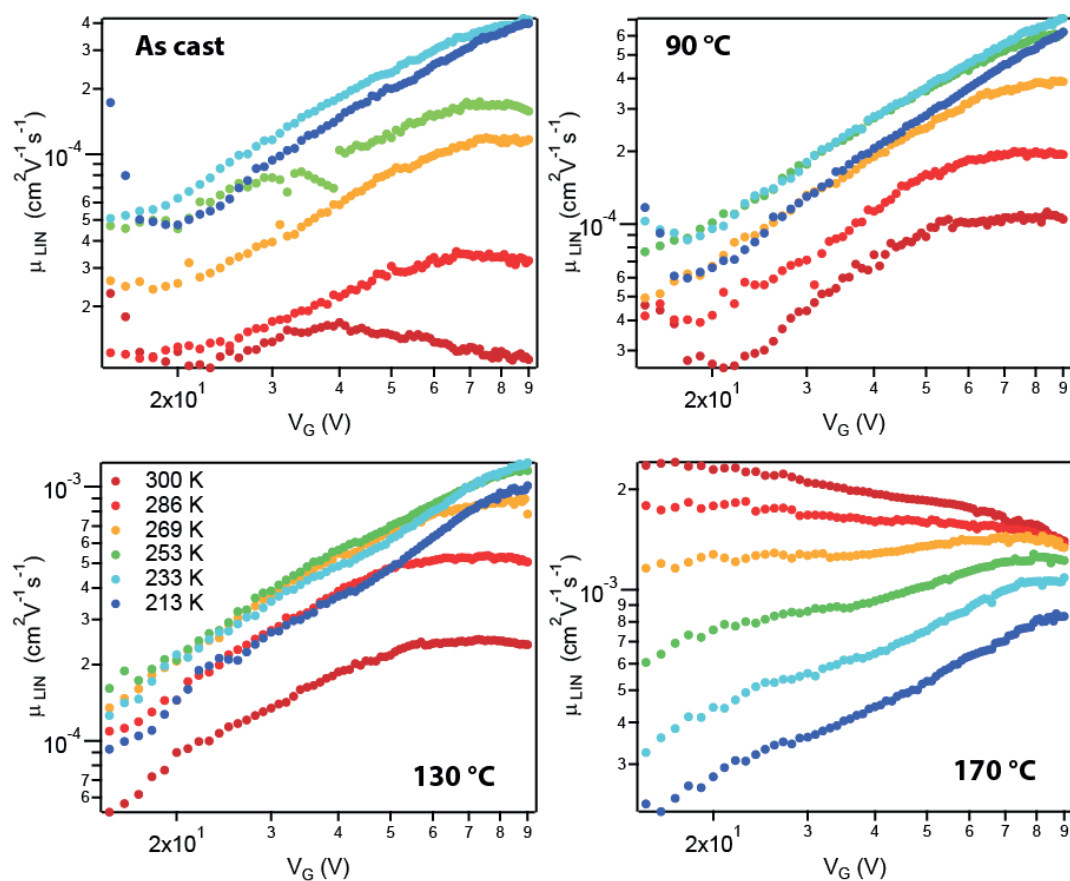


Figure A-6. Hole mobility extracted from linear regime plotted as function of gate voltage measured at specified temperature for as-cast DPP(TBFu)₂ FET and annealed at 90 °C, 130 °C and 170 °C as specified in bold.

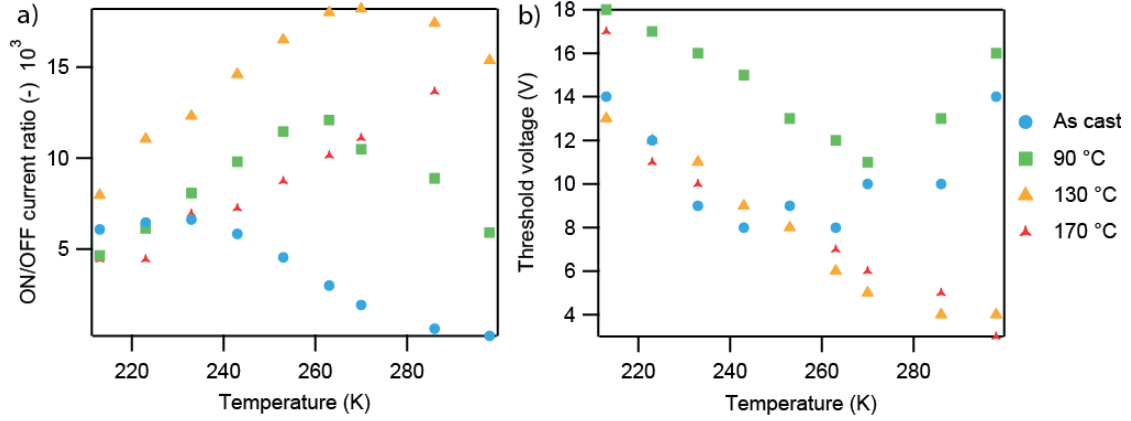


Figure A-7. (a) ON/OFF current ratio and (b) threshold voltage as function of temperature for DPP(TBFu)₂ FET as-cast and after annealing for 1h at 90 °C, 130 °C and 170 °C.

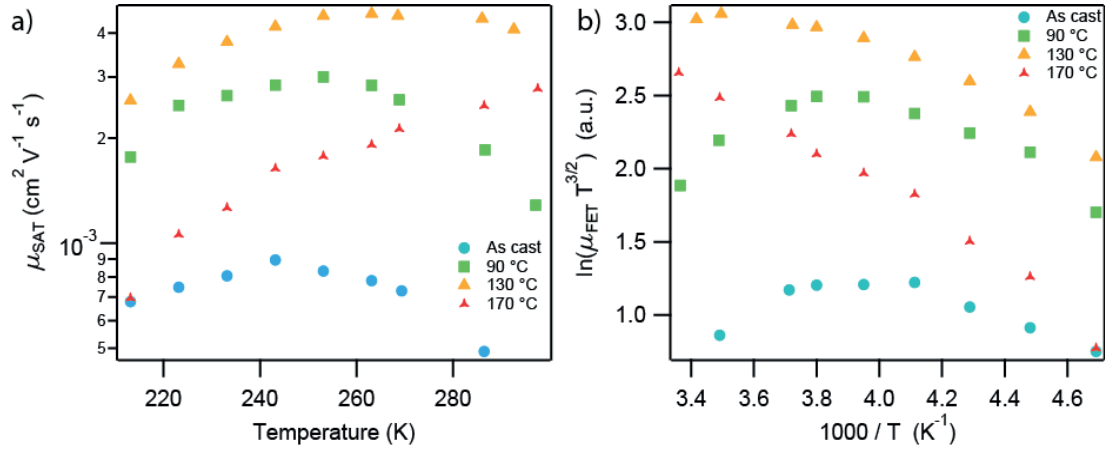


Figure A-8. (a) hole mobility extracted from saturated regime plotted as function of temperature for as-cast DPP(TBFu)₂ OTS.functionnalized FET and annealed at 90 °C, 130 °C and 170 °C. (b) shows the same data presented in form of an Arrhenius plot.

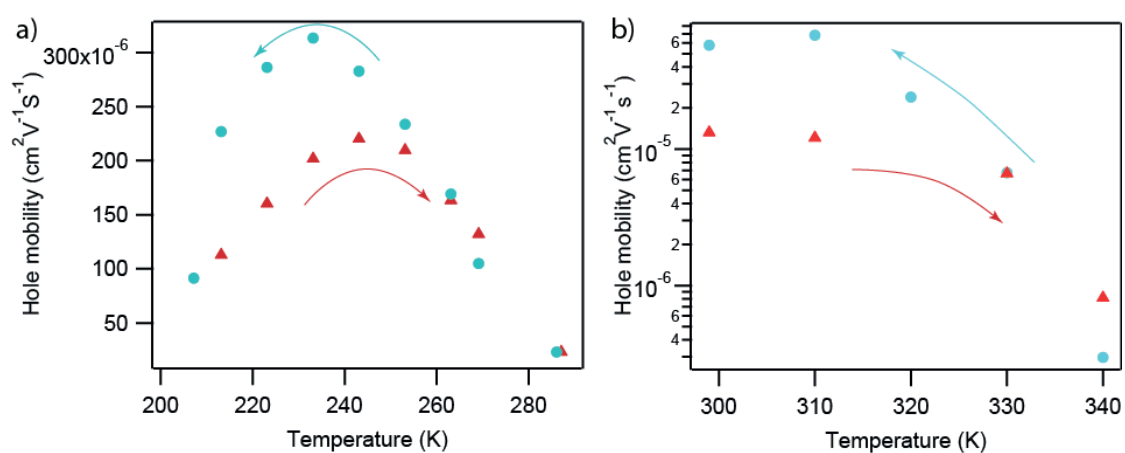


Figure A-9. (a) hole mobility extracted from saturated regime plotted as function of temperature for as-cast DPP(TBFu)₂ FET. (b) hole mobility extracted from saturated regime plotted as function of temperature for annealed DPP(TBFu)₂ FET at 90 °C for 1h. Blue dots represent measurement performed during cooling cycle, while red triangles shows measurements performed during heating cycle.

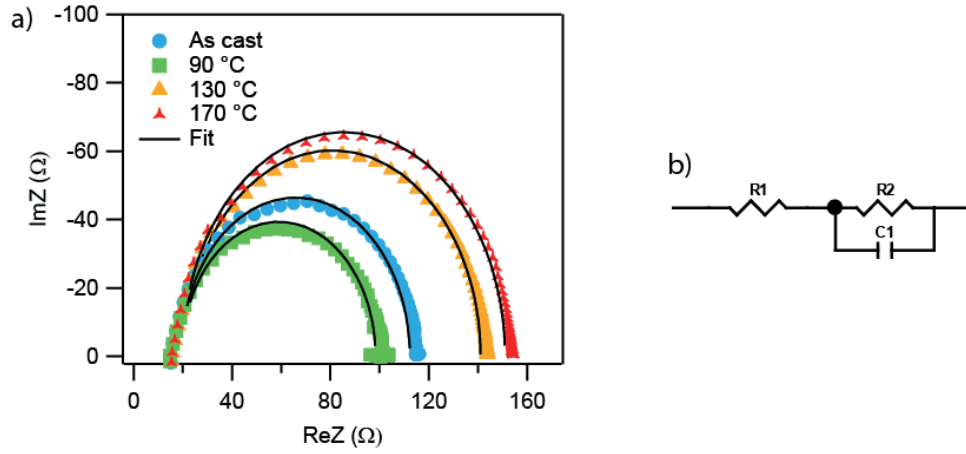


Figure A-10. (a) Typical impedance responses at an applied potential of 0.48 V and corresponding fit using equivalent circuit presented in (b) for hole-only diodes as-cast and annealed at 90 °C, 130 °C and 170 °C, measured in the dark.

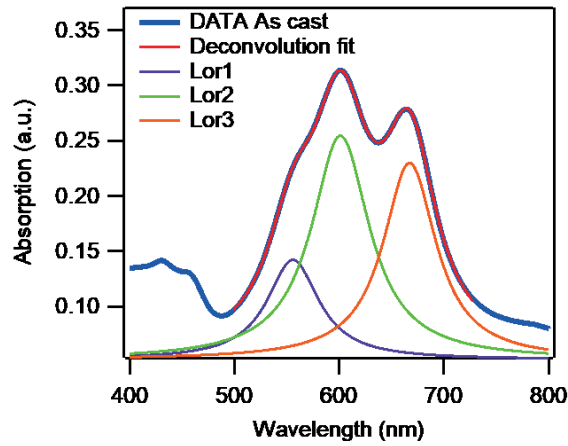


Figure A-11. UV-vis data of as-cast sample measured at RT and typical deconvolution of the three main spectroscopic transitions using a linear combination of three Lorentzian functions. The respective Lorentzian peaks are also shown.

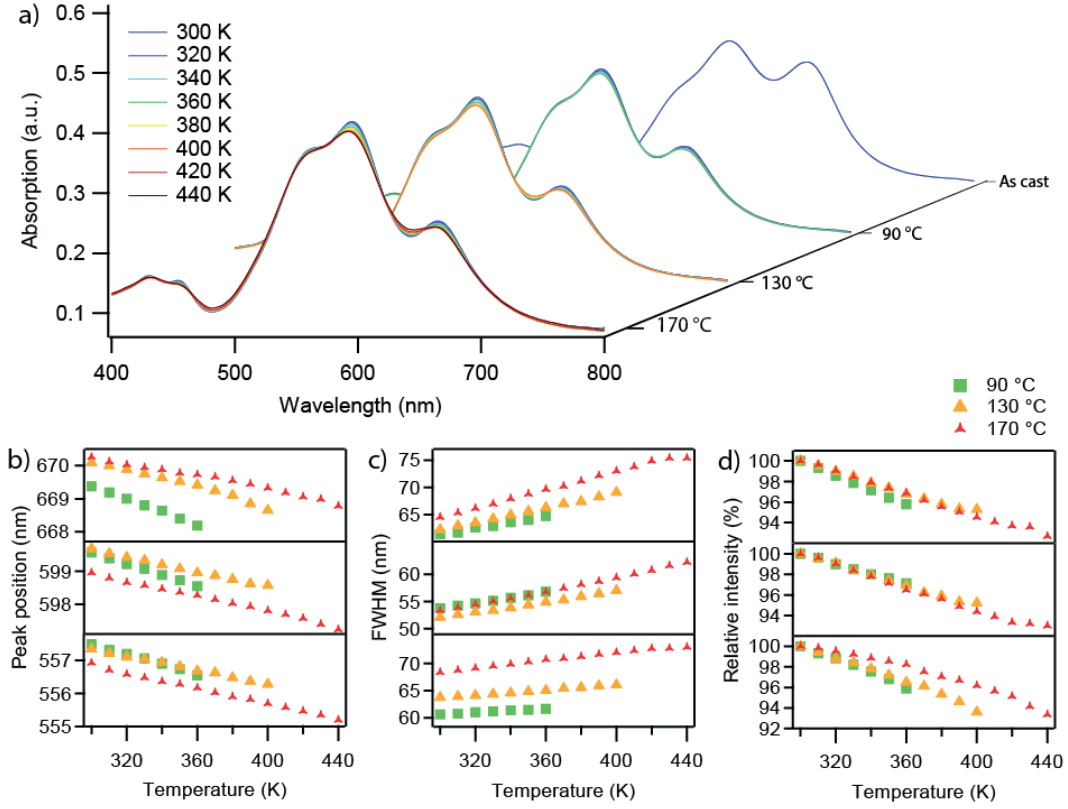


Figure A-12. (a) UV-vis spectrum of DPP(TBFu)₂ thin films as-cast and annealed at 90 °C, 130 °C and 170 °C and measured at varying temperatures. (b) peak position, (c) full width at half maximum and (d) peak height (relative to RT) obtained by deconvolution of the respective spectrum as function of temperature. Top, middle and bottom frame correspond to the peaks at 670, 599 and 557 nm, respectively.

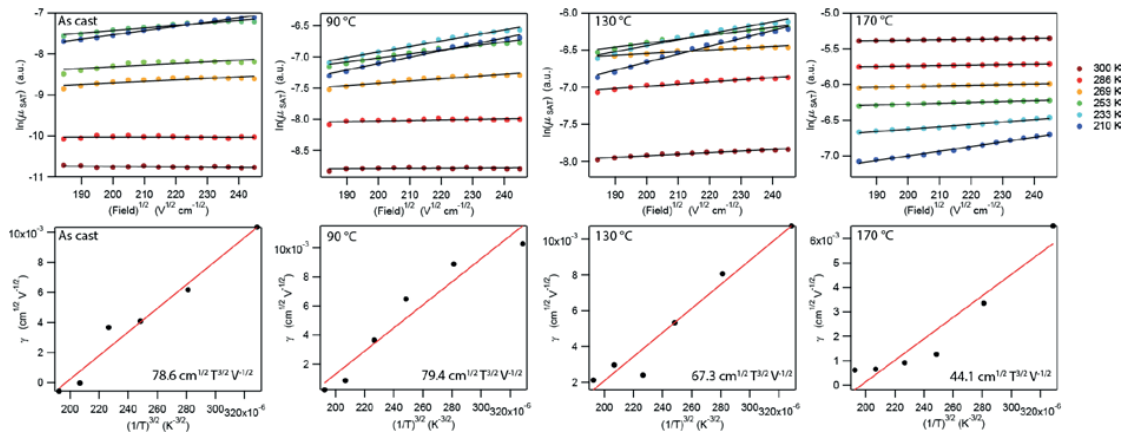


Figure A-13. $\frac{\partial \ln(\mu)}{\partial \sqrt{E}}$ expressed here as γ as function of temperature according to a PF relationship. Linear fitting is shown in red. The obtained slope varies from 44 to 79 $\text{cm}^{1/2} \text{T}^{3/2} \text{V}^{-1/2}$. Once corrected for the field the value obtained is in the order of $10^4 \text{T}^{3/2}$.

Appendix B

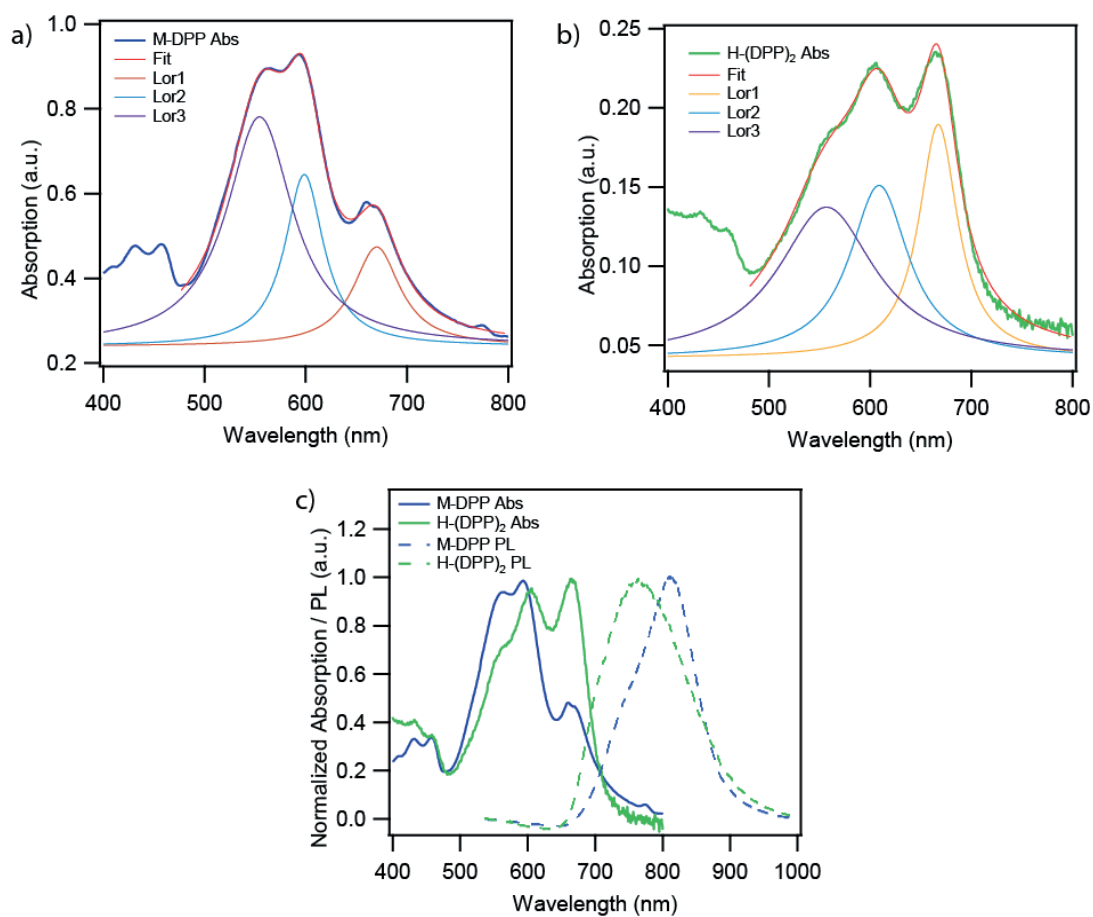


Figure B-1. Deconvoluted absorption spectrum of a) M-DPP and b) H-(DPP)₂ using a sum of 3 Lorentzian functions for the fitting. c) Absorption spectrum (solid) and emission spectrum (dashed) of H-(DPP)₂ (green) and M-DPP (blue) in solid-state.

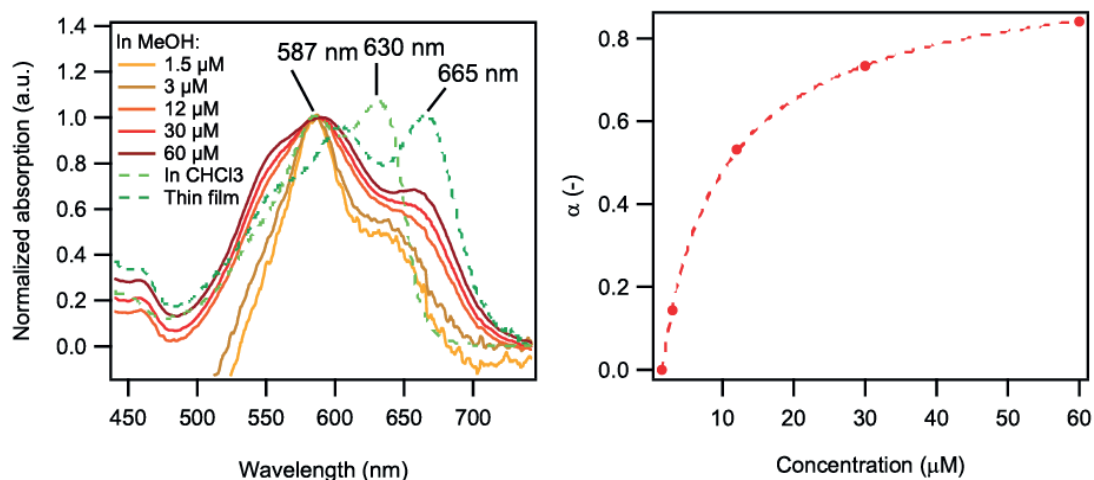


Figure B-2. (a) Absorption spectrum of $H-(DPP)_2$ in methanol at different concentration. Light green dashed line shows absorption spectrum of $H-(DPP)_2$ dissolved in $CHCl_3$ while dark green dashed line shows solid-state absorption. (b) Aggregated fraction obtained from the absorption at 700 nm in function of concentration in MeOH. Fitting for cooperative self-assembly is shown in dashed line.

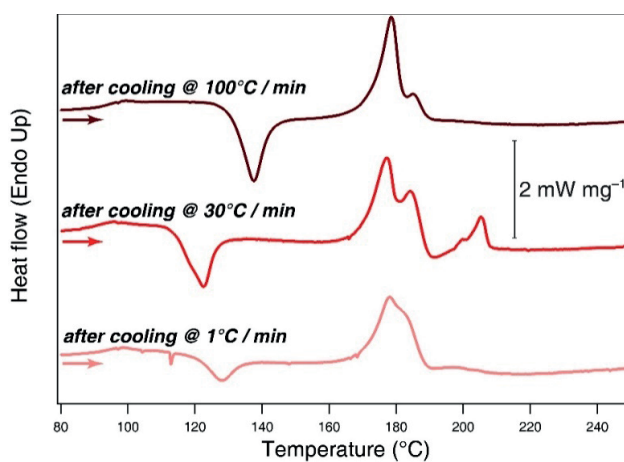


Figure B-3. Differential scanning calorimetry heating curves of $H-(DPP)_2$ drop-casted sample at 10 °C min⁻¹ after cooling from the melt at different speed as indicated.

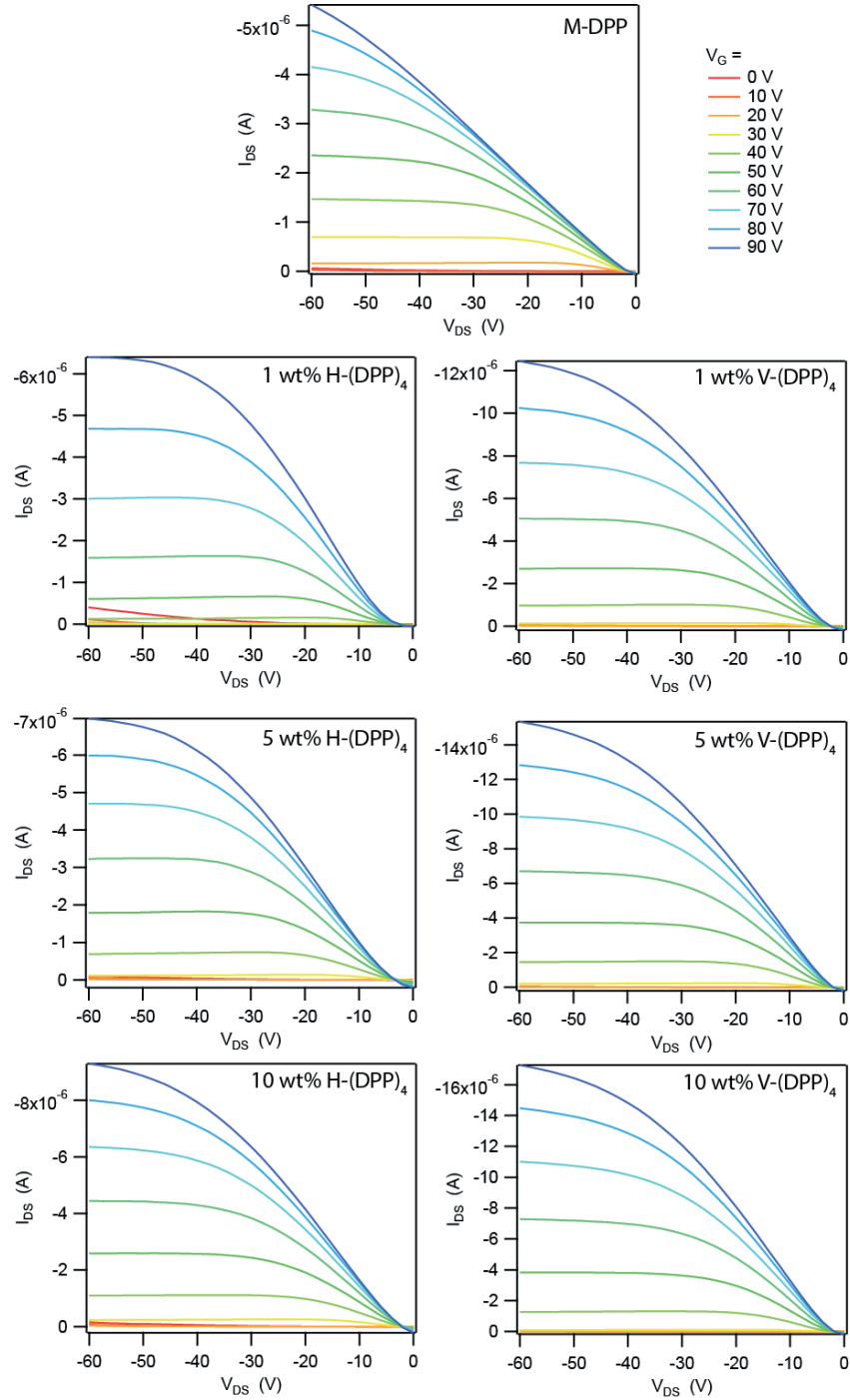


Figure B-4. Output curves for transistors (channel length $20\ \mu\text{m}$, channel width of $1\ \text{cm}$) prepared with neat M-DPP, 1, 5, 10 wt% H-(DPP)₂ and 1, 5, 10 wt% V-(DPP)₂ and annealed at $110\ ^\circ\text{C}$ for 10 min. Measured on more than 6 months old devices.

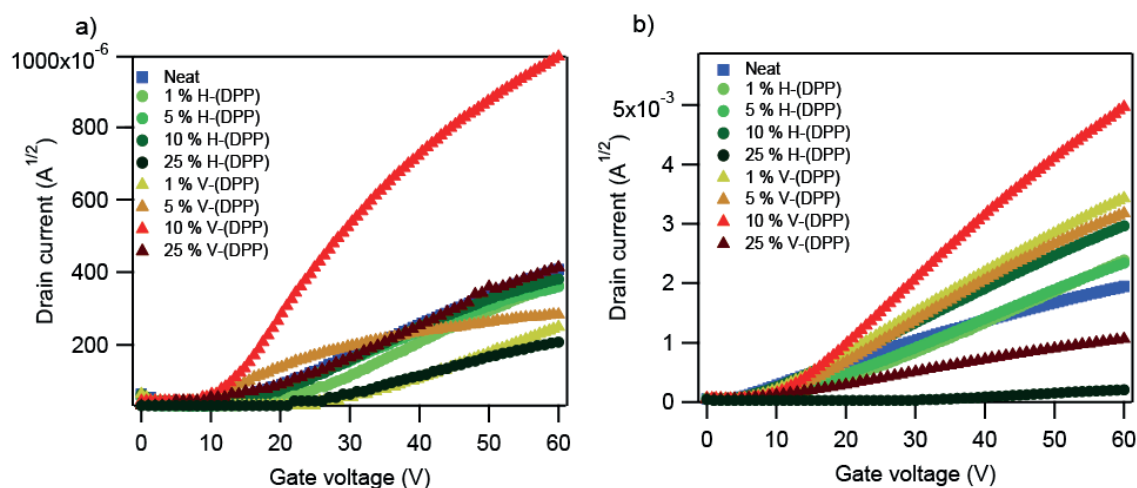


Figure B-5. OFET device transfer curves for the neat M-DPP and blend transistors as-cast (a) and after annealing (b) at 110 °C for 10 min. (channel length 20 μ m, channel width of 1 cm)

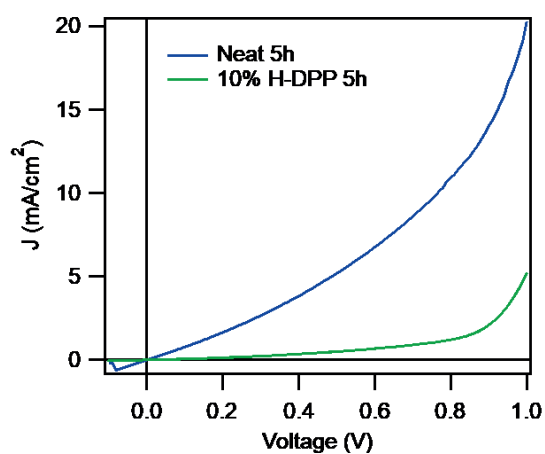
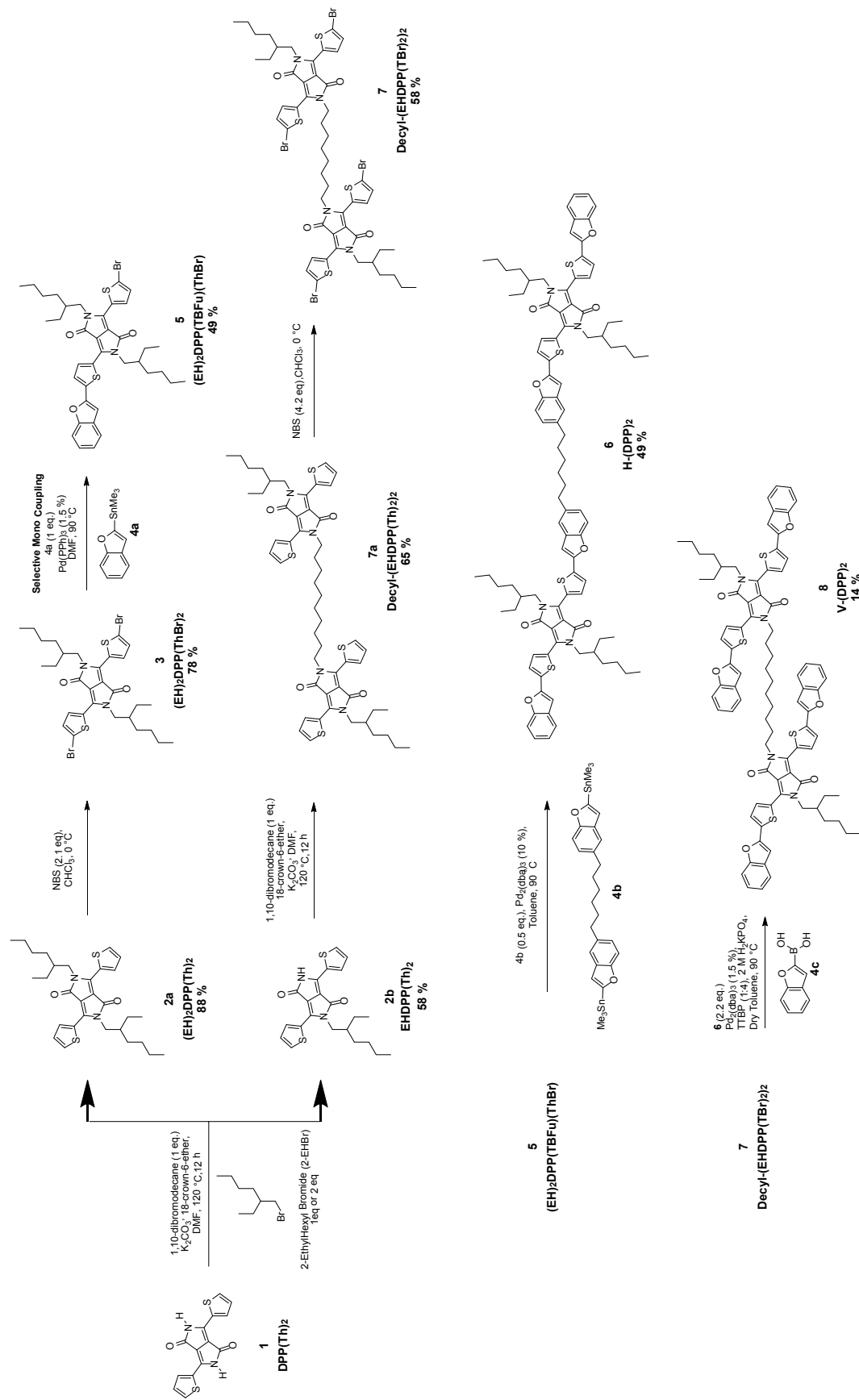


Figure B-6. J - V curves in dark conditions of M-DPP:PCBM neat and with 10 wt% H-(DPP) $_2$ after 5 h annealing prior to aluminium deposition.

Figure B-7. Full Synthetic Route of H-(DPP)₂ and V-(DPP)₂.

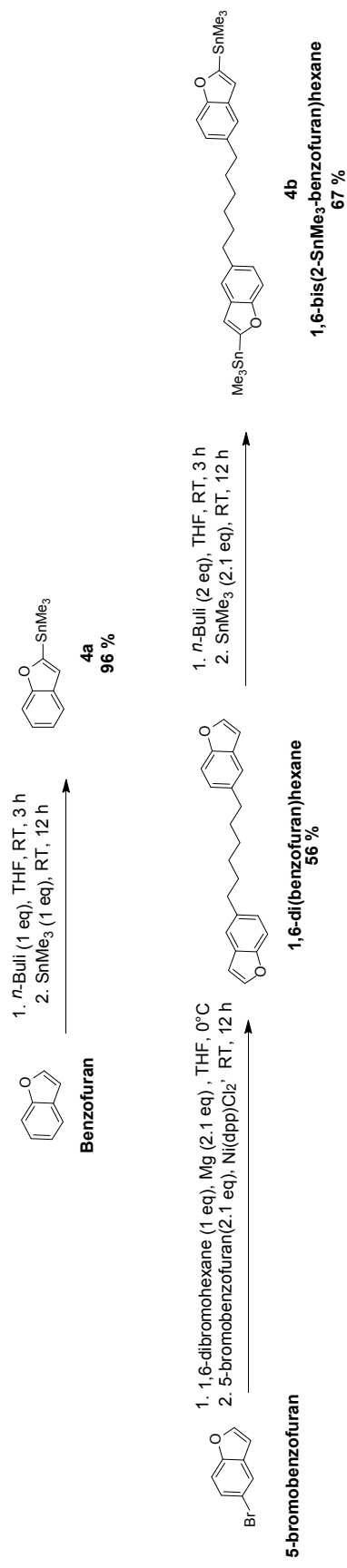


Figure B-8. Stannylation of Benzofuran moieties.

Synthetic Procedures

All reagents were of commercial reagent grade (Sigma-Aldrich, Acros or Fluorochem) and were used without further purification. Toluene, Chloroform, Tetrahydrofuran (Fisher Chemical, HPLC grade) and chlorobenzene (Alfa Aesar, HPLC grade) were purified and dried on a Pure Solv-MD Solvent Purification System (Innovative Technology, Amesbury, United States) apparatus. Normal phase silica gel chromatography was performed with an Acros Organic silicon dioxide (pore size 60 Å, 40–50 µm technical grade). The ^1H and ^{13}C NMR spectra were recorded at RT unless otherwise stated using per-deuterated solvents as internal standards on a NMR Bruker Advance III-400 spectrometer (Bruker, Rheinstetten, Germany). Chemical shifts are given in parts per million (ppm) referenced to residual ^1H or ^{13}C signals in CDCl_3 (respectively, 7.26 and 77.16) and dichloromethane- d_2 (respectively 5.32 and 53.84). EI-MS spectrum was recorded on an EI/CI-1200L GC-MS (Varian) instrument. Atomic-Pressure-Photoionization-Source (APPI) MS spectrum was recorded on an ESI/APCI LC-MS Autopurification System with a ZQ Mass detector (Waters, Milford, United States) instrument using a positive mode. Matrix-Assisted-Laser-Desorption/Ionization Time-of-Flight (MALDI-TOF) MS spectrum are recorded on a Bruker MALDI-TOF AutoFlex speed instrument using alpha-cyano-4-hydroxycinnamic acid, and 2,5-Dihydroxybenzoic acid as matrix. DPP(TBFu) $_2$ was synthesized according to literature procedure (*Adv. Funct. Mater.* **2009**, *19*, 3063-3069). Both H-(DPP) $_2$ and V-(DPP) $_2$ were purified using a Biotage IsoleraTM Spektra Accelerated Chromatographic Isolation SystemTM with a Biotage ZIP[®] Sphere cartridges (60µm spherical silica) before device fabrication. Synthesis of 2,5-Dihydro-3,6-di-2-thienyl-pyrrolo[3,4-*c*]pyrrole-1,4-dione (DPP(Th) $_2$ - **1**) (see *J. Polym. Sci. A Polym. Chem.* **2010**, *48*, 1669-1675)

Preparation of stannylated Benzofuran moieties

1,6-di(benzofuran)hexane was synthesized based on our previously published procedure (*Chem. Sci.* 2014, *5*, 4922-4927): To a solution of 1,6-dibromohexane (2.0 g, 8.2 mmol) in dried tetrahydrofuran (80 mL), magnesium turnings (418.4 mg, 17.2 mmol) was added dropwise at 0 °C over 1 h under argon. This was then allowed to warm up to room temperature and left to stir for 4 h. 5-bromobenzofuran (3.39 g, 17.2 mmol) and dichloro[1,3-bis(diphenylphosphino)propane]nickel (5 % eq, 0.41 mmol) were added quickly at –30 °C and was then left to stir at room temperature for 12 h. Saturated ammonium chloride was added to quench the reaction (approximately 30-40 mL). Diethyl ether was then used to extract the organic phase from the crude mixture, subsequently washed with brine and dried over magnesium sulfate, filtered and concentrated under vacuum. This was then subjected to silica gel chromatography using hexane as an elution solvent to obtain a white solid after precipitation in methanol affording the product (2.1 g, 80.5 %).

¹H NMR (400 MHz, CDCl₃) δ 7.63 (s, 2H), 7.45 (d, *J* = 11.0 Hz, 4H), 7.16 (d, *J* = 8.2 Hz, 2H), 6.75 (s, 2H), 2.74 (t, *J* = 7.8 Hz, 2H), 1.70 (p, *J* = 7.2 Hz, 2H), 1.35 (dd, *J* = 20.6, 6.6 Hz, 8H). δ_c (400 MHz, CDCl₃) 145.01, 137.43, 124.99, 120.39, 110.93, 106.42, 35.92, 32.19, 29.76, 29.74, 29.63, 29.58, 29.34.

General procedure for the stannylation of Benzofuran and 1,6-di(benzofuran)hexane

1-Benzofuran or 1,6-di(benzofuran)hexane (1 eq) was placed in an oven-dried 100 mL Schlenk flask and degassed by three vacuum/nitrogen cycles. Anhydrous THF (20 mL) was injected and the solution was cooled to -78 °C for 15 min after which, N-butyllithium (2.5 M in hexanes, at 1.1 and 2.1 eq respectively) was added slowly, and the reaction was left stirring for 1-2 h. Tributyltin chloride (1.1 and 2.1 eq, respectively) was added slowly, the reaction was allowed to heat up to room temperature over 12 h. H₂O (10 mL) was then added to quench the reaction, after which the crude was then concentrated under vacuum, diluted with water (200 mL), 1 M NaOH (50 mL) and extracted with hexane. The organic phase was collected, dried over MgSO₄, followed by solvent removal under vacuum to afford a yellow-oil of **4a** at a yield of 96 % and a white solid of **4b** at a yield of 67 %.

4a: ¹H NMR (400 MHz, CDCl₃) δ 7.66 (dd, *J* = 16.3, 7.6 Hz, 2H), 7.33 (dt, *J* = 16.5, 7.6 Hz, 2H), 7.05 (d, *J* = 2.2 Hz, 1H), 0.54 (d, *J* = 2.1 Hz, 9H); δ_c (300 MHz, CDCl₃) 193.83, 155.18, 127.76, 127.14, 124.09, 123.39, 116.76, 112.55, -9.55.

4b: ¹H NMR (400 MHz, CDCl₃) δ 7.43 (d, *J* = 8.3 Hz, 3H), 7.37 (s, 2H), 7.09 (d, *J* = 8.3 Hz, 2H), 6.90 (s, 2H), 2.71 (t, *J* = 7.6 Hz, 5H), 1.77 – 1.57 (m, 6H), 1.43 – 1.16 (m, 24H), 0.44 (s, 18H); δ_c (300MHz, CDCl₃) 136.86, 127.98, 124.42, 119.60, 117.40, 110.45, 35.89, 32.24, 29.74, 29.72, 29.63, 29.57, 29.29.

Preparation of diketopyrrolopyrrole(DPP) derivatives

General Procedure for the symmetric bi- or selective mono-alkylation of DPP(Th)₂ (**1**), EHDPP(Th)₂ (**2b**), and Decyl-(EHDPP(Th)₂)₂ (**7a**)

DPP(Th)₂ (**1**) or EHDPP(Th)₂ (**2b**) and anhydrous K₂CO₃ were stirred in anhydrous (DMF) under Argon at 130 °C for 1 h. 2-EthylhexylBromide or 1,10-dibromodecane was then added dropwise and the reaction mixture was stirred at 130 °C for a further 20 h for a symmetric bi- or selective mono-alkylation. The reaction mixture was allowed to cool to room temperature then it was poured into ice water (1 L) and the resulting suspension was stirred for 1 h. After the solid was dried under vacuum

to give the crude product, and separated via silica gel column chromatography using Hexane/Chloroform mixture as eluent.

For **(EH)₂DPP(Th)₂ (2a)**, 1 eq of **DPP(Th)₂ (1)** and 2.5 eq of 2-EthylhexylBromide was used to obtain the final product as red crystals after recrystallization with Ethanol (Average Yield 88 %).

¹H NMR (400 MHz, CDCl₃) δ 8.92 (d, *J* = 3.9 Hz, 2H), 7.65 (d, *J* = 5.0 Hz, 2H), 7.30 (d, *J* = 4.3 Hz, 2H), 4.13 – 3.98 (m, 4H), 1.89 (p, *J* = 6.3 Hz, 2H), 1.33 (dd, *J* = 37.4, 16.5, 9.2, 5.0 Hz, 8H), 0.89 (dt, *J* = 9.1, 7.1 Hz, 6H). MS: 524.25 (APPI): Calcd.[C₃₀H₄₀N₂O₂S₂]: 524.78.

For **EHDPP(Th)₂ (2b)**, 1 eq of **DPP(Th)₂ (1)** and 1 eq of 2-EthylhexylBromide was used to obtain the product as a red powder after precipitation with hexane/chloroform mixture at average Yield 58 %.

¹H NMR (400 MHz, CDCl₃) δ 8.86 (d, *J* = 3.7 Hz, 1H), 8.49 (s, 1H), 8.40 (d, *J* = 3.7 Hz, 1H), 7.69 (d, *J* = 5.1 Hz, 1H), 7.63 (d, *J* = 5.0 Hz, 1H), 7.37 – 7.23 (m, 5H), 4.06 (q, *J* = 7.1 Hz, 2H), 1.89 (q, *J* = 6.7 Hz, 1H), 1.48 – 1.18 (m, 8H), 0.98 – 0.82 (m, 7H). δ_C (300 MHz, CDCl₃) 135.46, 132.18, 130.89, 130.61, 129.23, 128.49, 45.91, 39.11, 30.22, 28.35, 23.54, 23.07. MS: 412.13 (APPI): Calcd. [C₂₂H₂₄N₂O₂S₂]: 412.57.

For **Decyl-(EHDPP(Th)₂)₂ (7a)**, 2 eq of **EHDPP(Th)₂ (2b)** and 1 eq of 1,10-dibromodecane was used to obtain the product as a dark red solid with an average yield of 65 % after separation via chromatography using CHCl₃ as eluent, and precipitation in CH₂Cl₂:Methanol.

¹H NMR (400 MHz, CDCl₃) δ 9.00 – 8.77 (dd, *J* = 26.7, 3.9 Hz, 4H), 7.70 – 7.56 (d, *J* = 5.1 Hz, 4H), 7.36 – 7.18 (m, 4H), 4.18 – 3.92 (dh, *J* = 14.8, 7.4, 6.6 Hz, 8H), 2.08 – 1.63 (m, 12H), 1.49 – 1.11 (m, 12H), 0.96 – 0.74 (q, *J* = 7.2 Hz, 12H); δ_C (300 MHz, CDCl₃) 161.76, 161.36, 140.38, 140.06, 135.38, 135.17, 130.69, 130.64, 130.59, 130.57, 129.84, 129.73, 128.65, 28.40, 108.05, 107.57, 63.03, 45.86, 42.18, 39.09, 32.74, 30.22, 29.91, 29.25, 29.16, 29.09, 29.05, 28.35, 26.79, 26.76, 25.64, 23.52, 23.08, 14.05, 10.50.

General Procedure for the bromination of **DPP(Th)₂ (1)** and **Decyl-(EHDPP(Th)₂)₂ (7a)**

To a solution of **1** or **7a** in an Argon filled chloroform flask, wrapped in aluminium foil to exclude light at 0 °C, N-bromosuccinimide at 2.1 eq and 4.2 eq respectively. After the reaction was completed as indicated from TLC, the mixture was poured into cold methanol, and left to stir for 1h. The precipitate was filtered and the solid was washed with methanol (2 × 200 mL) then dried under vacuum.

The crude product was recrystallized from Hexane/chloroform to give the product as a dark purple solid of **(EH)₂DPP(ThBr)₂ (3)** (Yield = 78%) and **Decyl-(EHDPP(TBr)₂)₂ (7)** (Yield = 57.8%).

(3) ¹H NMR (400 MHz, CDCl₃) δ 8.67 (d, *J* = 4.2 Hz, 4H), 7.25 (d, *J* = 4.2 Hz, 4H), 3.97 (h, *J* = 7.8 Hz, 4H), 1.86 (q, *J* = 6.5 Hz, 2H), 1.45 – 1.21 (m, 16H), 0.91 (q, *J* = 7.4 Hz, 12H); MS: 567.95 (APPI); Calcd. [C₂₂H₂₂Br₂N₂O₂S₂]: 570.36.

(7) ¹H NMR (400 MHz, CDCl₃) δ 8.68 (dd, *J* = 23.8, 4.1 Hz, 4H), 7.29 (s, 5H), 6.97 (d, *J* = 3.7 Hz, 1H), 3.97 (tq, *J* = 14.9, 7.3 Hz, 2H), 3.58 – 3.36 (m, 1H), 1.85 (q, *J* = 6.5 Hz, 1H), 1.72 (p, *J* = 8.3, 7.6 Hz, 1H), 1.49 – 1.08 (m, 22H), 1.00 – 0.75 (m, 7H). MS (APPI): *m/z* [M]⁺ = 1273.10

General Procedure for Stille Coupling the optimization of **(EH)₂DPP(TBFu)(ThBr) (5)**

In a 100 mL oven-dried Schlenk flask, EHDPP(TBr)₂ (2.89 g, 4.24 mmol), BFSnMe₃ **(2)** (1.19 g, 4.24 mmol) and tetrakis(triphenylphosphine) palladium(0) (0.489 g, 0.423 mmol) were placed. The flask was then degassed by three vacuum/nitrogen cycles. Anhydrous DMF or toluene (15 mL) was then injected into the flask and the solution mixture was stirred for 12 h at 100 °C under Argon. After cooling to room temperature, the reaction mixture was poured into water (300 mL) with brine (30 mL). The precipitate was filtered over Celite, washed with water and methanol, and then washed with CHCl₃ until the washings were colourless. The organic extract was then dried over MgSO₄, and the solvent was removed under vacuum and the product was purified by column chromatography (hexane/DCM) to afford EHDPP(TBFu)(ThBr) as a dark blue solid (1.50 g, 49.2 %).

¹H NMR (400 MHz, CDCl₃) δ 9.03 – 8.95 (d, *J* = 4.2 Hz, 1H), 8.68 – 8.61 (d, *J* = 4.2 Hz, 1H), 7.64 – 7.56 (m, 2H), 7.56 – 7.48 (d, *J* = 8.1 Hz, 1H), 7.38 – 7.30 (td, *J* = 8.2, 7.8, 1.4 Hz, 1H), 7.30 – 7.20 (s, 9H), 7.09 – 7.04 (s, 1H), 4.14 – 4.03 (m, 2H), 4.03 – 3.91 (m, 2H), 2.01 – 1.77 (m, 1H), 1.48 – 1.16 (m, 12H), 1.01 – 0.78 (m, 14H). MS (ESI): *m/z* [M]⁺ = 721.1962

Hexyl-(EHDPP(TBFu)₂)₂ **(6) H-(DPP)₂**

In a 50 ml oven-dried Schlenk flask 144 mg of 1,6-bis(2-(trimethylstannyl)benzofuran-5-yl)hexane (144 mg, 0.22 mmol) and EHDPP(TBFu)(ThBr) (353 mg, 0.49 mmol) were added in 10 ml of anhydrous chlorobenzene under an Argon atmosphere using 2 mol% of tris(dibenzylideneacetone)dipalladium and tri(*o*-tolyl)-phosphine as a catalyst. After, 24 h the reaction was left to cool down, and the crude was allowed to precipitate in methanol, and collected via filtration with several hexane and methanol washings. The crude was then filtered over Celite, washed with water and methanol, and then washed with CHCl₃ until the washings were colourless. The organic extract was then dried with

MgSO₄, and the solvent was removed under vacuum and the product was purified by column chromatography (hexane/DCM) to afford H-(DPP)₂ as a dark blue solid (1.50 g, 49.2 %).

¹H NMR (400 MHz, CDCl₃) δ 8.99 (t, *J* = 3.0 Hz, 4H), 7.55 (q, *J* = 5.2, 4.1 Hz, 6H), 7.50 (d, *J* = 8.1 Hz, 2H), 7.40 (d, *J* = 8.4 Hz, 2H), 7.31 (d, *J* = 6.9 Hz, 2H), 7.23 (s, 4H), 7.13 (d, *J* = 8.4 Hz, 2H), 7.01 (s, 2H), 6.94 (s, 2H), 4.17 – 3.97 (m, 5H), 2.68 (t, *J* = 7.6 Hz, 2H), 1.93 (q, *J* = 6.5 Hz, 3H), 1.67 (t, *J* = 7.3 Hz, 3H), 1.35 (dq, *J* = 45.5, 12.4, 10.0 Hz, 24H), 0.91 (dt, *J* = 13.5, 7.0 Hz, 15H); δ_C (400 MHz, CD₂Cl₂) 125.40, 125.37, 123.55, 121.25, 111.15, 103.72, 103.59, 53.96, 53.89, 53.69, 53.62, 53.42, 53.35, 53.15, 52.88, 29.96, 28.51, 28.12, 26.37, 23.10; MS (MALDI-TOF): *m/z* [M]⁺ = 1596.19

N-EthylHexy-N-Decyl-Bis-EHDPP(TBFu)₂ (7) *V*-(DPP)₂

In a 50 mL Schleck flask, Decyl-(EHDPP(TBr)₂)₂ (0.128 mg, 0.11 mmol) Benzofuran-2-boronic acid (73 mg, 0.45 mmol), tris(dibenzylideneacetone)dipalladium(0) (2.8 mg), and tri-tert-butylphosphonium tetrafluoroborate (3.6 mg) was mixed with 15 mL of anhydrous toluene and 2 mL of 2 M potassium phosphate and the resulting mixture was degassed for 10 min. The reaction mixture was stirred and heated to 90 °C under argon overnight. After which the reaction mixture was allowed to cool down to room temperature, and poured into 300 mL of methanol and then stirred for 1 h. The precipitated solid was then collected by vacuum filtration and washed with several portions of distilled water, methanol, isopropanol, and petroleum ether. The solid was then washed with hot methanol, and precipitated several times in methanol/Hexane/CH₂Cl₂. The crude product was purified by flash chromatography using chloroform as eluent, and the solvent was removed in vacuum to obtain a pure product of *V*-(DPP)₂ (0.020 mg, 14 %).

¹H NMR (400 MHz, CDCl₃) δ 9.08 – 8.92 (d, *J* = 4.3 Hz, 1H), 7.67 – 7.61 (m, 2H), 7.60 – 7.53 (d, *J* = 8.6 Hz, 1H), 7.41 – 7.33 (t, *J* = 7.7 Hz, 1H), 7.33 – 7.25 (d, *J* = 1.3 Hz, 25H), 7.16 – 7.10 (s, 1H), 4.73 – 4.56 (t, *J* = 11.4 Hz, 1H), 4.23 – 4.07 (d, *J* = 15.3 Hz, 1H), 3.58 – 3.46 (d, *J* = 5.3 Hz, 2H), 3.25 – 3.19 (s, 0H), 1.99 – 1.84 (s, 1H), 1.83 – 1.67 (s, 1H), 1.69 – 1.48 (d, *J* = 1.4 Hz, 32H), 1.42 – 1.24 (d, *J* = 32.4 Hz, 3H), 1.24 – 1.12 (s, 1H), 1.12 – 0.97 (m, 1H), 0.97 – 0.82 (dt, *J* = 14.6, 6.7 Hz, 6H); δ_C (600 MHz, CDCl₃) 161.69, 154.92, 149.98, 139.64, 138.03, 136.78, 136.47, 129.46, 128.85, 125.55, 125.45, 123.61, 121.29, 111.35, 108.67, 103.77, 77.37, 77.16, 77.11, 76.86, 46.00, 42.89, 42.73, 39.22, 38.07, 29.83, 28.48, 23.53, 23.23, 14.29, 10.57; MS (MALDI-TOF): *m/z* [M+Na]⁺ = 1450.9.

Appendix C

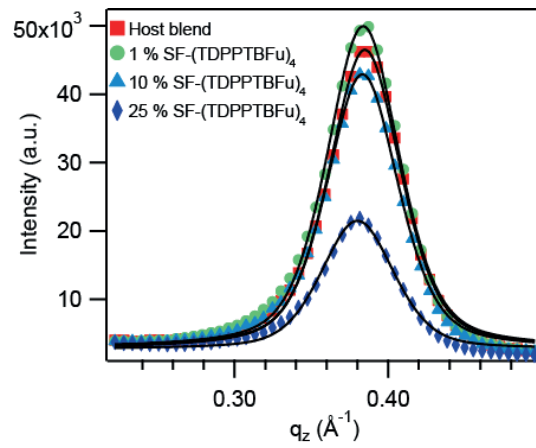


Figure C-1. Out-of-plane grazing incident wide angle X-ray diffraction of thin films with varying amount of ternary additive. Solid black lines are the respective Pseudo-Voigt fit.

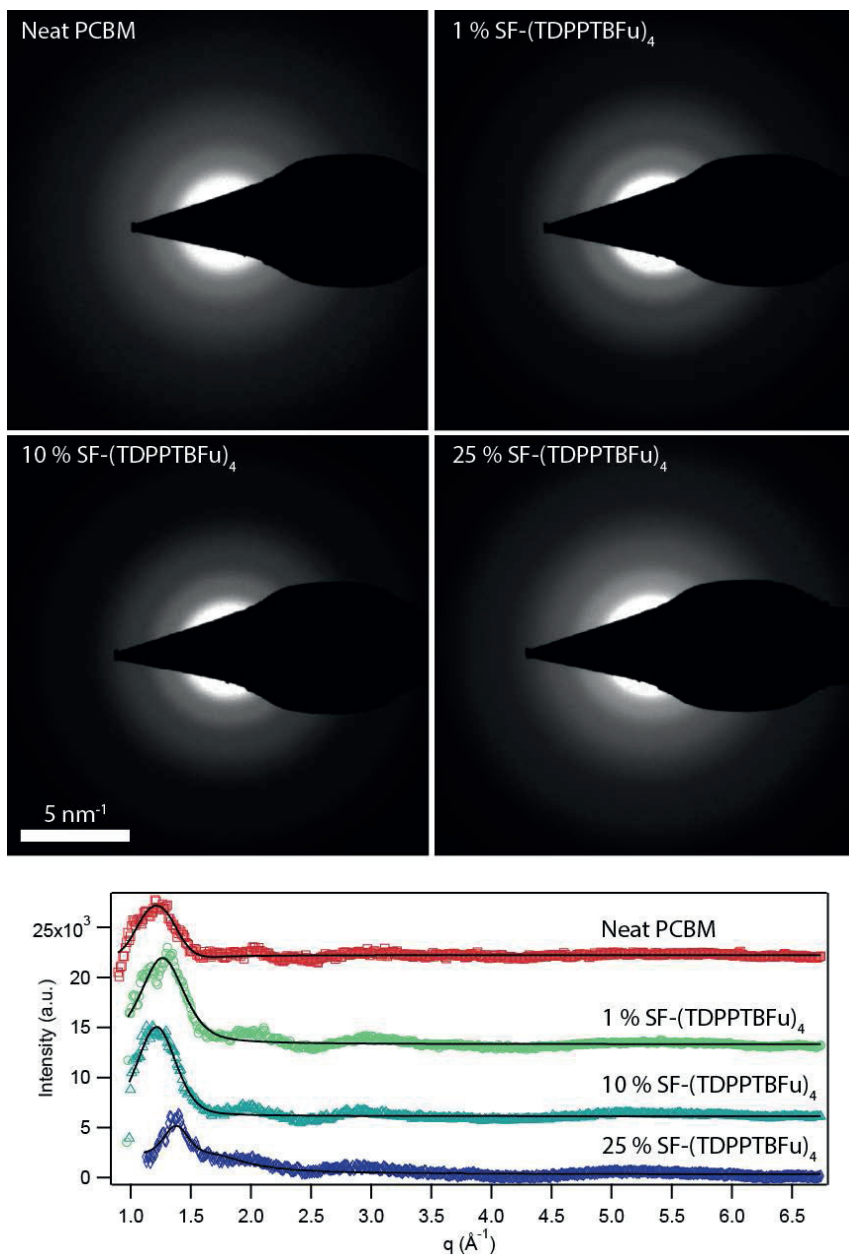


Figure C-2. Electron diffraction pattern of films with varying amount of ternary additive. Bottom graph shows cross sections of the diffraction intensity vs. q -vector. Solid black lines are the respective Pseudo-Voigt fit.

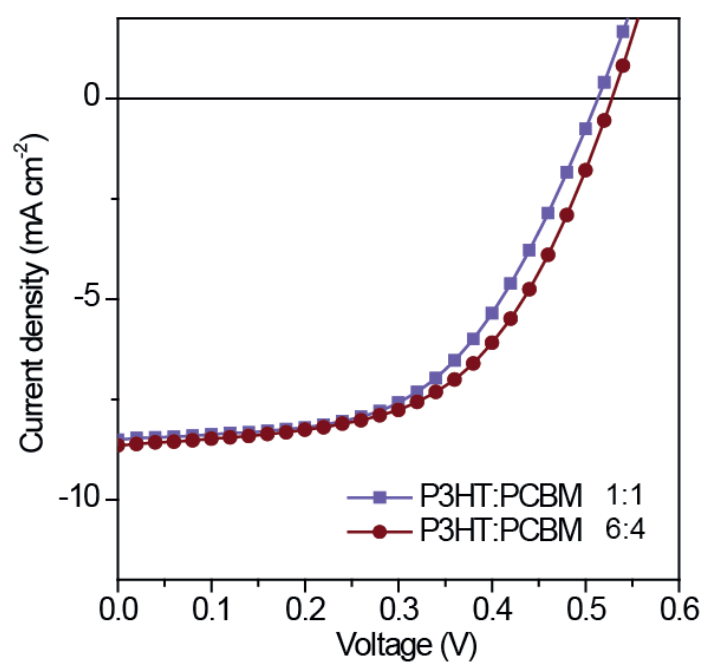


Figure C-3. Typical J - V curves for P3HT:PCBM blends at 1:1 and 6:4 ratios.

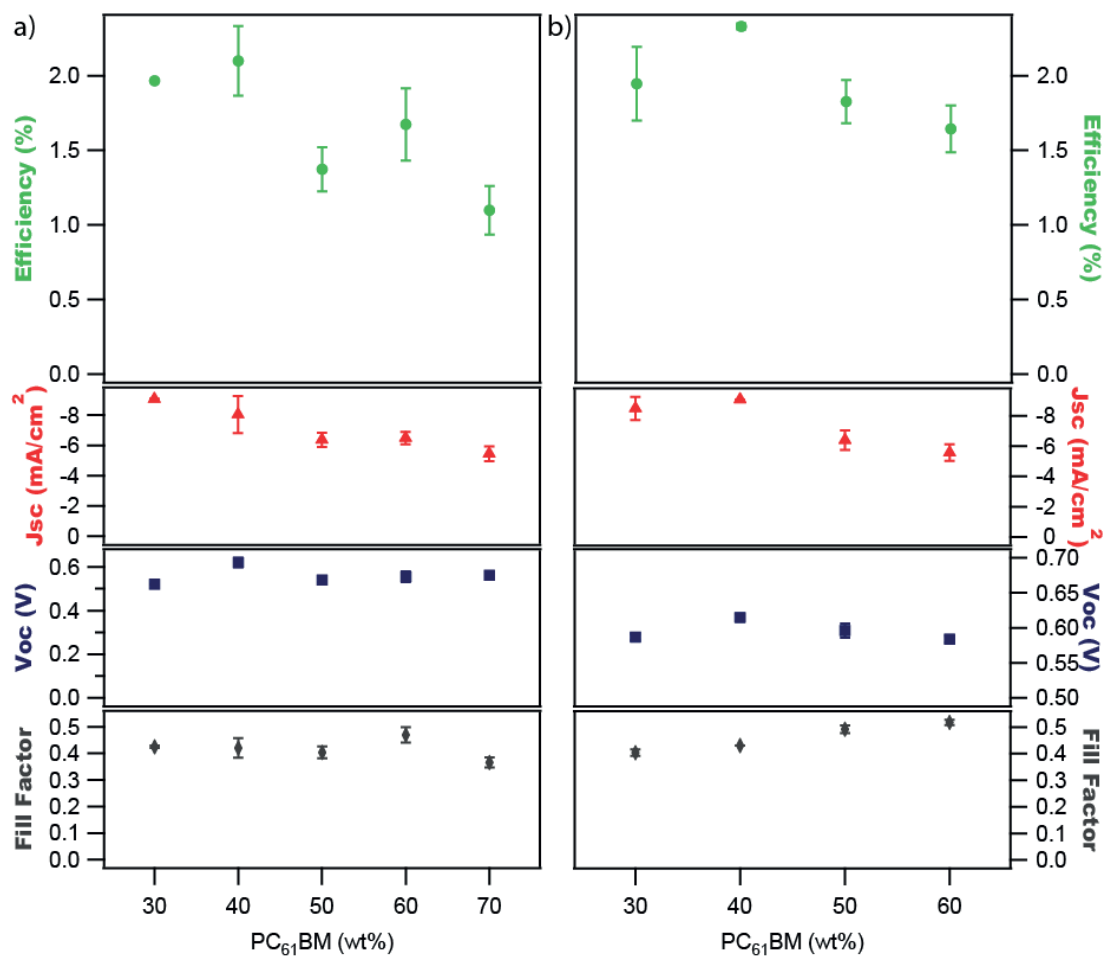


Figure C-4. Average figures of merit of devices containing 5 wt% (a) SF-(DPP)4 and (b) SF-(PDI)4 in function of PCBM content. Optimum efficiency is found at 6:4 P3HT:PCBM ratio, which is identical to the host blend optimum.

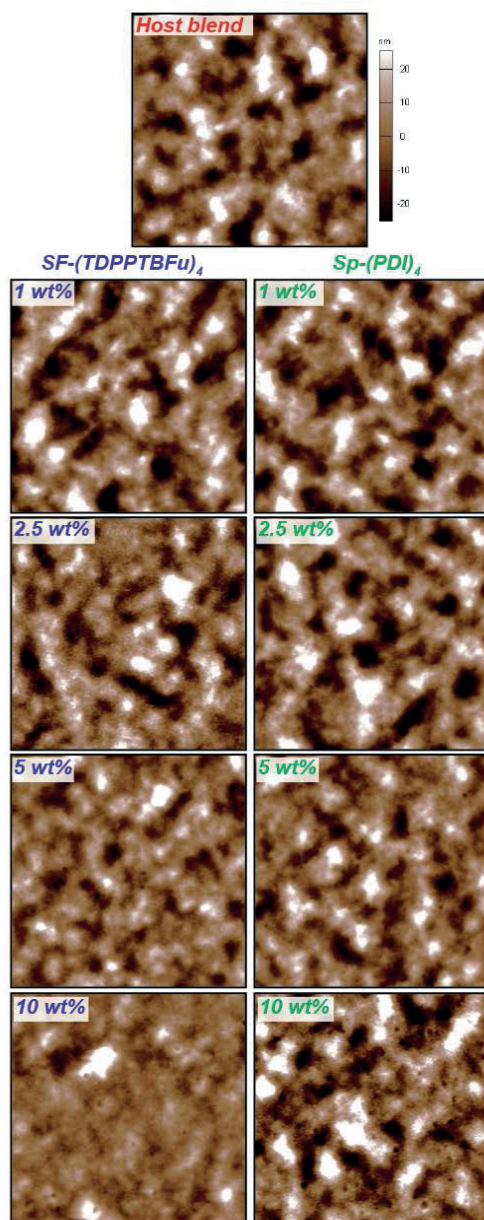


Figure C-5. Atomic force microscopy height images ($5\ \mu\text{m} \times 5\ \mu\text{m}$) of host blend and with additive. The slightly smoother surface at 10 wt% SF-(DPP)₄ might arise from the capping layer formation on the surface.

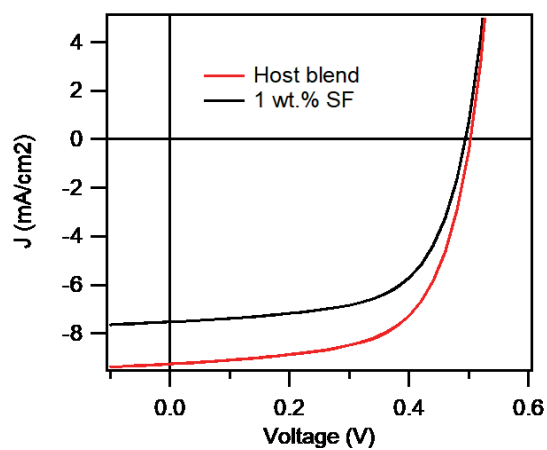


Figure C-6. *J-V* curve of P3HT:PCBM host blend and containing 1 wt% SF molecule (9,9'-spirobifluorene). Performances are decreased as expected from the large bandgap of the spirocore acting as an insulator inside the blend.

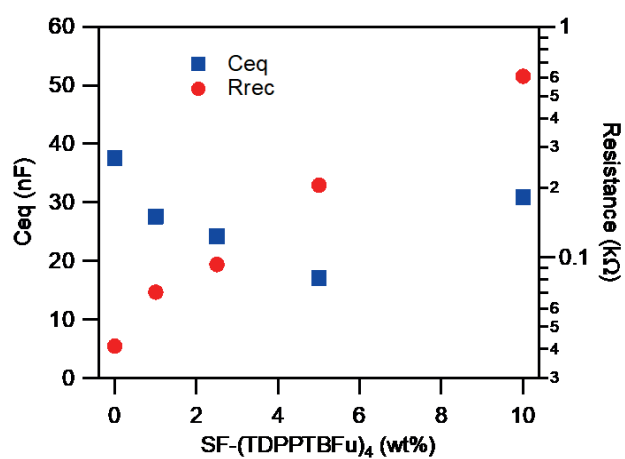


Figure C-7. Equivalent capacitance of the constant phase element (blue squares) and resistance (red dots) in function of SF-(DPP)₄ content.

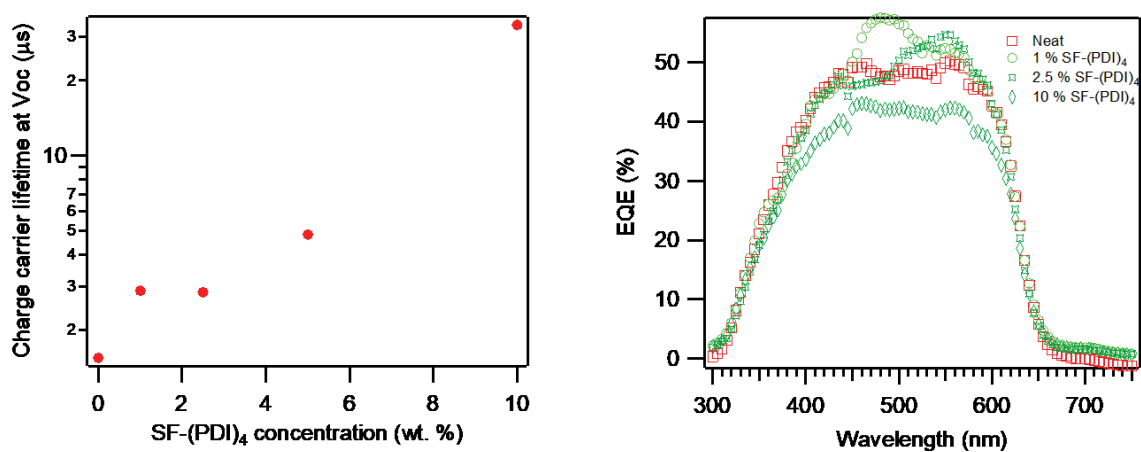


Figure C-8. (left) lifetimes extracted out of impedance spectroscopy under 1 Sun at OC for as function of SF-(PDI)₄ content. (right) external quantum efficiency for P3HT:PCBM host blend and containing varying amount of SF-(PDI)₄.

Synthesis Experimental Procedures

General

All reagents were of commercial reagent grade (Sigma-Aldrich, Acros or Fluorochem) and were used without further purification. Toluene, Chloroform, Tetrahydrofuran (Fisher Chemical, HPLC grade) and chlorobenzene (Alfa Aesar, HPLC grade) were purified and dried on a Pure Solv-MD Solvent Purification System (Innovative Technology, Amesbury, United States) apparatus. Normal phase silica gel chromatography was performed with an Acros Organic silicon dioxide (pore size 60 Å, 40–50 µm technical grades). The ¹H and ¹³C NMR spectra were recorded at room temperature using per-deuterated solvents as internal standards on a NMR Bruker Advance III-400 spectrometer (Bruker, Rheinstetten, Germany). Chemical shifts are given in parts per million (ppm) referenced to residual ¹H or ¹³C signals in CDCl₂ (¹H: 7.26, ¹³C: 77.16) and dichloromethane-*d*₂ (²H: 5.32, ¹³C: 53.84). EI-MS spectrum was recorded on an EI/CI-1200L GC-MS (Varian) instrument. Atmospheric-Pressure-Photoionization-Source (APPI) MS spectrum was recorded on an ESI/APCI LC-MS Autopurification System with a ZQ Mass detector (Waters, Milford, United States) instrument using a positive mode. Matrix-Assisted-Laser-Desorption/Ionization Time-of-Flight (MALDI-TOF) MS spectrum was recorded on a Bruker MALDI-TOF AutoFlex speed instrument using, 2,5-Dihydroxybenzoic acid as matrix. Both materials were purified using a Biotage Isolera™ Spektra Accelerated Chromatographic Isolation System™ with a Biotage ZIP® Sphere cartridges (60µm spherical silica) before device fabrication.

Synthesis of monomeric units of the SF Cascade molecules

Synthesis of the spiro-core (SF-Bpin₄) was performed following the literature procedures by Wu, Schumm *et. al. J. Org. Chem*, **1996**, 61 ,20, 6906-6921, and the synthesis of 2,5-Dihydro-3,6-di-2-thienyl-pyrrolo[3,4-*c*]pyrrole-1,4-dione (DPP(Th)₂) based on *J. Polym. Sci. A Polym. Chem.* **2010**, 48, 1669-1675.

Procedure for Monomeric units of SF-(DPP)₄

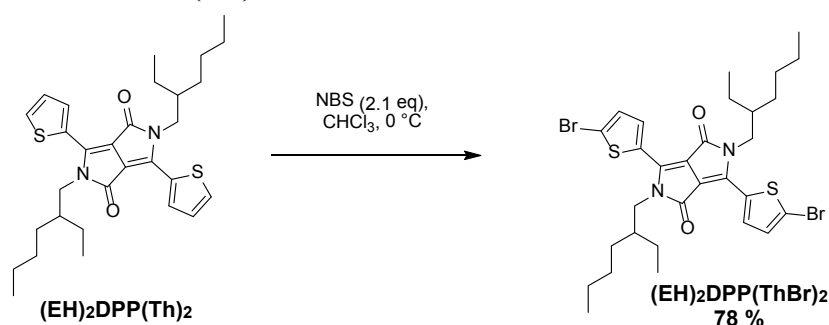
Alkylation of DPP(Th)₂ with 2-ethylhexylbromide



DPP(Th)₂ (1 eq) and anhydrous K₂CO₃ were stirred in anhydrous (DMF) under Argon at 130 °C for 1 h. 2-EthylhexylBromide (2 eq) was then added drop wise and the reaction mixture was stirred at 130 °C for a further 20 h for a symmetric alkylation of the DPP(Th)₂ core. The reaction mixture was allowed to cool to room temperature then it was poured into ice water (1 L) and the resulting suspension was stirred for 1 h. After the solid was dried under vacuum to give the crude product, and separated via silica gel column chromatography using an Hexane/Chloroform mixture as eluent to obtain the **EH₂DPP(Th)₂** as red crystals after recrystallization with Ethanol with a yield of 88%;

¹H NMR (400 MHz, CDCl₃) δ 8.92 (d, *J* = 3.9 Hz, 2H), 7.65 (d, *J* = 5.0 Hz, 2H), 7.30 (d, *J* = 4.3 Hz, 2H), 4.13 – 3.98 (m, 4H), 1.89 (p, *J* = 6.3 Hz, 2H), 1.33 (dd, *J* = 37.4, 16.5, 9.2, 5.0 Hz, 8H), 0.89 (dt, *J* = 9.1, 7.1 Hz, 6H). MS: 524.25 (APPI): Calcd.[C₃₀H₄₀N₂O₂S₂]: 524.78.

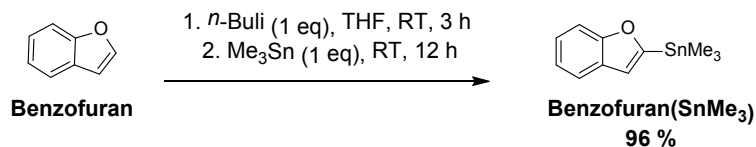
Bromination of EH₂DPP(Th)₂



To a solution of **EH₂DPP(Th)₂** in an Argon filled chloroform flask, wrapped in aluminium foil to exclude light at 0°C, N-bromosuccinimide (2.1 eq) and left o stir overnight. After completed the crude was poured into cold methanol, and left to stir for 1 h. The precipitate was filtered and the solid was washed with methanol (2 × 200 mL) then dried under vacuum. The crude product was recrystallized from Hexane/Chloroform to give the product as a dark purple solid of **(EH)₂DPP(ThBr)₂** (Yield = 78 %).

¹H NMR (400 MHz, CDCl₃) δ 8.67 (d, J = 4.2 Hz, 4H), 7.25 (d, J = 4.2 Hz, 4H), 3.97 (h, J = 7.8 Hz, 4H), 1.86 (q, J = 6.5 Hz, 2H), 1.45 – 1.21 (m, 16H), 0.91 (q, J = 7.4 Hz, 12H); MS: 567.95 (APPI): Calcd. [C₂₂H₂₂Br₂N₂O₂S₂]: 570.36.

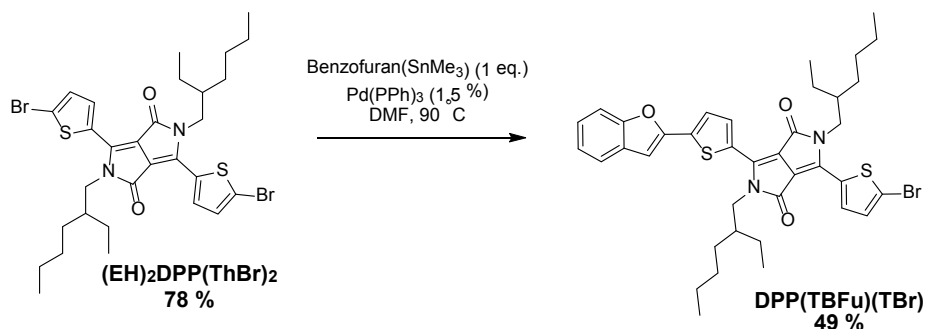
Stannylation of Benzofuran



Benzofuran (1 eq) was placed in an oven-dried 100 mL Schlenk flask and degassed by three vacuum/nitrogen cycles. Anhydrous THF (20 mL) was injected and the solution was cooled to -78 °C for 15 min after which, N-butyllithium (2.5 M in hexanes, at 1.1 and 2.1 eq respectively) was added slowly, and the reaction was left stirring for 1-2 h. Tributyltin chloride (1.1 and 2.1 eq respectively) was added slowly, the reaction was allowed to heat up to room temperature over 12 h. H₂O (5-20 mL) was then added to quench the reaction, after which the crude was then concentrated under vacuum, diluted with water (200 mL), 1 M NaOH (50 mL) and extracted with hexanes. The organic phase was collected, dried over MgSO₄, followed by solvent removal under vacuum to afford a yellow-oil of **4a** at a yield of 96 %.

¹H NMR (400 MHz, CDCl₃) δ 7.66 (dd, J = 16.3, 7.6 Hz, 2H), 7.33 (dt, J = 16.5, 7.6 Hz, 2H), 7.05 (d, J = 2.2 Hz, 1H), 0.54 (d, J = 2.1 Hz, 9H); δ_c (300MHz, CDCl₃) 193.83, 155.18, 127.76, 127.14, 124.09, 123.39, 116.76, 112.55, -9.55.

General Procedure for Stille Coupling reaction of (EH)₂DPP(ThBr)₂



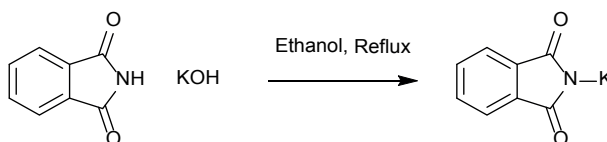
In a 100 mL oven-dried Schlenk flask, EHDPP(TBr)₂ (2.89 g, 4.24 mmol), BFs₃SnMe₃ (1.19 g, 4.24 mmol) and tetrakis(triphenylphosphine) palladium(0) (0.489 g, 0.423 mmol) were placed. The flask was then degassed by three vacuum/nitrogen cycles. Anhydrous DMF or toluene (15 mL) was then injected into the flask and the solution mixture was stirred for 12 h at 100 °C under Argon. After cooling to room temperature, the reaction mixture was poured into water (300 mL) with brine (30 mL). The precipitate was filtered over Celite, washed with water and methanol, and then washed with

CHCl_3 until the washings were colourless. The organic extract was then dried over MgSO_4 , and the solvent was removed under vacuum and the product was purified by column chromatography (hexane/DCM) to afford $\text{EHDPP}(\text{TBFu})(\text{ThBr})$ as a dark blue solid (1.50 g, 49.2 %).

^1H NMR (400 MHz, CDCl_3) δ 9.03 – 8.95 (d, $J = 4.2$ Hz, 1H), 8.68 – 8.61 (d, $J = 4.2$ Hz, 1H), 7.64 – 7.56 (m, 2H), 7.56 – 7.48 (d, $J = 8.1$ Hz, 1H), 7.38 – 7.30 (td, $J = 8.2, 7.8, 1.4$ Hz, 1H), 7.30 – 7.20 (s, 9H), 7.09 – 7.04 (s, 1H), 4.14 – 4.03 (m, 2H), 4.03 – 3.91 (m, 2H), 2.01 – 1.77 (m, 1H), 1.48 – 1.16 (m, 12H), 1.01 – 0.78 (m, 14H). MS (ESI): m/z $[\text{M}]^+ = 721.1962$

Procedure for Monomeric units of SF-(PDI)₄

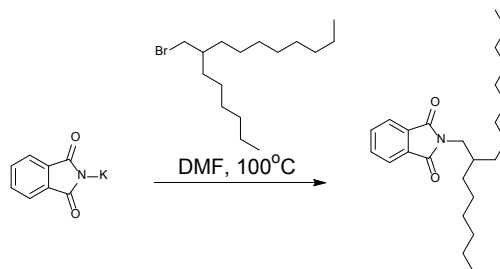
Synthetic steps of 2-hexyldecan-1-amine (HDNH₂) Potassium 1,3-dioxoisindolin-2-ide



Phthalimide (20 g, 0.136 mol) was added to 400 ml absolute ethanol. The mixture was gently heated under reflux and then the hot solution was decanted into a solution of potassium hydroxide (7.6 g, 0.136 mol) in water (7.5 ml) and ethanol (23 ml). The mixture was stirred and cooled quickly to room temperature, and the precipitate was filtered with suction. The crystals obtained were washed with 12 ml of acetone twice to remove any unchanged phthalimide. The yield of air-dried potassium phthalimide is 18.6 g. (82 %).

^1H NMR (400 MHz, CDCl_3) δ 7.95 – 7.88 (dt, $J = 7.6, 3.7$ Hz, 2H), 7.84 – 7.75 (dd, $J = 5.5, 3.1$ Hz, 2H). ^{13}C NMR (300 MHz, CDCl_3) δ_{C} 134.36, 123.65; MS: 184.99 (APPI).

Synthesis of 2-(3-hexylundecyl)isoindoline-1,3-dione

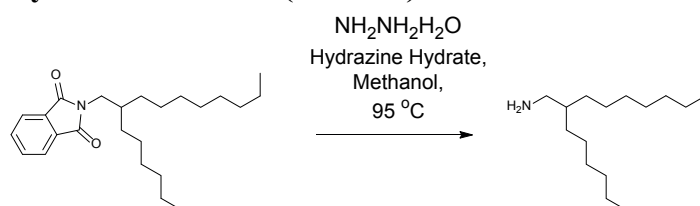


Potassium phthalimide (7.5 g, 0.0404 mol) was added to a solution of 2-decyl-1-tetradecylbromide (15.7 g, 0.0376 mol) in 45 ml dry DMF. The reaction was stirred for 16 hours at 90 °C. After cooling to room temperature, the reaction mixture was poured into 150 ml water and extracted with dichloromethane (3 x 100 ml). The combined organic layers were washed with 200 ml 0.2 M KOH, water,

saturated ammonium chloride, dried over anhydrous MgSO_4 , and concentrated under reduced pressure. The resulting crude yellow oil was purified via column chromatography (silica gel: dichloromethane) giving the product as a pale yellow oil (17.83 g, 98 %).

^1H NMR (400 MHz, CDCl_3) δ 7.79 (dd, $J = 5.4, 3.1$ Hz, 2H), 7.66 (dd, $J = 5.6, 3.0$ Hz, 2H), 3.53 (d, $J = 7.2$ Hz, 2H), 1.85 (h, $J = 6.3$ Hz, 1H), 1.41 – 1.16 (m, 26H), 0.88 – 0.77 (m, 6H); MS: 371.28 (APPI); Calcd. $[\text{C}_{24}\text{H}_{37}\text{NO}_2]$: 371.28.

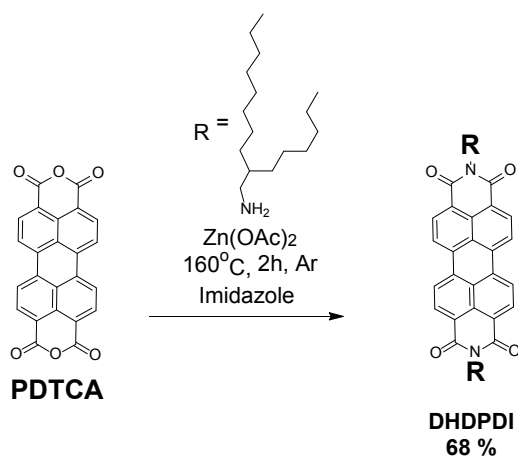
Synthesis of 2-hexyldecan-1-amine (HDNH_2)



The alkyl Phthalimide (1 eq) and Hydrazine hydrate (3 eq) were dissolved in methanol (10 g per 100 mL), and left to stir at 95 °C. The reaction was monitored by TLC until all the starting imide has disappeared and the reaction was stopped. Reaction mixture was then transferred to an RBF, and methanol was evaporated. DCM (100mL) was added into the crude, and was then washed with 10% KOH. Phase separation of the organic layer was done with DCM and the crude was dried and solvent evaporated to afford a yellow oil of the alkyl amine. ^1H NMR (400 MHz, CDCl_3) δ 3.38 (s, 1H), 2.57 (d, $J = 4.2$ Hz, 2H), 1.97 (s, 1H), 1.24 (s, 26H), 0.86 (t, $J = 6.5$ Hz, 6H). MS: 241.28 (APPI); Calcd. $[\text{C}_{16}\text{H}_{35}\text{N}]$: 241.28

Synthetic steps of HD-PDIMBr

Alkylation of PDTCA with HDNH_2

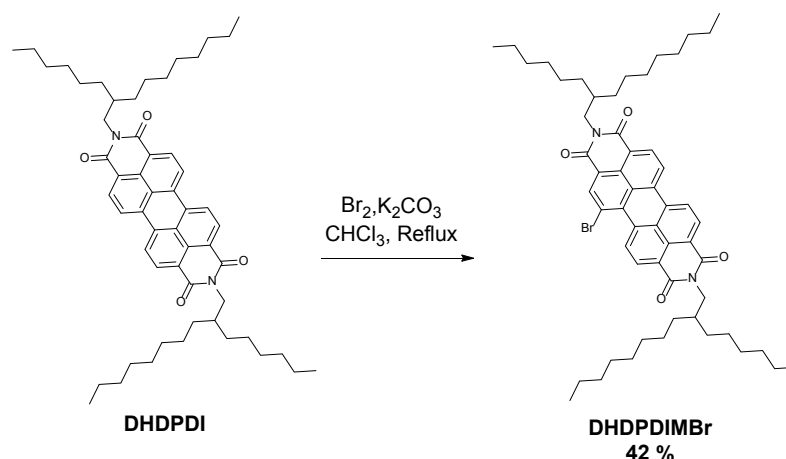


A mixture of perylene-3,4,9,10-tetracarboxylic dianhydride PDTCA (1.0 mmol), $\text{Zn}(\text{OAc})_2$ (0.75 mmol), imidazole (4.0 g) and the respective alkyl amine (3.0 mmol) was vigorously stirred at 160 °C

for 2 h. After cooling to RT, the mixture was dissolved in minimum amount of THF and precipitated in 300 mL 2M HCl/MeOH 2:1 V/V. The precipitate was collected by filtration, washed with H₂O followed by MeOH and dried at 80 °C in vacuum. The crude product was further purified by column chromatography using Chloroform as eluent. **DHDPDI** was obtained as a bright red powder at an average Yield 68 %.

¹H NMR (400 MHz, CDCl₃) δ 8.34 (d, J = 7.8 Hz, 4H), 8.13 (d, J = 8.1 Hz, 4H), 4.08 (d, J = 7.3 Hz, 4H), 1.98 (p, J = 6.4, 6.0 Hz, 2H), 1.47 – 1.37 (m, 2H), 1.35 (s, 4H), 0.86 (q, J = 6.5 Hz, 24H); MS: 838.56 (APPI): Calcd. [C₅₆H₇₄N₂O₄]: 839.22.

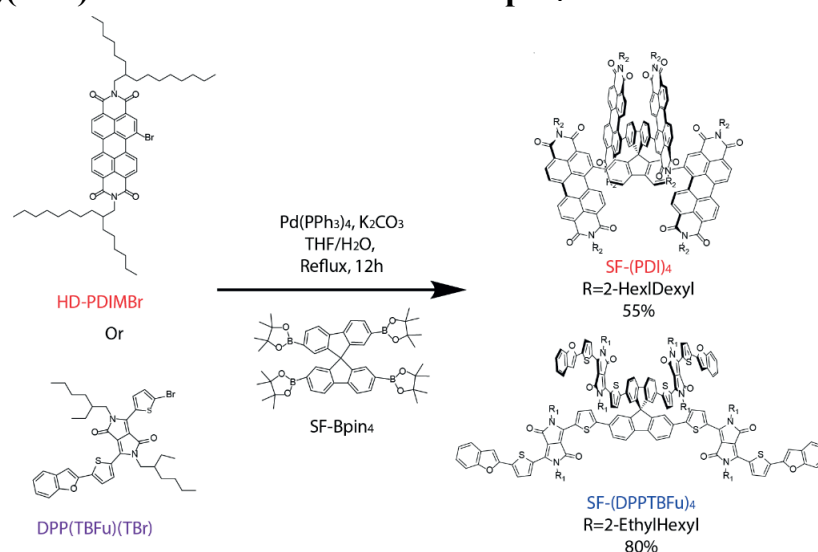
Mono Bromination of DHDPDI



A mixture of DHDPDI (3.5 g, 6.6 mmol), K₂CO₃ (3.5 g, 25.4 mmol), 70 mL CHCl₃ and 17 mL Br₂ was stirred at reflux for 4 h. The excess bromine was removed by adding aqueous Na₂SO₃. Then, the crude product was purified by silica gel column chromatography with dichloromethane as eluent. DHDPDIMBr (1.9 g, 42 %) were obtained as red solid.

¹H NMR (400 MHz, CDCl₃) δ 9.54 (d, J = 8.3 Hz, 1H), 8.62 (s, 1H), 8.49 – 8.39 (m, 3H), 8.25 (dd, J = 8.2, 4.8 Hz, 2H), 4.08 (dd, J = 17.3, 7.3 Hz, 4H), 1.99 (dq, J = 17.8, 6.0 Hz, 2H), 1.53 – 1.18 (m, 48H), 0.87 (q, J = 6.8, 6.3 Hz, 12H); MS: 916.48 (APPI): Calcd. [C₅₆H₇₃BrN₂O₄]: 918.11

General Synthetic Procedure for Suzuki Coupling reaction of the DPP(TBFu)(TBr) and HE-PDIMBr with SF-Bpin₄



Scheme S1. Final Suzuki Coupling reaction of the respective DPP(TBFu)(Tbr) and HD-PDIMBr chromophoric unit with the central spiro core SF-Bpin₄

A mixture of SF-Bpin₄ (1 eq), DPP(TBFu)(Tbr) or HD-PDIMBr (4.5 eq), Pd(PPh₃)₄ (10 %), Potassium Carbonate (1 M), was added into a solution of THF/H₂O (Volume Ratio-10:3), and was degassed using a vacuum/argon flushing cycle three times before refluxing at 66 °C for 24 h under Argon atmosphere. After 24 h, the reaction mixture was then cooled to RT and precipitated in excess methanol which was filtered with celite, and extracted with CHCl₃. The crude solution was then washed with brine dried over MgSO₄, and organic extract was concentrated in vacuum. The residue was then purified by flash column chromatography (eluent: dichloromethane:*n*-hexane = 1:1) to get the product as SF-(PDI)₄ as a red solid with a yield of 55 %, while a dark green solid was obtained for SF-(DPPTBFu)₄ with a yield of 80 %.

¹H and ¹³C NMR and Mass Characterization

SF-(PDI)₄: ¹H NMR (400 MHz, CDCl₃) δ 8.74 (s, 4H), 8.71 (d, *J* = 8.0 Hz, 4H), 8.47 (d, *J* = 8.1 Hz, 4H), 8.24 (s, 8H), 8.06 (d, *J* = 7.8 Hz, 4H), 7.35 (d, *J* = 9.4 Hz, 8H), 7.25 (d, *J* = 8.6 Hz, 4H), 6.95 (d, *J* = 8.2 Hz, 4H), 4.25 (d, *J* = 7.4 Hz, 16H), 3.68 (b, 8H), 3.37 (t, *J* = 10.5 Hz, 8H), 2.14 (b, 8H), 1.68 – 0.96 (m, 192H), 0.85 (dt, *J* = 18.8, 5.5 Hz, 48H); ¹³C NMR (300MHz, CDCl₃) 163.69, 163.56, 162.95, 162.56, 161.75, 151.65, 143.40, 141.66, 141.04, 135.10, 134.11, 133.98, 133.76, 131.91, 130.66, 128.95, 128.80, 128.47, 128.36, 128.09, 127.40, 126.53, 124.72, 123.57, 123.24, 123.16, 122.82, 122.36, 122.01, 121.40, 44.94, 44.09, 36.77, 36.50, 36.35, 31.96, 31.93, 31.86, 31.80, 31.70, 31.46, 30.20, 30.17, 30.02, 29.96, 29.87, 29.82, 29.70, 29.65, 29.60, 29.53, 29.37, 29.34, 29.30. (MALDI-TOF): *m/z* [M]⁺ = 3665.21

SF-(DPPTBFu)₄: ¹H NMR (400 MHz, CDCl₃) δ 8.97 (d, *J* = 4.0 Hz, 4H), 8.85 (d, *J* = 3.9 Hz, 4H), 8.02 (d, *J* = 8.0 Hz, 4H), 7.83 (d, *J* = 8.0 Hz, 4H), 7.60 (d, *J* = 7.5 Hz, 8H), 7.53 (d, *J* = 8.2 Hz, 4H), 7.41 – 7.31 (m, 8H), 7.28 (b, 4H), 7.13 (s, 4H), 7.06 (s, 4H), 4.03 (dp, *J* = 14.8, 7.4, 6.3 Hz, 16H), 1.89 (dq, *J* = 25.4, 6.7 Hz, 8H), 1.48 – 1.05 (m, 64H), 0.88 (tt, *J* = 16.4, 7.3 Hz, 48H); ¹³C NMR (300 MHz, CDCl₃) 161.72, 161.58, 154.97, 150.03, 149.34, 139.80, 139.35, 137.77, 136.68, 136.32, 133.58, 129.58, 128.94, 128.86, 125.45, 125.34, 124.89, 123.53, 121.46, 121.34, 121.18, 53.44, 45.93, 39.23, 31.61, 30.32, 29.72, 28.47, 28.40, 23.75, 23.65, 23.08, 23.03, 22.67, 14.14, 14.06,

Curriculum Vitae

Xavier JEANBOURQUIN

École polytechnique fédérale de Lausanne

Date of birth: April 2nd, 1989
Origin: Switzerland

E-mail: xavier.jeanbourquin@epfl.ch

Academic Formation

- 2013-2017 PhD Student in the Laboratory for Molecular Engineering of Optoelectronic Nanomaterials at EPFL
Title: Engineering of supramolecular self-assembly in solution-processed organic semiconductors.
Supervisor: Prof. Kevin Sivula
- 2012 – 2013 Master Thesis at Imperial College London, (EPFL Erasmus)
Title: Mechanism study of the guanidinium additive in Dye Sensitized Solar Cells and characterization of CH₃NH₃PbI₃ perovskite solid state cells.
Supervisors: Dr. B. O'Regan and Prof. M. K. Nazeeruddin
- 2011 – 2013 Master of Science in Molecular & Biological Chemistry, EPFL
Specialization in physical, inorganic and bio-chemistry.
Master project in the group of Prof. J.-E. Moser entitled "Effect of TiO₂ morphology and TiCl₄ treatment on electron back reaction in dye sensitized solar cells."
- 2008 - 2011 Bachelor in chemistry, EPFL

Professional and Teaching Experiences

- 2014-2017 Teaching assistant for the following courses at EPFL,
"Introduction to chemical engineering Laboratory Works" (3 semesters)
"Chemical equilibria and reactivity" (3 semesters)
"General chemistry I (for medical student)" (1 semester)
Supervision of a master project in chemical engineering & biotechnology
- 2013 Research Assistant in the Nanostructured Materials & Devices Group of Imperial College London,

Technical skills

Basic organic synthesis, column chromatography and recrystallization.

Fabrication and characterisation of organic solar cells, organic field effect transistors, space-charge limited current diodes and dye-sensitized solar cells. Vacuum deposition of thin film via sputtering or thermal evaporation.

Surface characterisation via atomic force microscopy, kelvin probe force microscopy, nanomechanical young modulus mapping and conductive measurements.

Crystallinity of thin film characterisation via X-ray diffraction and differential scanning calorimetry.

Transient photocurrent and photovoltage measurements.

Programming on Igor and Labview.

Languages

French: Native language

English: Advanced oral and written competences

German: Basic oral and written competences

Scientific publications

Engineering the self-assembly of diketopyrrolopyrrole-based molecular semiconductors via an aliphatic linker strategy.

Jeanbourquin, X. A., Rahmanudin, A., Gasperini, A., Ripaud, E., Yu, X., Johnson, M., Guijarro, N., and Sivula, K. *Journal of Materials Chemistry A*, **2017**, 5, 10526–10536.

Rediscovering a Key Interface in Dye-Sensitized Solar Cells: Guanidinium and Iodine Competition for Binding Sites at the Dye/Electrolyte Surface.

Jeanbourquin, X. A., Li, X., Law, C., Barnes, P.R.F., Humphry-Baker, R., Lund, P., Asghar, M.I., and O'Regan, B.C. *Journal of the American Chemical Society*. **2014**, 136, 7286–7294.

Enhancing the Thermal Stability of Solution-Processed Small-Molecule Semiconductor Thin Films Using a Flexible Linker Approach.

Gasperini, A., Jeanbourquin, X. A., Rahmanudin, A., Yu, X., and Sivula, K. *Advanced Materials*. **2015**, 27, 5541–5546.

Effect of molecular weight in diketopyrrolopyrrole-based polymers in transistor and photovoltaic applications.

Gasparini, A., Jeanbourquin, X.A., and Sivula, K. *Journal of Polymer Science Part B: Polymer Physics*. **2016**, 54, 2245–2253.

Evaluating Charge Carrier Transport and Surface States in CuFeO₂ Photocathodes.

Prévo, M.S., Jeanbourquin, X.A., Bourée, W.S., Abdi, F., Friedrich, D., van de Krol, R., Guijarro, N., Le Formal, F., and Sivula, K. *Chemistry of Materials*. **2017**, 29, 4952–4962.

Intrinsic Halide Segregation at Nanometer Scale Determines the High Efficiency of Mixed Cation/Mixed Halide Perovskite Solar Cells.

Gratia, P., Grancini, G., Audinot, J.-N., Jeanbourquin, X.A., Mosconi, E., Zimmermann, I., Dowsett, D., Lee, Y., Grätzel, M., De Angelis, F., et al. *Journal of the American Chemical Society*. **2016**, 38, 15821–15824.

Robust Hierarchically Structured Biphasic Ambipolar Oxide Photoelectrodes for Light-Driven Chemical Regulation and Switchable Logic Applications.

Bourée, W.S., Prévo, M.S., Jeanbourquin, X.A., Guijarro, N., Johnson, M., Formal, F.L., and Sivula, K. *Advanced Materials*. **2016**, 28, 9308–9312.

Semiconducting alternating multi-block copolymers via a di-functionalized macromonomer approach.

Gasparini, A., Johnson, M., Jeanbourquin, X.A., Yao, L., Rahmanudin, A., Guijarro, N., and Sivula, K. *Polymer Chemistry*. 2017, 8, 824–827.

Hybrid Heterojunctions of Solution-Processed Semiconducting 2D Transition Metal Dichalcogenides.

Yu, X., Rahmanudin, A., Jeanbourquin, X.A., Tsokkou, D., Guijarro, N., Banerji, N., and Sivula, K. *ACS Energy Letters*. **2017**, 2, 524–531.

CuInGaS₂ photocathodes treated with SbX₃ (X = Cl, I): the effect of the halide on solar water splitting performance.

Guijarro, N., Prévo, M.S., Johnson, M., Yu, X., Bourée, W.S., Jeanbourquin, X.A., Bornoz, P., Formal, F.L., and Sivula, K. *Journal of Physics D: Applied Physics*. **2017**, 50, 044003.

Heterotetracenes: Flexible Synthesis and in Silico Assessment of the Hole-Transport Properties.

Li, Y., Gryn'ova, G., Saenz, F., Jeanbourquin, X.A., Sivula, K., Corminboeuf, C., and Waser, J. *Chemistry a European Journal*. **2017**, 23, 8058–8065.

Autodecomposition Approach for the Low-Temperature Mesostructuring of Nanocrystal Semiconductor Electrodes.

Guijarro, N., Prévo, M.S., Jeanbourquin, X.A., Yu, X., and Sivula, K. *Chemistry of Materials*. **2015**, 27, 6337–6344.

A Bottom-Up Approach toward All-Solution-Processed High-Efficiency Cu(In,Ga)S₂ Photocathodes for Solar Water Splitting.

Guijarro, N., Prévo, M.S., Yu, X., Jeanbourquin, X.A., Bornoz, P., Bourée, W., Johnson, M., Le Formal, F., and Sivula, K. *Advanced Energy Materials*. **2016**, 6, n/a-n/a.

Templating Sol–Gel Hematite Films with Sacrificial Copper Oxide: Enhancing Photoanode Performance with Nanostructure and Oxygen Vacancies.

Li, Y., Guijarro, N., Zhang, X., Prévo, M.S., Jeanbourquin, X.A., Sivula, K., Chen, H., and Li, Y. *ACS Applied Materials & Interfaces*. **2015**, 7, 16999–17007.

Conferences and Summer Schools

Hybrid and Organic Photovoltaics Conference, May 2013, Seville, Poster contribution

“Effect and mechanism of the guanidinium additive in dye-sensitized solar cells”

Organic (Opto)Electronics International Summer School, June 2014, Boutheon, no contribution

European Materials Research Society Fall Meeting, September 2015, Warsaw, Oral contribution *“Morphology control in organic semiconductor thin films”*

Euro AFM Forum, June 2016, Geneva, Oral contribution

“AFM characterization of solution-processed materials for low-cost solar energy conversion”

Materials Research Society Fall Meeting, December 2016, Boston, Oral contribution *“Aliphatically linked conjugated small molecules for crystal structure engineering and stability enhancement in organic solar cell”*

American Chemical Society National Meeting, April 2017, San Fransisco, Oral contribution *“Self-assembly engineering of organic semiconductors”*

Scholarship

Erasmus scholarship

Swiss chemical society travel award

Membership

Swiss Chemical Society (SCS)

References

Prof. Kevin Sivula

Ecole Polytechnique Fédérale de Lausanne

Dr. B. O'Regan

Imperial College London

Dr. Néstor Guijarro

Ecole Polytechnique Fédérale de Lausanne

